Thermal methods for fatigue characterization of components

Department of Mechanics, Mathematics and Management
Aerospace Science and Engineering
Ph.D. Program
SSD: ING-IND/14– MECHANICAL DESIGN AND MACHINE CONSTRUCTION

Final Dissertation

Thermal Methods for Fatigue Characterization of Components

by
Mohammad Zaeimi

Supervisors:

Prof. U. Galietti

Asst. Prof. R. De Finis

Coordinator of Ph.D. Program:
Prof. M. D. De Tullio

Course n°36, 01/11/2020-31/01/2024

Politecnico di Bari

Department of Mechanics, Mathematics and Management

Aerospace Science and Engineering

Ph.D. Program

SSD: ING-IND/14– MECHANICAL DESIGN AND MACHINE CONSTRUCTION

Final Dissertation

Thermal Methods for Fatigue Characterization of Components

by

Mohammad Zaeimi

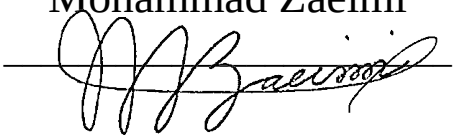

Referees:

Assoc. Prof. G. Pitarresi

Asst. Prof. C. Colombo

Supervisors:

Prof. U. Galietti

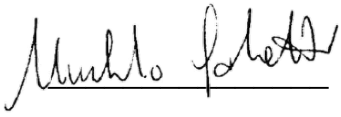

Asst. Prof. R. De Finis

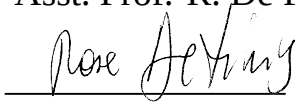

Coordinator of Ph.D Program:

Prof. M. D. De Tullio

Course n°36, 01/11/2020-31/01/2024


this too shall pass

Acknowledgments

To my family, words cannot express my gratitude for the sacrifices you have made and the endless love and encouragement you have provided. Your belief in me has been my greatest source of strength, and I am forever grateful for your endless support.

My deepest gratitude to my advisor Professor Umberto Galietti and Co-Advisors Professor Rosa De Finis and Professor Davide Palumbo, for their unwavering support, invaluable guidance, and endless patience throughout this journey. Their expertise and encouragement have been instrumental in shaping the direction of my research and in helping me navigate the challenges along the way.

A heartfelt thank you to the professor Michael M. Khonsari and Dr. Ali Mahmoudi at Louisiana State University, USA, for their warm welcome, invaluable insights, and enriching experiences during my period abroad.

To Dr. Zahra Isania, and all my close friends, your constant support, understanding, and encouragement have made all the difference. Your presence in my life has brought joy, laughter, and much-needed perspective, reminding me of the importance of balance and friendship amidst the rigors of academic pursuit.

Abstract

In recent years, the thermographic technique has been regarded as a key tool to investigate the fatigue behavior of materials instead of time and cost consuming traditional methods. One way to assess the fatigue as an irreversible process is studying the temperature signature due to the heat dissipation during the cyclic loading. Numerous studies have suggested that the shift from anelastic to inelastic strains results in a significant level of intrinsic dissipation, indicating the presence of the fatigue damage.

The primary objective of this study is to explore heat dissipation in fatigue tests through a combination of experimental methods and numerical models by utilizing the fundamental temperature component related to dissipation, the second amplitude harmonic (SAH) of the temperature. The proposed hybrid approach integrates experiments with a numerical model to pinpoint the specific volume generating heat during the fatigue test. The investigation also delves into the impact of loading frequency on the fundamental temperature component associated with dissipation.

In experimental part of the study, a comprehensive campaign was carried out to capture the material's response under both static and cyclic loading conditions. The experimental data are employed for comparing the accuracy of different thermal indices in fatigue limit estimation and establishing the numerical model, act as reference data for comparison.

In the numerical part of the study, models are established in COMSOL Multiphysics 5.6 to simulate the temperature distribution on the surface of the specimen. After the verification with analytical solution of 1-D heat equation, a model is proposed for heat source identification. One of the main controversial issues in fatigue characterization is addressed in this study, whether the entire gauge volume dissipates or not. Additionally, the effect of loading frequency on SAH of temperature reveals its limitation in thermographic measurement and fatigue assessment.

Keywords: Heat source, Fatigue test, Thermographic technique, Finite element simulation, Second harmonic amplitude of temperature

Contents

List of Figures

List of Tables

1 Introduction

Fatigue phenomena have been a challenging issue as one of the primary causes of failure due to the complexities involved in modeling material behavior. The cyclic nature of the load induces the creation of dislocations, which in turn leads to plastic deformation. In other words, depending on the loading level, it leads microscopic flaws [1-3] to grow and accumulates into macroscopic cracks and by macroscopic crack propagation, fatigue failure occurs [4]. Since most of the structures are subjected to cyclic loadings during their life, probing into the fatigue phenomenon provides key features for selection of efficient materials [5].

Back in 1829, the initial fatigue test was conducted in Germany. It involved steel chains undergoing 100,000 cycles of tension at a rate of 10 cycles per minute. Following that, a substantial number of valuable researches have focused on the fatigue characteristics of materials. This is because the importance of this topic in the field of engineering [1, 6, 7]. Out of these research efforts, fracture mechanics has emerged as a prominent method for comprehending and explaining fatigue behavior over the past few decades.

While enthusiasm still surrounds concepts like fracture toughness and fatigue endurance limits, challenges arise during fatigue testing of industrial components and structures due to the time and cost consuming nature of the tests. As a result, increasing attention has been directed toward nondestructive evaluation (NDE) techniques because of their critical role in assessing fatigue life, evaluating structural integrity, preventing failures, and material savings.

In this domain, various NDE techniques, such as ultrasonics, acoustic emission, X-ray, neutron, and computed tomography, have been employed to monitor mechanical damage [2, 8-12]. However, most of these methods have inherent limitations. Some methods demand specialized sample preparations and may not be applicable in typical working conditions, such as X-ray and neutron. Others rely on sensors affixed to only a few points on the materials of interest, as seen with ultrasonics, acoustic emission. In the present study, the infrared thermography detection technology, as a NDE method, which requires no contact with the specimen has been used to assess the dissipation phenomenon during the fatigue test by proposing a hybrid approach, linking the experimental thermal footprint from the surface of the specimen and a numerical model.

The Motivation of this study is to obtain more comprehensive information on the fatigue behavior of components and structures in a rapid way and develop procedures for fatigue damage monitoring.

Specifically, the main goal is the investigation of the heat dissipations during the fatigue test using both experiments and numerical models. It is planned to identify the volume producing heat during fatigue test by means of a FEM model, and study the effect of loading frequency on the fundamental temperature component related to dissipation, experimentally and numerically. The former aids in determining the validity of the assumption made by previous models, which consider the entire gauge volume as the source of heat [13-15]. Meanwhile, the latter delves into how diffusion phenomena (arising from loading frequency in this study or geometrical complexity) can impact the aforementioned temperature component, thereby assisting in thermographic measurements. Neither of these investigations can be solely conducted through the experiment; hence, proposing a hybrid approach that integrates a numerical model with experimental data to address the above challenges is the most important novelty of this work.

This study is organized as follows, according to the above purposes.

Chapter 2 intends to meticulously examine and assess the different thermography-based methodologies used for rapid estimating the fatigue behavior of materials. The focus extends to a comparison between the just said methodologies in evaluating the fatigue of metals and components, elucidating the potential of diverse thermal indices in this area. Furthermore, it involves a comprehensive discussion dissecting the advantages and drawbacks of each method, while also focusing on unresolved aspects that merit further investigation. The outcomes from the present analysis help to step forward the research on the use of thermography-based methodologies.

Chapter 3 begins with an exploration of the material and geometry employed. Following this, the tensile test section deals with the material mechanical properties assessment and their responses under tension. Two types of steels for different purposes were used, comparing different thermal indices in fatigue limit estimation and heat source identification. Some parts of this campaign were done during the abroad activities and the rest at the home university. Subsequently, the focus shifts to the cyclic loading test, which comprises two key sub-sections, the stepwise test and constant amplitude test. The last sub-section introduces the data processing, providing a glimpse into the methods employed to analyze and interpret the experimental data. The aim of this section is mainly to provide details about the procedure and experimental setup for rapid evaluation of fatigue presented in pervious section, using thermography-based techniques.

Chapter 4 presents the numerical model in two main parts. The first part introduces and details the numerical model along with its verification process, emphasizing the utilization of a finite element model featuring a single heat source. The primary method of verification involves the utilization of an

analytical solution of the 1D heat equation, found originally in this work, which incorporate both constant and cyclic heat sources. The second part is dedicated to heat source identification, where a finite element model incorporating randomly distributed heat volumes is employed. Next, the comprehensive process of heat source identification, covering aspects such as the definition of imposed heat, reference experimental data, preliminary considerations, and criteria for identifying dissipated volumes, is proposed. This chapter proposes a useful framework for creating a hybrid approach linking the proposed numerical model with experimental data for heat source identification, and generally investigating the dissipation phenomenon in fatigue.

Chapter 5 presents both experimental and numerical results. For the first one, after data preparation and extracting the actual fatigue limit from the S-N curve, the prediction of the fatigue limit is done by extracting the variation of thermal indices with stress amplitude. For this purpose, the thermal indices trend is analyzed based on both threshold method and Loung's method. It should be noted that, through an investigation, a potential issue with the threshold method is revealed: the sensitivity of the method to its parameters in fatigue estimation. Additionally, the study also investigates the challenges associated with measuring one of the thermal indices, specifically the initial slope of temperature. One significant feature of this part of the results is employing the same dataset for comparing different methods' efficiency. Moving to the numerical results, firstly, the main verification of the numerical model with a single heat source is presented. Next, the influence of the number of pixels and the distribution of heat sources on the numerical results are proposed, before proposing the initial model with randomly distributed heat sources. Additionally, a detailed investigation of the impact of noise sources (e.g. motion) is presented. After comparing the results with the corresponding experimental ones, showing the effect of considered noises on the numerical output, a modified model is presented based on the size of the heat sources in the proposed model. Afterwards, further investigation on the effect of the movement noise based on the hypothetical data is proposed, giving a guide to explain the temperature pattern present in the experimental data. Finally, the effect of loading frequency on the second harmonic amplitude of the temperature is studied. Actually, the thermographic measurements may be influenced by the lack of signal stabilization and sample motion resulting from imposing high loading frequencies. Thus, investigating this effect poses a significant challenge through experiments, in contrast to utilizing a validated numerical model

Finally, Chapter 6 concludes the study and presents the future works.

2 Thermographic techniques for fatigue characterization and assessment: a literature review

Throughout the years, infrared thermography has demonstrated its versatility as a valuable tool in the realms of experimental mechanics and mechanical design. This non-contact and non-destructive method enables thorough examinations of structural integrity [16, 17] (including the detection of defects in steel plates [18], composites [19-22], 3D printed materials [23] and welded joints [24], the evaluation of fatigue cracks [25]), the stress analysis (thermoelastic stress analysis-TSA) evaluations [26-31] and energy-based assessments to study fatigue processes [32, 33].

Advancements in equipment and robust data analysis tools have propelled the evolution of thermography-based techniques. Presently, the robustness and reliability these methods can be affirmed, providing valuable support for fatigue studies encompassing damage analysis, assessment, residual life predictions, and crucially, estimations of fatigue limits [34, 35].

Basically, the drive to create alternative and inventive methods for determining the fatigue limit, utilizing an experimental technique in fatigue tests, can be traced back to two main points:

1. The speed of the testing procedures in contrast to traditional protocols,
2. The opportunity to acquire additional information regarding the material's condition during loading.

Referring to the first point, traditional and widely recognized methods for characterizing fatigue [36, 37], such as conducting constant amplitude tests to derive the Wöhler curve, serve as a standard approach.

Nevertheless, these methods are both time and cost-consuming, given the necessity to test a substantial number of samples for a statistically valid fatigue limit estimation. The testing duration involves considerable energy, operational, and maintenance costs. In general, a classic fatigue test involves a pristine material tested until it fails under specific conditions of stress level, stress ratio, and mechanical frequency.

In order to minimize both testing duration and expenses, rapid fatigue tests were developed according to the approach of La Rosa and Risitano [37]. This approach involves a series of constant amplitude loading blocks applied incrementally. In each block, the stress amplitude and mean stress progressively increase, maintaining a constant frequency and stress ratio for a specified number of cycles, until the

material experiences failure.

During such a test program, the material undergoes various damage phases [38, 39], as elaborated upon later. Transitioning from one phase to another induces changes in behavior that correlate with crucial stages in the fatigue life, ultimately facilitating the estimation of the fatigue limit.In other words, the fundamental idea behind the 'stepwise' test is that the fatigue limit corresponds to the initial substantial temperature fluctuation linked to the damage, using a specific loading procedure [37-40].

Regarding the second point, a pivotal factor in the advancement of this thermography-based method lies in the potential to gather additional complementary information about fatigue behavior beyond what a conventional test offers. This encompasses the assessment of energy dissipation resulting from fatigue and the identification of the initiation and locations of damage [41]. The processing of thermal signal ensures somehow the just said outputs.

Certainly, it has been forty years since the inception of tests utilizing an infrared (IR) camera to consistently capture parameters delineating fatigue processes [42-46]. The mentioned method has evolved from its initial procedure and has witnessed numerous enhancements, particularly in assessing heat sources associated with intrinsic dissipations [47, 48]. The methods outlined in the literature, based on estimating heat sources associated with damage phenomena [46, 49, 50], are based on the assessment of specific energy-based indices/parameters, including:

a) Mean temperature rise [51-55],
b) Initial slope of the mean temperature [35, 56, 57],
c) Energy loss per each cycle [58],
d) Harmonic components of temperature [41, 47, 59, 60],
e) Loss of the adiabaticity (the study of the thermoelastic signal and the thermoelastic phase shift) [41, 61-63], and
f) Fracture fatigue entropy [64].

Providing an overall perspective, Figure 1 underscores significant advancements in fatigue assessment using thermographic methods. It is noteworthy that, in addition to these progressions, further studies in this context will be addressed later.

(All of the works proposed in the timeline can be found in the reference list)

Figure 1 Some milestones in developing history of thermographic techniques for fatigue assessment

2-1 State of art and the application of the infrared thermography

It all commenced with the discovery of infrared radiation by Sir William Herschel [65] and the development of IR cameras. These cameras contributed to the widespread adoption of thermography, enabling the analysis of objects without direct contact. Prior to the advent of IR cameras, temperature variations in specific object areas were measured using thermocouples. However, contemporary high-resolution IR cameras are now employed in various innovative techniques for studying materials and stress.

A comprehensive summary and elucidation of the fundamental concepts underlying thermography proposed by Meola [66], while Maldague [67] presented the advancements in 1994. Throughout its history, thermography has been used in various ways, including analyzing stress [68, 69], studying how cracks grow and how materials break [70, 71], looking at materials and fatigue [72, 73], like composites [74] and construction materials [75], welding check [66], exploring topics like integrated electric circuits [76], and even in medical uses [77]. One interesting use among these applications is studying fatigue. The fundamental concept behind employing thermography for fatigue lies in comprehending the energy released by a material during repeated loading and unloading. At the heart of this principle is "thermoelasticity," a theory initially explored by Lord Kelvin in 1853 [78] and 1857 [79], and also discussed by physicist Biot in 1956 [80].

The use of thermography in thermoelastic stress analysis (TSA) originated in the 1970s. In this method, slight temperature variations are induced by applying minimal stress. Typically, the stress applied is maintained below the threshold at which the material can endure at least one million cycles, referred to as the endurance limit. As the material undergoes compression and tension, its temperature fluctuates. If the cycling occurs at a sufficiently high frequency, the specimen effectively behaves as an adiabatic system, and the data captured by an infrared camera can be correlated with the primary stresses in the material. Regions of the specimen exhibiting notably elevated temperatures can be examined to understand the impact of stress concentration on the component.

The fatigue analysis applications of IR thermography follow a comparable principle. However, there is no longer a necessity for the applied load to stay below the endurance limit. When a specimen undergoing cyclic loading is outfitted with a strain gauge or an extensometer, it becomes feasible to measure a hysteresis loop. The region enclosed by this loop represents the energy released by the specimen. Subsequently, IR thermography can be employed to quantify this energy. Numerous researchers have explored hysteresis loops, and Morrow [81], for instance, formulated an equation for

predicting hysteresis energy. Later works have used hysteresis energy as a method for predicting fatigue life and studying cyclic loading [58, 82, 83].

2-2 Theory

2-2-1 Heat sources related to fatigue damage

2-2-1-1 Micro/macro mechanisms involved in fatigue

As evidenced by pioneering research [84], it is firmly established that fatigue constitutes a dissipative process [1, 85-88] originating at the microscopic level [89-91] and progressing to fatigue cracks, as elucidated by Schijve [5], where crack initiation occurs at stress amplitudes below the yield limit.

Bauschinger [90] demonstrated that under cyclic loading, very minute inelastic, specifically plastic, micro-strains occur [92]. However, the microscopic causes of fatigue failure remained unclear and were not thoroughly investigated until the early twentieth century. It was during this period that Ewing and Humfrey [93] observed the emergence of slip bands and microcracks on the surface of fatigued steel. Subsequently, damage mechanics explained that the manifestation of cyclic slips, considered a non-recoverable phenomenon due to strain hardening [5], leads to slip accumulation. This, in turn, results in the development of a microcrack, with the potential for further growth when subjected to additional cyclic loading, as depicted in Figure 2a.

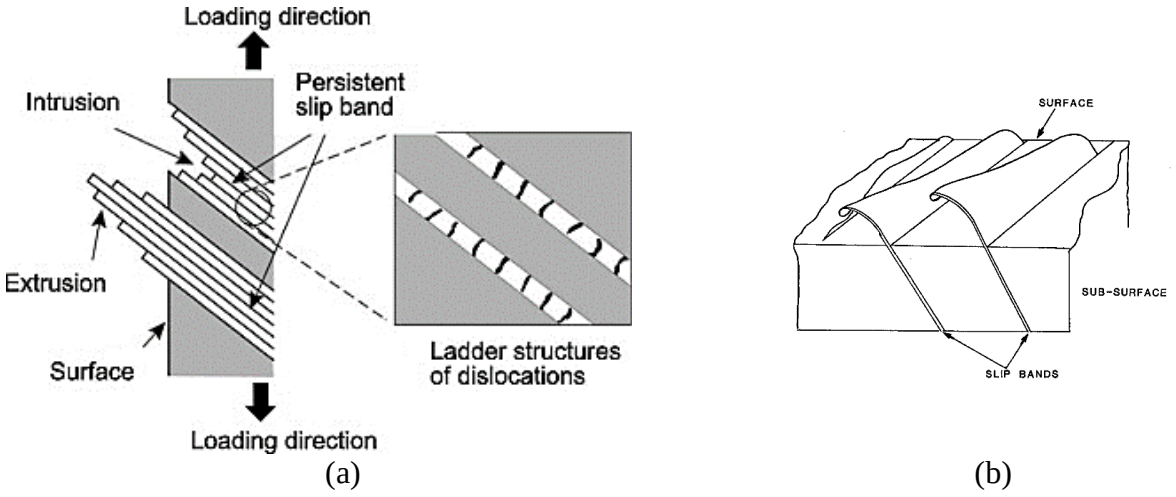

Figure 2 (a) Fatigue crack initiation mechanism [94], b) schematic illustration of slip band extrusions during a cyclic straining [95]

From a macroscopic perspective, the slip bands generated during cyclic loading lead to the creation of extrusion-intrusion pairs, subsequently causing surface roughness. This surface roughness could directly contribute to the initiation of cracks (see Figure 2).

As per Murakami [92], the fatigue limit can be characterized as the 'threshold stress for crack propagation' rather than the 'critical stress for crack initiation'. The enduring and pertinent insight derived from the studies of Bauschinger [90] and Ewing & Humfrey [93] is that fatigue damage stems from the accumulation of numerous extremely small irreversible cyclic micro-strains that develops macrocracks.

2-2-1-2 Energy Dissipation in fatigue

From an energetic standpoint, in a fatigue test, disregarding potential phase transformations in the material (e.g., shape memory alloys or crystallizable rubbers), two internal heat sources are generated due to mechanical loading: dissipative and thermoelastic sources [96]. The former contributes to the rise in the specimen's temperature, while the latter, the reversible source, is associated with thermomechanical coupling phenomena. In the work of Boulanger [48], the authors analytically separated the thermal contributions of these sources to analyze their individual influence on fatigue damage. Concerning the dissipative heat component, it is linked to fatigue damage mechanisms arising from the inelastic/anelastic behavior of the material [91, 97].

As mentioned earlier, irreversible plastic deformations play a role in crack nucleation, growth, and propagation. In fatigue tests, when there are macroscopic strains in the material, mechanical energy is dissipated in each loading cycle. This dissipation of energy can be graphically depicted by a hysteresis loop in the stress-strain curve [98-100] with the area serving as a measure of the dissipated energy. Some of this energy transforms into heat, while another portion remains internally stored, resulting in irreversible deformations [14, 97, 101].

As can be seen in Figure 3a, in accordance with the initial principle of thermodynamics applied to a body under mechanical loading, the total power equilibrium is outlined as follow [14, 101]:

$$\dot{W} + \dot{Q} = \dot{U} = \dot{E}_{rev} + \dot{E}_d + \dot{E}_s \quad (1)$$

where $\dot{W}$ is the rate of total work energy supplied to the material; $\dot{Q}$ is the rate of the heat exchanged with the environment and $\dot{U}$ is the internal energy variation. $\dot{E}_{rev}$ is the variations of power of reversible energy; $\dot{E}_d$ is the portion of mechanical power that converts in heating and $\dot{E}_s$ is the rate of internal energy that does not convert in heating. The combination of $\dot{E}_d + \dot{E}_s$ shows the rate of irreversible energy variations which are related to the fatigue damage. Different techniques indirectly

derived it by analyzing the difference between the mechanical energy ($\dot{W}$) and the energy released as heat ($\dot{Q}$) [14].

It is important to highlight that an internal heat source resulting from damage (depicted by the blue circle in Figure 5a) generated during cyclic loading can be identified by its signature on the surface of the sample (the red circle in Figure 3a) using the Infrared thermography technique. For instance, in Figure 3b, a temperature map corresponding to a C45 specimen subjected to fully reversed loading (R = -1) is displayed. These maps demonstrate how temperature variations on the specimen's surface, serving as an indicator of dissipation, correlate with the stress amplitude. Below the fatigue limit, this temperature increase is minimal. However, beyond the fatigue limit, it substantially rises as damage accumulates, eventually reaching its peak when the specimen fails.

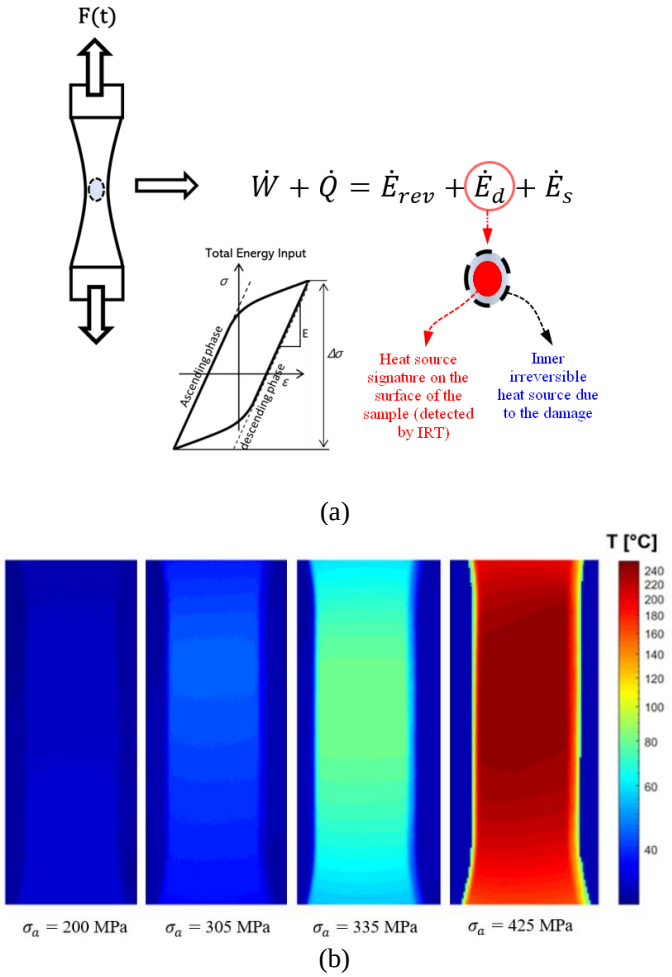

Figure 3 (a) Energy balance during cyclic loading [101] (b) the temperature change during the fatigue test for C45 specimen tested at R=-1 ($\boldsymbol{\sigma_a}$=200 MPa and 305 MPa below the fatigue limit, $\boldsymbol{\sigma_a}$=335 MPa above the fatigue limit and $\boldsymbol{\sigma_a}$=425 MPa at end of the test) [102]

2-2-1-3 The Relationship between Energy Dissipation and Temperature

The stress-strain hysteresis characteristics in metals rely on the micro-mechanisms responsible for dissipating energy during cyclic deformation. These mechanisms determine a loss of linearity between the applied stress and the corresponding strain, causing a delay in the material's response (strain) to the applied stress [99], and ultimately the appearance of the hysteresis loop (from Greek ὑστέρησις= hysteresis=delay). The ability of materials to dissipate energy through internal adjustments is known as damping [100].

In essence, when a material undergoes cyclic loading, it produces heat. This heat dissipation results from the internal friction and damping of the material. The total energy dissipated through this internal friction during cyclic loading is the sum of all the individual work done within the various elements of the material. When a sinusoidal stress is applied to the material, the imperfect elasticity of the material causes the unit deformation to intermittently deviate from the theoretical value of the stress-to-modulus of elasticity ratio (σ/E), as predicted by elastic theory. Consequently, the stress-strain diagram takes the form of a closed curve, commonly known as a 'hysteresis loop.' The area enclosed by this loop represents the energy dissipated by internal damping within a unit volume during a single cycle [103, 104].

Given that temperature serves as an indicator of internal heat sources generated by cyclic loading, various researchers have investigated the thermal patterns linked to both reversible and irreversible heat sources [27, 28, 33, 61, 101, 105, 106] as shown in Figure 4. In this figure, the quantities $\Delta\theta_E$ and $\Delta\theta_D$ represent the phase lags attributed to the thermal diffusion of the first harmonic and second harmonic, respectively, and $\Delta\theta$ the difference between them.

The reversible energy variations produced by small volume changes inducing the ‘thermoelastic effect’ [41] are represented in Figure 5. For uniaxial sinusoidal loading, the temperature fluctuations associated with thermoelastic coupling can be articulated as follows:

$$T = T_{the} \sin(2\pi f t + \pi + \varphi) \quad (2)$$

where T is the temperature variations at the loading frequency f, T_{the} is half of the peak-to-peak signal amplitude, and φ is the phase angle between temperature and loading signal [107]. In accordance with the conventional theory of thermoelastic stress analysis, the temperature and the first stress invariant exhibit opposite signs [28], which is why ‘π’ is included in Eq. (2). Figure 5 depicts the relations between T and φ in two opposite cases [41, 62].

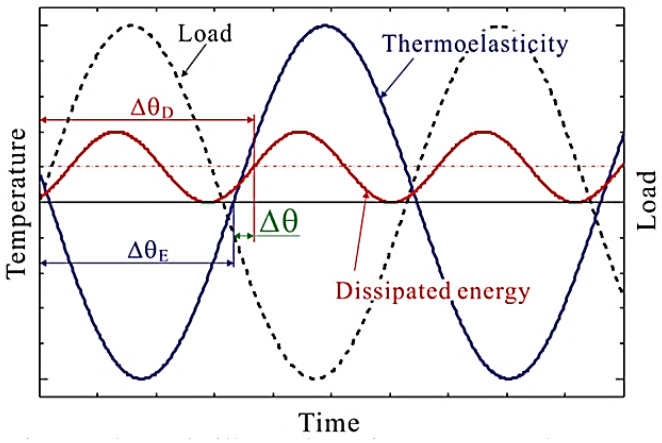

Figure 4 Schematic illustration of temperature variations due to reversible (thermoelastic) and irreversible (dissipated energy) phenomena [47].

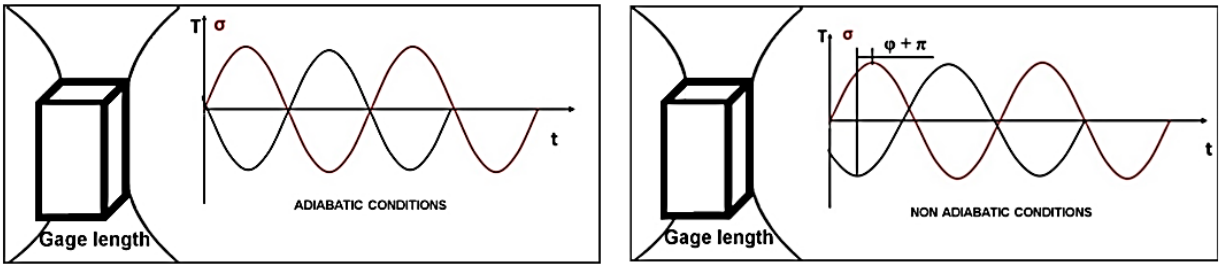

(a) (b)

Figure 5 Thermoelastic phase shift φ: temperature and stress relation (a) under adiabatic condition, (b) under non-adiabatic conditions [41]

A phase shift, influenced by various factors, may arise in the presence of phenomena leading to the breakdown of adiabatic conditions. The loss of adiabaticity can be linked to a thermal dissipative process. Typically, intrinsic dissipations result in heating through two distinct contributions:

- the heat produced under the hysteresis conditions (anelastic regime) [91],
- the heat produced under visco-plastic deformations regime [88, 108],

These heat contributions significantly impact the adiabatic nature of the processes, consequently influencing the variation in φ values. It is important to note that in the case of a purely elastic cyclic response, the level of adiabaticity (and the φ value) is contingent on the loading frequency. A higher loading frequency corresponds to a higher adiabaticity level.

By examining the irreversible energy changes during fatigue tests (Figure 3a), the irreversible work energy supplied to the material depends on the chosen stress ratio. In cases where the stored energy

(E_s) is negligible, the heat-converted energy (E_d) can be directly derived from thermodynamic balance. However, E_d can also be evaluated by scrutinizing the surface temperature of the sample [21, 109] and can be articulated as:

$$E_d = \rho C_p \Delta T_d \quad (3)$$

where ΔT_d are the dissipative temperature variations, ρ is the density and C_p is the heat capacity at constant pressure. In earlier investigations, Jordan [45] identified a direct correlation between the variation in mechanical energy (area under the hysteresis loop) and the energy transformed into heat during fatigue.

2-2-1-4 Self-heating effect

Figure 6a illustrates the evolution of the hysteresis loop within the fatigue regimes during traditional constant amplitude tests used to construct Wöhler's curve [97]. In rapid fatigue tests [110], a self-heating effect (representing mean steady-state temperature variations with the stress amplitude) [50, 111] occurs in the material, involving two mechanisms. As explained by Mareau [111], the first mechanism is linked to a reversible movement of dislocations (mechanically reversible but thermally irreversible), and the second is associated with plastic activity. The latter involves the gradual emergence of microplasticity [112], while certain aspects of the mechanisms occurring during the primary regime are still not fully understood.

In Figure 6b, according to Munier's study [50], a model was introduced to establish a connection between self-heating measurements and the high cycle fatigue characteristics of metals in relation to temperature variations. Specifically, in Figure 6b, a representative elementary volume (REV) is defined as an elasto-plastic matrix containing various lattice discontinuities, such as inclusions.

Under low stress amplitudes, it was assumed that inclusions exhibited behavior similar to the matrix, with dissipation primarily attributed to the elasto-plastic behavior of the matrix. Nevertheless, when the stress surpassed a specific threshold, plastic hardening within the inclusions came into play. Under these circumstances, the dissipation associated with the matrix aligned with the primary regime, while the dissipation in the group of inclusions was associated with the secondary regime. The latter, according to Munier's approach [50] governed the physical process of fatigue damage initiation.

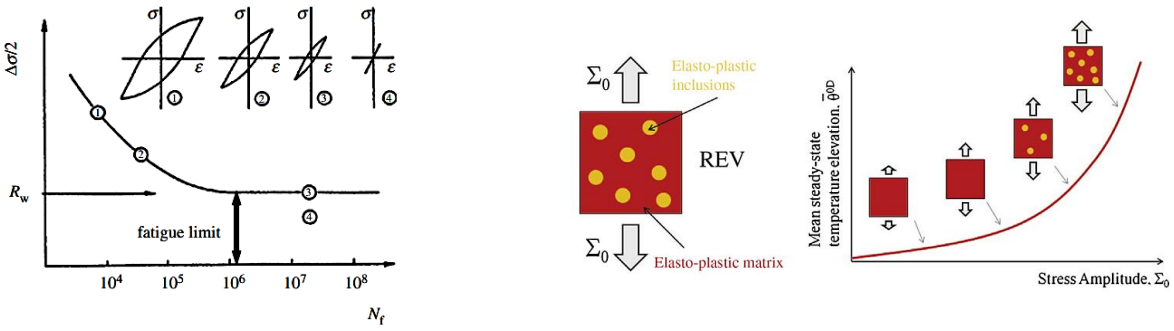

(a) (b)

Figure 6 (a) fatigue life and dissipated energy [97] (b) modeling of men temperature variations and micromechanical damage processes [50]

2-2-2 Estimation of the dissipated heat during the fatigue

2-2-2-1 Estimation based on the mean temperature

From a thermo-mechanical perspective, fatigue is recognized as a quasi-static dissipative process [113]. Employing the thermodynamics of irreversible processes, a local heat equation can be developed to elucidate the experimental data [113], encompassing temperature variations resulting from heat exchanges and material deformation, subsequently leading to heat generation. This equation has been commonly employed in various studies to approximate the heat dissipation from surface temperature using thermographic techniques [108, 114]. A brief explanation of the approximate derivation of heat dissipation from the heat equation is provided below.

The idea relies on a collection of N state variables that characterizes the equilibrium state of each element within the material. The chosen variables are the absolute temperature, T, a strain tensor ε and $N-2$ scalar components $\xi_1, \xi_2, \dots, \xi_{N-2}$ completing the description of the thermodynamic state. The latter describe the macroscopic effects of complex and usually coupled microstructural phenomena. The heat equation is expressed in the following manner [48, 113]:

$$\rho C_p \frac{\partial T}{\partial t} + div\ q = d_1 + s_{th} + s_i + r_e \tag{4}$$

Where ρ and C_p are density and specific heat at constant pressure, respectively; q being the heat influx and d_1 shows the intrinsic dissipation as below [48]:

$$d_1 = \sigma : D - \rho \frac{\partial \Psi}{\partial \varepsilon} : \dot{\varepsilon} - \rho \frac{\partial \Psi}{\partial \xi} : \dot{\xi} \quad (5)$$

Where σ is the Cauchy stress and Ψ is the Helmholtz free energy and D is the Eulerian strain-rate tensor ($\sigma : D$ is the deformation energy, $\rho \frac{\partial \Psi}{\partial \varepsilon} : \dot{\varepsilon}$ is the elastic energy rate and $\rho \frac{\partial \Psi}{\partial \xi} : \dot{\xi}$ is the stored energy rate) [115]. The second and third terms next to the d_1 in Eq. (4), the thermomechanical coupling sources, include the thermoelastic source ($s_{th} = \rho T \frac{\partial^2 \Psi}{\partial T \, \partial \varepsilon} : \dot{\varepsilon}$) and the internal coupling sources ($s_i = \rho T \frac{\partial^2 \Psi}{\partial T \, \partial \xi} \dot{\xi}$); and the external volume heat supply r_e is the last term.

In theory, by assessing the left-hand side of Eq. (4) through experimental measurements (e.g., employing thermographic techniques), it is possible to approximate the overall heat source and dissipation [48, 116]. However, without introducing any simplifications, this estimation process becomes a challenging ill-posed inverse problem [113].

In general, to estimate d_1 using thermal data from thermographic techniques [113], certain fundamental assumptions need to be considered. These may include:

1. Negligible thermal gradient throughout the thickness;
2. Constant values for ρ, C_p thermal conductivity (k), and convection coefficient (h);
3. Time independence of r_e;
4. The temperature variation induced by the fatigue test having no impact on the microstructural state (typically neglected when the temperature rise is relatively low [114]).

Additionally, other assumptions found in the literature [114] include neglecting heat conduction between the loading machine gripper and the specimen, using a simple linear function for heat exchange through convection and radiation, and disregarding heat sources arising from thermoelastic effects. With all these assumptions, Zhao et al. [114] derived the heat dissipation as:

$$d_1 = A \frac{\rho C_p}{\tau} \quad (6)$$

Where A has a constant value can be obtained from the experimental temperature variation and τ is a characteristic time constant related to the heat diffusion from the surface of the sample [114].

It is important to highlight that d_1 is expected to be defined solely within the gauge length of the sample during the fatigue test since the amount of deformation is highly dominant in comparison to the domains outside it [114].

The experimental values of d_1 in Eq. (6) were predicted by Zhao et al. [114] utilizing the thermographic technique and measuring the mean surface temperature.

2-2-2-2 Estimation based on the second amplitude harmonic of temperature

Rather than relying on the mean surface temperature, the second amplitude harmonic (SAH) of temperature can also be employed for estimating energy dissipation. This is justified by its fundamental association with heat-converted energy, as demonstrated by De Finis et al. [45] in the case of C45 steel under fully reversed loading (R=-1). Over recent years, attention has grown towards the SAH component, recognizing it as a valuable parameter for fatigue assessment [47, 59, 60, 117].

In Eq. (1), the energy balance, $\dot{W}$ can be determined from changes in stress and strain over time. As the cyclic load in the fatigue test induces periodic fluctuations in both strains and stresses, therefore, it can be anticipated that the mechanical energy rate ($\dot{W}$) also exhibits a periodic form, given that it equals the scalar product of stress and strain rates [101].

Besides, by ignoring the stored energy rate ($\dot{E}_s \approx 0$), based on the 1st law of the thermodynamic and for R=-1, the heat dissipation rate is theoretically almost equal to the mechanical energy rate, $\dot{E}_d \approx \dot{W}$. Therefore, a periodic behavior can also be expected for $\dot{E}_d$ [101].

In the case of C45 steel subjected to fully reversed loading, it was proven that the second harmonic of heat dissipation, $\dot{E}_{d_{2\omega}}$, is the dominant component of the $\dot{E}_d$ (the same as for $\dot{W}$) [101]. Through the application of Discrete Fourier Transform (DFT) on the surface temperature signal, $\dot{E}_{d_{2\omega}}$, can be determined based on the SAH of temperature [101] (similar to Eq. (3)):

$$\dot{E}_{d_{2\omega}} = 2f\rho C T_{2\omega} \tag{7}$$

where $2f$ represents twice the loading frequency and $T_{2\omega}$ is the second harmonic amplitude of the temperature. However, the estimation of heat dissipation from the average of the SAH of surface temperature is only an approximation. Because it is calculated from the surface temperature [101] and does not offer insights into the processes taking place within the gauge volume.

2-3 Different methods to investigate the thermal behavior for fatigue prediction

In this section, the well-established and recent advanced approaches to obtain thermal parameters to study fatigue behavior are presented.

2-3-1 Direct Temperature Assessment

2-3-1-1 Mean temperature increase

The phenomenon of self-heating can be traced back to the research conducted by Stromeyer in 1914 [118]. Subsequently, it has been employed for the swift prediction of fatigue limits. In 1983, the pioneering researcher Risitano [38], and in 1986, Curti et al. [119], investigated the potential of thermography as a non-contact sensing technique for assessing the fatigue limit based on surface temperature [37].

It is important to highlight that the fluctuation in surface temperature primarily arises as a macroscopic consequence of energy transfer. The onset of heat dissipation and the self-heating regime during cyclic loading can be predominantly attributed to internal mechanisms of fatigue damage, such as microplasticity. Additionally, external factors, including thermal convection and radiation, can exert a substantial influence on temperature variations [55, 102, 105].

La Rosa and Risitano [37] investigated the surface temperature patterns of specimens subjected to cyclic loading. As illustrated in Figure 7, (N_s and N_f are the number of cycles to reach the stabilized temperature and the failure, respectively), for loads exceeding the fatigue limit, the temperature demonstrates a characteristic pattern. It experiences an initial rise at the commencement of the test (phase 1), followed by a "stabilization" phase (phase 2) until shortly before failure, and ultimately, a rapid ascent just before failure (phase 3).

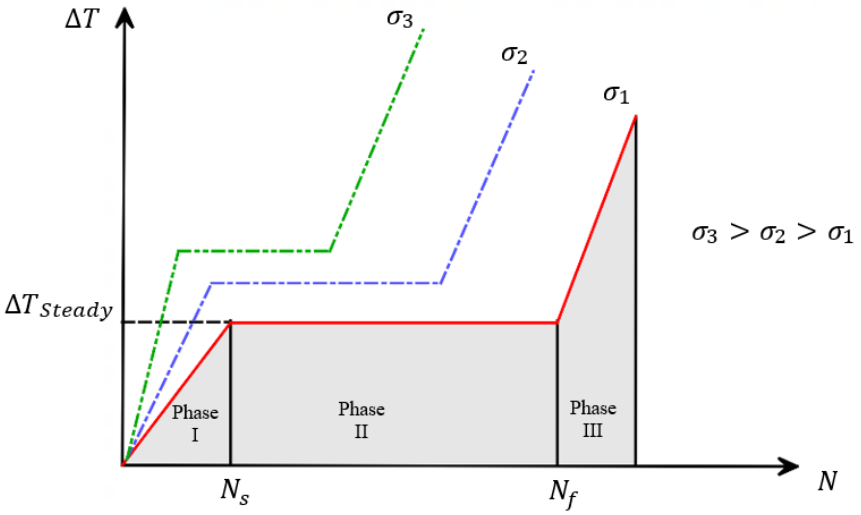

Figure 7 Surface temperature behavior and phases (thermal increments vs number of cycles) [120]

They observed that as the stress relative to the fatigue limit increases, both the temperature rise rate in phase 1 and the "stabilization" temperature in phase 2 also increase [37, 39]. Using the temperature of the steady state (ΔT_{steady}) obtained during a stepwise loading procedure allows for an exploration of the fatigue behavior of materials and components [40, 41].

In another pioneer study [36], Luong introduced intrinsic dissipation as a precise indicator of damage initiation. Using the coupled thermomechanical equation and subtracting the thermal image at different reference times, it became possible to estimate intrinsic dissipation based on the mean temperature.

It is important to highlight that accurately quantifying intrinsic dissipation in engineering materials presents some challenges. Surface thermal signature measurements can be influenced by heat exchanges, resulting in measurements that are essentially estimates of the internal energy dissipated [40]. The quantification of intrinsic dissipation becomes more intricate when dealing with brittle or highly diffusive materials, primarily due to minimal temperature changes [40], which requires the development of specific smoothing procedures.

For this purpose, De Finis et al. [40] introduced a novel thermal data analysis procedure, which involved filtering out superficial temperatures, including environmental temperature and those generated by heating from the hot servo-hydraulic fixture of the loading machine. To address the ambient temperature effect, they subtracted the surface temperature of a dummy specimen from that of the sample. Simultaneously, the contribution from the loading machine was eliminated by assuming a linear temperature increase and employing a specific data fitting procedure for thermal profiles along the longitudinal direction of the gauge length. These recent advancements in image processing have significantly improved the capability of infrared thermography in detecting the fatigue limit for various materials, particularly in automotive components subjected to different stress paths (reversed tension, rotating bending, cyclic torsion, etc.) [109].

As shown in Figure 8, the initiation of damage and defects triggers alterations in dynamic characteristics, influencing properties like the specific damping capacity (Ψ) and the natural frequency of materials, both associated with damping parameters (e.g., loss factor and damping ratio) [106]. Damping, a property of materials or systems to dissipate energy under cyclic loading, can be determined either from the exponential free decay curve or the half-power bandwidth method in the time or frequency domain, respectively [106]. Crupi established a relationship between the stabilized emperature increment, $\Delta T_{stabilized}$, and the square of the applied stress amplitude (σ_a^2) based on damping parameters as follows [106]:

$$\begin{cases} \Delta T_{stabilized} = 0, & \sigma_a < \sigma_c \\ \Delta T_{stabilized} = a\,\sigma_a^2 + b, & \sigma_c \le \sigma_a \le \sigma_y \end{cases} \quad (8)$$

where a and b denote material constants depending on the specific damping capacity Ψ and σ_c and σ_y are the fatigue limit and the stress amplitude, respectively.

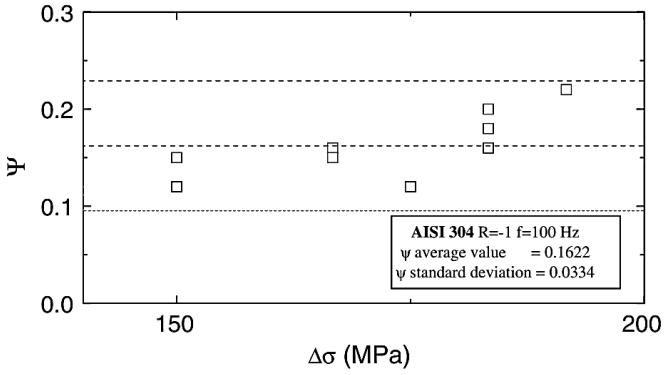

Figure 8 Specific damping $\boldsymbol{\Psi}$ versus the stress range $\boldsymbol{\Delta\sigma}$, relative to AISI304 specimens at a load ratio R = 1 and a frequency f = 100 Hz [106]

The specific damping capacity is linked to the stabilized hysteresis loop, a fatigue parameter, and $\Delta T_{stabilized}$. In essence, $\Delta T_{stabilized}$ corresponding to various loading levels can be determined by capturing thermal sequences during a stepwise loading of a single specimen [106]. It is important to mention that similar relationships, employing power functions, can also be identified in the literature, albeit with different exponents [37, 121-124].

The relationship between $\Delta T_{stabilised}$ and σ_a was further developed by considering the number of cycles to the failure (N_f).

Utilizing the shakedown theory and multiscale concept, Wang et al. [125] provided theoretical support for the analysis of energy and identified an intrinsic correlation among the three mentioned parameters. They termed this correlation Quantitative Thermographic Methodology (QTM). More recently, Feng et al. [126] proposed an enhanced version of QTM, integrating heat exchange through the heat diffusion equation [33, 48, 116] and accounting for variable amplitude loading. They posited that damage could be equivalently transferred from one loading block to another [127].

2-3-1-2 Initial slope of the temperature curve

Through fatigue testing, it was observed that a close link exists between the temperature increase and

material degradation under cyclic loading. In the case of Aluminum 6061-T6, Figure 9 depicts the variation of the temperature slope concerning the normalized number of cycles relative to the cycles leading to failure. The graph indicates an initial increase, followed by a sharp decline, and then a relatively stable phase that persists for approximately 90% of the lifespan. Finally, there is a sharp increase towards the end of the test [110].

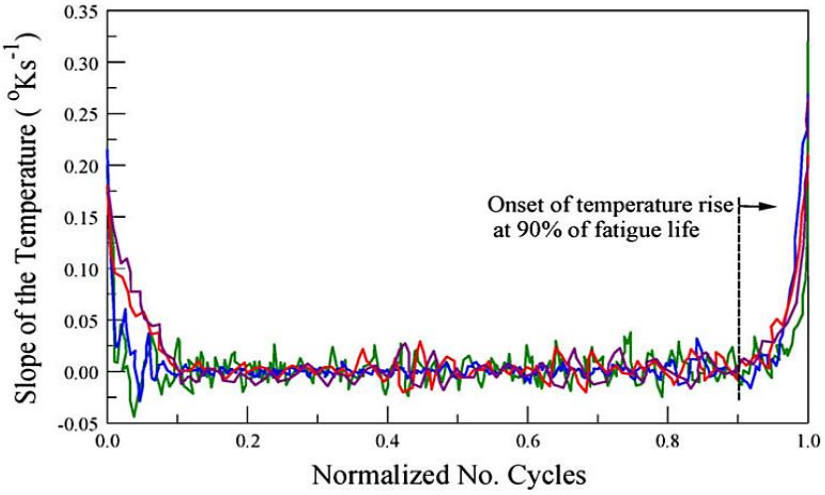

Figure 9 The evolution of the temperature slope in bending fatigue of Aluminum 6061-T6 [110]

Being pioneers in the field, Huang et al. [128] observed a significant temperature spike in certain stainless steel and superalloys shortly after reaching a stable state. This temperature increase, illustrated in Figure 10, was connected to the initiation and spread of macrocracks [50] and the forthcoming fracture [52]. However, this temperature increase seems to be an ineffective indicator as it is determined after substantial accumulation of damage and involves a time-consuming process.

However, in the initial phase I on the left side of the temperature curve, before stabilization, the angle of temperature rise has been suggested as a potential indicator for fatigue assessment. This notion has been previously highlighted in pioneering studies by Curti et al. [119] and Botny and Kaleta [129]. Boulanger et al. [48], demonstrated that the initial slope of the temperature rise is valuable for investigating fatigue behavior, specifically in estimating dissipated energy. Mehdizadeh and Khonsari [64] proposed that the effectiveness of this slope (refer to Figure 11a) for estimating fatigue limit depends on the sharp change in slope in the $R_\theta - \sigma$ curve (see Figure 11b for SS 304 with fatigue limit around 230 MPa [64]). Additionally, Amiri and Khonsari [56, 57] presented a relationship for determining fatigue life based on the temperature slope in the initial phase of the temperature trend.

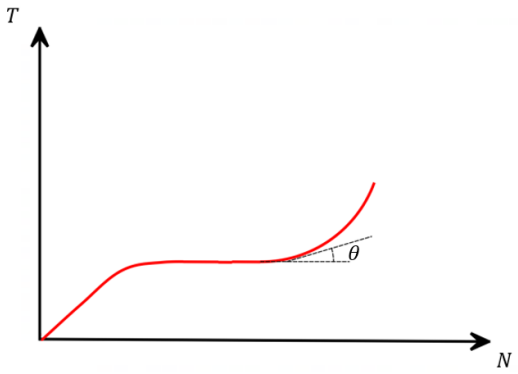

Figure 10 Temperature slope just after a steady-state condition [120]

As the temperature evolution slope, denoted as $R = \Delta T/N$, is measured during the initial phases of testing, it provides a swift method for predicting fatigue life, thereby saving testing time and preventing catastrophic failure. However, a limitation is that this relationship specifically applies to fatigue tests conducted on pristine specimens without prior damage history. In other words, it does not account for the history of the specimen. Meyendorf et al. [130] illustrated that when a specimen has undergone fatigue, its microstructure changes, leading to a distinct thermal response compared to a pristine specimen. Through a series of fatigue tests on cylindrical dog-bone samples obtained from forged titanium, they observed a gradual alteration in the temperature rate as the number of cycles accumulated [130]. To address this limitation, Khonsari and colleagues adjusted the mentioned relationship by considering accumulated damage for non-undamaged samples [35].

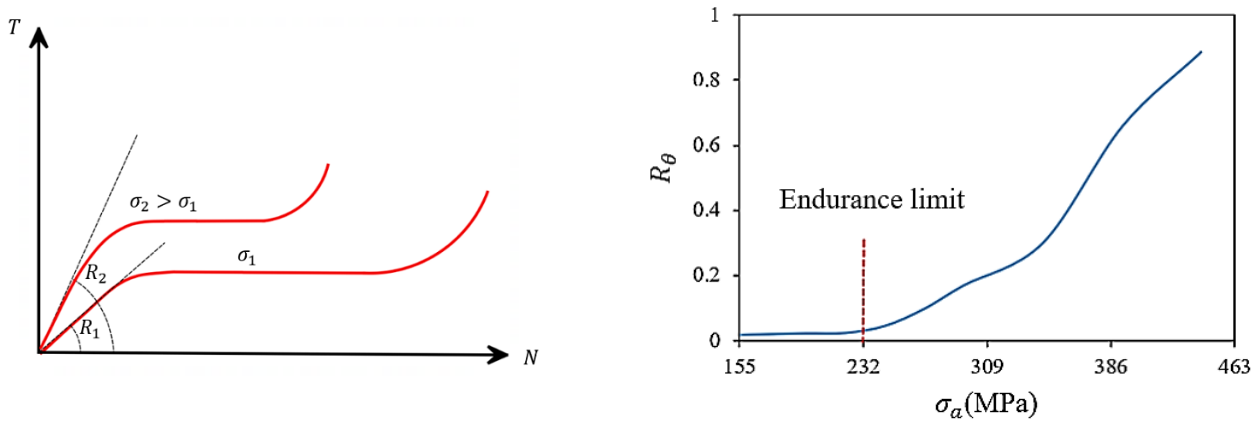

Figure 11 (a) Temperature Slope at the beginning of the test and (b) fatigue limit predicted by initial slope of temperature for SS 304 [120]

As the sample undergoes cyclic fatigue, there is a substantial increase in temperature after each step. Based on this observation, Amiri and Khonsari [35] suggested that this slope, considered as a function of time, can be employed to estimate the remaining fatigue life. This method enables the quantification of previous fatigue damage. It is noteworthy that all of these investigations were conducted under

under excitation loading, which entails short-term mechanical loading [130].

In another work by Liakat and Khonsari [131], the relative slope (R_r) was introduced for predicting the remaining fatigue life. It was characterized as the disparity between the temperature rise slope (R) and the intercept of the slope and the number of load cycles (R-N) curve. Through the introduction of the relative slope, denoted as R_r, Liakat and Khonsari [131] [128] demonstrated its linearity with respect to N, making it applicable for both constant and variable amplitude cyclic loadings. Moreover, the temperature slope can be employed to forecast fatigue life by estimating the accumulation of entropy and the generation of plastic energy[132], as later discussed.

2-3-2 Thermoelastic Stress Analysis

Gough [51] first observed the thermoelastic effect, but the initial experiments were conducted by Weber [133]. The theoretical foundations were later established by Thomson, who is also known as Lord Kelvin [134]. In summary, Thermoelastic Stress Analysis (TSA) is based on the reversible temperature changes that occur during the elastic deformation of a homogeneous solid under adiabatic conditions. Under these assumptions, it is possible to define a linear relationship between surface temperature variations and the first invariant of stress [30, 31, 135-137], called the classic TSA equation [137]:

$$\rho C_p \frac{\Delta T}{T_0} = -\alpha \Delta s \tag{5}$$

where ρ is the density, C_p is the specific heat under constant strain, ΔT is temperature variation, T_0 is the reference temperature, α is the linear thermal expansion coefficient and Δs is the change of the first invariant of the stress tensor [136]. A comprehensive examination of this equation and the revised versions can be found in the research conducted by Wong et al. [136, 138, 139]. It should be noted that the presence of non-adiabatic phenomena (such as visco-plastic behavior of the material or the presence of a high stress gradient) disrupts this linearity [30].

In the classic TSA equation, as mentioned in Eq. (2), the temperature changes can be defined as follows by considering uniaxial stresses with sinusoidal loading:

$$T = \frac{\alpha}{\rho C} T_a \sin(\omega t + \pi + \varphi) \tag{9}$$

Eq. (9) introduces a phase angle between the temperature and loading signal, influenced by factors like painting thickness or grippers. When there are high-stress gradients and viscoelastic-plastic behavior,

significant alterations in the phase signal occur due to deviations from adiabatic conditions and the onset of fatigue damage [62].

As previously mentioned, the utility of TSA extends beyond adiabatic conditions. Both the thermoelastic temperature amplitude and thermoelastic phase serve as indicators of non-adiabatic conditions. This indirectly facilitates the investigation of material damage behavior and estimation of fatigue limits during stepwise loading tests [45, 59, 60, 140, 141], as elucidated below.

2-3-2-1 Loss of adiabaticity (thermoelastic phase analysis)

Palumbo and Galietti [62] introduced a novel empirical approach termed Thermoelastic Phase Analysis (TPA) to examine the fatigue behavior of stainless steels. This method relies on analyzing the phase of the thermoelastic signal. Additionally, TPA proves useful in estimating the fatigue limit. Essentially, changes in the phase can be attributed to either the visco-plastic behavior of the material [107, 142] or the presence of a high stress gradient, causing heat conduction and a departure from adiabatic conditions [28, 30, 69, 143]. As a result, this loss of adiabaticity leads to shifts in the trend of the thermoelastic phase.

For a better explanation, Figure 12a illustrates the shift in the phase signal across four stress amplitudes. The first two are below the fatigue limit (around 170 MPa for ASTM A182), and the remaining two surpass the fatigue limit. Notably, there is a significant elevation in the phase observed when stress amplitudes exceed the fatigue limit. This in escalation crease indicates the loss of adiabatic conditions and the onset of damage [62].

In TPA, the thermoelastic data were obtained following Loung's method, specifically during the second phase of the temperature trend where the average surface temperature remains constant [62]. For each loading step, the maximum phase change ($\Delta\varphi_{max}$) was computed by taking the difference between the maximum and minimum phase values during a specific thermographic sequence. Then, by analyzing how $\Delta\varphi_{max}$ varies with stress amplitudes, the fatigue limit can be determined at the point where the curve undergoes a distinct and abrupt change in its slope (see Figure 12b) [62].

A similar variation, ϕ_{EI} in Figure 13, was also reported by Cappello et al. for C45 [144]. Compared with the classical thermographic method (ΔT_{max}) in Loung's method, TPA demonstrated superior efficacy, particularly for materials or components undergoing relatively minor temperature fluctuations. Reports indicate that TPA surpasses approaches relying solely on stabilized temperatures, especially in materials exhibiting higher ductility [62]. In Figure 13, The green and blue cross marks

show the minimum value (5th percentile) and the maximum value (95th percentile), which were changed with the loading amplitude [144].

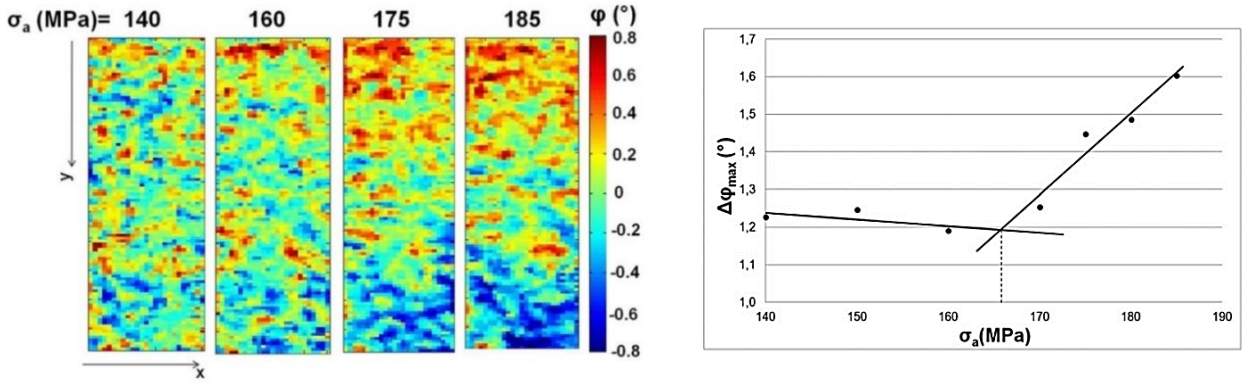

(a) (b)

Figure 12 (a) Thermoelastic phase map for four different loading steps of ASTM A182 and (b) the maximum phase change curve [62]

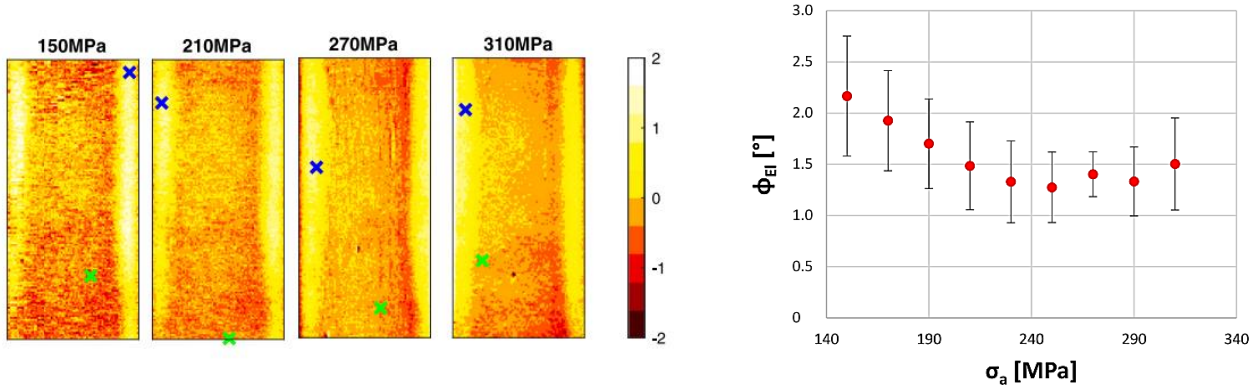

(a) (b)

Figure 13 (a) Thermoelastic phase map for four different loading steps and (b) its variation for C45, R=0.1 [144]

The accuracy of predicting fatigue limits using phase shift data was investigated by De Finis et al. [41]. Furthermore, they illustrated that the phase's sensitivity to stress amplitudes [41] positions it as a suitable metric for tracking the transition between plastic and viscous phenomena. It is also effective in describing dissipative phenomena linked to the plastic stress regime.

2-3-2-2 Loss of linearity of FAH (first amplitude harmonic)

Krapez et al. [45, 60], and later De Finis et al. [41, 145], introduced similar temperature models that leverage the first amplitude harmonic of temperature. Through comparing the first temperature amplitude with its linear trend assessed at the beginning of the test, a noticeable distinction was

observed when the stress amplitude surpassed the fatigue limit. In essence, TSA equation loses validity in the presence of damage, particularly when microplastic phenomena occur in the material. Under such conditions, the prediction of the fatigue limit becomes feasible when a loss of linearity in the first harmonic is detected for a given stress level. In Figure 14a, displays full field maps of the first harmonic amplitude of temperature for C45 (with an approximate fatigue limit of 200 MPa) and its variation (E_I in [144]) are shown. Noted that green and blue crosses in Figure 14a indicate minimum and maximum related values [144].

Figure 14b illustrates the nonlinearity occurring around 220 MPa, very close to the material's fatigue limit [45]. Importantly, the intensity of the slope change in the curve depends on both the material and the stress ratio [41, 45]

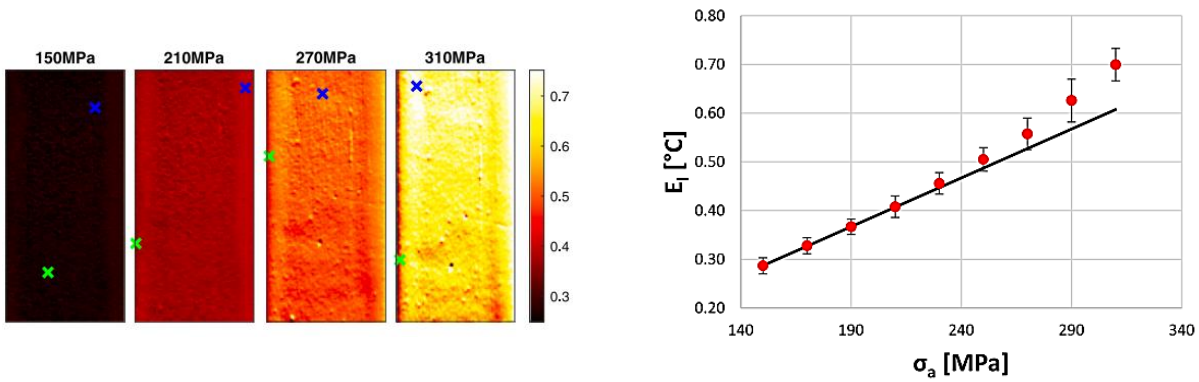

(a) (b)

Figure 14 (a) First harmonic amplitude map for four different loading steps and (b) its variation for C45, R=0.1 [144]

2-3-3 Energy-based approaches

Research on the connection between fatigue (or failure) and energy has roots dating back to the 1920s [146]. However, it was not until the early 1940s and 1950s that numerous researchers started exploring the correlation between a material's fatigue life and the dissipation of strain energy throughout the fatigue process [32, 98].

Feltner and Morrow [32] attribute the initial connection between Strain Energy Density (SED) and fatigue life to Hanstock [147] around 1947. Subsequently, in 1965, Morrow made a significant contribution by introducing a power function that links plastic SED, plastic work, and fatigue life. This function is considered the prototype for contemporary SED-based models [148]. Following this, various forms of SED-based fatigue approaches were developed and refined [148-151]. For a detailed

historical development of SED and a collection of equations directly correlating SED with fatigue life, one can refer to the work by Lia et al. [148].

A promising insight is that the strain energy necessary for the failure of a material in a static test closely aligns with the strain energy dissipated during a fatigue process [45]. As depicted in Figure 15, the strain energy (or its normalized counterpart, which is the strain energy density per cycle divided by the strain energy density in the steady-state strain region) increases with the number of cycles as plastic deformation or damage elevates [98].

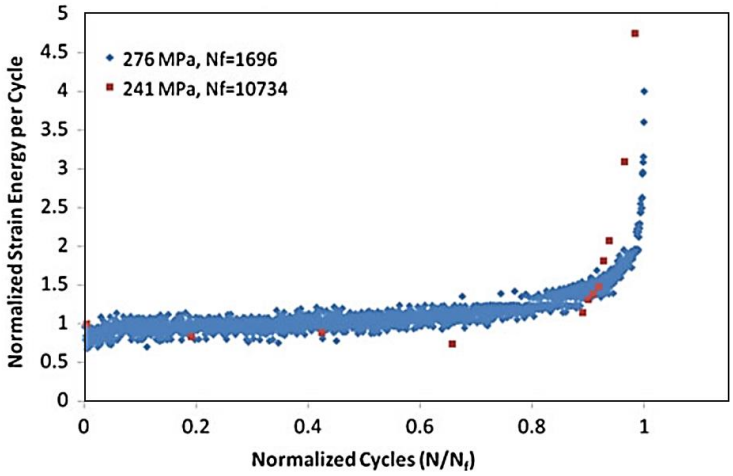

Figure 15 Normalized strain energy variation during the fatigue test for Al 6061-T6 [98]

2-3-3-1 Second amplitude harmonics (SAH)

Enke and Sandor [59] illustrated how the assessment of dissipative heat sources can be employed to gauge material damage. Assuming negligible mean strain, corresponding to fully reversed cyclic loading, they introduced a general form of thermo-elastic-plastic response. They applied the Fourier sine series to the thermal signal recorded by an infrared camera and highlighted that the amplitudes at the frequency and twice the frequency of the mechanical loading are proportionate to the elastic and plastic strains (or deformation), respectively.

Illustrated in Figure 16 is a schematic representation of the hysteresis loop for sinusoidal loading, depicting the variations in stress, strain, and temperatures. During the transition from point 'a' to 'b,' elastic strain increases, while temperature concurrently decreases, both following a sinusoidal pattern. In the elastic unloading phases from 'b' to 'c' and then 'd' to 'e,' the temperature is solely attributed to elastic deformation ($T_{elastic}$). This cyclic behavior repeats for subsequent cycles ('c-d' and 'd-e'), but with opposite signs for the elastic temperature contribution. As clarified by Enke and Sandor [59], for

each cycle of elastic temperature response, two cycles of plastic temperature response occur. Consequently, twice the loading frequency, 2f, plays a fundamental role in assessing $T_{plastic}$. It is worth noting that at the test's commencement, this temperature contribution is negligible, but it increases with plastic deformation and damage. As an example, the full field maps of the second harmonic amplitude of temperature (D_I in [144]) for C45 with the fatigue limit of around 200 MPa are shown in Figure 17.

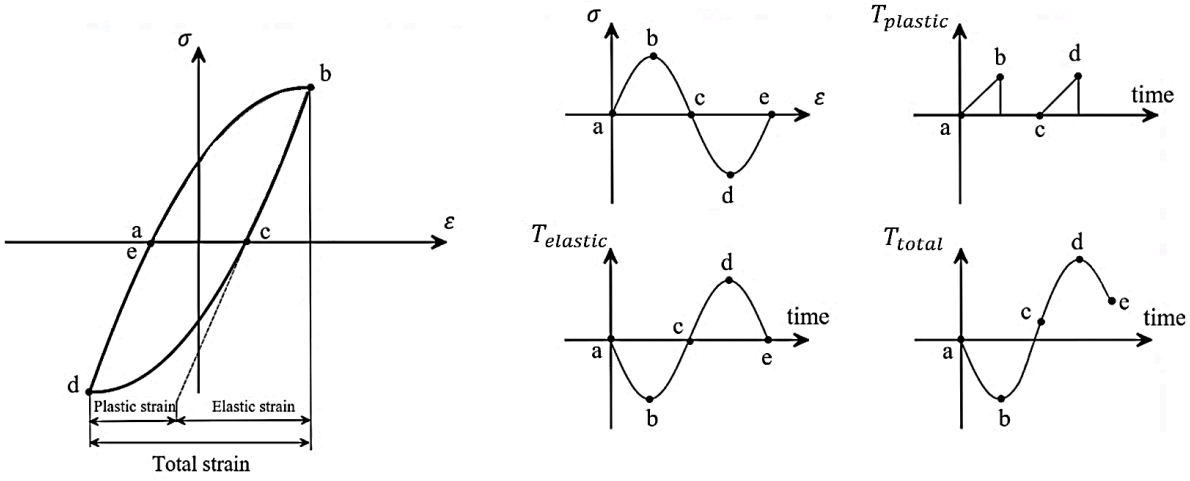

Figure 16 A schematic representation of hysteresis loop and temperature variations during a single cycle under a sinusoidal stress [120]

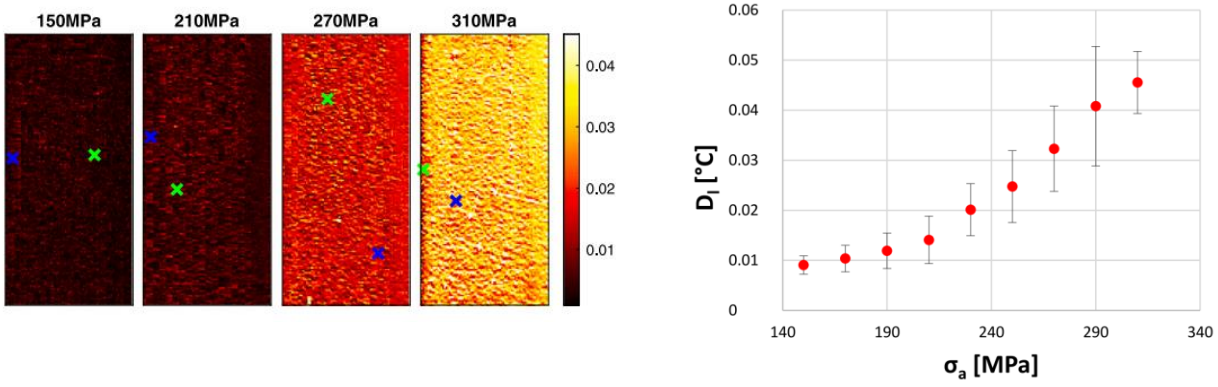

(a) (b)

Figure 17 (a) Second harmonic amplitude map for four different loading steps and (b) its variation for C45, R=0.1 [144]

In continuation of prior research, Krapez et al. [45, 60] demonstrated that energy variations resulting from irreversible processes generate a secondary harmonic temperature component, serving as a fatigue indicator. They conducted an analysis of the thermal signal in the frequency domain to differentiate between dissipative and thermoelastic sources [45, 60]. The original concept was initially

proposed by Bremont and Potet [46].

To enhance the precision of dissipated energy measurements, Shiozawa et al. [47, 152] introduced a method utilizing the phase 2f lock-in infrared technique. This method employs a double-frequency component of temperature change, encompassing the effects of both energy dissipation and thermoelastic sources (refer to Figure 4). Notably, this technique effectively eliminates the superficial portion of dissipated energy, or noise components generally associated with thermoelastic temperature (ΔT_E), resulting from the harmonic vibration of the loading machine. The primary objective was to ascertain the genuine temperature rise attributable to the dissipated energy (ΔT_d) and the rate of energy dissipation (q). They are formulated as follows:

$$\Delta T_E = -kT\Delta\sigma \tag{10}$$

$$q = \rho C_p \Delta T_d \tag{11}$$

where k is thermoelastic coefficient, T is the absolute temperature and $\Delta\sigma$ is the sum of principal stresses.

De Finis et al. [101] conducted further exploration into the second amplitude harmonic (SAH) of temperature, denoted as ΔT_{2w}. Specifically, they investigated the potential of the ΔT_{2w} signal as an indicator for predicting the dissipated heat energy. Additionally, the study revealed a correlation between the SAH of heat dissipated rate $\Delta\dot{E}_{d_{2w}}$ and mechanical energy rate $\Delta\dot{W}_{2w}$ for C45 steel under two stress ratios ($R = \frac{\sigma_{min}}{\sigma_{max}}$, σ_{min} and σ_{max} are the applied minimum and maximum stresses, respectively) R= 0.1 and -1, as follows:

$$\Delta\dot{W}_{2w} = A_1\,\Delta\dot{E}_{d_{2w}} + A_2 \tag{12}$$

where A_1 and A_2 depend on the material. While the first one was reported to be dimensionless, the second dimension has the same of either $\Delta\dot{W}_{2w}$ or $\Delta\dot{E}_{d_{2w}}$.

The endurance limit can be estimated from the latter one, $\Delta E_{d_{2w}}$, [117] and subsequently the area under the hysteresis loop. However, the accuracy of this approach is contingent on several assumptions, including (i) the complete conversion of mechanical energy into heat, (ii) consideration of only a fraction of ΔE_{d}, and (iii) determination of $\Delta E_{d_{2w}}$ from ΔT_{2w} on the surface, which is smaller than the value associated with the actual heat source. Additionally, Pitarresi and Cappello [61, 153] introduced a thermoelastic stress analysis method aimed at experimentally detecting and assessing crack closure during mode I fatigue loading on isotropic cracked samples. They found that the second harmonic of

surface temperature, measured over a short period during the fatigue test, served as a sensitive indicator of crack closure. The study revealed distinctive signal patterns in the second harmonic amplitude, enabling direct visualization of the crack closure area. The researchers also elucidated the mechanisms underlying the correlation between the second harmonic and crack closure. Recently, Meneghetti and Ricotta [13-15, 154] proposed a method for estimating the heat dissipation from T_{2w}. They assumed that the whole of the gauge volume in a dog bone specimen dissipating the same way, under cyclic loading, and the temperature of a small area on the surface of the gauge volume is a representative of the whole. They introduced an adjusting parameter depending on the material behavior and thermal boundary conditions, and neglecting the diffusion effect (or material diffusivity), to make a relationship between the heat dissipation and T_{2w}. This paper served as a pivotal source of motivation for the inception and development of the current work presented in this thesis; answering what is the volume producing heat and how the experimental measurement of T_{2w} of the real heat source can be affected by the diffusion [13-15, 154].

2-3-3-2 Specific Heat loss

Meneghetti [58] introduced a promising parameter for fatigue characterization centered on the energy per cycle within a unit volume, as opposed to surface temperature. Utilizing the energy balance equation, a connection was made between thermal power dissipated per unit volume (encompassing conduction, convection, and radiation) and the cooling rate ($\partial T/\partial t$). It was found from the temperature evolution curve after a sudden interruption of the fatigue test, see Figure 18.

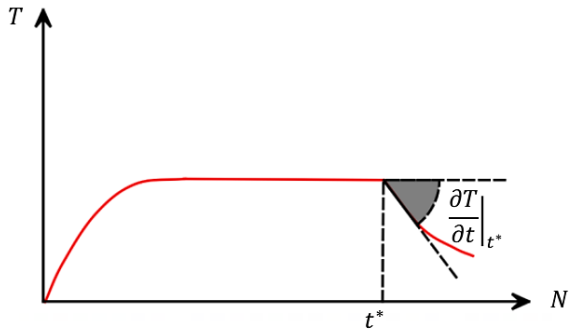

Figure 18 Slope of the cooling rate [120]

After getting the cooling rate from experimental measurements, the heat dissipated was measured [58, 102] as follows:

$$\dot{Q} = -\frac{\rho C}{f}\frac{\partial T}{\partial t}\Big|_{t=t^*} \tag{13}$$

where ρ and C represent respectively the mass density and the specific heat, and f is the frequency.

The dissipation of heat is solely determined by the characteristics of the cyclic loading applied, including the mean, amplitude, and stress state. The effectiveness of this approach has been documented in the literature for various steels and fracture mechanics approaches [155-157]. As an illustration, Figure 19 displays the predicted fatigue limit for AISI 304L stainless steel based on either the dissipated thermal energy or the cooling gradient.

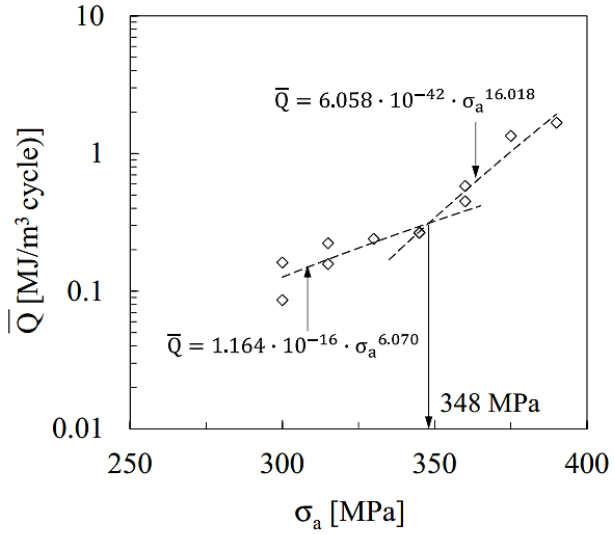

Figure 19 fatigue limit prediction with thermal energy dissipated or the cooling gradient for AISI 304L stainless steel [158]

In a specific material with designated loading and mechanical boundary conditions, the surface temperature is influenced by the sample's geometry, loading frequency, and heat exchange with the surroundings. Conversely, the dissipated energy is solely contingent on the applied stress amplitude and load ratio. Therefore, surface temperature cannot be adopted for geometries and testing conditions different from the reference ones [58].

Rigon et al. [159] demonstrated that the cooling gradient immediately after t* is at least one order of magnitude higher than the heating gradient at the same time. Consequently, the dissipated fraction significantly surpasses the self-heating portion within the total heat production. Additionally, in a more recent investigation, Rigon et al. [49] effectively applied this method to fatigue tests conducted under in-phase and out-of-phase axial/torsional multiaxial loadings. It is noteworthy that the thermographic technique is primarily employed in uniaxial fatigue tests, where achieving temperature stabilization is feasible. However, this assumption may not always hold true in the case of multiaxial loadings, which is not the focus of this study. For more details on the application of thermography in predicting fatigue life under multiaxial and non-proportional fatigue loadings, readers can refer to the work by Skibicki et al. [160].

2-3-3-3 Entropy based methods

Built upon the thermodynamic theory of irreversible processes, as proposed by Naderi et al. [73], the accumulation of entropy during a fatigue test is considered a measure of degradation. According to their study, entropy continues to accrue until it attains a specific value referred to as the fatigue fracture entropy (FFE), defined as follows:

$$\gamma_f = \int_0^{t_f} \left(\frac{W_p}{T} - \frac{q.grad\,(T)}{T^2} \right) \tag{14}$$

where γ_f is the fatigue fracture entropy (FFE), t_f is the time up to the fatigue failure and q is the heat flux across the boundary. During the entire test, an infrared camera was employed to capture the temperature evolution, T, and Morrow's cyclic plastic energy dissipation formula [81] determined the plastic energy, W_p. An illustrative depiction of the entropy flow rate evolution for aluminum 6061 until failure is presented in Figure 20a.

In low-cycle fatigue, where entropy generation is predominantly attributed to plastic deformation, it has been demonstrated that the second term in the integral is negligible [132]. It was verified that γ_f remains a material constant, unaffected by the geometry, load, and frequency [132].

As depicted in the temperature trend illustrated in Figure 20b, following the steady-state phase, there is a sharp increase in entropy at approximately 90% of the fatigue life. This pattern corresponds with the temperature slope presented in Figure 9. From this observation, Naderi and Konsari [161] stated that the operation, or loading, should be continued until $\gamma \leq 0.9\,\gamma_f$, avoiding fracture.

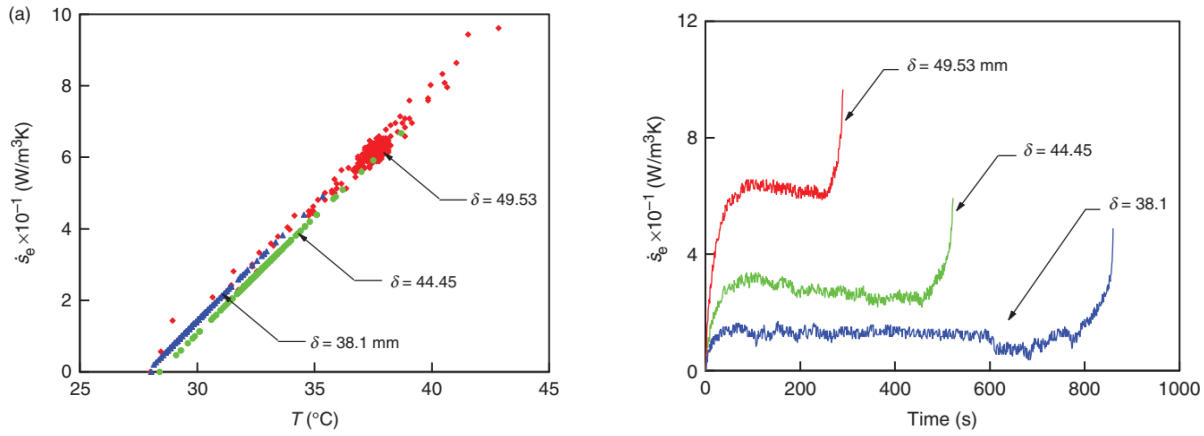

(a) (b)

Figure 20 Evolution of rate of entropy flow of aluminum until failure occurs: (a) variation with temperature; (b) variation with time [110]

In alternative research, it has been demonstrated that cyclic energy dissipation in the form of thermodynamic entropy can be successfully employed to assess the progression of fatigue damage [110] and the remaining life [64]. Jang and Khonsari [162] presented an experimentally validated analytical approach, highlighting that the energy dissipation attributed to recoverable internal friction must be subtracted from the irreversible microplastic deformation (see Figure 21) to precisely find the FFE value [162-165].

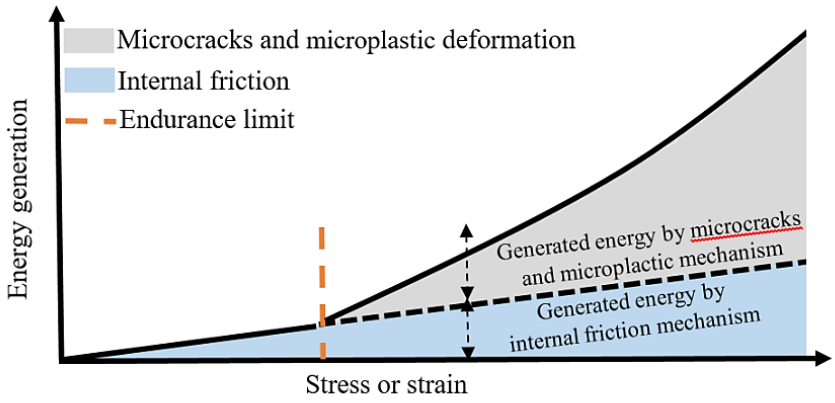

Figure 21 The schematic diagram of energy generation as a function of stress or strain showing the contribution of microplastic and internal friction [166]

2-3-4 Thermoelastic point inversion assessment

A distinct methodology, termed the "Static Thermographic Method," has been employed by Risitano and Risitano [167] to estimate the fatigue limit by evaluating the termination of the thermoelastic effect during a static test. According to their approach, a static tensile test can be considered as a part of the initial cycle of a fatigue test under fully reversed loading. This perspective allows for determining the stress amplitude associated with the fatigue limit by monitoring surface temperature changes during a static test [167]. It is noteworthy that while this method drew some inspiration from the work of Bottani and Caglioti [168] its primary foundation lies in the research conducted by Plekhov and Naimark [53] and Risitano et al. [169].

Typically, the thermal behavior of metals or crystalline solids under a tensile test can be discerned through two distinct zones: the elastic zone, characterized by a linear stress–strain relationship, and the plastic zone, where not all crystals deform within an elastic field.

As mentioned by Risitano and Risitano [167] during tensile tests, fatigue failures occur at points in the material’s stress–strain curve where local stress induces plastic deformation. These localized stresses

intensify compared to the average applied stress (load/area), resulting in fatigue failure. Consequently, the specimen fails when the load surpasses this average value [167]. This critical value is identified when the linear trend of the maximum surface temperature in Figure 22 (thermoelastic behavior) is lost [167].

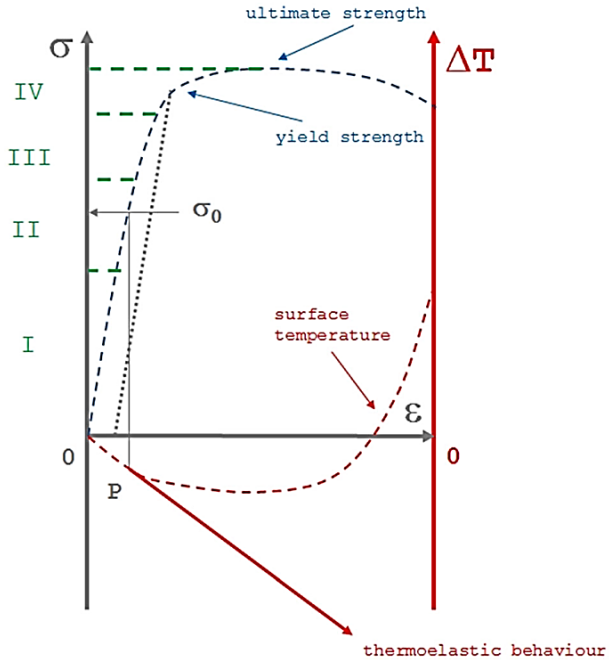

Figure 22 Qualitative stress–strain and temperature - strain curves [167]

The emergence of non-linearity is attributed to the localized intensified stress inducing irreversible micro-plastic deformations (zone II in Figure 22) and consequently heat dissipation [167]. It is highlighted that, apart from a few crystals undergoing plastic deformation, the majority experience stress within an elastic field. In contrast, plastic deformation intensifies within zone III, eventually encompassing every crystal in zone IV [167].

In another work, Risitano et al. [170] demonstrated the method's reliance on the applied stress rate during the tensile test. Nevertheless, this dependence does not exert any influence on the attained results in relation to the fatigue limit. The method can be implemented efficiently even with a restricted number of specimens and within a brief time frame [34, 171-173]. However, for a more robust estimation of the fatigue limit, it is recommended to test a minimum of five samples.

2-4 Procedure and typical setup for rapid fatigue tests

A standard experimental setup comprises an infrared camera and a set of computer-controlled components, as illustrated in Figure 23. Tests are conducted utilizing a mechanical excitation source provided by a servo-hydraulic testing machine equipped with a suitable load cell capacity. The testing environment is maintained at an almost constant temperature. Sample dimensions should adhere to established standards [174] and typically exhibit a dog-bone or hourglass geometry.

As depicted in Figure 23, a computer collects both the load cell signal, serving as the reference signal for the noise rejection process, and the thermographic signal. Subsequently, the software computes temperature from the infrared signal, presenting it as colorful temperature maps.

The fatigue assessment testing procedure involves a series of loading blocks, each featuring an identical duration of loading cycles, and fixed values for loading frequency and stress ratio [40]. This process is repeated until the material ultimately undergoes failure. As illustrated in Figure 24, the sequence of loading blocks is determined by incrementally raising the applied stress level, a method known as stepwise loading.

Each block encompasses a specific number of cycles, and after completing each block, the stress is elevated until the material fails. For the initial block, it is recommended that the maximum stress be set at 20-30% of the ultimate tensile strength of the material to ensure a sufficient collection of data points below the fatigue limit [175]. The stress increment between each block may vary but should be established to maintain a practical total test duration while still gathering an adequate number of data points around the fatigue limit [117].

Throughout each block, thermographic acquisitions are conducted for a predefined time period and sampling frequency. Naturally, the quality of the thermal acquisition depends on the camera specifications (e.g., cooled or uncooled) and settings (such as frame rate, integration time, and temperature range).

In general, the Thermographic method [40] necessitates continuous temperature acquisition, achievable through a typical uncooled micro-bolometer camera. However, if the test objective involves extracting harmonic components of the temperature, a cooled camera becomes indispensable. This is particularly crucial for appropriately reconstructing the thermal signal, which demands higher acquisition frame rates. An effective approach to implement all the presented approaches for fatigue assessment is to employ both cooled and uncooled IR detectors simultaneously [36, 37, 40]. Readers

interested in a comprehensive comparison between cooled and uncooled cameras can refer to the study by Deane et al. [176].

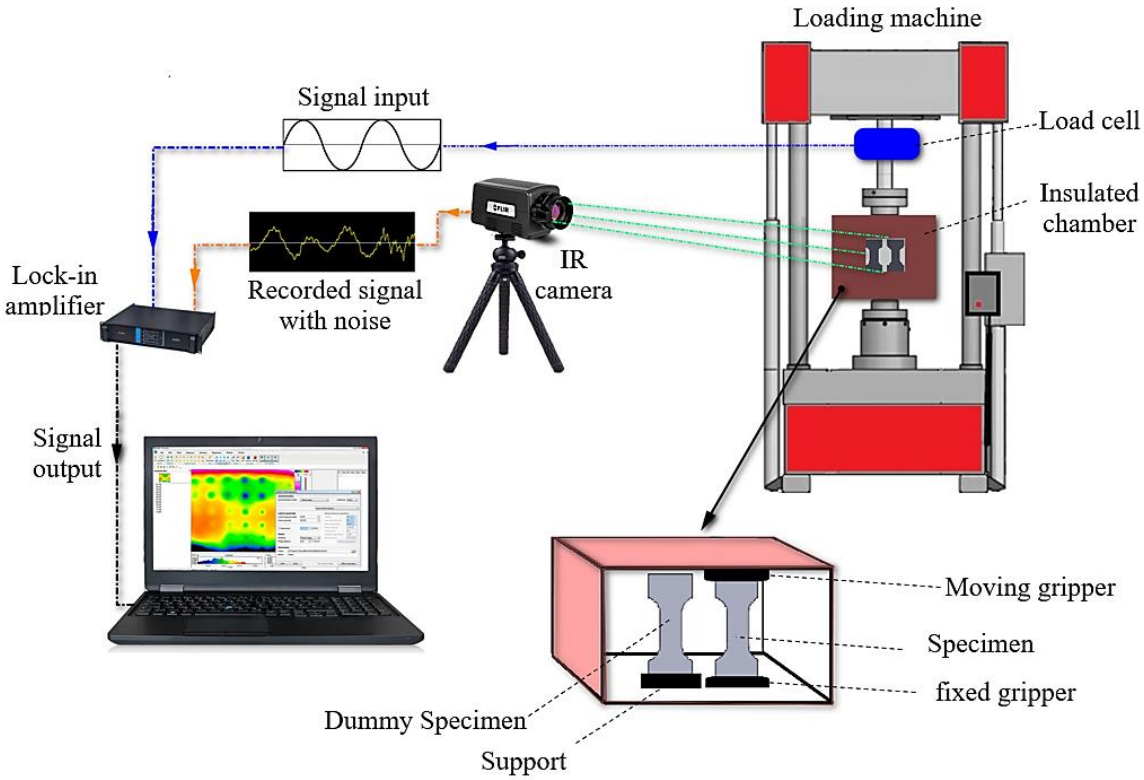

Figure 23 Experimental setup for the rapid fatigue test [120]

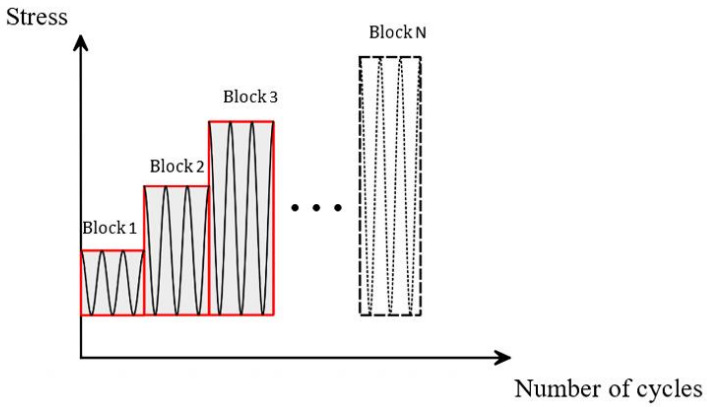

Figure 24 A schematic of stepwise loading [120]

Key factors significantly influencing measurement accuracy are categorized into three groups, as elucidated in the work by Bagavathiappan et al. [11].

The first group encompasses operational factors, which pertain to the available information and experiences regarding the test conditions and samples. The involvement of skilled thermographers can

help minimize these factors, resulting in superior thermal images from the region of interest.

Technical factors constitute the second group, encompassing variables such as the emissivity of the object under investigation and the distance between the camera and the object. Emissivity is considered a critical parameter in measurements. To address this, samples are typically coated with a layer of black paint of suitable thickness. This coating enhances their emissivity and prevents reflections caused by heat sources in proximity to the samples during the test.

The last group encompasses environmental factors such as ambient air temperature, humidity, and convection. To mitigate these effects, it is recommended to enclose samples in an insulating chamber whenever possible [40]. Additionally, placing a dummy-unloaded specimen made from the same material as the one being tested inside the insulated chamber serves as a temperature reference [62].

Table 1 delineates the essential experimental conditions to acquire different thermal indices. It is important to note that the experimental setup needed to obtain these thermal indices is akin to the one previously elucidated, with specific requirements for each index outlined below.

From the information presented in Table 1, the initial consideration pertains to selecting an appropriate IR camera that can capture pertinent data for a specific thermal index. Unlike the mean temperature-related indices (i.e., indices 1, 2, and 6, which involve mean temperature increase, initial slope of the temperature, and specific heat loss), and necessitate a typical low-cost uncooled camera, acquiring the harmonic components of temperature (indices 3, 4, and 5, associated with thermoelastic phase, first amplitude harmonic, and second amplitude harmonic) requires the use of a high-performance cooled camera [11, 57, 58, 62, 101].

Table 1 Experimental requirements for the acquisition of different thermal indices [120]

Requirements			**Thermal indices**					
			1	2	3	4	5	6
			Mean temperature increase	Initial slope of the temperature	Thermoelastic phase	First amplitude harmonic	Second amplitude harmonic	Specific heat loss
1	IR Camera	Uncooled camera	X	X				X
		Cooled camera			X	X	X	
2	High frame rate				X	X	X	
3	High loading frequency					X		
4	Dummy specimen		X	X				
5	Insulating chamber		X	X	X	X	X	
6	Thermal acquisition type	Continuous	X					
		Discrete		X	X	X	X	X

The second row of Table 1 pertains to the sampling rate employed for recording the thermal sequence. In contrast to indices 1, 2, and 6, which do not require a high frame rate, thermal indices 3 to 5 necessitate an elevated frame rate. This increased frame rate is essential to ensure precise reconstruction of the temperature signal, a critical prerequisite for obtaining the aforementioned indices [41, 45, 145].

Furthermore, from the third row of Table 1, when capturing the first harmonic amplitude, conducting the test at a high loading frequency is imperative. This ensures adiabatic conditions during the initial loading stages and allows for the observation of linearity loss caused by damage [30, 113, 177].

From the fourth row of Table 1, when opting for the first two indices, it is crucial to include a dummy pristine sample to eliminate the environmental temperature effect from the mean surface temperature of the sample [62]. For all indices except the specific heat loss, the use of an insulating chamber is recommended to mitigate the influence of environmental factors [178, 179].

The final consideration revolves around the manner in which each index should be captured. As depicted in Table 1, with the exception of the mean temperature index, which needs to be recorded for the entire temperature trend, the other indices can be discretely captured by selecting appropriate time windows during the test [37, 41, 42, 109, 144].

2-5 Methods for rapid estimating of the fatigue limit

In this section, the emphasis is on established approaches utilized for promptly estimating the fatigue limit. Commencing with the pioneering method, a survey of recent advancements in the field is provided. Indeed, there exist only a few of methods for fatigue limit estimation, outlined as follows: Thermographic Method by Luong-Risitano's or referred also so as Luong's method" [37, 109], "Iterative method" by Cura` et al. [54], "Threshold method" by De Finis et al. [40] and "Thermoelastic point inversion" by Risitano and Risitano [167].

In Figure 25, an overview of the main idea of the well-established methods based on the thermal parameters is presented. Once the parameters have been assessed, well-established procedures [36, 37, 142, 167, 180] can be applied to estimate the fatigue limit.

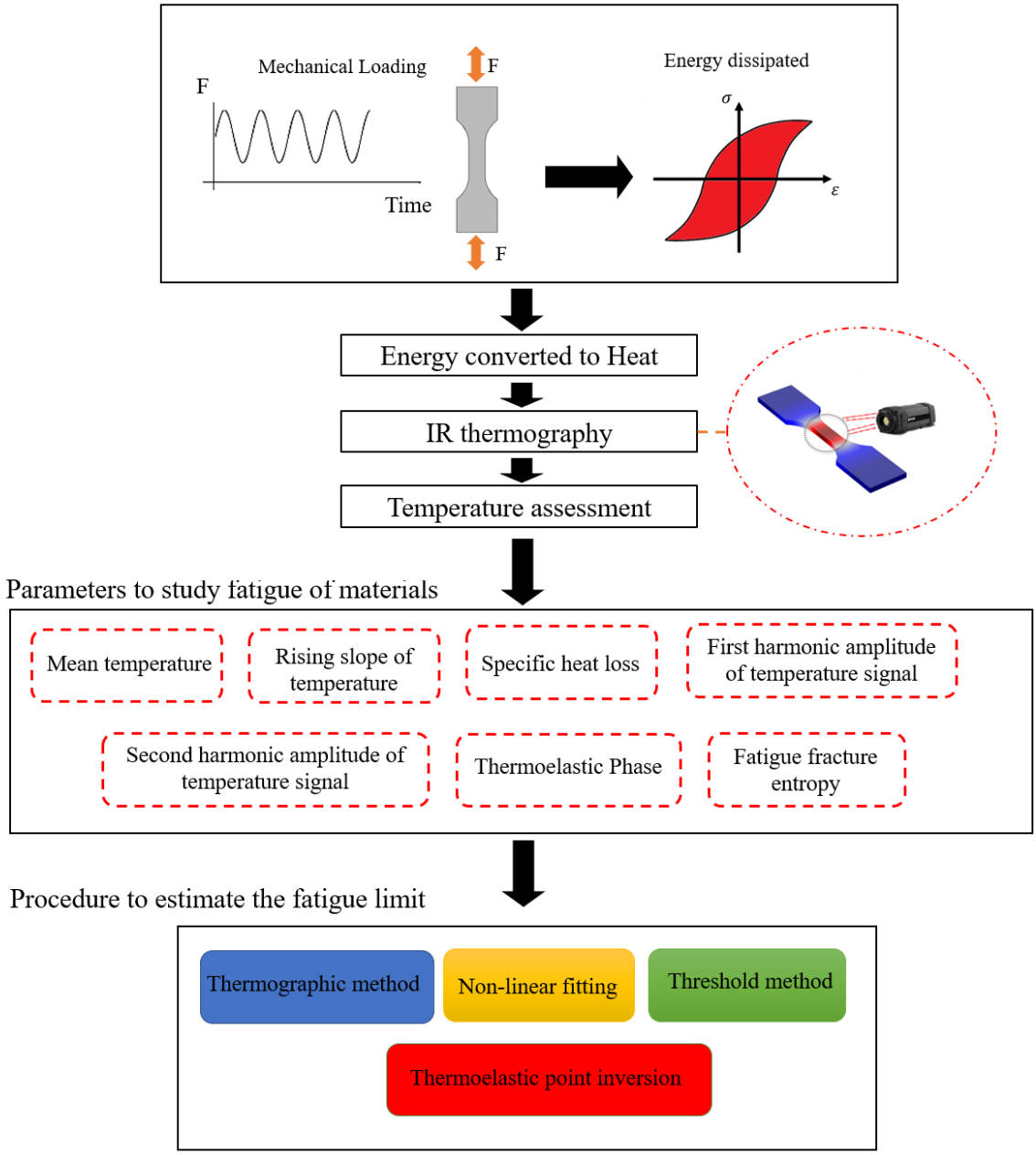

Figure 25 Thermal parameters to study fatigue and procedures for estimating fatigue limit [120]

2-5-1 Luong-Risitano's method

As previously discussed, the stabilization temperature is observed throughout the fatigue test. La Rosa and Risitano [37] proposed a method where the curves of the stabilized temperature or the initial thermal gradient are plotted against the stress magnitude (see Figure 26). They suggested that the fatigue limit could be estimated as the intercept of the curve on the x-axis. Notably, this method is noteworthy for its efficiency, as the initial temperature increase occurs over a few cycles in the

stabilization temperature. This allows the process to be completed within a very small number of cycles, typically around 10% of the entire lifespan. Consequently, it becomes feasible to use the same specimen for various levels of loading. With this limited number of cycles, the cumulative damage to the specimen is considered negligible [42, 44].

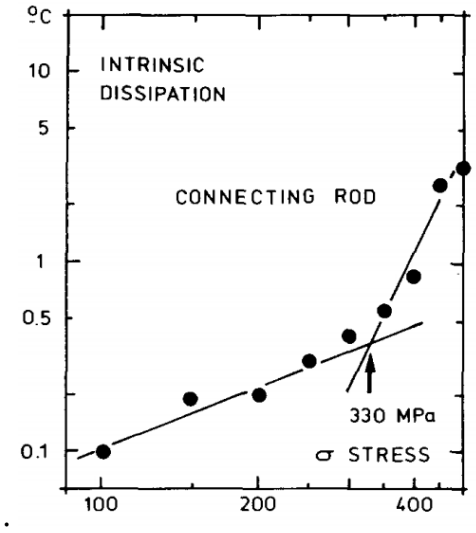

Figure 26 Graphical determination of the fatigue limit of a steel by Luong [109]

Moreover, as highlighted by La Rosa and Risitano [37], only three specimens are deemed adequate due to the minimal scattering observed in the data. Illustrated in Figure 26, by graphing the temperature associated with high dissipation (observed from the surface of the sample) against stress level, Loung identified a breakpoint - a point characterized by a sharp change in slope - that can be utilized for predicting fatigue life [36, 109].

2-5-2 Iterative method

Cura`et al. [54], proposed another rapid method based on the stabilized temperature for predicting the fatigue limit of materials and components based on the Luong approach [36, 109]. As shown in Figure 27, first, the approach involves selecting a trial stress magnitude to categorize thermal data into two groups: below and above the specified stress value. Subsequently, two linear interpolations were applied to fit each set of data in the space of temperature difference and stress amplitude. The intersection of these two lines was identified as a trial fatigue limit. If the difference between the trial stress and the estimated fatigue limit is positive, the subsequent trial stress must be chosen lower than the initial one, and vice versa. This trial stress and fatigue limit determination process was continued via an iteration method until the discrepancy between them fell below a predefined threshold. In such

a scenario, the trial stress was deemed a reliable estimation of the fatigue limit. In contrast, Luong's method does not involve a trial-and-error procedure. After identifying the first intersection point, its corresponding stress value is directly reported as the fatigue limit. Consequently, the accuracy of the method is significantly dependent on the chosen trial stress.

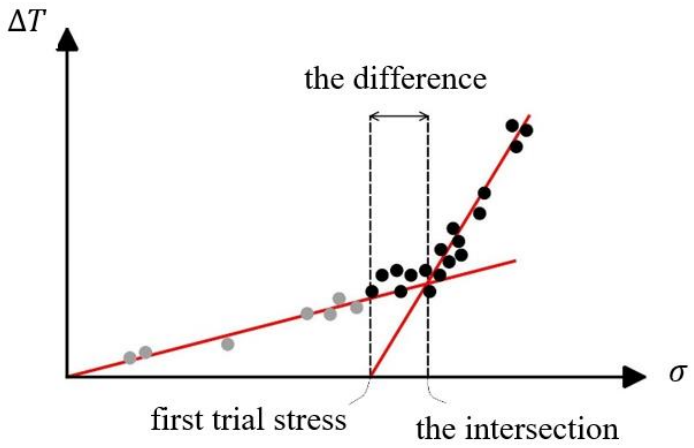

Figure 27 Schematic representation of Cura` et al. method [120]

As mentioned before, Crupi [106] proposed a non-linear relationship between stabilized temperature increment ($\Delta T_{stabilized}$) and stress amplitude (σ_a). To predict the fatigue limit, a fitting was applied on all data pairs ($\Delta T_{stabilized}, \sigma_a^2$) using least-squared and by extrapolating the regression line down to zero at the σ_a^2 - axis. Similar relationships can be found in the literature, albeit with distinct exponents [37, 121-124].

2-5-3 Threshold method

By eliminating the influences of environmental factors and the loading machine on temperature, De Finis et al. [40] modeled the temperature variation attributed to damage using a linear equation in terms of stress amplitude. The two constants in the equation were determined in the initial loading stages through fitting a line to the experimental data, serving as known values for subsequent steps. As shown in Figure 28 b, they showed that when the "residual" or ΔT_{max_r} which represents the difference between the maximum temperature change (or steady-state temperature) obtained from the surface through an infrared camera and the linear function, surpasses a predefined threshold, fatigue failure is anticipated. The threshold is determined as six times the standard deviation of residuals based on the initial five sets of experimental data ($\Delta T_{h\_6\sigma}$). Moreover, as shown in Figure 28b, in contrast to Luong's method [109] in Figure 28a, continuing the test until failure is not necessary for assessing the fatigue

limit [40]. The Threshold method determines the transition that occurs in the behavior of the material.

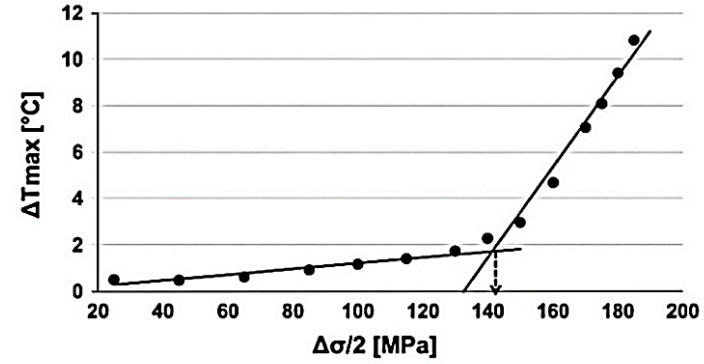

(a)

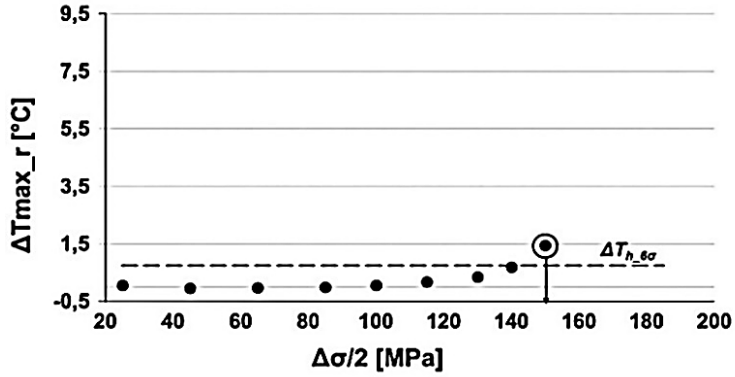

(b)

Figure 28 Comparison between (a) Luong's method and (b) Threshold method for ASTM A 182 grade F6NM [40]

2-5-4 Thermoelastic point inversion in tensile test

As indicated by Risitano and Risitano [167], the fatigue limit estimation involves incorporating the temperature curve into the conventional stress–strain curve (depicted in Figure 29). By identifying the onset of nonlinearity in the temperature curve, a corresponding stress value can serve as a reliable estimation of the fatigue limit. In Figure 29, the temperature evolution manifests three distinct zones: (I) an initial nearly linear decrease attributed to the thermoelastic effect, (II) the introduction of non-linearity due to the conversion of mechanical energy into heat (indicating the initiation of micro-plastic deformation) and reaching a minimum temperature, and (III) a subsequent rise leading to material failure.

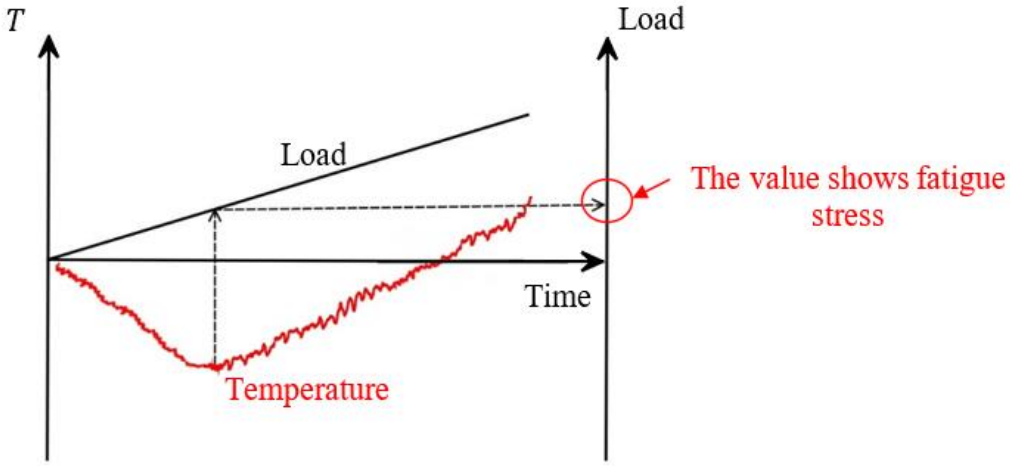

Figure 29 Fatigue limit prediction from tensile test [120]

2-6 Discussion and open points

2-6-1 Comparison of Fatigue indictors and capabilities

In the present section, a discussion on the methods and still open points is presented. In Table 2, to resume all the parameters adopted in the literature for estimating fatigue limit are presented. It summarizes the parameters used in literature to estimate fatigue limits, along with references and procedures. It is noteworthy that the procedures discussed earlier for estimating fatigue limits can be applied to both temperature and energy-based parameters.

Table 2 A summary of fatigue indicators and specific implementation [120]

Method	Index	Author(s)	Year	Procedures	Fatigue limit estimation procedure
Direct temperature assessment	Mean temperature increase	La Rosa & Risitano [37, 38]	1983 & 2000	The first usage of thermography on the fatigue using stabilization temperature for fatigue limit estimation; slope of $T_{stabilized} - \sigma_a$ curve that could be associated with the fatigue limit.	Luong-Risitano's method
		Luong [36]	1995	Estimating the intrinsic dissipation from the mean temperature; a sharp change in the dissipation-stress amplitude curve can be related to the fatigue limit.	
		Cura` et al. [54]	2005	The method is also used as a basic procedure for other methods based on other indices; using the mean temperature; Considering a trial fatigue limit and applying stress below and above it to find thermal data; finding the intersection of two fitted lines on the thermal data and comparing it with trial one, continuing the process until the trial value and the one from intersection of thermal data are almost the same; at the end, updated trial value shows the fatigue limit.	Iterative method
		De Finis et al. [40]	2015	Filtering out the superficial temperatures; modeling a linear relation between $\Delta T_{stabilized}$ and σ_a; evaluating the residual of $\Delta T_{stabilized}$. The first statistically significant value of temperature residuals was used to estimate the fatigue limit.	Threshold method
	Initial slope of the temperature	Khonsari and colleagues [56, 57, 64]	2012	Using the slope of the mean temperature evolution; a sharp change of the temperature rise at the beginning and stress amplitude ($R_\theta - \sigma_a$) curve is used for fatigue limit estimation.	Luong-Risitano's method
Loss of adiabaticity within the Thermoelastic Stress Analysis framework	Thermoelastic phase analysis	Palumbo & Galietti [62]	2017	Observing the phase change of the temperature signal; a sharp point in the $\Delta\varphi - \sigma_a$ curve shows the fatigue limit.	Luong-Risitano's method
	First amplitude harmonic	Krapez et al. [45]	2000	Using the loss of linearity of the trend of the first harmonic of thermoelastic signal with stress amplitude used to estimate the fatigue limit.	/
		De Finis et al. [41]	2019	Using the first amplitude and phase shift of the thermal signal; the sharp change in the slope of either of them with stress amplitude is used for fatigue limit estimation.	Threshold-like method
Energetic approaches	Second amplitude harmonics (SAH)	Shiozawa et al. [47]	2016	Assessing the dissipated energy $q = \rho C(\Delta T_d)$ using temperature change (ΔT_d); finding a sharp change in $q - \sigma_a$ curve as a fatigue limit.	Luong-Risitano's method
		De Finis et al. [101]	2021	Using the SAH of temperature to find the relationship between the heat dissipated rate and mechanical energy rate; estimating the fatigue limit with the trend SAH and plastic work.	/
	Specific Heat loss	Meneghetti [58]	2007	Finding the heat dissipation based on the cooling rate; drawing dissipated energy per cycle – σ_a curve to estimate the fatigue limit.	Luong-Risitano's method
Thermoelastic point inversion or minimum temperature in a tensile test		Risitano and Risitano [167]	2013	Inspiring from temperature gradient due to the advent of the plastic zone in a tensile test; adding a temperature curve to the typical stress–strain curve; finding a point in the curve shows the beginning of the nonlinearity of the temperature and the corresponding stress value was reported as the fatigue limit.	Thermoelastic point inversion method

In this section, the capability of all studied thermal indices is investigated according to different factors that can affect the measurement and/or the analysis. To enhance simplicity and readability, Table 2 is proposed to summarize this investigation; each index is numbered as follows:

1) Mean temperature increase
2) Initial slope of the temperature
3) Thermoelastic Phase
4) First amplitude harmonic of temperature
5) Second amplitude harmonic of temperature
6) Specific heat loss

Regarding sensitivity to the heat diffusion effect (highlighted in the first row of Table 3), methods dependent on direct temperature measurement, such as mean temperature approaches, face challenges when applied to materials with high thermal diffusivity. Capturing subtle temperature variations, particularly mean temperature changes, proves intricate and requires advanced equipment like IR-cooled cameras [37, 40, 54, 109]. Indices 3, 4 and 5 which rely on either the harmonic amplitudes [41, 45, 47, 60, 101] or the phase information [62], are likely the most accurate for fatigue limit estimation. This is attributed to their involvement in post-processing analysis of thermal data. Numerous studies emphasize their effectiveness compared to mean temperature methods.

Kawai et al. [181] conducted a study comparing the effectiveness of mean temperature and the second amplitude harmonic. They explicitly emphasized that the mean temperature is not suitable for use in regions with high stress concentrations, unlike the second amplitude harmonic. This limitation arises due to the significant temperature gradient formation between the stressed region and its surroundings. As the load level increases, this gradient becomes more pronounced, causing a distortion in the correlation between load amplitude and mean temperature, ultimately impacting the assessment of fatigue limit [181]. In another investigation, De Finis et al. [182] demonstrated the efficacy of the second harmonic amplitude and thermoelastic phase in martensitic stainless steels characterized by stress concentrations during cyclic loading. Furthermore, in a more recent study by Lepitre et al. [183], they showcased the reliable performance of the first amplitude harmonic in detecting fatigue cracks in steel.

From the second row of Table 3, the microstructure of the material presents another limitation for fatigue limit prediction with certain indices. Among them, index 3 stands out as the only one with almost insensitive behavior to this problem [62]. As explained by Palumbo and Galietti [62], attribute this sensitivity to the fact that heat generation and maximum temperature attainable during the test are considerably lower when dealing with brittle materials. Consequently, accurate data processing

becomes crucial to extract the signal from the noise in this case.

In terms of environmental conditions, indicated in the third row of Table 3, all indices relying on mean temperature, except for the specific heat loss index, demonstrate sensitive behavior. However, harmonic components have been reported to exhibit less sensitivity compared to others, as they are analyzed in the frequency domain, effectively filtering out the impact of environmental factors [41, 47].

Certainly, various factors can influence the mentioned indices, but their impact is relatively consistent across all considered indices. These factors may include inaccuracies associated with assuming that surface temperature is representative of the entire thickness, material geometry, loading frequency, loading ratio, and heat conduction generated by the hot oil in the loading machine gripper [158, 184].

Table 3 The capability of different indices to different factors [120]

Item /factor #	**Description of the item**	**Parameters/Indices***					
		1	**2**	**3**	**4**	**5**	**6**
1	Sensitivity to the heat diffusion effect	x	x				x
2	Sensitivity to the microstructures, i.e., ductility or brittleness	x	x		x	x	x
3	Sensitivity to the environmental condition	x	x	x			

* *Indices:*

1) Mean temperature increase
2) Initial slope of the temperature
3) Thermoelastic Phase
4) First amplitude harmonic of temperature
5) Second amplitude harmonic of temperture
6) Specific heat loss

Considering the information summarized in Table 3, in summary, it can be inferred that the parameters presented have the potential to be utilized synergistically, offering complementary information for fatigue characterization. This approach allows for the selection of the most appropriate parameter based on specific test conditions.

2-6-2 Accuracy and uncertainty in predicted fatigue limit by thermographic methods

In this section, we assess the accuracy of various methods for estimating fatigue limits. A comparison is made among four rapid methods: (I) Loung-Risitano's method [37], (II) the iterative method [54] (III) the threshold method [40] and (IV) the thermoelastic point inversion method in tensile test [167], in comparison to the conventional Staircase method. The effectiveness of each method is examined, and uncertainties in predicted fatigue limits are discussed based on specific characteristics.

As can be seen in Table 4, methods (I)-(III) yield fatigue limit estimates closely aligned with those

determined by the Staircase method [37, 40, 54]. It is important to note, however, that method (IV), as proposed by Risitano et al. [170], tends to provide a conservative estimation of the fatigue limit, significantly below the values obtained through the traditional Staircase procedure [170].

Table 4 Comparison fatigue limits obtained from each method with the traditional one [120]

Material	Method for fatigue limit prediction	Fatigue limit (Mean value)	Difference (%)
XC55 steel [37]	Staircase	399	-
	Luong - Risitano	375	6
Fe 510 steel [54]	Staircase	203	-
	Iterative method	199	1.97
17-4 PH Steel [40]	Staircase	212.1	-
	Threshold method	201.7	4.9
Fe360 steel [167]	Staircase	43.5	-
	Thermoelastic point inversion	44	1.15

It is essential to acknowledge that the reported results originate from the initial publications introducing each method. Additionally, it's crucial to highlight that the predicted values from each method were derived from a single test or specimen, which may not be sufficient for a precise comparison with the Staircase method.

When only one specimen is tested, the standard deviation theoretically approaches zero, causing thermal methods to underestimate the variability in the predicted fatigue limit compared to the Staircase method. However, a meaningful comparison can be achieved by examining the difference between the fatigue limit estimated through thermographic techniques and the fatigue limit determined using the Staircase procedure for a 50% survival probability. Another recommendation is to incorporate more samples in thermographic methods for a more comprehensive evaluation.

Following the accuracy comparison outlined in Table 5, a brief analysis of various factors influencing the effectiveness (highlighted in the first row of Table 5) and practicality (rows 2, 3, and 4 in Table 5) of the thermographic method in predicting fatigue limits is presented. These features offer insights into the uncertainties associated with fatigue limit estimation procedures.

Examining Table 5, the first feature under consideration is the impact of loading block definition and the number of samples on the precision of the predicted fatigue limit.

It is crucial to acknowledge that the definition of loading blocks significantly impacts the accuracy of fatigue limit predictions, potentially leading to underestimation or overestimation. As indicated in Table 5, the step dimension, encompassing the load increment from one step to another and the number

of cycles for each block (refer to Figure 24), plays a pivotal role in loading block definition for methods (I) to (III).

Additionally, the number of loading blocks is a critical aspect of this procedure. According to existing literature [37, 40, 54], method (III) can make accurate predictions with fewer than 10 loading blocks, unlike methods (I) and (II), which require a greater number. Consequently, it can be inferred that method (III) is more time-efficient compared to methods (I) and (II). Finally, the stress level of the first block is the concluding part of the loading block definition. Unlike methods (I) and (II), the load of the initial block is explicitly specified for method (III) and is approximately 30% of the ultimate tensile stress (in terms of maximum stress) [40].

Table 5 Summary of different features of the fatigue limit prediction methods [120]

Features				**Fatigue limit estimation procedure**			
				(I) Luong-Risitano	**(II) Iterative method**	**(III) Threshold method**	**(IV) Thermoelastic point inversion**
1	Factors affecting the accuracy of fatigue limit estimations	Loading block definition	'Step dimension' between two loading blocks	YES	YES	YES	-
			Minimum number of loading blocks	More than 10 [37]	More than 10 [54]	Below 10 [40]	-
			Stress of the first loading block	Not specified	Not specified	σ_{max} =30% UTS	-
		Number of specimens required		Dependence on the definition of loading blocks	Dependence on the definition of loading blocks	Dependence on the definitions of loading blocks	Dependence on the loading rate in the tensile test
2	Possibility to be done automatically			NO	YES	NO	NO
3	Applicability to more than one thermal index			YES	-	YES	NO
4	Analytical expression to evaluate the uncertainty			NO	NO	NO	NO

another aspect emphasized in Table 5 concerns the quantity of samples necessary for accurately estimating the fatigue limit. Table 5 demonstrates that this requirement primarily hinges on how the loading block is defined. Furthermore, the method (IV) also varies in its sample requirement based on the loading rate applied during the tensile test.

Certainly, the minimal number of samples required for each method significantly impacts both the

duration and cost of the test. In methods (I)-(III), samples need to undergo cyclic loading until they reach a stabilized temperature for each loading block. Theoretically, only one sample is required to estimate the fatigue limit since the loading is stopped before any damage occurs [37, 40, 158].. However, uncertainties arising from environmental conditions, material microstructure, geometry, etc., introduce statistical variations in results among samples [158]. To address this variability while maintaining test efficiency, it is typically recommended to use at least three samples [37, 158]. Therefore, relying solely on one specimen for estimating the fatigue limit is mainly beneficial for exploratory purposes.

In method (II a lack of sufficient points in $T - \sigma_a$ could pose challenges in fitting straight lines to the thermal data [54]. Thus, it can be inferred that this method requires more thermal data than methods (I) and (III). As a result, obtaining additional thermal data may prolong testing time, and naturally, more samples might be needed (since a higher number of thermal points increases the likelihood of damage initiation).

In method (III), establishing the correlation between temperature rise and stress amplitude, along with determining the threshold value, can be achieved during the initial loading phases. Upon surpassing the threshold value, the fatigue limit estimation can be made without additional loading. Theoretically, this approach holds promise for a novel era of non-destructive fatigue testing, implying that method (III) could deliver quicker predictions of fatigue limits compared to methods (I) and (II).

According to Risitano & Risitano [167], the thermoelastic point inversion technique is swifter compared to cyclic loading methods (I)-(III). Nonetheless, it is crucial to acknowledge that this method hinges on the loading rate during the tensile test, as outlined in Table 5. To implement this method effectively, conducting preliminary tests at varying stress rates is essential to observe a distinct and abrupt slope change in the temperature trend. Following this, additional tests should be conducted using the loading rate identified in the previous step, considering possible scatter as explained by Foti et al. [34].

The second characteristic highlighted in Table 5 pertains to the automated execution of a thermographic technique. Among the four methods listed, only method (II) possesses this capability.

Among the third feature's attributes, method (IV) distinguishes itself by its exclusive utilization of the mean temperature, unlike methods (I) and (III). It's worth mentioning that the Iterative method (method (II)) hasn't been examined with indices beyond the mean temperature. Nevertheless, in theory, there could be potential for applying this method to other indices, particularly indices 5 and 6 as discussed

in the previous section.

Ultimately, as depicted in the final row of Table 5, it is crucial to emphasize that all the methods under consideration share a universal constraint: none of them offer an estimation of the uncertainty linked to the determined fatigue limit.

2-6-3 Fatigue limit prediction in components

In this section, following an exploration of various aspects concerning thermal fatigue indicators and thermographic techniques, it becomes imperative to address the challenges entailed in assessing component fatigue through thermographic methods.

A challenge encountered with thermographic methods lies in their application to real-world scenarios beyond the controlled laboratory environment, particularly in conducting in-situ inspections of components under operational loads. Practically, performing in-situ inspections necessitates adequate space to accommodate equipment (such as an infrared camera and computer) with high spatial resolution, as well as the option to enhance component emissivity through the application of a black coating. Additionally, prior knowledge of the critical regions of components and their loading conditions is indispensable for effective implementation.

Implementing laboratory techniques in practical settings presents an extra challenge, especially concerning component geometry. In thicker components, internal heat sources may produce a subtle thermal imprint on the surface, posing a detection challenge without conducting targeted post-processing analyses to distinguish the heat source's signal from background noise. Without these analyses, discerning the most crucial areas in components with intricate shapes becomes challenging due to heat dissipation occurring at multiple points. In such scenarios, employing a finite element model is recommended as it offers valuable assistance in identifying the most stressed regions.

Besides the previously discussed challenges, determining the stress history and the current stress state is often uncertain, particularly for components experiencing operational loads. Consequently, establishing a direct correlation between the measured thermal data and the stress state, as well as predicting remaining life, is not a straightforward endeavor.

Based on the analyses conducted in earlier sections, it becomes clear that prior to implementing a particular thermographic method on a specific component composed of a particular material, it is essential to meticulously refine all procedures in the laboratory.

Certainly, considering the aforementioned challenges, establishing the fatigue limit of metals at the component level presents a notable obstacle. This is underscored by the scarcity of studies dedicated to this subject concerning components, particularly when contrasted with the extensive research focused on flat and cylindrical samples. To date, only two prominent studies are evident in the literature on this matter.

The initial endeavor was carried out by Luong [43, 109] concerning tension-compression fatigue tests on XC55 steel connecting rods. The research demonstrated that the fatigue limit could be determined within a few hours, marking a substantial enhancement compared to the standard staircase method, which typically requires several months [43, 109].

In the latest investigation conducted by Faria et al. [185], a thermographic approach was employed to predict rapidly the fatigue behavior of a comparatively intricate component, a cast iron crankshaft. The findings indicated a notable correlation between the thermographic results and the data derived from the Staircase method, especially evident in the dog-bone samples extracted from the crankshaft counterweights.

2-7 Conclusions

This section undertook a thorough comparative analysis of thermography-based techniques and protocols for estimating the fatigue limit. It is crucial to gain a deeper understanding of these methods to elucidate the current state of knowledge, stay abreast of recent advancements, and comprehend the advantages and disadvantages of various approaches. Such insights are pivotal for selecting the most suitable methodology for conducting fatigue assessments in metals utilizing thermography.

The domain of thermal fatigue assessment was thoroughly investigated, encompassing an exploration of various thermal indices such as mean temperature rise, initial temperature slope, thermoelastic phase, first amplitude harmonic of temperature, second amplitude harmonic of temperature, and specific heat loss. These indices are utilized for either predicting fatigue limits or evaluating material damage. Additionally, a comprehensive examination of all rapid methods—including Luong-Risitano's method, the iterative method, the threshold method, and thermoelastic point inversion in tensile tests—for estimating fatigue limits was conducted.

On one hand, the section provided an analysis of the strengths and weaknesses of each thermal index, aiding in the selection of the most suitable one for specific testing conditions. On the other hand, it conducted a comparison among rapid thermographic methods for estimating the fatigue limit. This

comparison considered factors such as accuracy and key features affecting their effectiveness, such as the definition of the loading block and the number of required specimens. Additionally, the discussion delved into the applicability of thermographic methods, including potential automation, suitability for various thermal indices, and the level of variability in estimations. Through this analysis, uncertainties in the estimation of fatigue limits were revealed.

Moreover, obstacles encountered when employing thermographic techniques for fatigue assessment in practical applications were identified, including constraints such as space availability for in-situ inspections, prerequisite understanding of critical regions and loads, complexity of component geometry, and uncertainty surrounding the component's stress history.

In summary, it can be stated that [120]:

- The thermal indices tied to specific physical processes (thermoelastic effect, intrinsic dissipation, non-adiabatic effects...) are effective parameters for studying the damage from both qualitative and quantitative points of view;
- Further exploration of the connection between these processes and the microstructural phenomena related to damage is needed to understand better the meaning of the thermal fatigue limit;
- The harmonic parameters of the temperature signal provide a more robust method for damage assessment than simply using the mean temperature;
- While thermographic methods for estimating the fatigue limit are rapid and promising, additional work is needed to establish a procedure for calculating the uncertainty of the prediction, even with limited samples, to align with standard test methods;
- The application of thermographic methods and procedures in real-world applications is an ongoing topic that requires more effort.

According to the above explanations, the second harmonic amplitude of the temperature was decided to be used as an efficient thermal index for establishing a strong methodology to create a hybrid approach linking a numerical model with the experimental data for heat source identification. In addition, the efficiency of this thermal index is shown further in fatigue limit estimation through an experimental campaign proposed in the following sections.

3 Experimental campaign

In this chapter, the utilized materials and the implemented tests are proposed. The unique dataset collected from this part of the work are basically used for two distinct purposes:

(i) SS 316 data: comparing the efficiency of different thermal indices in fatigue limit prediction with the reference value obtained from the traditional fatigue test (see sections 3-3-1-1 and 3-3-2-1);

(ii) C45 data: obtaining both mechanical and thermal data for creating a numerical model and establishing a hybrid approach linking the numerical and experimental methods for heat source identification and the heat diffusion study (see sections 3-3-2-1 and 3-3-2-2).

3-1 Material and geometry

To investigate the dissipation and fatigue behavior, it is necessary to use samples designed according to the available standards [174]. Two carbon steels including tempered steel C45 and Stainless Steel 316 (SS 316) were used in this study. The first is widely utilized in industry for the construction of shafts, cranks, keys, pins, supports, rods, drive shafts, due to its strength and durability. The latter one is usually used in food processing and marine equipment due to its superior corrosion resistance properties as well as pharmaceutical equipment due to its low particle contamination levels.

Because of the availability of the data in the literature, the material used for the main verification of the numerical model of heat source identification, is C45 with the properties listed in Table 6 which are taken from the work by De Finis et al. [101]. In the table, ρ is the density, C_p, α and k are respectively the specific heat at constant pressure, thermal expansion and conductivity coefficients; ϵ is the emissivity factor. The geometry of the samples for C45 was a flat dog bone designed according to the related standard [174] as shown in Figure 30.

On the other hand, the comparison between different thermal methods in terms of estimating the fatigue limit was performed using SS 316 samples. The material parameters and the design of the SS 316 cylindrical dog bone specimens are depicted in Table 7 and Figure 31, respectively.

Table 6 Material parameters for C45 [101]

$\rho\left(\frac{kg}{m^3}\right)$	$C_p\left(\frac{J}{kg\,℃}\right)$	$k\left(\frac{W}{m\,℃}\right)$	$\alpha\left(\frac{1}{℃}\right)$	ϵ
7850	486	42.5	13.3e-6	0.98

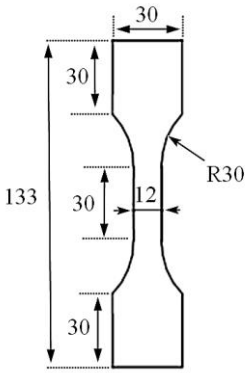

Figure 30 Flat dog bone geometry for C45 material (in mm), thickness is 6 mm

Table 7 Material parameters for SS 316

$\rho\left(\frac{kg}{m^3}\right)$	$C_p\left(\frac{J}{kg\,℃}\right)$	$k\left(\frac{W}{m\,℃}\right)$	$\alpha\left(\frac{1}{℃}\right)$	ϵ
7900	490	16.3	17.2e-6	0.98

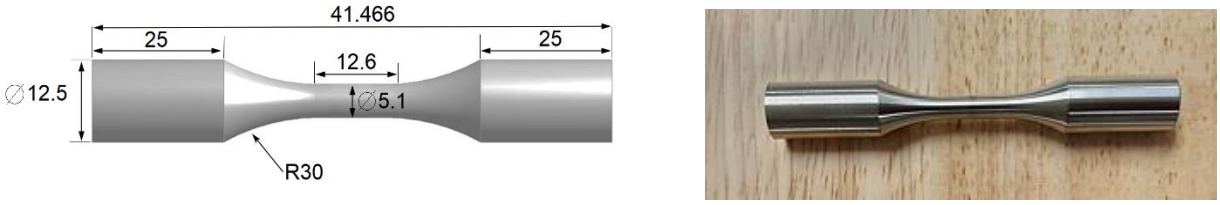

(a) (b)

Figure 31 SS 316 material (a) cylindrical dog bone geometry (in mm) and (b) fabricated sample

3-2 Tensile test

The static tests were conducted on SS316 specimens (for C45, the data are available in [101]) to identify material properties. These tests were performed at Center for Rotating Machinery, Louisana State University, USA during the abroad period. The tensile data were used to define the stepwise loading table (Figure 24).

For C45 samples, tensile tests were carried out for 5 samples under displacement control with a rate of 1 mm/min using MTS model 370 servo-hydraulic loading frame (loading capacity of 100 kN) [101].

For SS 316, two samples were planned for tensile test using an Instron universal testing machine Model 1,000 Hz 810 (loading capacity of 25 kN) and a high precision extensometer, Epsilon Model 3542-0100-050-ST as shown in Figure 32, to accurately measure the strain. In Figure 33, the stress-strain curves from the tensile test for two SS 316 samples are proposed. In addition, Table 8 indicates the mechanical properties for both materials, C45 and SS 316.

Table 8 Mechanical properties of C45 and SS 316

Material	E: Young's modulus (GPa)	σ_y: Yield strength (MPa)	σ_u: Ultimate Strength (MPa)
C45 [101]	205	450	760
SS 316 [186]	171	335	640

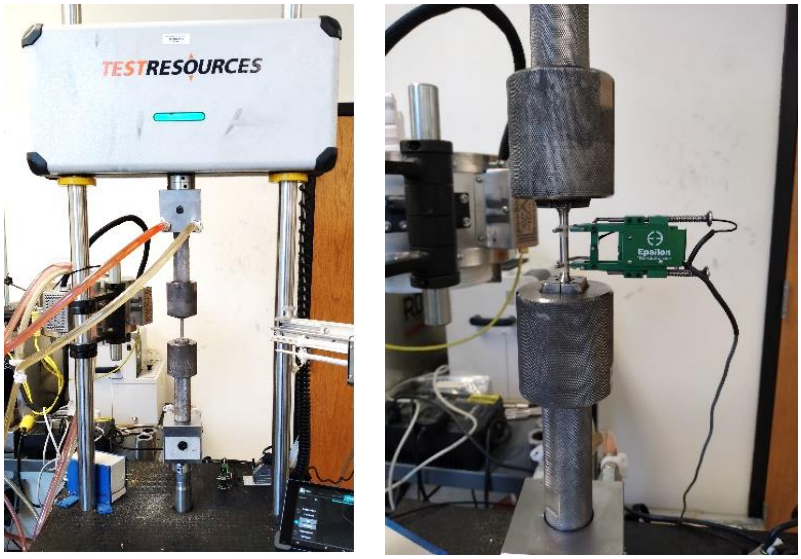

Figure 32 Test equipment for tensile test of SS 316

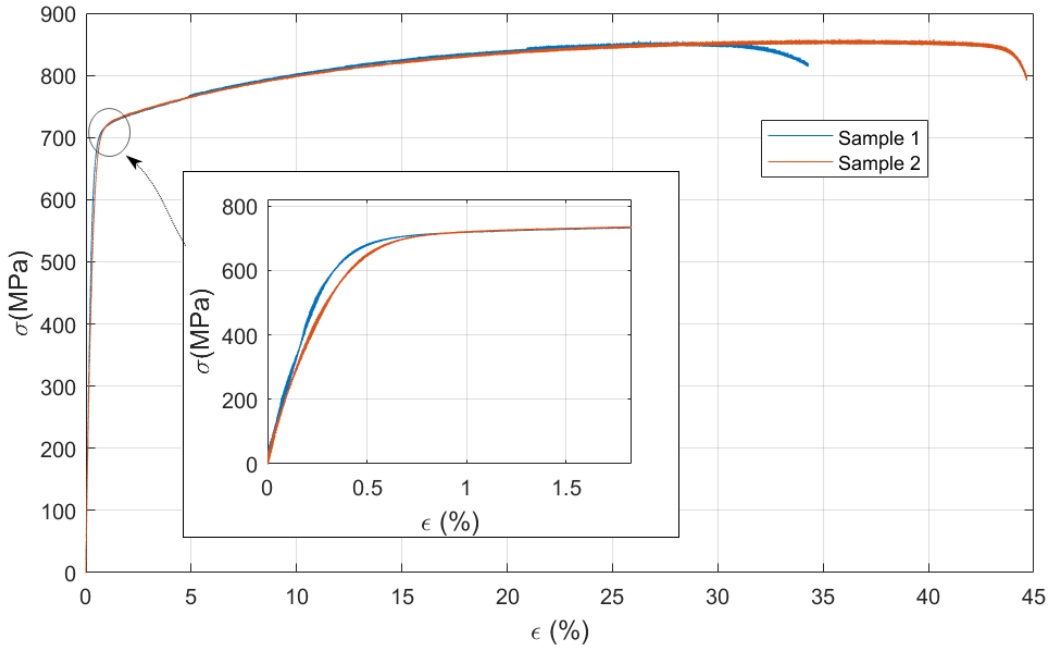

Figure 33 Stress-strain curve of two samples of SS 316

3-3 Cyclic loading test

As shown in Table 9, two types of cyclic loading tests, including constant amplitude test and stepwise test, were performed on both C45 and SS 316 for distinct purposes. The stepwise tests were conducted to compare various thermal indices for estimating fatigue limit of SS 316 and to identify heat sources in C45, numerically.

The constant amplitude fatigue tests were performed for two purposes: (i) acquiring the S-N curve for SS 316, which serves as a reference to compare the efficiency of different thermal methods in terms of fatigue limit estimation; and (ii) probing into the effect of loading frequency on the SAH of temperature for C45.

As summarized in Table 9, one part of the cyclic loading tests was performed at Center for Rotating Machinery, Louisiana State University (LSU), USA, and the rest at Structural Diagnostic and Thermal methods for Experimental Mechanics lab, Politecnico di Bari (POLIBA), Italy.

Table 9 Cyclic loading tests

		The goal of the test	
Material		SS 316	C45
Test type	Stepwise test	Comparing different thermal indices in fatigue limit estimation (at POLIBA)	Heat source identification (at POLIBA)
	Constant amplitude test	S-N curve acquisition (at LSU)	Effect of loading frequency on the SAH of temperature (at POLIBA)

3-3-1 Stepwise test

The stepwise includes a sequence of loading blocks of the same duration in terms of loading cycles with fixed values for loading frequency and stress ratio [40]; involving incremental stress amplitude and mean stresses up to the material failure. The sequence of loading blocks is usually characterized by an increase in the mean stress, which is why the method is termed stepwise loading (see Figure 24). However, in a complete reversed loading (R= -1) studied in this work, the steps are defined by the stress amplitude.

For the first block, the maximum stress should be around 20-40% of the ultimate tensile strength of the material to ensure enough data below the fatigue limit [175]. The stress increment between each block can be adjusted to ensure reasonable testing time and an adequate number of points around the fatigue limit [117]. During each block, thermographic acquisitions are performed for a predefined time period and sampling frequency. Of course, first and foremost, the quality of the thermal acquisition

depends on the camera specifications and settings (i.e., cooled or uncooled, the frame rate, the integration time and the temperature range), as mentioned section 2.

3-3-1-1 Stepwise test on SS 316

In this work, the stepwise tests were designed to involve a series of 12 incremental loading steps, as outlined in Table 10. All steps are carried out at a fixed loading frequency of 11 Hz and the stress ratio R= -1. After completing approximately 20,000 cycles for each step, the stress is increased according to Table 10 until the material fails. Samples geometry and dimensions were shown in Figure 31.

The tests were performed with a servo hydraulic fatigue machine MTS model 370 with loading capacity of 100 kN and two thermal cameras. As shown in Figure 34, a micro bolometric IR camera FLIR A20 (160x140 pixels and a thermal sensitivity NETD < 50 mK) was used to obtain thermographic data in a single sequence up to the end of the test; mainly for observing the temperature stabilization. While the second camera, a cooled IR camera X6540 (640x512 pixels and a thermal sensitivity NETD < 20 mK), was utilized to acquire three thermographic sequences with higher frame rate. A dummy-unloaded specimen made from the same material was used to provide a temperature reference, as suggested in the previous section, to eliminate the environmental temperature effect from the mean surface temperature of the sample. The gage section of the specimens was polished using sand papers and progressed through 480, 800, 1200, and 1500 grit sizes to reduce the surface roughness. In addition, a matte black coating was applied to improve thermal signal accuracy.

During the test, thermographic acquisitions are performed both at 213 Hz for 10 seconds (2130 frames acquired) using an IR camera X6540 and at 5 Hz for the same period (50 frames acquired) using a micro bolometric IR camera, FLIR A20. The thermal sequence during each loading step is recorded after a specific cycle count.

Figure 35 shows a schematic representation of the thermal data acquisition. Thermal measurements for each loading step (including 20,000 cycles) were conducted in four sub-steps. This approach enabled the analysis of damage progression throughout the loading cycles. Sub-steps 1, 2 ,3 and 4 corresponded to the data acquired between 1000 -1110 cycles, 5000 and 5110, 10000-10110 cycles and 15000-15110 cycles, respectively. The region of interest corresponds to the gauge length area between the clips of the extensometer.

Figure 34 Stepwise test setup for SS 316

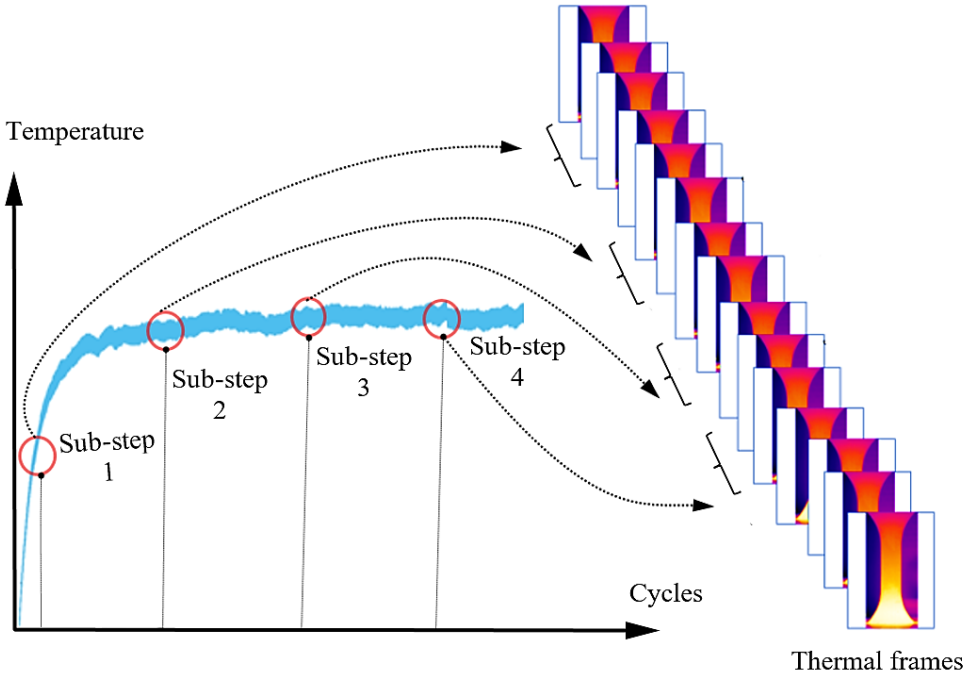

Figure 35 A schematic of thermal data acquisition process

Table 10 Loading table for stepwise test of SS 316

loading block	% UTS (MPa)	Stress amplitude (MPa)
1	39.8	255
2	41.4	265
3	43.0	275
4	44.5	285
5	46.1	295
6	46.9	300
7	47.7	305
8	48.4	310
9	49.2	315
10	50.0	320
11	52.3	335
12	54.7	350

3-3-1-2 Stepwise test on C45

For heat source identification by a numerical model, the experimental thermal data are necessary to be used as a reference for setting the parameters of the model.

For this purpose, fatigue tests were performed on dog bone samples of C45 steel with the mechanical properties and geometry as proposed in Figure 30, Table 6 and Table 8. The specimens designated for fatigue testing were initially polished by applying acetone, and surface roughness or irregularities were eliminated using a mechanical air die grinder. Then, the surface of the samples was coated with a mat black to enhance their emissivity and thus improve the accuracy of the acquired thermal signal.

The setup is the same as previous test for SS 316 but incorporating also an extensometer, as shown in Figure 36. The mechanical data were collected by processing the loading machine unit at a frequency of 204 Hz. At R=-1 and a frequency of 11 Hz, the fatigue tests were done through a stepwise test [40] under four stress amplitudes above the fatigue limit of around 290 MPa [101], including 300, 310, 320 and 340 MPa, where the damage and heat dissipation are significant. The thermographic sequences were recorded for a duration of 10 seconds at a rate of 123 Hz; the integration time was set at 0.97 milliseconds; and the temperature range was between 10 and 90 °C. Each infrared sequence acquisition corresponded to 110 mechanical loading cycles. Thermal measurements were taken for each loading block after temperature stabilization.

Figure 36 Stepwise test setup for C45

3-3-2 Constant amplitude test

3-3-2-1 S-N curve acquisition for SS 316

A S-N curve, also known as the stress-life curve or fatigue curve, is a graphical representation that illustrates the relationship between the stress amplitude (S) and the number of cycles to failure (N_f) for a given material under cyclic loading conditions. It is a fundamental tool used in the field of fatigue analysis to predict the fatigue life of a material. The S-N curve typically exhibits the following characteristics:

- Fatigue Limit: for some materials, there is a stress level below which the material can theoretically endure an infinite number of cycles without failing. This stress level is known as the fatigue limit. In the S-N curve, this corresponds to a horizontal line where the number of cycles to failure approaches infinity as the stress amplitude decreases.
- Fatigue Strength: the stress level at which failure occurs after a specific number of cycles is known as the fatigue strength at that cycle count. As the number of cycles decreases, the stress level at which failure occurs increases, approaching the material's static strength.
- S-N Slope: the slope of the S-N curve represents the rate at which the fatigue life decreases with increasing stress amplitude. Steeper slopes indicate that the material's fatigue life is more sensitive to variations in stress levels.

For S-N curve acquisition, the fatigue tests were performed at a fixed loading frequency equal to 11 Hz and the stress ratio R=-1. They were performed using an Instron universal testing machine with a maximum loading capability of ±25 KN (see Figure 32). The test samples were fastened to the machine by appropriate grips. A load-control mode was used, and different stress levels ranging from 300 MPa to 350 MPa were applied on 18 samples of SS 316, as shown in Table 11. The force was applied in a sinusoidal waveform in the fatigue experiments.

Table 11 Loading table for S-N curve acquisition of SS 316

Sample #	1	2	3	4	5	6	7	8	9
Stress amplitude (MPa)	300	310	310	310	312.5	315	315	315	320
Sample #	10	11	12	13	14	15	16	17	18
Stress amplitude (MPa)	320	325	325	330	335	337.5	340	345	350

3-3-2-2 Loading frequency effect on SAH of temperature for C45

For acquiring necessary data to study the effect of the loading frequency on SAH of temperature, a fatigue test was designed and performed on a pristine C45 dog bone sample with the geometry as shown in Figure 30. Tests were done under a constant loading amplitude of 300 MPa and different loading frequencies including 1.5, 2.5, 3.5, 4.5 and 5.5 Hz, and the stress ratio R=-1. For each loading frequency after reaching the temperature stabilization, three thermal acquisitions were performed. After acquiring the data for each frequency, the loading frequency was changed to another one. It should be noted that the setup is the same as shown in Figure 36; the data acquisition and sample preparation are the same as those for stepwise test on C45, mentioned before. It is worth noting that low loading frequency and relatively low imposed stress were planned for avoiding the vibration of the loading frame (it increases with frequency and load level) and achieving a stabilization phase in the signal.

3-4 Data processing

The data processing involves the assessment of the mean and harmonic components of a thermal signal through a method called Lock-in thermography [102]. It needs a reference signal (load or strain) for processing the temperature field via the Fast Fourier Transform (FFT), which enables the conversion of the temperature signal into its frequency-domain representation. In this way, all of the temperature components can be acquired by modeling the temperature as below [45]:

$$T(t) = T_0 + \Delta T f t + T_1 \sin(\omega t + \varphi_1) + T_2 \sin(\omega t + \varphi_2) \quad (15)$$

where f is the loading frequency, T_0 is the temperature level at the beginning, ΔT is the mean rise of the temperature per cycle, T_1, φ_1, T_2, φ_2 are the amplitudes and phases of the first and second Fourier components, respectively. A schematic presentation of thermal signal processing is shown in Figure 37.

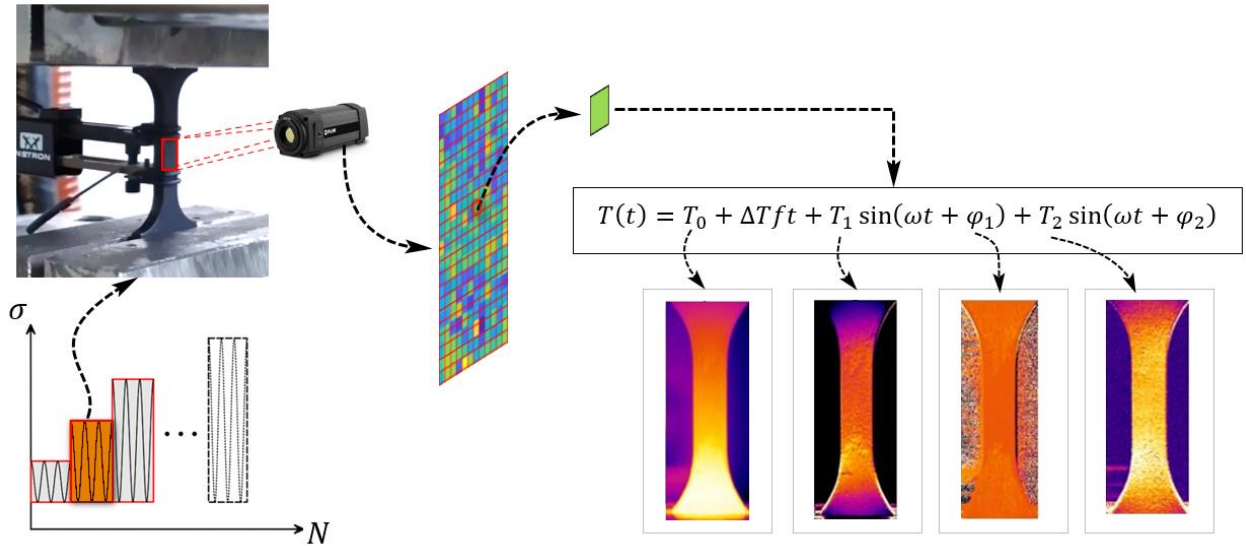

Figure 37 From the thermographic signal to temperature components acquisition

The thermal data processing involved a series of consecutive steps. Firstly, the infrared thermal camera was used to acquire the temperature signal ($T(t)$) with the mm/pixel ratio of almost 0.194 mm and 0.116 mm for C45 and SS316 samples, respectively. Next, a specific region of interest (ROI) was defined in IRTA® software, and its temperature data over time were extracted for subsequent analysis. The average temperature value ($T_0(t)$) for this ROI was computed for each frame in the time sequence. After that, the temperature signal was subjected to a Discrete Fourier Transform (DFT) using a specialized algorithm in MATLAB (see Appendix A) [187].

In this study, the mean of temperature, the first and second harmonic amplitudes are utilized for comparing different thermal indices in fatigue limit estimation, while the second harmonic amplitude is also used for heat source identification via numerical model.

4 Numerical simulation

The primary objective of this chapter is to propose a framework for developing a hybrid approach that integrates numerical models with experimental data for heat source identification. The initial section of this chapter presents the established numerical model and its verification process, while the second section elaborates on the process of heat source identification employed in this study.

Numerical models were set up using COMSOL Multiphysics 5.6 to simulate the surface temperature distribution of the specimen. This simulation focused on the heat source(s) applied within the gauge volume of a dog bone sample, representing the area where heat is dissipated due to plastic deformation [101]. As depicted in Figure 38, the gauge volume and the area held by the gripper are highlighted in red and blue, respectively.

It is assumed that the temperature at both ends connected to the grippers are equal to the environmental temperature, $T_\infty = 20$ ℃ [114, 188], except the model for the main verification process where domains outside the guage volume have this fixed temperature. Keeping a constant temperature at gripper sides, is nearly impossible due to continues heat conduction in the contact region between the sample and grippers, especially the one connected to the loading machine actuator. Nevertheless, as the gauge length is potentially under the damage and usually used to estimate the fatigue behavior of the material, focusing only on the temperature change of this domain can be practically efficient and the above assumption is not consequential [188]. Radiation and heat convection are applied on all external surfaces and the simulations are performed using Heat Transfer in Solids Interface and Time Dependent study in COMSOL.

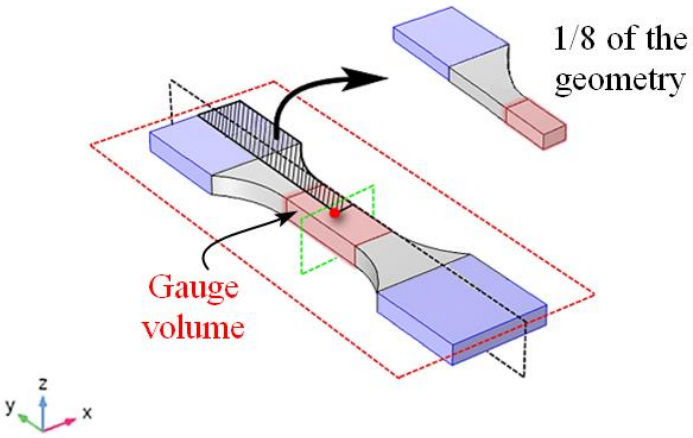

Figure 38 Model of a dog bone sample

Firstly, the proposed model is verified with a single heat source, and then the heat source identification process is presented with randomly distributed heat sources.

4-1 Numerical model with a single heat source and the verification process

For verifying the model, a single heat source is imposed in the whole of the gauge volume (red domain red in Figure 38). In this part of the study, since the heat source does not disrupt the symmetry of the entire geometry, modeling only 1/8 of the geometry is sufficient, thus saving computational time.

Figure 39 summarizes the model verification procedures, presenting the input and output data (or comparison metrics) for the numerical model.

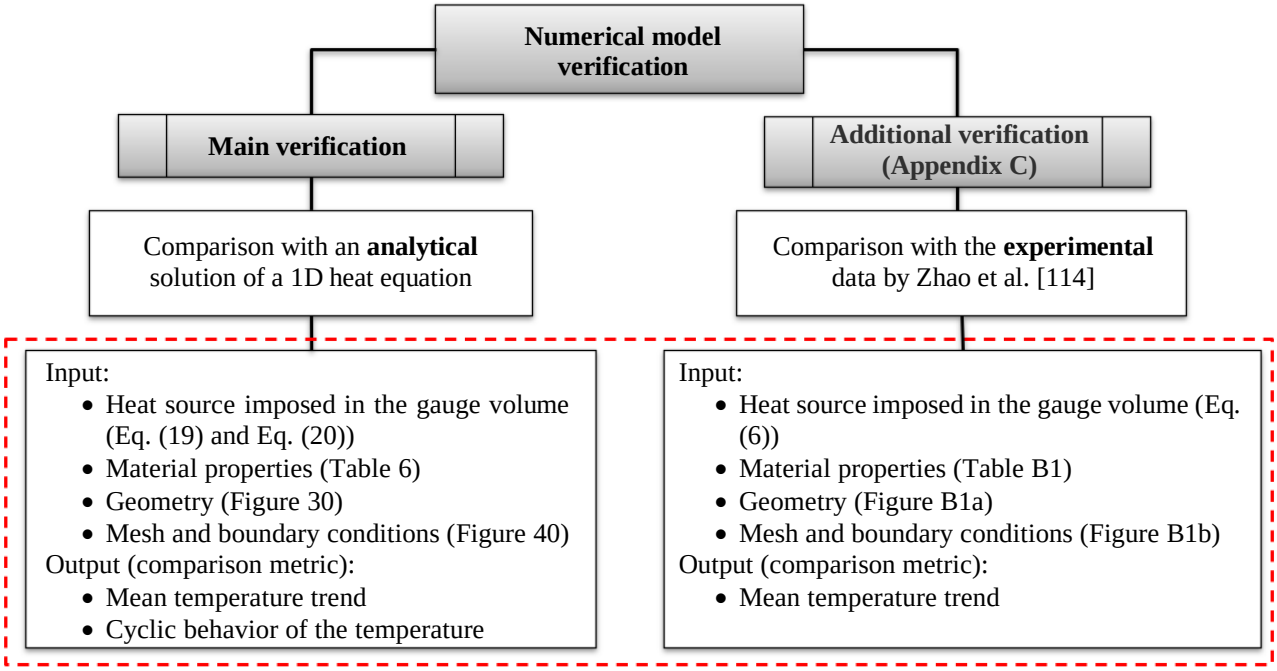

Figure 39 Verification procedures of the numerical model

Due to the absence of sufficient experimental data in the literature concerning estimated heat dissipation or the cyclic temperature trend induced by cyclic mechanical loading ([37, 109, 157, 189]), the main verification method involves employing analytical solutions of the 1D heat equation. These solutions can include both constant and cyclic heat sources (the details can be found in section 5-2-1, Eq. (19) and Eq. (20)). This method allows for a direct comparison between the numerical and analytical thermal data, specifically in terms of the mean temperature and the cyclic trend of the temperature of a point situated on the top surface of the gauge volume (the red point in Figure 38 and Figure 40).

It should be noted that the choice to utilize a 1D heat equation for model verification was made due to the significant complexity involved in defining and solving two or three-dimensional heat equations with cyclic heat sources. In addition, 1D equation is an acceptable approximation for thermal behavior of the geometry shown in Figure 38. This is because the predominant thermal changes occur along the longitudinal direction of the sample, making variations in other dimensions insignificant. It is important to highlight that, finding the solution of the 1D heat equation incorporating a cyclic heat source is one of the findings of this work.

The material used for the verification is C45 with the properties listed in Table 6; and the geometry is the same as in Figure 30. As mentioned before, all regions outside the gauge volume where the heat source is imposed (yellow domain in Figure 40), were fixed to the ambient temperature (see Figure 40). This was done because a constant cross-section is assumed for deriving 1D heat equation (see section 5-2-1, for more information).

As shown in Figure 40, hexahedral elements with quadratic Lagrange discretization including 27 nodes for each element were used for meshing, and the number of elements were set after mesh convergency check. More details about the mesh selection are provided in Appendix B.

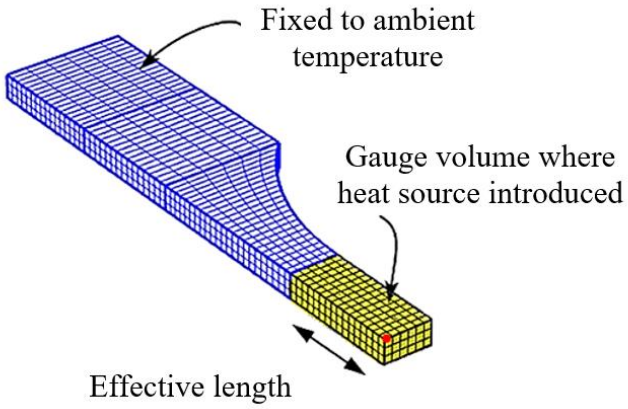

Figure 40 The meshed model for the main verification with analytical results - C45

Furthermore, an additional verification (see Appendix C) is also conducted based on the experimental work by Zhao et al. [114] to compare the 3D model with the same geometry in reality, albeit only in terms of the mean temperature, as the cyclic trend was not proposed in their work.

4-2 Heat source identification

Once the correctness of the numerical model is verified, it is possible to use the model for heat source

identification, by comparing the numerical results with proper experimental data.

4-2-1 Finite element model with randomly distributed heat volumes

As the damage area created during the fatigue load cannot be estimated in advance both in terms of the location and the geometry, using only one single heat source in the gauge volume of the numerical model as a representative of the whole dissipated volume is far from the actual scenario. To address this, the geometry of the heat volume in the simulation is designed based on the model proposed by Munier et al. [50]. Briefly, this model defines a Representative Elementary Volume (REV) as a matrix that contains multiple inclusions randomly distributed in a matrix. Under low stress amplitudes, the inclusions behave similarly to the matrix, and the dissipation is primarily due to the elasto-plastic behavior of the matrix. However, at higher stress levels, significant additional plastic hardening is activated within the inclusions which governs the physical process of fatigue damage initiation.

In this study, as mentioned before, the stress amplitudes are above the fatigue limit of the material, thus, it can be assumed that damage regions where heat sources are established behave similarly to the randomly distributed inclusions with dominant plastic deformation compared to other regions (or matrix in the work by Munier et al. [50]). Inspired by this hypothetical model, the gauge volume was presumed to be filled with randomly distributed unit heat volumes (or inclusions) with a specific size.

A schematic representation of the idea is shown in Figure 41, where the size of unit heat volumes is assumed to be 1 mm^3.

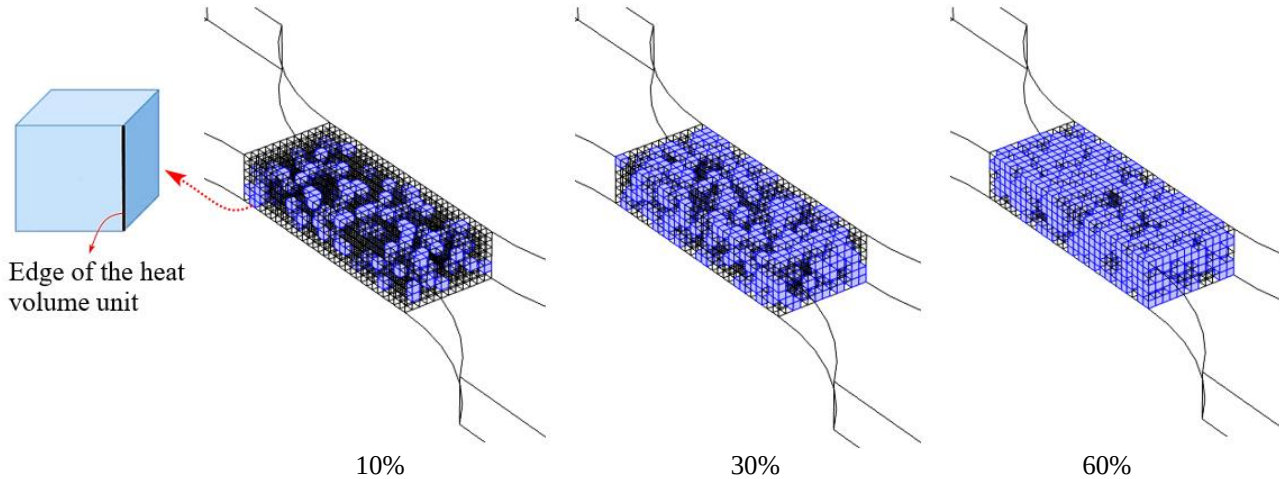

Figure 41 A schematic representation of the unit heat volumes (with the size of 1 mm^3) randomly filled in 10%, 30% and 60% of the gauge volume

It is worth mentioning that exploring smaller sizes, potentially close to the pixel size in experimental maps, is necessary to identify the most appropriate one that provides comparable numerical results to those obtained experimentally. However, reducing the size of unit volumes is constrained by the available computational resources as it results in smaller element sizes or a higher number of elements in the FEM, which can significantly increase the computational load for simulation.

Starting from a relatively big size (i.e., 1 mm^3) can be computationally beneficial to check the overall behavior of the model, or in other words, the examination of factors unaffected by the unit size of heat volumes (as proposed below, including the change of the studied temperature component with total heat volume, the number of pixels defined on the surface of the model for data acquisition and the distribution of unit volumes). In the following sections, the steps for heat source identification processor are presented.

4-2-2 Heat source identification process

This section demonstrates a procedure for identifying the heat volume that produces the same temperature variations as the experimental data for each considered loading level. The identification is based on the average of the SAH of temperature, T_{2w}.

Throughout this process, the mechanical properties in Table 6 and the sample geometry in Figure 30 are used; and the model is meshed with 1260 hexahedral elements, as shown in Figure 40. After preparing geometry and material properties, next steps for identifying the volume producing heat are shown in Figure 42 and explained in the following subsections. As shown in the figure, the process is designed under the assumptions of uniform size and heat amplitude for all randomly distributed unit volumes, a non-interacting behavior between units and a criterion based on the mean value of T_{2w} from the surface of sample.

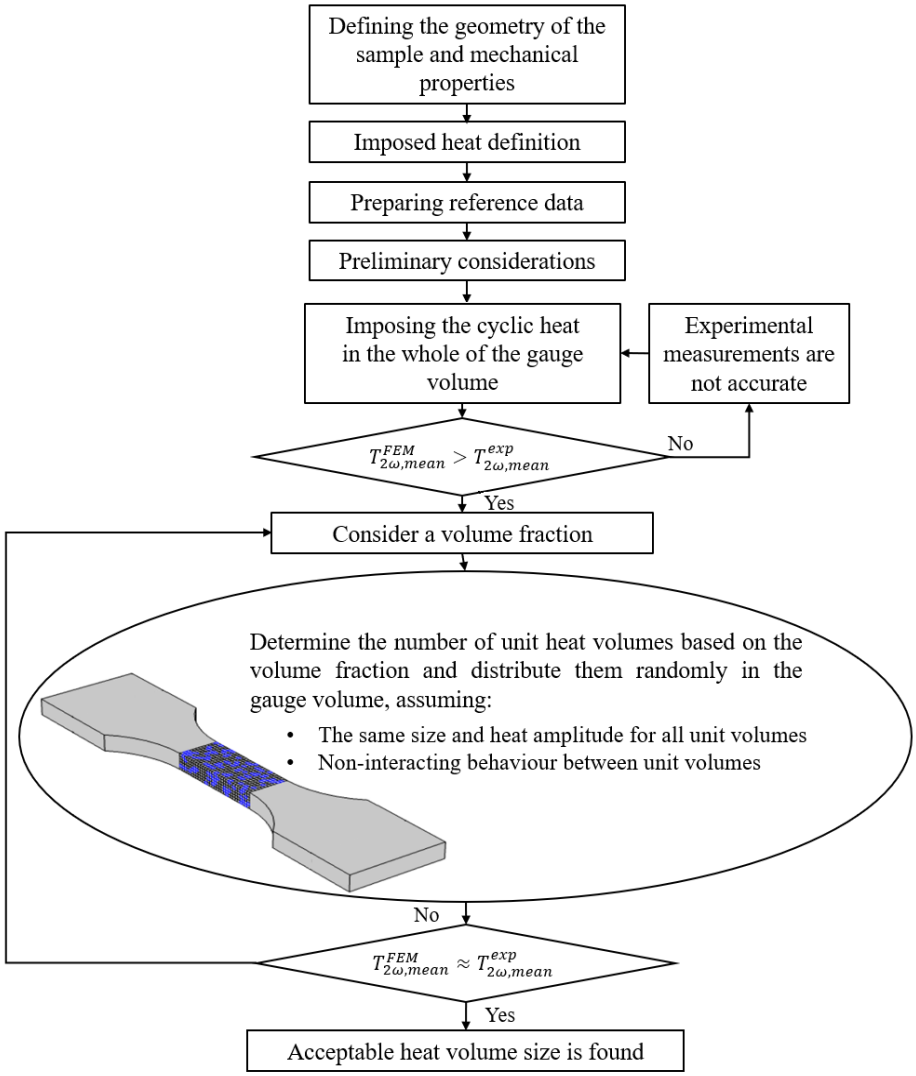

Figure 42 A schematic representation of heat source identification

4-2-2-1 The imposed heat definition

As shown in Figure 43 and according to the experimental data, a cyclic heat source can be introduced based on either the experimental heat dissipation estimated from the surface temperature or the mechanical data. As mentioned before, the estimation of heat dissipation from the average SAH of temperature, $T_{2\omega}^{exp}$, (Eq. (7) is an approximation as it relies solely on surface temperature without providing insights into the processes occurring within the gauge volume. Thus, it can be said that the mechanical energy is the most accurate option to define the imposed heat in the numerical model as it is measured via extensometer and the loading machine.

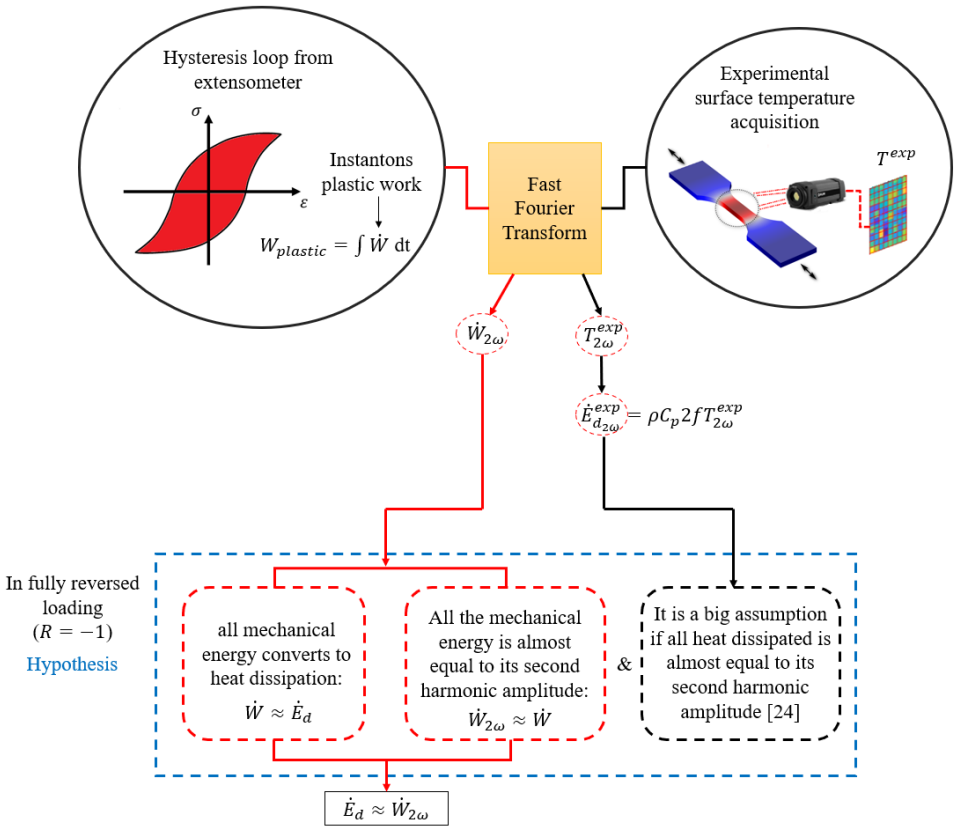

Figure 43 Heat as an input for numerical model

De Finis et al. [101] showed that for C45 steel under fully reversed loading (R=-1), the SAH of mechanical energy, $\dot{W}_{2\omega}$, is almost equal to the total mechanical energy, $\dot{W}$. Generally, W can be defined from scalar product of the instantaneous values of stress and strain over the time through a simple viscoelastic model, and then $\dot{W}$ can be found by derivation of W along the time. By applying DFT on $\dot{W}$, $\dot{W}_{2\omega}$ can be determined. In this work, $\dot{W}_{2\omega}$ is utilized as the amplitude of the imposed heat with a sinusoidal form of $\dot{W}_{2\omega}\ (1 + sin(2\pi\ (2f)\ t))\ (W/m^3)$.

4-2-2-2 Reference experimental data

After defining the imposed heat, essential experimental data including $T^{exp}_{2\omega}$, $\dot{W}_{2\omega}$, the noise resulted from the thermal measurements and the sample deformation should be collected. $T^{exp}_{2\omega,mean}$ is mainly used for comparing the numerical results with the experimental ones, establishing a criterion for heat source identification. Incorporating noise-related data into the numerical model is imperative as they constitute an integral part of the experimental dataset which are used for comparison.

4-2-2-2-1 Data for checking the quality of the numerical results

For four loading steps including 300, 310, 320 and 340 MPa, above the fatigue limit where the damage presents considerably (the fatigue limit is around 290 MPa [101]), the experimental values of the SAH of temperature, $T_{2\omega}^{exp}$, were acquired based on the data processing mentioned before.

For this purpose, an appropriate size of ROI, as shown in Figure 44, was applied on the gauge length with 52*99 pixels. As proposed in Figure 45 for each loading level, the values of $T_{2\omega}^{exp}$ of each pixel in ROI provides a thermal map. They are then utilized for qualitative comparison with the numerical maps obtain from the same ROI as in experiment.

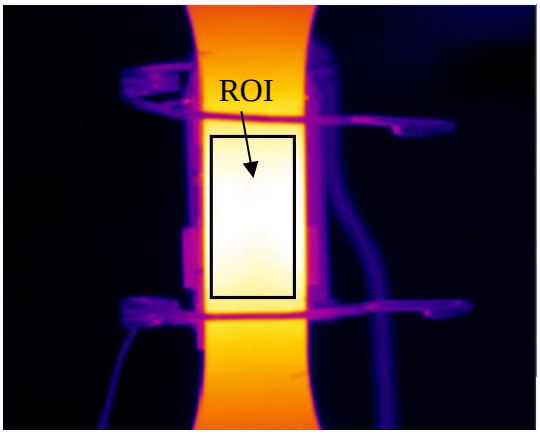

Figure 44 Region of Ineterst (ROI) for laoding amplitude of 340 MPa

The mean of $T_{2\omega}^{exp}$ values in ROI for each loading level is proposed in the Table 12; they serve as reference values for both identifying the volume producing heat and improving the numerical model.

In addition, the SAH of the total mechanical energy, $\dot{W}_{2\omega}$, are also listed in Table 12. They can be found from the stabilized hysteresis loops at each loading step to define the amplitude of the cyclic heat source imposed in the numerical model, $\dot{W}_{2\omega}\ (1 + sin(2\pi\ (2f)\ t))\ (W/m^3)$.

Table 12 $\boldsymbol{T_{2\omega,mean}^{exp}}$ for heat amplitude $\boldsymbol{\dot{W}_{2\omega}}$

$\sigma_a\ (MPa)$	300	310	320	340
$T_{2\omega,mean}^{exp}$ (°C)	0.0023	0.0025	0.0054	0.0132
$\dot{W}_{2\omega}\ (W/m^3)$	1.70E+07	2.13E+07	2.93E+07	4.11E+07

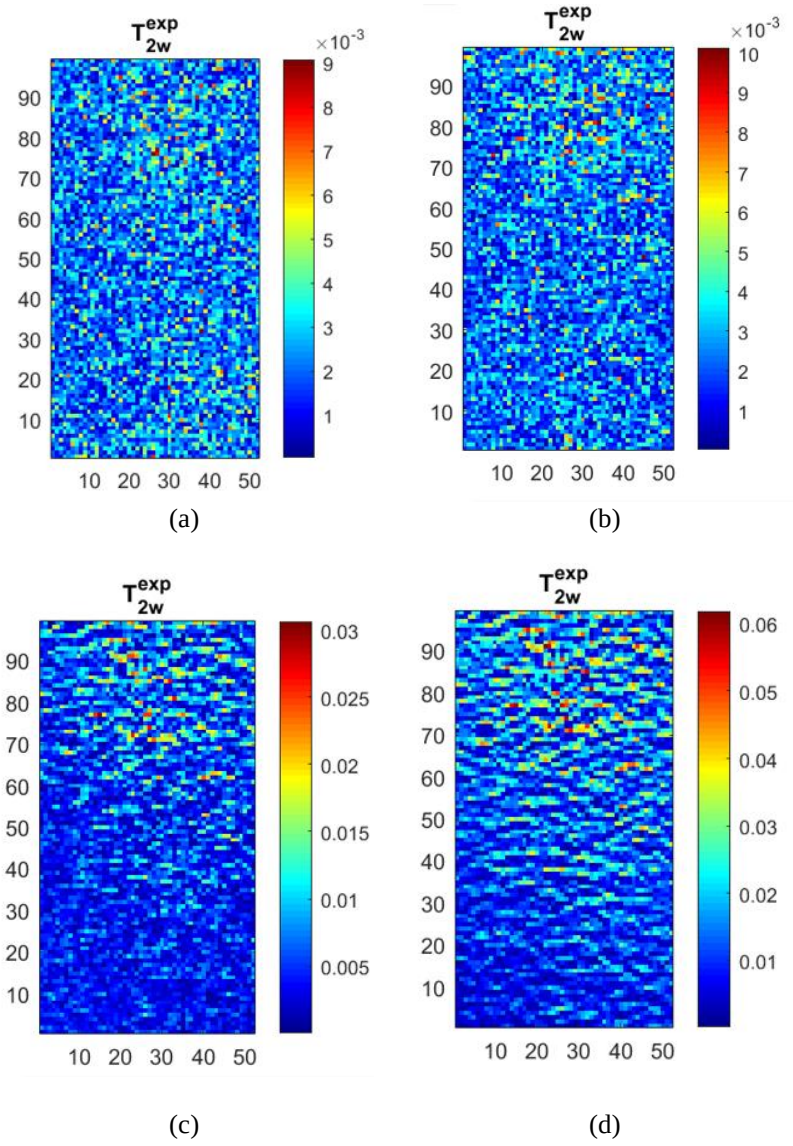

Figure 45 The map of $T_{2\omega}^{exp}$ for loading amplitudes: (a) 300 MPa (b) 310 MPa (c) 320 MPa and (d) 340 MPa

4-2-2-2-2 Noise resulted from the thermal acquisition

Thermal acquisition noise is due to the noise of detector in measuring the temperature, resulted from inherent electronics, the calibration of camera and so on. One possible solution to account for this kind of noise is the acquisition of the temperature data at the beginning of the test (before loading or at very low loading level) where all possible artifacts (e.g., the deformation of the sample, the vibration of the loading machine, etc.) are negligible.

Using the same ROI as before, $T_{2\omega}^{exp}$ values were extracted before imposing the first loading step; the $T_{2\omega}^{exp}$ map and histogram are shown in Figure 46. Simulating this noise is preferable to simply adding it to the numerical maps. By fitting different distribution functions, the Weibull function with scale

parameter of 0.0025 and shape parameter of 1.9783 (see Table 13) found to be the best fit for simulating this experimental noise. Next, this simulated noise is added pixel by pixel to the numerical maps.

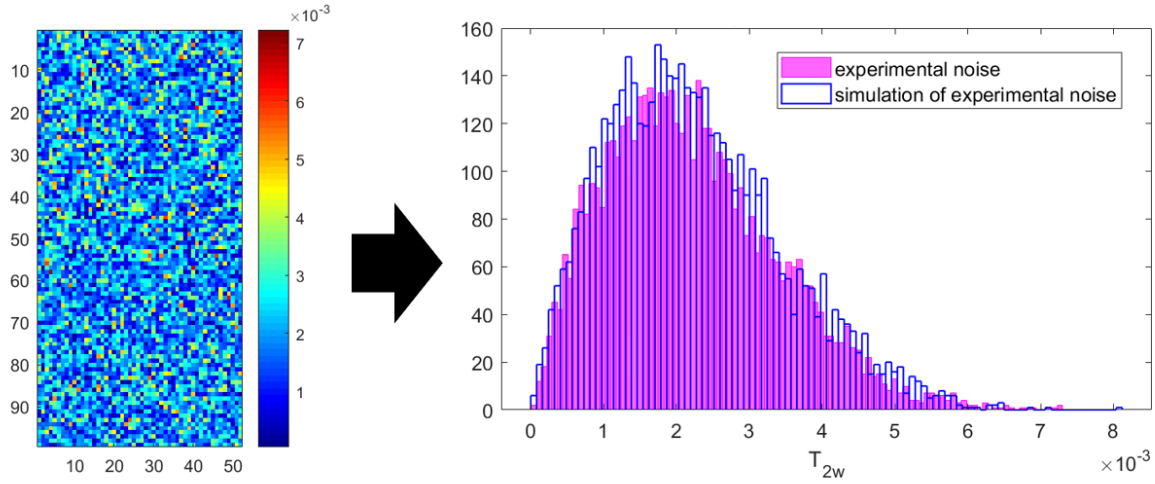

(T_{2w} map of the thermal acquisition noise) (Histogram of the experimental noise and the simulated one)

Figure 46 Thermal acquisition noise from experimental data and the simulated noise

Table 13 Thermal acquisition noise

$T_{2\omega}^{exp}$		Simulated $T_{2\omega}^{exp}$ Weibull distribution parameters	
Mean	Standard deviation	Scale parameter	Shape parameter
0.0022	0.0001	0.0025	1.9783

4-2-2-2-3 Noise due to the deformation of the sample

In experiment, when the imposed stress level (or stress amplitude here as R=-1) is higher than the fatigue limit of the material, the sample deforms in the gauge length as a response to the applied load. In this situation, as shown in Figure 47, the points on the material coordinate (or in the initial coordinate, with the origin same as the red point in Figure 38) initiate movement while ROI of the thermal camera and pixels inside it are fixed in the space.

On the other hand, in the numerical model, sample deformation is not accounted for as it is only a thermal model, not a coupled thermo-mechanical one. Thus, the points on the material coordinate are fixed in the gauge length. However, this movement can be simulated and imposed on the numerical results. For this purpose, a linear displacement can be considered from the fixed gripper to the moving gripper; it changes from zero at the fixed side to a maximum value on the other side.

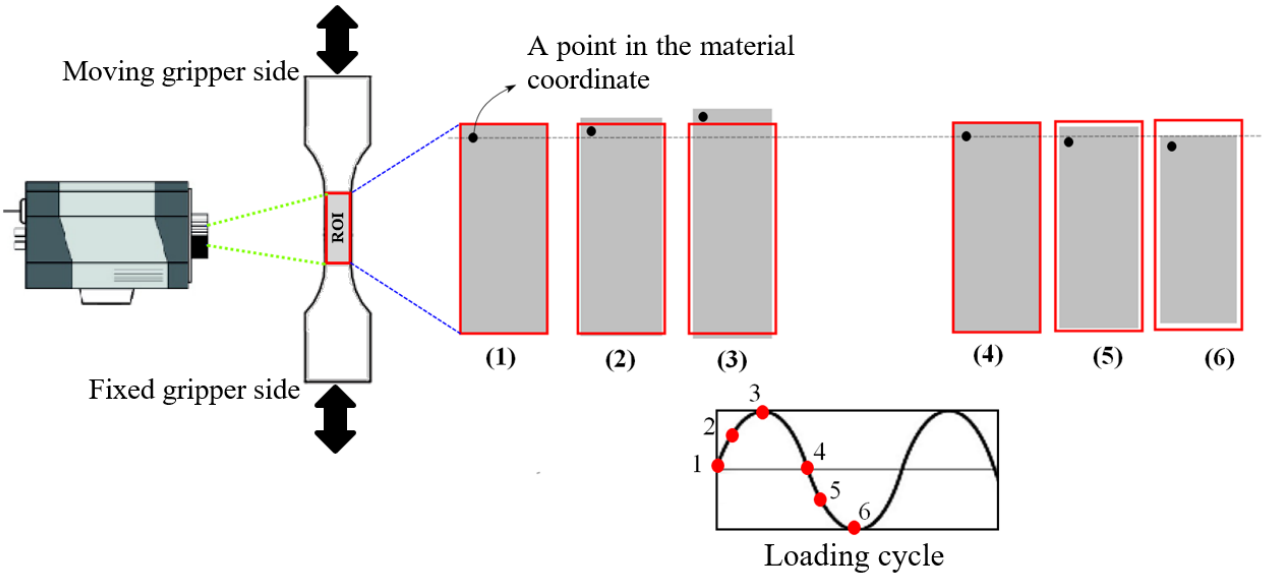

Figure 47 A schematic representation of the movement of a single point on the surface of the sample during loading

Based on the collected data in this work, displacement can be estimated through either the utilization of thermal images with an edge detection function in MATLAB or extensometer data (as mentioned in Appendix D). However, the effectiveness of the former method heavily relies on the size of the pixel or pixel ratio (i.e., length divided by the number of pixels) in the thermal acquisition. Due to insufficiently small pixel ratios, accurate displacement measurements were not feasible using this method. Consequently, the second method was employed.

The maximum and minimum elongations of the gauge length are listed in Table 14, for each load cycle when the hysteresis loops are stabilized. As the stress ratio in the experiments was R=-1, it was assumed that the absolute value of the maximum and minimum elongations is equal.

Table 14 Maximum and minimum elongations of the gauge length from extensometer for C45

Stress amplitude (MPa)	Maximum or minimum (mm)
300	0.0443
310	0.0465
320	0.0523
340	0.0583

As shown in Figure 48, after finding the maximum displacement and simulating the movement of points inside ROI frame by frame, modified temperatures can be estimated through the extrapolation and interpolation functions in MATLAB, by having the old and new positions of points and the temperature of points in old positions. These modified temperatures, can then be compared with those directly observed from thermal camera. The details of simulating of this noise are proposed in Appendix D.

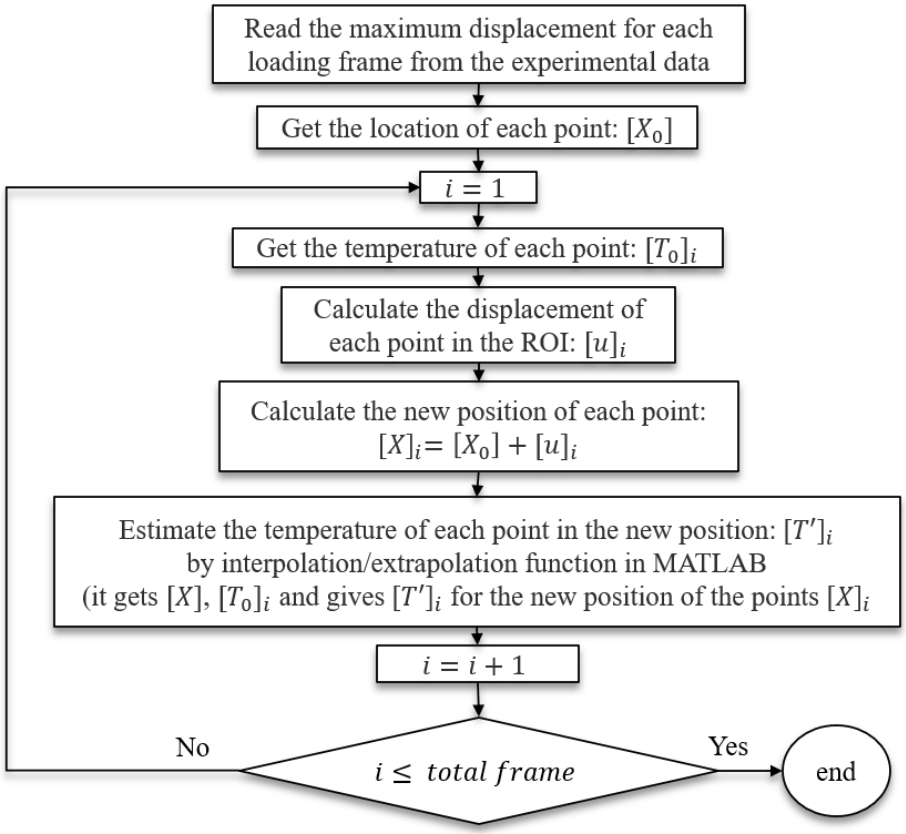

Figure 48 Imposing the noise due to the deformation of the sample on the numerical output

4-2-2-3 Preliminary considerations on the number of pixels and the random distribution

Similar to the experimental procedure in thermography-based techniques, the numerical temperature data are extracted from the surface of the gauge volume and specifically from the same ROI. The following two primary considerations should be taken into account:

I. To ensure the consistency of numerical results, it is essential to define a proper grid of points (which play the role of pixels in the experiment) on the surface of the gauge volume in the numerical model. Each point provides a temperature history throughout the runtime. It is worth noting that increasing the number of points leads to an increase in the time required for data extraction, thus reducing the number of pixels (or points) as far as possible in numerical model while still maintaining the accuracy, can be beneficial. As mentioned before, the number of pixels in thermal acquisition and ROI was 52*99.

II. Since the unit heat volumes (see Figure 41) are randomly distributed in gauge volume, the effect of the distribution should also be explored.

For investigating the above considerations, it is assumed that only 15% of the gauge volume of a C45 dog bone sample with the unit size of 1 mm^3 for randomly distributed heat sources produces heat. Two different grids of points including 13*31 and 52*99 (same as in the experiments) are considered and the simulation is performed for 10 random distributions of the unit volumes.

4-2-2-4 Criteria for identifying the dissipated volume

As shown in Figure 42, after defining the geometry and mechanical properties of the sample, defining imposed heat, collecting reference data and preliminary considerations, the cyclic heat is imposed in the whole of the gauge volume.

Considering the whole of the gauge volume producing heat is not prevalent in a fatigue test since the heat dissipation is usually localized in a fraction of it. However, initially, the entire gauge volume is considered as a trial heat volume to check if $\dot{W}_{2\omega}$ is a sufficient heat power to satisfy $T_{2\omega,mean}^{FEM} \geq T_{2\omega,mean}^{exp}$, where $T_{2\omega,mean}^{FEM}$ is the average of the SAH of surface temperature found numerically. It should be noted that $T_{2\omega,mean}^{FEM} > T_{2\omega,mean}^{exp}$ can be a case because (i) it is assumed the whole of the gauge volume is damaged and (ii) the producing heat is equal to the $\dot{W}_{2\omega}$. Actually, in fully reverse loading, it is just an assumption that the whole of the mechanical energy converts to heat; there will be a small portion potentially remaining unconverted. When the heat dissipation imposed in the entire gauge volume is equal to the whole of the mechanical energy, it can be expected that the temperature increase is higher than the acquired value in the experiment. By extending this fact to the harmonic components of temperature and mechanical energy, it can also be exapted that $T_{2\omega,mean}^{FEM} > T_{2\omega,mean}^{exp}$.

When $T_{2\omega,mean}^{FEM} > T_{2\omega,mean}^{exp}$ is satisfied, it is the time to introduce the randomly distributed heat units in different fractions of gauge volume to satisfy the final criteria, $T_{2\omega,mean}^{FEM} \approx T_{2\omega,mean}^{exp}$, and consequently identifying the dissipated volume numerically, for each loading level.

5 Results

5-1 Experimental results: fatigue limit estimation by thermal indices

In this section, based on the same dataset collected from the experimental campaign, the objective is to provide the behavior of different thermal indices with stress amplitudes to assess how effectively they can pinpoint the fatigue limit. To estimate the fatigue limit accurately, two distinct methodologies were employed on each temperature index trend, the threshold method [40] and Loung's method [109]. Before presenting the comparison, the preparation of data for each temperature index is described. It should be noted that the iterative method was not applied as it requires more thermal data than the threshold method and Loung's method, as mentioned in section 2.

As represent schematically in Figure 49, the chosen thermal indices for the comparison are as below:

- The mean temperature rise in stabilization stage (ΔT)
- The slope of the mean temperature in initial stage (R_i)
- The first amplitude harmonic of temperature signal at the stabilization ($T_{1\omega}$)
- The second amplitude harmonic of temperature signal ate the stabilization ($T_{2\omega}$)
- The slope of the mean temperature in cooling stage (R_c)

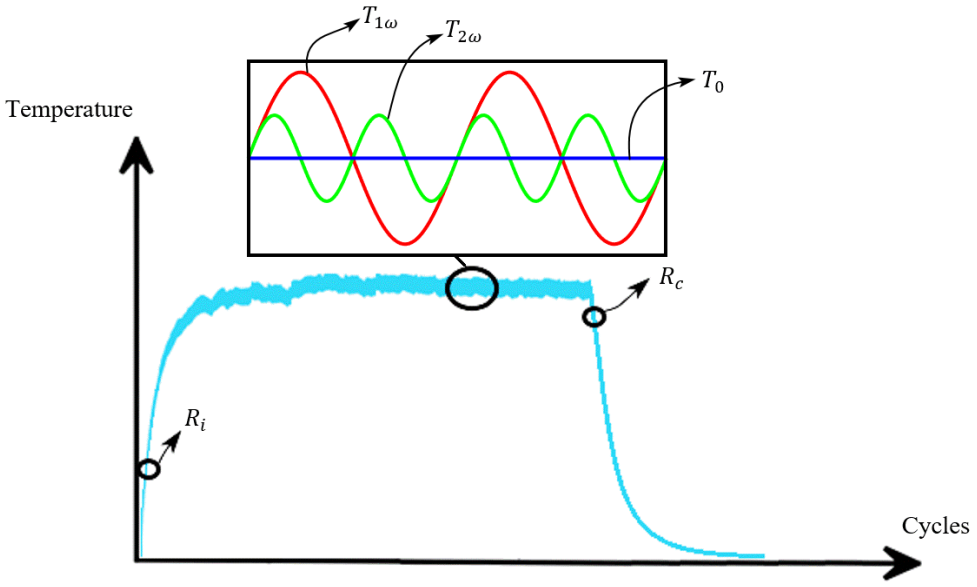

Figure 49 A schematic representations of thermal indices for fatigue estimation

The experimental setup adopted during the stepwise tests, the loading table, loading frequency, sampling frequency and thermal acquisition process were explained before in Section 3. The stepwise tests were conducted on three separate samples of SS 316 to guarantee the precision and reliability of the comparisons made.

The general thermal behavior of the samples under different loading level are presented below. In Figure 50, the mean change of the surface temperature of three SS 316 samples acquired by a micro bolometric camera during the stepwise tests are presented. Following each loading step, when a stable temperature and a specific cycle count are reached, a cooling period of around one minute begins before proceeding to the subsequent loading step until failure of the sample. The maximum temperature observed at failure falls within the range of 160-200 ºC. This high temperature can be due to the ductile behavior (as can be seen from its relatively high elongation in Figure 33) and work hardening of this steel. In Figure 51, the temperature map for the third sample of SS 316 subjected to fully reversed loading is shown. It can be seen that the temperature rises minimally below the fatigue limit but significantly beyond it, indicating damage accumulation until the specimen fails (step 11 is the step before the failure of the sample). The same behavior can be seen in Figure 52 and Figure 53 for T_{1w} and T_{2w}, respectively. For samples 1 and 2, the thermal maps are shown in Appendix E with the same behavior as sample 3. Note that in Figure 53, the accumulation of higher values of T_{2w} at the bottom side of the specimen can be due to the heat conduction between the loading machine gripper and the sample or the noise due to the movement of the gripper.

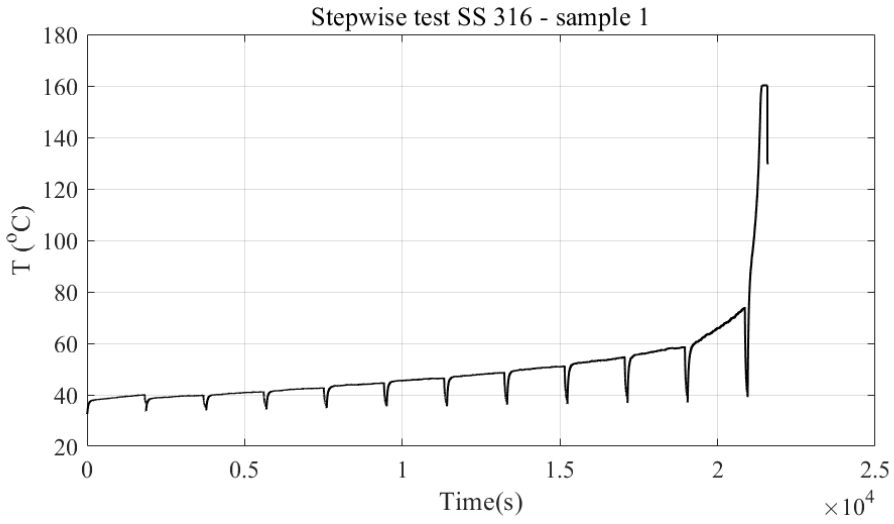

(a)

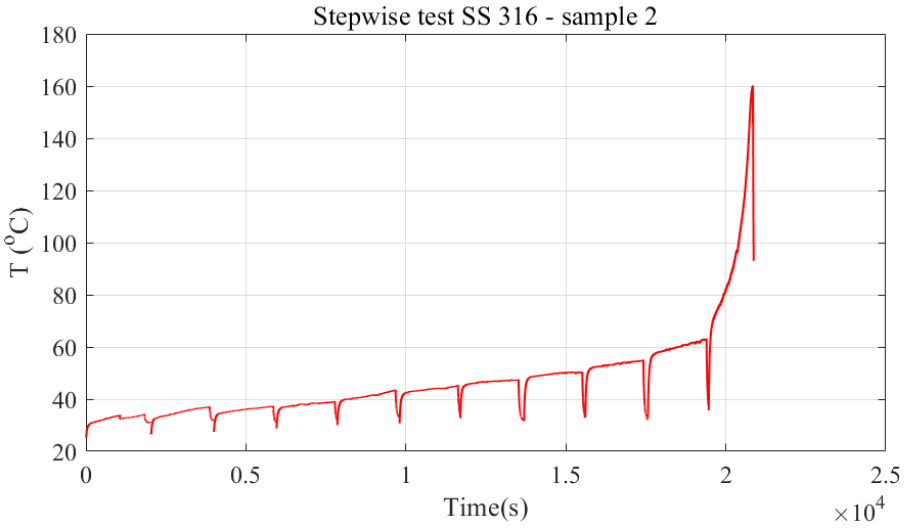

(b)

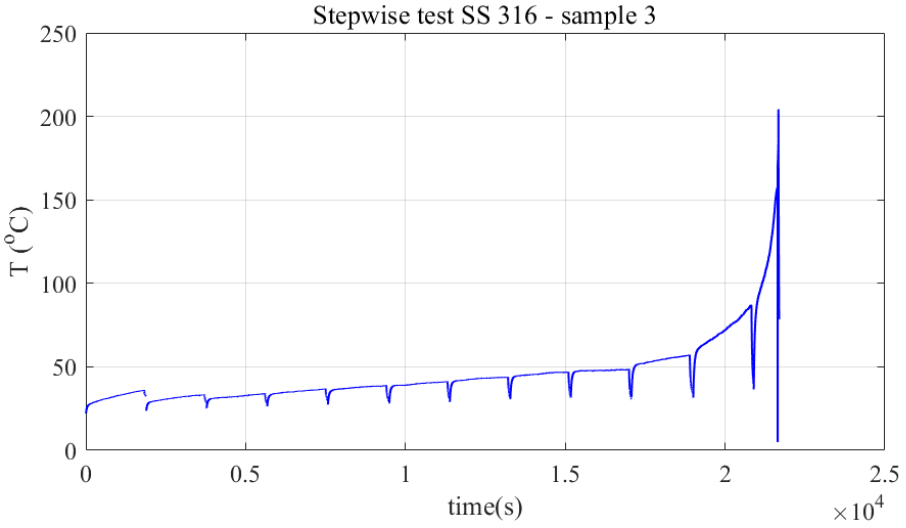

(c)

Figure 50 Temperature trend of SS 316 acquired by a cooled camera during stepwise tests (a) sample 1 (b) sample 2 (c) sample 3

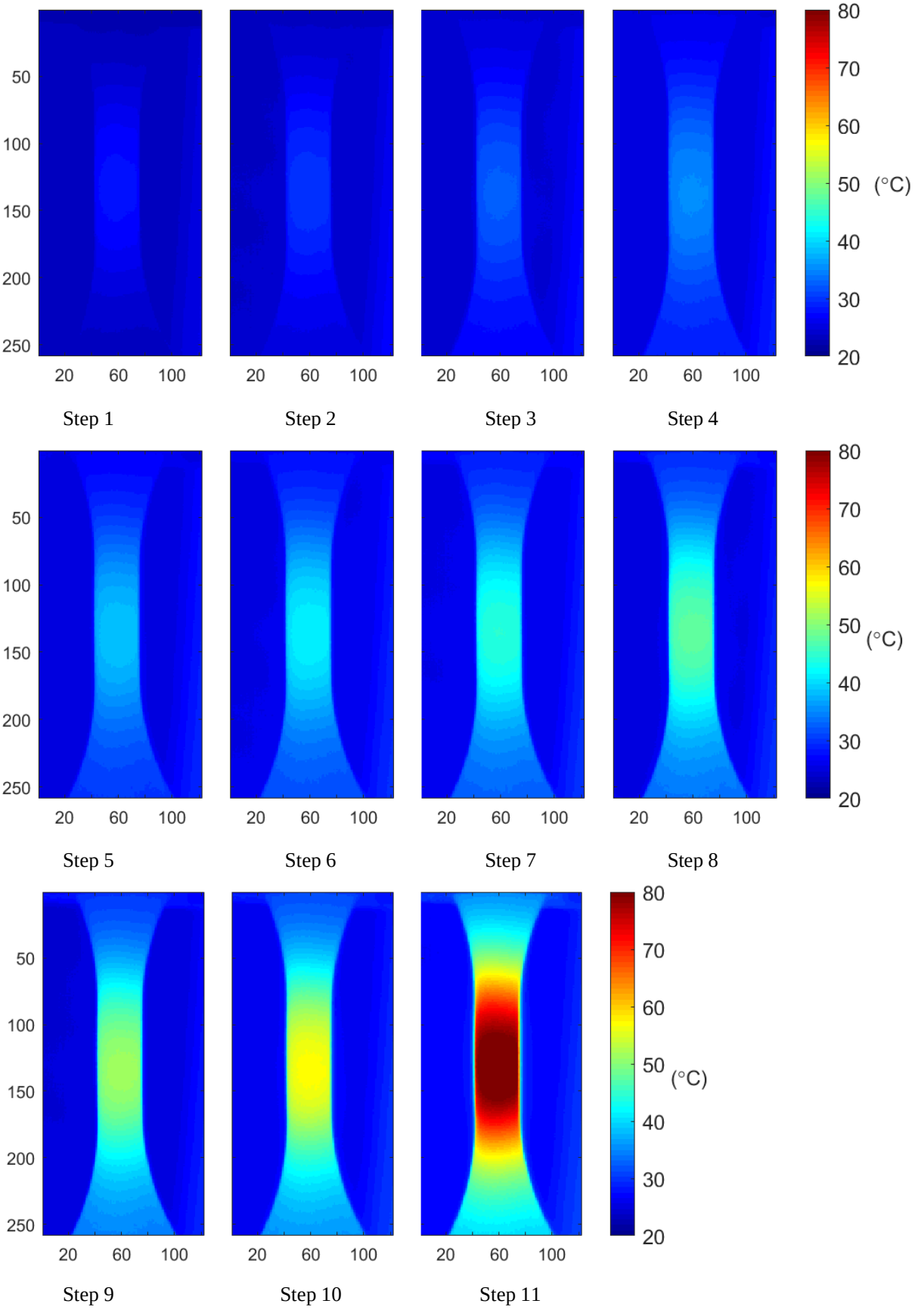

Figure 51 Thermal footprint on the surface of the SS 316 sample for each loading step during stepwise test – sample 3

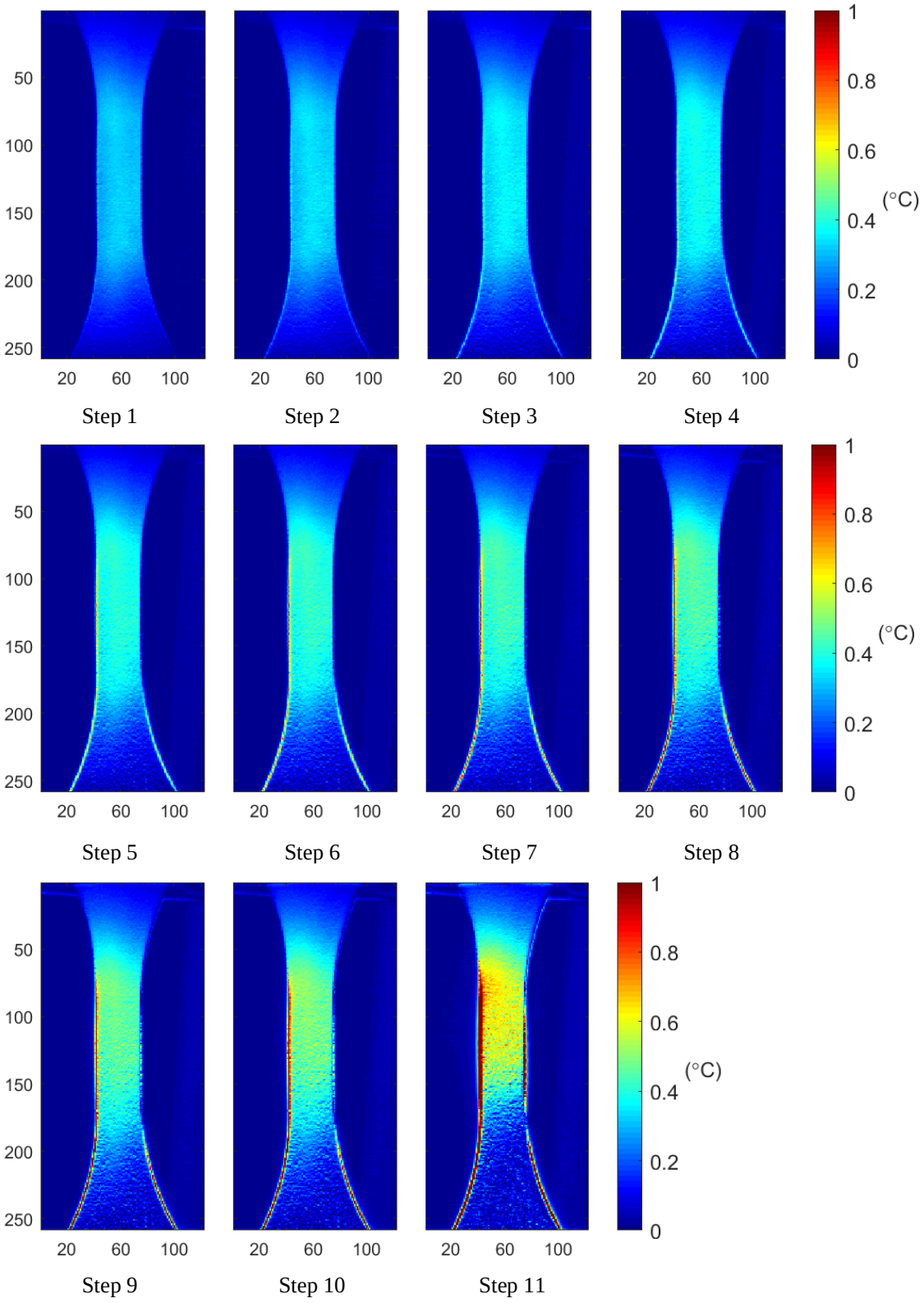

Figure 52 T_{1w} on the surface of the SS 316 sample for each loading step during stepwise test – sample 3

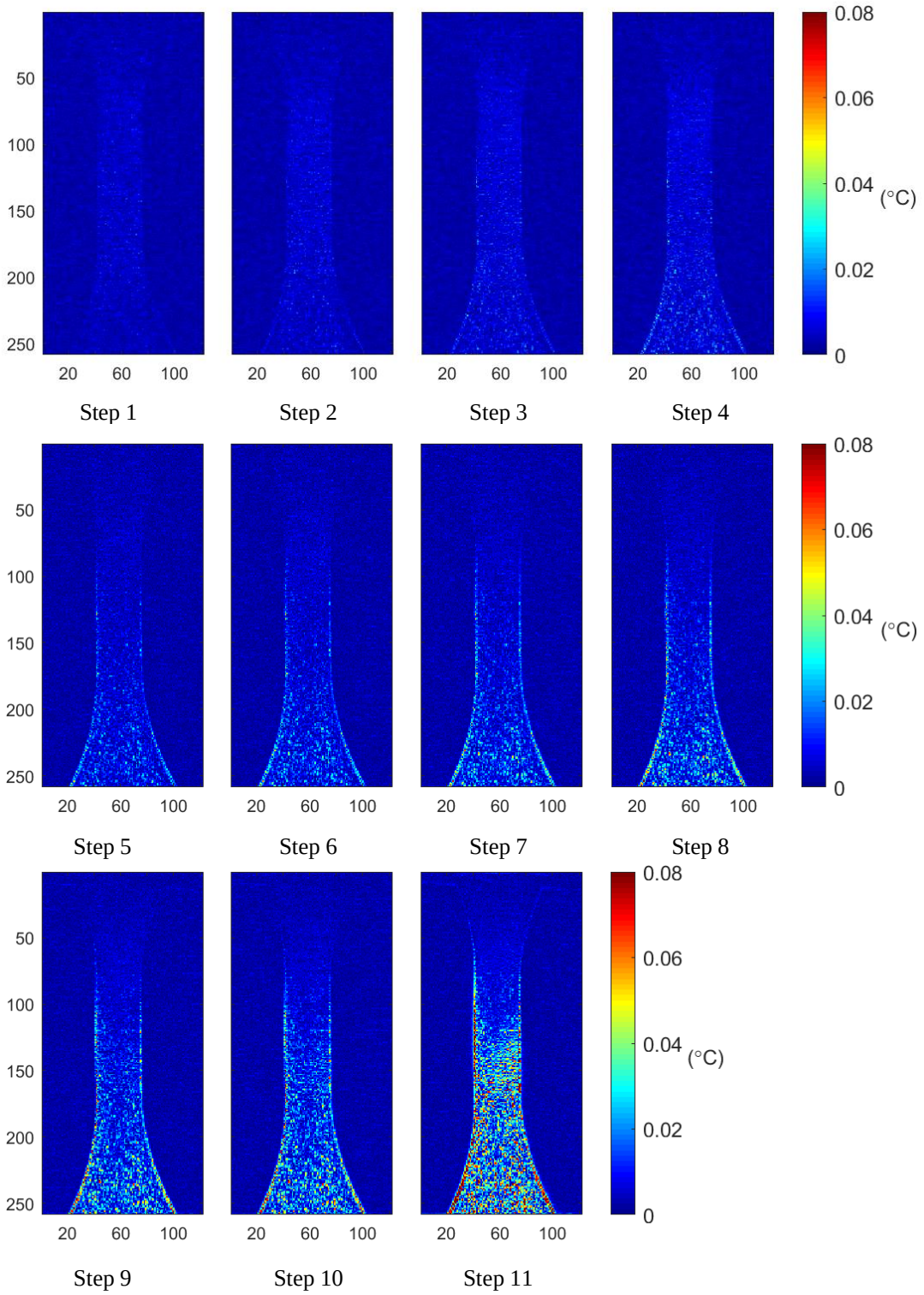

Figure 53 T_{2w} on the surface of the SS 316 sample for each loading step during stepwise test – sample 3

5-1-1 Data preparation

5-1-1-1 Fatigue limit from S-N curve

Based on the details in section 3-3-2-1, the S-N curve is found which are presented in Table 15 and Figure 54. The fatigue limit by adopting an average runout of 5000000 cycles is around 306 MPa as mentioned by our collaborators at LSU [186]. This value is then used as a reference to check the accuracy of thermal indices in prediction of the fatigue limit.

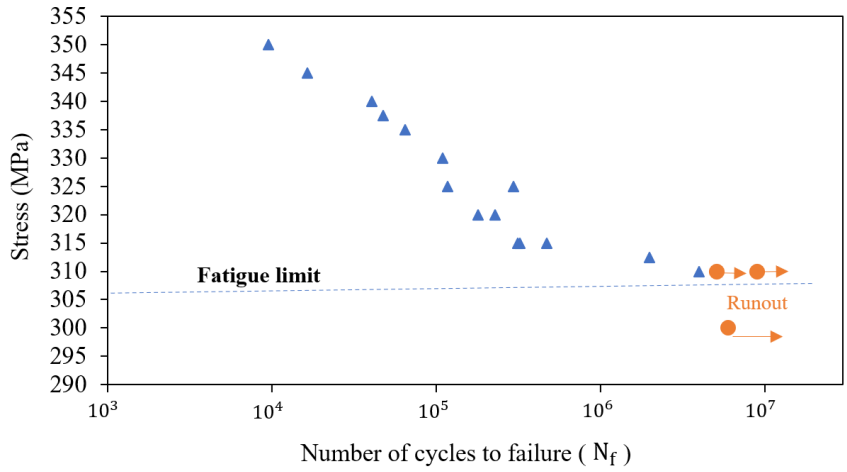

Figure 54 S-N curve - SS 316 [186]

Table 15 Loading table for S-N curve acquisition of SS 316

Sample #	Stress amplitude (MPa)	Number of cycles to failure
1	300	6000000
2	310	5100000
3	310	9000000
4	310	4000000
5	312.5	2000000
6	315	325000
7	315	471000
8	315	313000
9	320	179324
10	320	228871
11	325	296000
12	325	118000
13	330	109329
14	335	65000
15	337.5	47744
16	340	40410
17	345	16500
18	350	9500

5-1-1-2 Variation of thermal indices with the load

The thermal data from an uncooled camera was employed to extract the trend of ΔT and R_c with stress amplitudes. ΔT was determined by assessing the difference between the average surface temperature of the sample (red ROI in Figure 55) and the dummy sample (green ROI in Figure 55). Meanwhile, R_c was found by calculating the gradient of the average of surface temperature during the cooling stage. The measured values are presented in Table 16, Figure 56 and Figure 57.

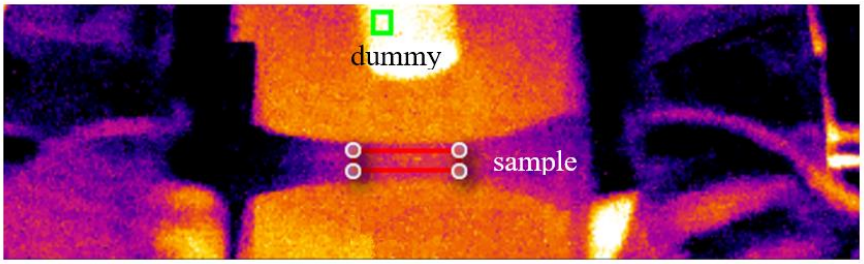

Figure 55 Region of interests for thermal acquisition – uncooled camera – SS 316

Table 16 Mean temperature rise (ΔT) and the cooling slope of temperature (R_c) - SS 316

Stress amplitude (MPa)	Sample 1		Sample 2		Sample 3	
	ΔT (℃)	R_c (℃/s)	ΔT (℃)	R_c (℃/s)	ΔT (℃)	R_c (℃/s)
255	5.230	0.150	4.360	0.102	2.561	0.123
265	6.240	0.174	5.259	0.183	4.202	0.175
275	7.485	0.215	6.983	0.213	6.030	0.203
285	8.977	0.260	8.853	0.287	7.745	0.278
295	10.972	0.320	11.307	0.366	10.219	0.343
300	12.545	0.376	14.145	0.452	15.075	0.424
305	14.222	0.458	17.233	0.530	14.528	0.527
310	16.572	0.522	20.540	0.641	17.355	0.589
315	19.447	0.611	25.174	0.820	21.964	0.746
320	23.574	0.777	31.991	1.069	24.702	0.865
335	38.914	1.215	76.849	2.524	55.951	2.159

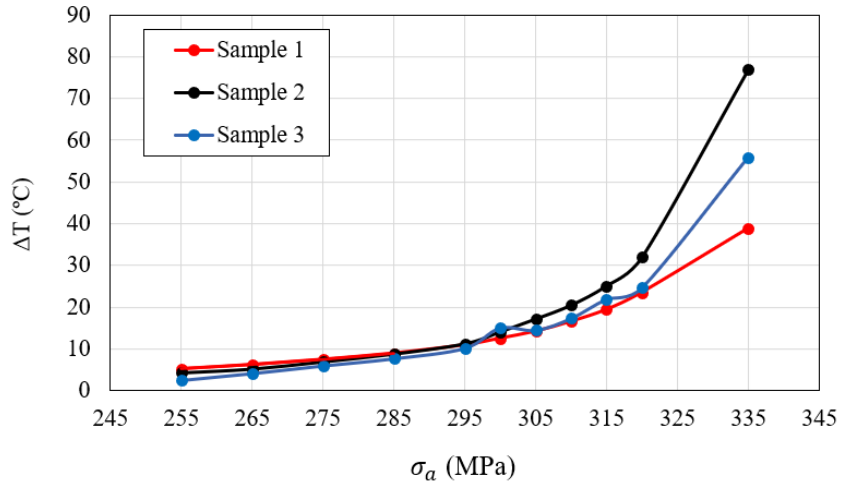

Figure 56 Temperature rise at the stabilization – SS 316

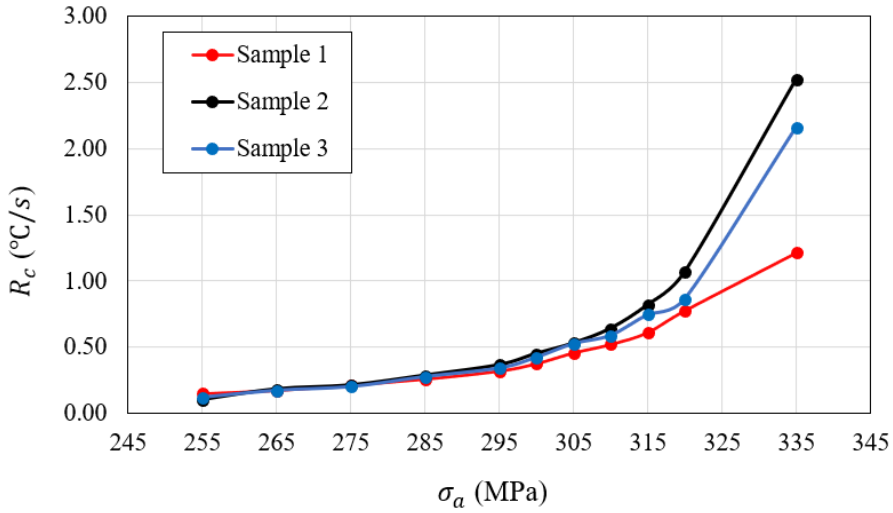

Figure 57 Cooling slope of the temperature – SS 316

When it came to $T_{1\omega}$ and $T_{2\omega}$, the data acquired from a cooled camera were utilized as a higher sampling rate is needed for reconstructing the temperature signal and consequently quantifying the first and second harmonic amplitudes of temperatures. The ROIs are shown in Figure 58, and the measured values are proposed in Table 17, Figure 59 and Figure 60.

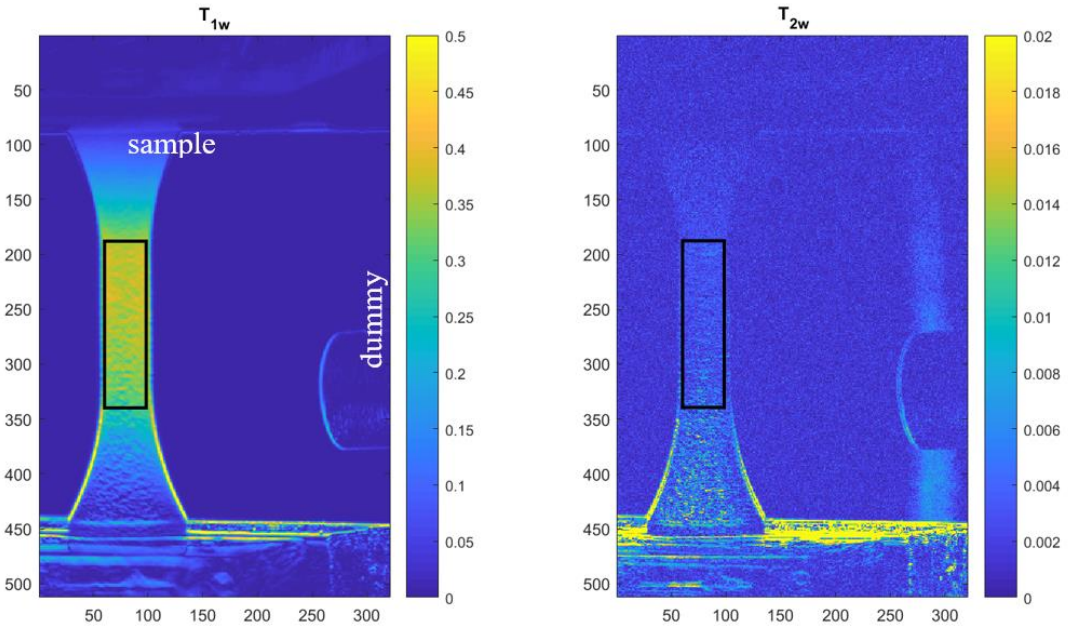

Figure 58 Region of interests for thermal acquisition – cooled camera – SS 316

Table 17 First and second harmonic amplitudes of the temperature - SS 316

Stress amplitude (MPa)	Sample 1		Sample 2		Sample 3	
	$T_{1\omega}$ (°C)	$T_{2\omega}$ (°C)	$T_{1\omega}$ (°C)	$T_{2\omega}$ (°C)	$T_{1\omega}$ (°C)	$T_{2\omega}$ (°C)
255	0.2771	0.0042	0.3154	0.0052	0.3132	0.0049
265	0.2920	0.0040	0.3231	0.0049	0.3308	0.0057
275	0.3083	0.0030	0.3376	0.0045	0.3508	0.0061
285	0.3256	0.0027	0.3533	0.0050	0.3708	0.0063
295	0.3444	0.0029	0.3705	0.0033	0.3904	0.0047
300	0.3444	0.0028	0.3813	0.0035	0.4043	0.0052
305	0.3676	0.0031	0.3927	0.0037	0.4168	0.0054
310	0.3819	0.0034	0.4055	0.0044	0.4305	0.0061
315	0.3968	0.0039	0.4221	0.0055	0.4469	0.0074
320	0.4158	0.0047	0.4366	0.0073	0.4631	0.0087
335	0.4789	0.0096	0.4972	0.0227	0.5352	0.0165

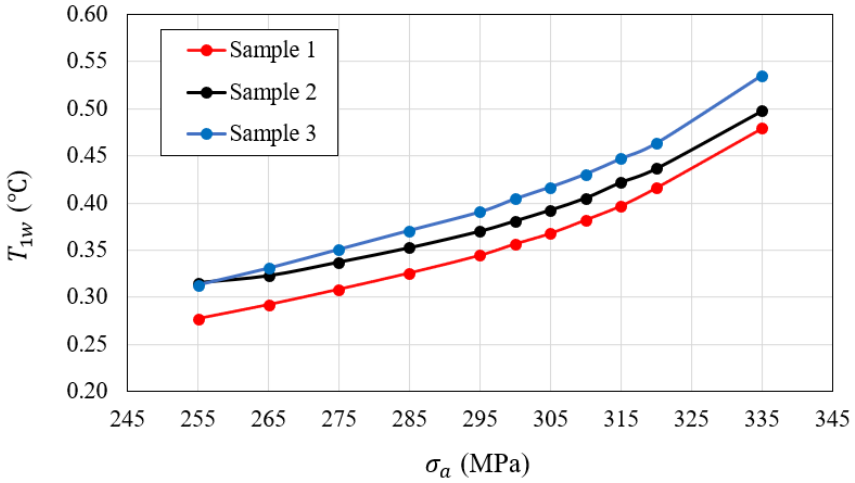

Figure 59 First amplitude harmonic of the temperature - SS 316

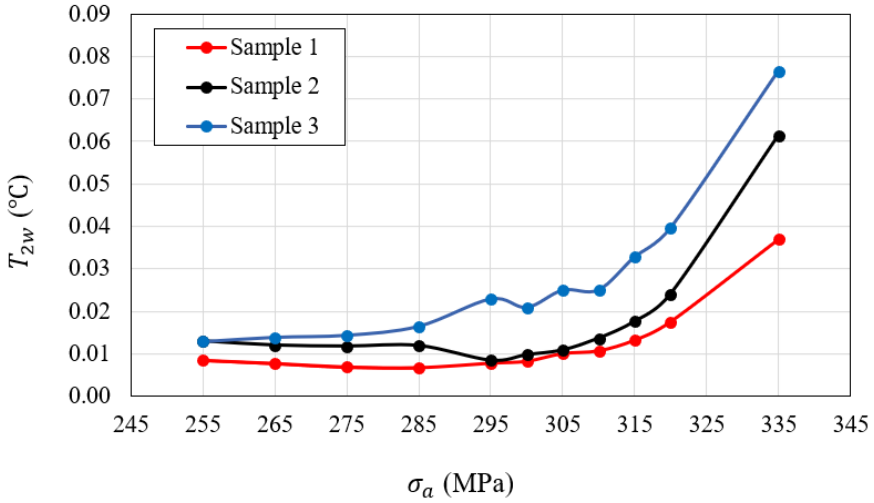

Figure 60 Second amplitude harmonic of the temperature - SS 316

Unlike the other indices, for R_i (the slope of temperature in the rising stage), a more comprehensive analysis was performed to investigate how its measurement can be affected by thermal acquisition (cooled or uncooled camera) and the curve fitting methods (both the order of the fitting and the time period over which the fitting is applied).

Using same ROIs as in Figure 55 and Figure 58, the linear and quadratic fitting ($T = m_1 t + c_1$ and $T = at^2 + m_2 t + c_2$, respectively; where T is the temperature, t is the time, m_1 and m_2 are the slopes, c_1 and c_2 are constants, and a is the degree to which the curve deviates from being a straight line) were applied on the thermal data within the time durations varied from 1 to 10 seconds. Noted that the slope

was calculated from the data points where temperature starts to rise and exhibits cyclic behavior. The results are proposed in Table 18 to Table 20 and plotted in Figure 61 to Figure 70. It should be noted that the data from cooled camera is only available for the last two samples. As can be seen, unlike the curves obtained from fitting on the data from a cooled camera, those obtained from an uncooled camera exhibit severe irregular trends (or fluctuations) that make it impossible to estimate the fatigue limit from the datapoints. These trends are obvious for a time duration of 1 second when linear fitting is used, and for time durations of 1 and 2 seconds when quadratic fitting is applied.

The analysis conducted here, for the first time, underscores the importance of careful consideration when measuring the initial slope of the temperature trend. Therefore, it is advisable to utilize more data points and a cooled camera when measuring the temperature slope. Alternatively, if an uncooled camera is the only option, it is suggested that the curve fitting be conducted for the time durations beyond 2 seconds, irrespective of the fitting order.

Table 18 Slope of temperature in the rising stage – sample 1 – uncooled camera - SS 316

			Stress amplitude (MPa)										
		time duration (sec)	255	265	275	285	295	300	305	310	315	320	335
R_i	Linear fitting	1	0.162	0.313	0.272	0.259	0.258	0.253	0.421	0.296	0.554	0.611	0.702
		2	0.177	0.216	0.211	0.228	0.249	0.307	0.388	0.395	0.540	0.631	0.736
		3	0.176	0.184	0.184	0.215	0.256	0.326	0.389	0.419	0.521	0.626	0.694
		4	0.167	0.166	0.175	0.214	0.267	0.318	0.381	0.415	0.507	0.613	0.671
		5	0.162	0.157	0.174	0.209	0.266	0.307	0.375	0.411	0.494	0.600	0.654
		6	0.157	0.154	0.172	0.201	0.261	0.298	0.366	0.407	0.485	0.586	0.638
		7	0.154	0.149	0.167	0.196	0.257	0.289	0.357	0.401	0.471	0.573	0.622
		8	0.150	0.146	0.164	0.194	0.251	0.281	0.348	0.393	0.465	0.559	0.605
		9	0.146	0.142	0.162	0.193	0.246	0.275	0.340	0.385	0.454	0.546	0.591
		10	0.144	0.138	0.160	0.193	0.240	0.267	0.331	0.377	0.443	0.531	0.581
	Quadratic fitting	1	0.912	0.685	0.457	1.155	-0.834	-1.215	0.002	-0.655	-0.296	0.039	1.836
		2	0.366	0.297	0.201	0.540	-0.118	-0.066	0.279	0.201	0.275	0.446	0.998
		3	0.285	0.231	0.204	0.376	0.055	0.155	0.326	0.349	0.431	0.566	0.820
		4	0.257	0.215	0.183	0.302	0.122	0.236	0.368	0.414	0.486	0.617	0.764
		5	0.232	0.192	0.169	0.278	0.183	0.277	0.385	0.427	0.509	0.641	0.743
		6	0.218	0.177	0.170	0.272	0.221	0.296	0.399	0.434	0.515	0.655	0.732
		7	0.206	0.174	0.177	0.259	0.240	0.314	0.406	0.443	0.547	0.658	0.727
		8	0.201	0.170	0.179	0.245	0.255	0.321	0.411	0.449	0.528	0.662	0.729
		9	0.197	0.170	0.175	0.231	0.265	0.325	0.411	0.453	0.533	0.663	0.723
		10	0.190	0.172	0.177	0.221	0.278	0.329	0.420	0.456	0.548	0.679	0.707

Table 19 Slope of temperature in the rising stage – sample 2 - SS 316

			Stress amplitude (MPa)										
		time duration (sec)	255	265	275	285	295	300	305	310	315	320	335
R_i	Linear fitting, uncooled camera	1	0.026	0.262	0.214	0.236	0.229	0.322	0.329	0.323	0.385	0.749	0.869
		2	0.127	0.220	0.215	0.213	0.280	0.346	0.356	0.525	0.540	0.734	0.951
		3	0.127	0.198	0.208	0.205	0.325	0.358	0.379	0.506	0.579	0.720	0.988
		4	0.154	0.191	0.211	0.229	0.319	0.360	0.405	0.522	0.616	0.737	1.002
		5	0.161	0.188	0.193	0.237	0.306	0.357	0.419	0.516	0.590	0.735	1.016
		6	0.168	0.187	0.193	0.236	0.293	0.355	0.406	0.506	0.585	0.729	1.018
		7	0.170	0.184	0.184	0.229	0.285	0.349	0.401	0.500	0.578	0.722	1.015
		8	0.158	0.181	0.182	0.225	0.277	0.343	0.404	0.492	0.568	0.716	1.002
		9	0.149	0.181	0.182	0.226	0.269	0.337	0.403	0.481	0.561	0.703	0.980
		10	0.148	0.179	0.180	0.223	0.262	0.335	0.389	0.471	0.551	0.689	0.966
	Quadratic fitting, uncooled camera	1	0.854	-0.042	0.061	-0.603	-0.059	-0.507	1.702	0.412	0.010	0.199	1.003
		2	0.322	0.137	0.151	0.135	0.017	0.063	0.496	0.316	0.303	0.499	0.827
		3	0.195	0.182	0.169	0.236	0.240	0.207	0.374	0.514	0.449	0.659	0.866
		4	0.150	0.183	0.192	0.172	0.338	0.280	0.378	0.496	0.461	0.636	0.920
		5	0.155	0.180	0.251	0.193	0.374	0.318	0.385	0.515	0.601	0.678	0.920
		6	0.147	0.181	0.222	0.220	0.380	0.337	0.445	0.548	0.609	0.712	0.945
		7	0.162	0.185	0.228	0.252	0.368	0.354	0.452	0.555	0.620	0.732	0.986
		8	0.199	0.189	0.219	0.249	0.362	0.365	0.426	0.553	0.629	0.744	1.035
		9	0.209	0.186	0.206	0.237	0.356	0.373	0.425	0.560	0.630	0.769	1.082
		10	0.198	0.193	0.200	0.241	0.350	0.372	0.458	0.573	0.635	0.796	1.099
	Linear fitting, cooled camera	1	0.110	0.156	0.216	0.245	0.347	0.397	0.452	0.453	0.659	0.858	1.140
		2	0.140	0.201	0.222	0.267	0.297	0.405	0.400	0.401	0.709	0.824	1.190
		3	0.142	0.200	0.220	0.253	0.287	0.397	0.381	0.382	0.718	0.802	1.203
		4	0.139	0.197	0.216	0.245	0.277	0.385	0.369	0.369	0.714	0.782	1.195
		5	0.137	0.194	0.213	0.237	0.268	0.377	0.358	0.358	0.703	0.763	1.178
		6	0.134	0.190	0.210	0.231	0.260	0.369	0.348	0.349	0.690	0.745	1.155
		7	0.132	0.186	0.205	0.227	0.252	0.362	0.341	0.342	0.676	0.728	1.133
		8	0.131	0.182	0.201	0.224	0.245	0.355	0.334	0.335	0.659	0.711	1.110
		9	0.129	0.179	0.197	0.220	0.239	0.349	0.326	0.327	0.644	0.695	1.088
		10	0.127	0.176	0.194	0.216	0.233	0.342	0.319	0.320	0.630	0.681	1.068
	Quadratic fitting, cooled camera	1	0.150	0.106	0.162	0.309	0.345	0.431	0.458	0.459	0.617	0.788	1.036
		2	0.156	0.206	0.211	0.287	0.292	0.453	0.410	0.411	0.698	0.839	1.143
		3	0.157	0.222	0.222	0.295	0.288	0.445	0.403	0.404	0.709	0.855	1.180
		4	0.159	0.219	0.230	0.285	0.302	0.442	0.407	0.408	0.737	0.852	1.224
		5	0.157	0.219	0.229	0.280	0.302	0.431	0.405	0.406	0.754	0.855	1.252
		6	0.155	0.219	0.231	0.275	0.303	0.425	0.402	0.403	0.762	0.853	1.273
		7	0.152	0.218	0.232	0.266	0.302	0.419	0.394	0.395	0.771	0.849	1.282
		8	0.149	0.216	0.234	0.260	0.302	0.415	0.392	0.393	0.781	0.846	1.288
		9	0.149	0.214	0.234	0.260	0.297	0.414	0.394	0.394	0.781	0.842	1.287
		10	0.149	0.213	0.233	0.259	0.297	0.413	0.392	0.393	0.782	0.839	1.289

Table 20 Slope of temperature in the rising stage - sample 3 – SS 316

			Stress amplitude (MPa)										
R_i		time duration (sec)	255	265	275	285	295	300	305	310	315	320	335
	Linear fitting, uncooled camera	1	0.128	0.198	0.235	0.049	0.308	0.320	0.432	0.492	0.492	0.412	0.683
		2	0.136	0.182	0.176	0.205	0.291	0.330	0.416	0.466	0.466	0.491	0.647
		3	0.157	0.172	0.174	0.211	0.284	0.332	0.444	0.464	0.464	0.511	0.639
		4	0.172	0.164	0.172	0.208	0.276	0.334	0.436	0.456	0.456	0.516	0.634
		5	0.160	0.159	0.172	0.205	0.271	0.340	0.433	0.449	0.449	0.515	0.626
		6	0.163	0.162	0.169	0.201	0.265	0.339	0.424	0.440	0.440	0.509	0.618
		7	0.159	0.160	0.164	0.197	0.261	0.334	0.412	0.432	0.432	0.501	0.606
		8	0.156	0.156	0.160	0.193	0.256	0.327	0.400	0.423	0.423	0.493	0.596
		9	0.155	0.152	0.156	0.189	0.251	0.319	0.390	0.414	0.414	0.483	0.585
		10	0.154	0.151	0.155	0.183	0.248	0.311	0.379	0.403	0.403	0.476	0.573
	Quadratic fitting, uncooled camera	1	1.290	0.187	0.550	-0.807	0.601	0.230	-0.113	0.194	1.060	1.501	1.074
		2	0.303	0.202	0.302	-0.130	0.374	0.304	0.280	0.348	0.679	0.918	0.955
		3	0.189	0.195	0.200	0.037	0.325	0.331	0.329	0.403	0.610	0.814	0.928
		4	0.189	0.191	0.183	0.114	0.315	0.336	0.411	0.444	0.586	0.722	0.924
		5	0.206	0.183	0.175	0.155	0.305	0.334	0.436	0.460	0.576	0.704	0.955
		6	0.177	0.168	0.181	0.176	0.300	0.348	0.460	0.471	0.579	0.696	0.949
		7	0.195	0.171	0.186	0.189	0.295	0.363	0.477	0.478	0.580	0.694	0.966
		8	0.195	0.179	0.190	0.199	0.295	0.375	0.483	0.483	0.580	0.688	0.973
		9	0.180	0.186	0.189	0.206	0.296	0.383	0.485	0.486	0.582	0.690	0.983
		10	0.179	0.176	0.183	0.217	0.292	0.393	0.485	0.503	0.579	0.704	0.985
	Linear fitting, cooled camera	1	0.103	0.216	0.224	0.176	0.310	0.307	0.383	0.366	0.430	0.735	1.045
		2	0.146	0.174	0.176	0.188	0.276	0.330	0.375	0.401	0.496	0.676	0.983
		3	0.153	0.164	0.171	0.205	0.265	0.327	0.382	0.401	0.483	0.662	0.954
		4	0.151	0.157	0.164	0.211	0.258	0.323	0.384	0.392	0.472	0.650	0.934
		5	0.150	0.154	0.160	0.204	0.255	0.319	0.382	0.384	0.462	0.637	0.916
		6	0.148	0.150	0.156	0.197	0.250	0.313	0.377	0.375	0.447	0.625	0.899
		7	0.146	0.146	0.152	0.195	0.245	0.307	0.370	0.367	0.437	0.612	0.881
		8	0.143	0.143	0.149	0.193	0.240	0.301	0.363	0.360	0.426	0.599	0.863
		9	0.140	0.140	0.146	0.188	0.235	0.295	0.355	0.353	0.416	0.585	0.844
		10	0.138	0.137	0.144	0.183	0.231	0.289	0.349	0.346	0.406	0.574	0.828
	Quadratic fitting, cooled camera	1	0.138	0.228	0.235	0.112	0.324	0.415	0.403	0.372	0.473	0.717	1.036
		2	0.138	0.177	0.180	0.148	0.266	0.334	0.361	0.429	0.465	0.694	1.005
		3	0.157	0.171	0.169	0.151	0.275	0.338	0.357	0.430	0.538	0.678	1.006
		4	0.163	0.173	0.174	0.179	0.275	0.343	0.369	0.437	0.527	0.684	1.001
		5	0.163	0.167	0.174	0.217	0.270	0.343	0.382	0.435	0.524	0.690	0.999
		6	0.163	0.168	0.175	0.226	0.272	0.347	0.397	0.435	0.535	0.690	0.997
		7	0.165	0.169	0.175	0.216	0.275	0.350	0.407	0.432	0.522	0.694	0.999
		8	0.165	0.167	0.174	0.215	0.276	0.349	0.411	0.426	0.520	0.698	1.002
		9	0.165	0.166	0.172	0.222	0.275	0.350	0.415	0.425	0.517	0.701	1.003
		10	0.165	0.165	0.170	0.227	0.276	0.351	0.415	0.423	0.517	0.701	1.003

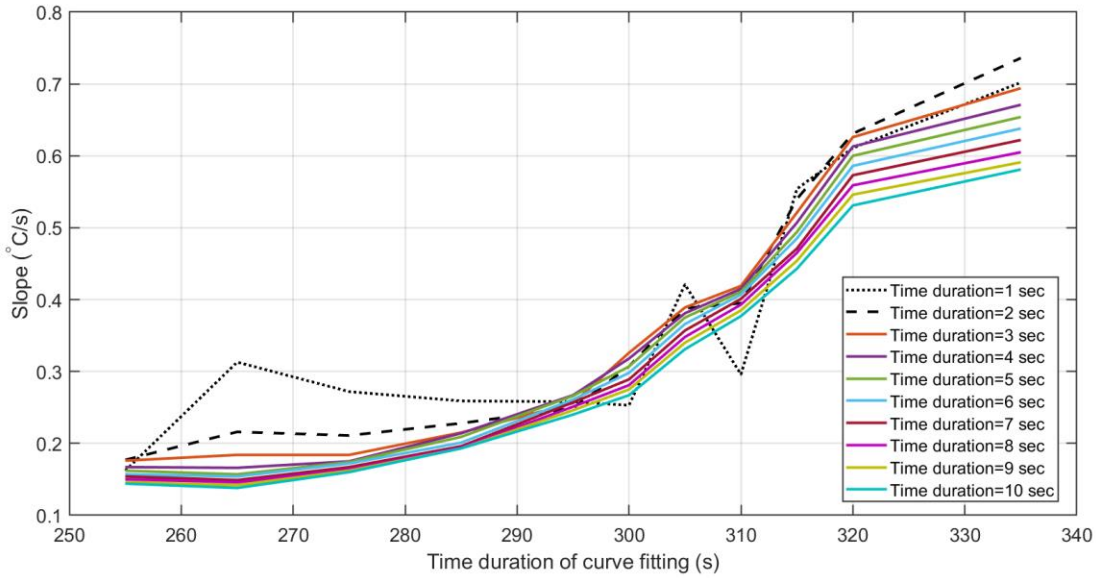

Figure 61 Rising slope of temperature; sample 1 - Linear fitting – uncooled camera

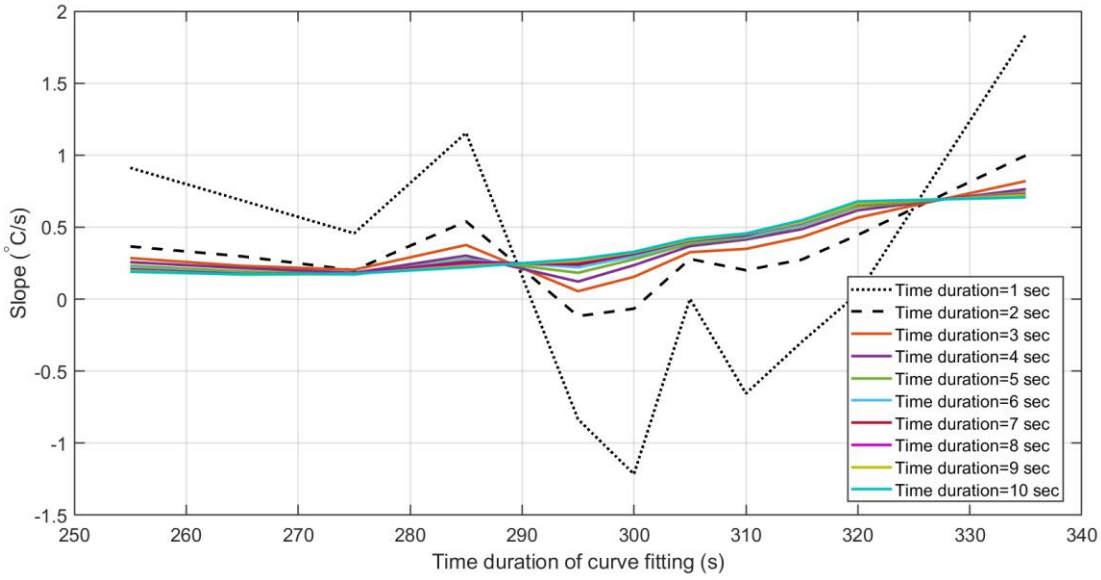

Figure 62 Rising slope of temperature; sample 1 - Quadratic fitting – uncooled camera

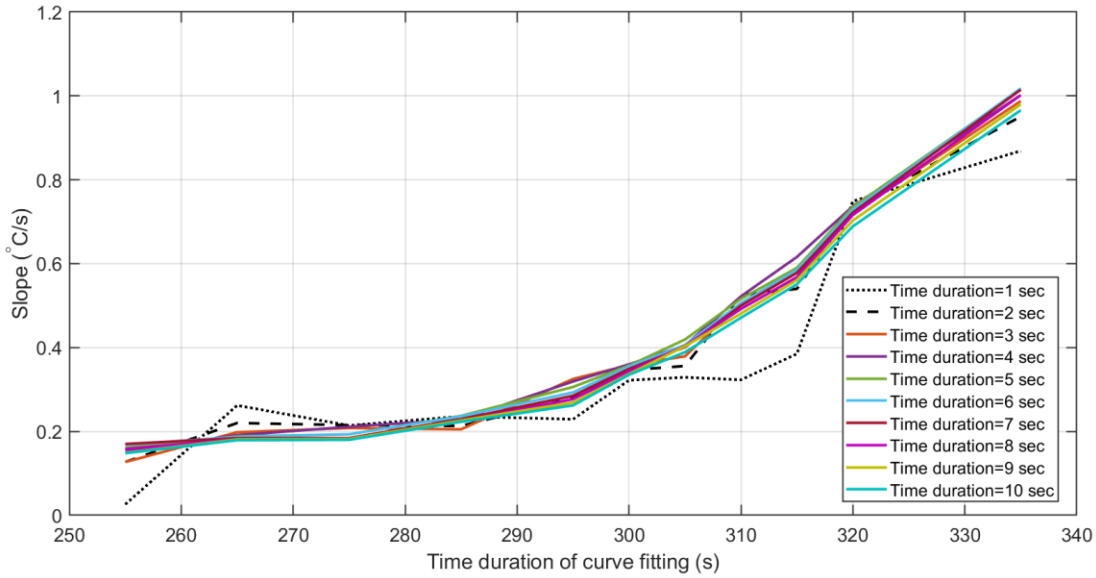

Figure 63 Rising slope of temperature; sample 2 - Linear fitting – uncooled camera

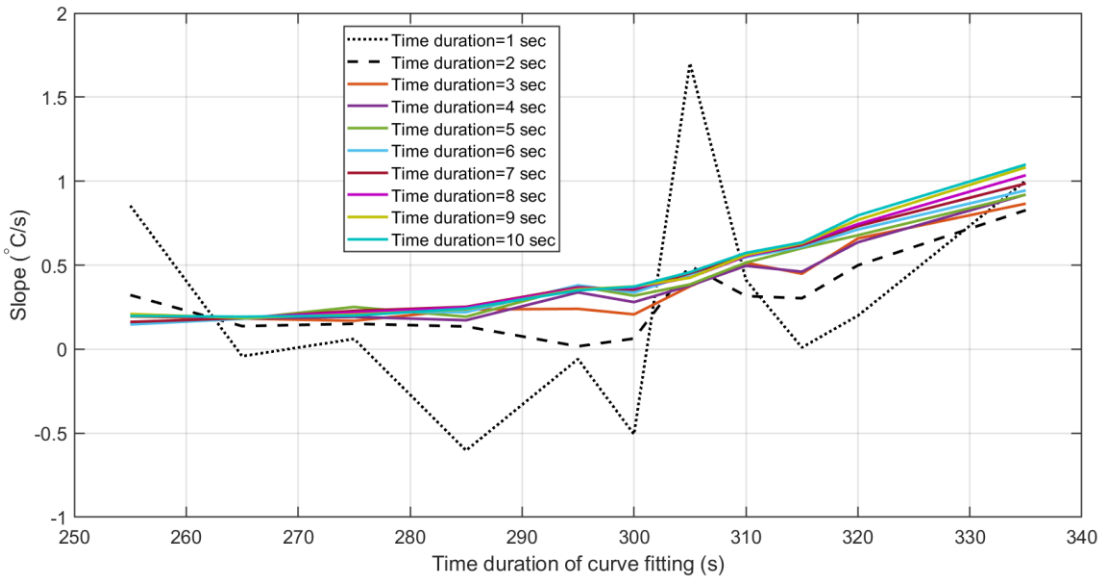

Figure 64 Rising slope of temperature; sample 2 - Quadratic fitting – uncooled camera

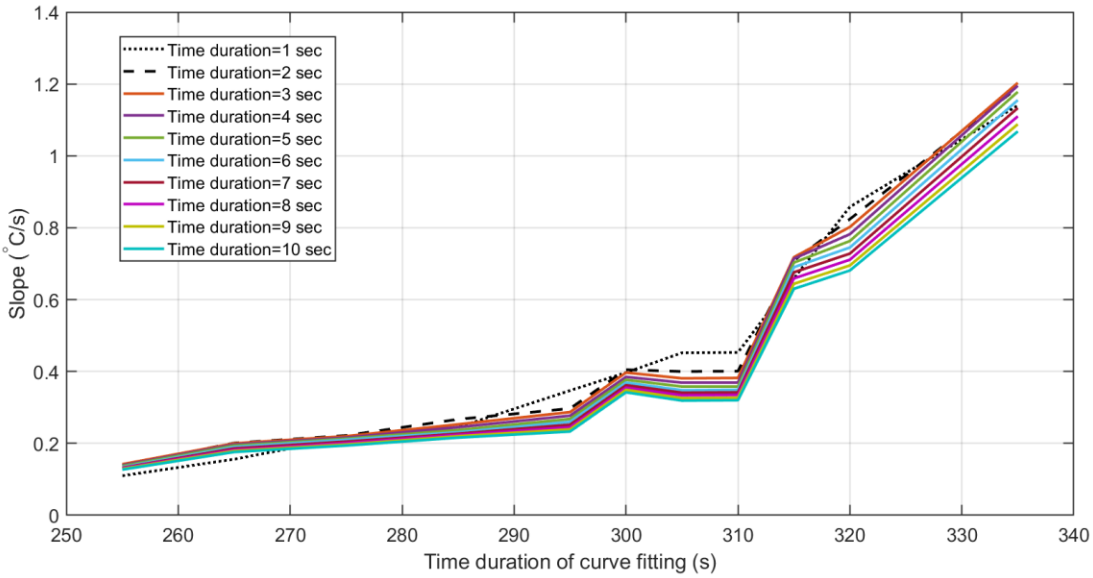

Figure 65 Rising slope of temperature; sample 2 - Linear fitting – cooled camera

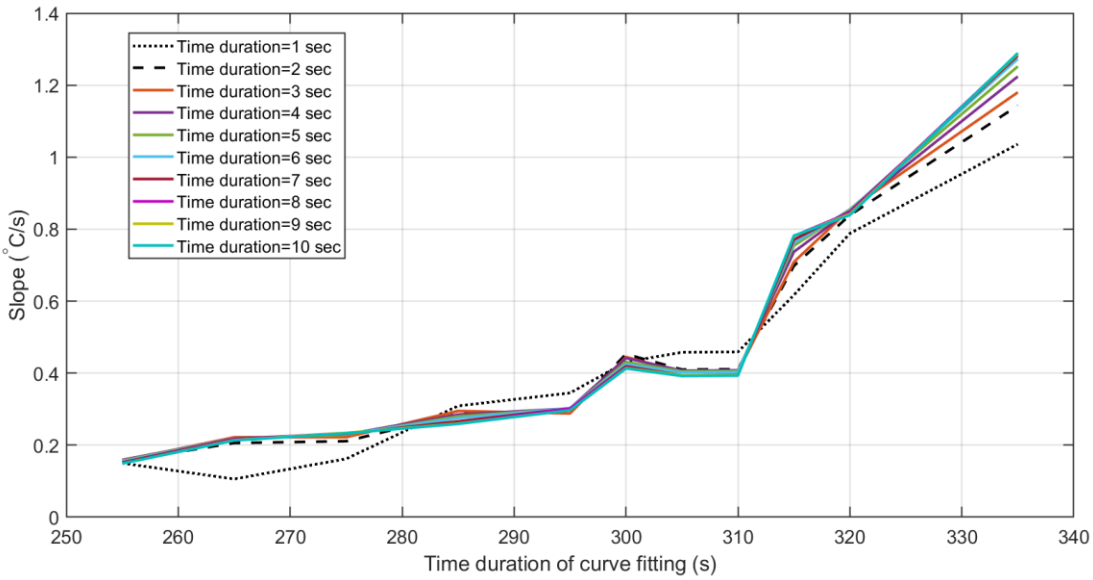

Figure 66 Rising slope of temperature; sample 2 - Quadratic fitting – cooled camera

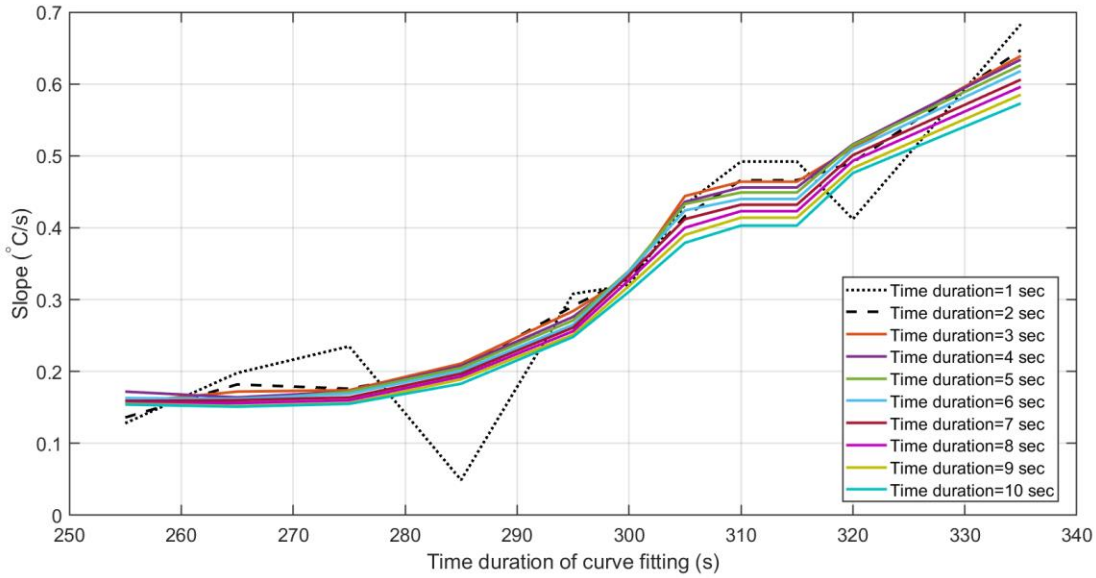

Figure 67 Rising slope of temperature; sample 3 - Linear fitting – uncooled camera

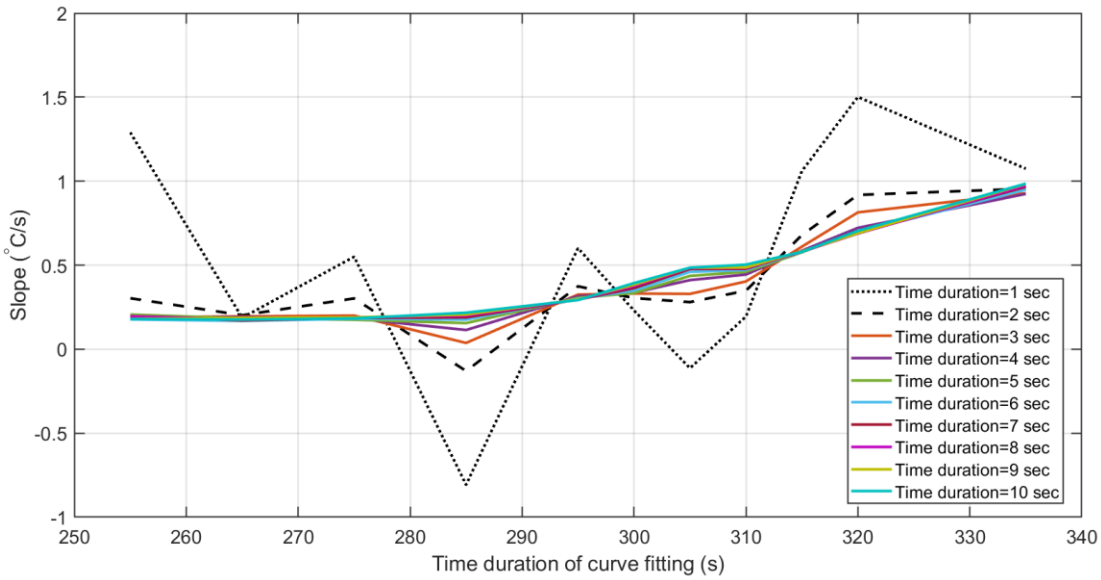

Figure 68 Rising slope of temperature; sample 3 - Quadratic fitting – uncooled camera

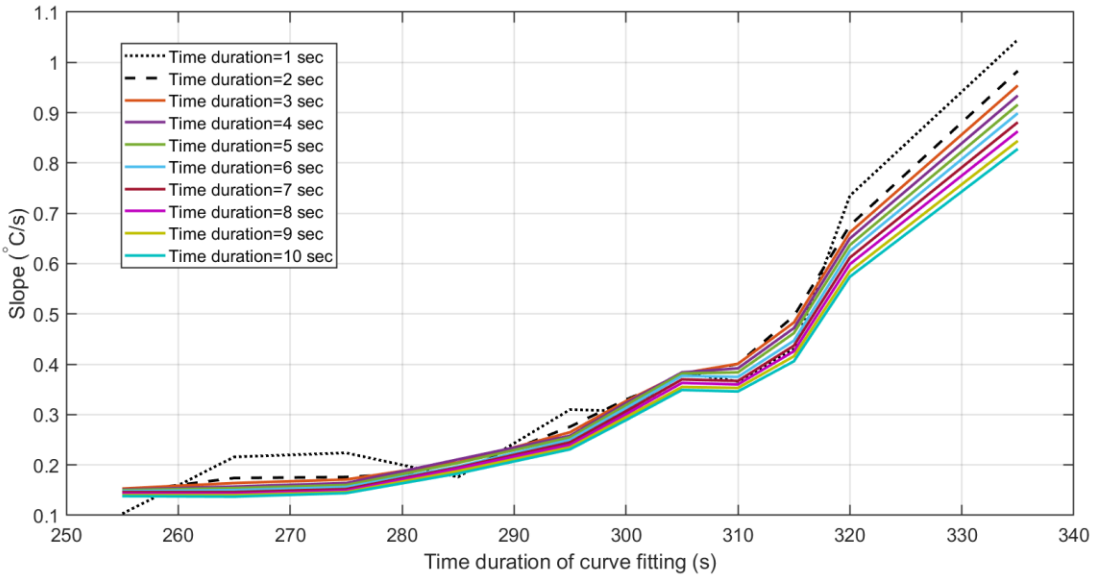

Figure 69 Rising slope of temperature; sample 3 - Linear fitting – cooled camera

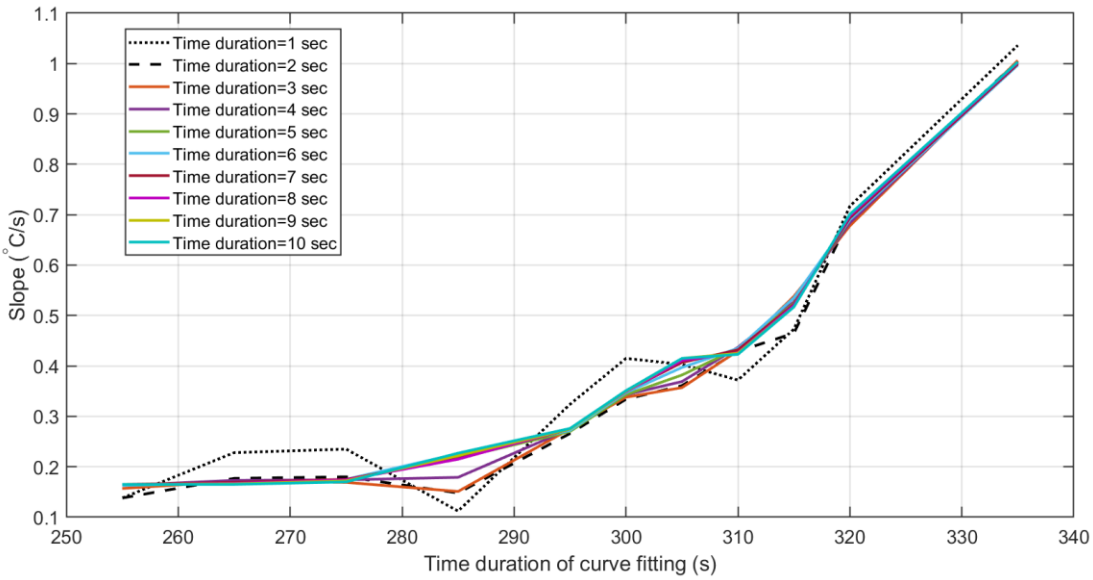

Figure 70 Rising slope of temperature; sample 3 - Quadratic fitting – cooled camera

5-1-2 Fatigue limit estimation by thermal indices

5-1-2-1 Comparison based on the threshold method

As mentioned before, the threshold method is based on the "residual" which is the difference between the measured temperature at a specific stress level and the fitted line constructed from the measured temperatures at the initial stress levels.

In the original description of the method, the authors used a fixed number of points for creating the fitted line and a constant factor for the criterion that predicts the fatigue limit, without analyzing their effect on the prediction. In this study, to delve deeper into the method's functionality, an examination was conducted to find out the sensitivity of the method to its parameters. For convenience, the pseudo code of threshold method is presented below [40]:

1. Finding the equation of the fitted line as ($y = mx + q$) by performing a linear regression analysis on the first μ pairs of a data (temperature index (TI) - stress level (σ_a) pair).
2. Finding the residuals for each loading step: $\mathcal{R}_i = TI_i - \left(m\sigma_{a_i} + q\right),\ i = 1,2,3,\dots,n$; where n is the number of loading steps.
3. Assessing the standard deviation of residuals ($STD_{\mathcal{R}}$) from the initial μ data points across all experiments (comprising 3 specimens, resulting in a total of 3μ data points).
4. Evaluation of the threshold value: $\mathcal{R}_{th} = \lambda * STD_{\mathcal{R}}$.
5. Comparing $\mathcal{R}_i$ with $\mathcal{R}_{th}$ for all loading steps.
6. Report the lower stress amplitude that satisfies $\mathcal{R}_i > \mathcal{R}_{th}$, as the fatigue limit.

μ and λ were fixed to 5 and 6 in the reference [40]. however, for checking the sensitivity of the threshold method, the estimated fatigue limits are compared for $\mu = 4, 5\ or\ 6$ and $\lambda = 1, 3\ or\ 5$, as proposed in Table 21.

The table also shows the difference between the average of predicted fatigue limits for three samples and the fatigue limit obtained from the S-N curve. The bold values in the table highlights the minimum difference for a specific combination of μ and λ.

It becomes apparent that the effectiveness of the threshold method is significantly influenced by both μ and λ, making it challenging to identify an index that consistently outperforms others. Thus, the dependency of this method on these parameters hampers the selection of a single index with superior predictive performance.

A potential issue with the threshold method could arise from its reliance on initial data points to establish the threshold value. If a relatively high noise level is present in the first loading steps, it highly affects the threshold and eventually the predicted fatigue limits. This investigation sheds light on a potential concern with the threshold method and the necessity for further investigations.

Hence, to ensure the quality of the comparison and revealing the efficiency of each thermal index in fatigue limit estimation, it is preferable to employ an alternative method that is less sensitive or reliant on fewer parameters. In the next section, the Loung's method is used for this purpose.

Table 21 Predicted fatigue limit by threshold method for - SS 316

λ	μ		Predicted fatigue limit (MPa)							
			ΔT (℃)	$T_{1\omega}$ (℃)	$T_{2\omega}$ (℃)	R_c (℃/s)	R_i (℃/s)			
							Linear fitting		Quadratic fitting	
							Cooled camera	Uncooled camera	Cooled camera	Uncooled camera
5	4	sample 1	295	305	300	335	300	295	300	295
		sample 2	295	300	315	295	300	295	300	295
		sample 3	300	305	335	335	300	295	300	295
		Difference* (%)	3.05	**0.87**	3.49	5.12	1.96	3.59	1.96	3.59
	5	sample 1	305	310	320	NM	300	305	300	310
		sample 2	300	305	320	NM	300	305	300	315
		sample 3	300	310	320	335	300	305	300	305
		Difference (%)	1.42	0.76	4.58	9.48	1.96	**0.33**	1.96	1.31
	6	sample 1	315	310	320	NM	315	310	315	315
		sample 2	310	310	315	NM	315	310	315	315
		sample 3	315	315	320	NM	320	320	320	315
		Difference (%)	2.40	**1.85**	4.03	NM	3.49	2.40	3.49	2.94
3	4	sample 1	295	305	295	335	300	295	300	295
		sample 2	295	295	315	295	300	295	300	295
		sample 3	295	300	320	335	295	295	295	295
		Difference (%)	3.59	1.96	**1.31**	5.12	2.51	3.59	2.51	3.59
	5	sample 1	300	305	315	335	300	300	300	310
		sample 2	300	300	315	300	300	300	300	310
		sample 3	300	305	315	335	300	300	300	305
		Difference (%)	1.96	0.87	2.94	5.66	1.96	1.96	1.96	**0.76**
	6	sample 1	310	305	315	NM	315	310	315	310
		sample 2	305	305	315	305	315	310	315	310
		sample 3	315	310	315	335	315	305	315	305
		Difference (%)	1.31	**0.22**	2.94	4.75	2.94	0.76	2.94	0.76
1	4	sample 1	295	295	265	310	265	295	300	255
		sample 2	255	255	285	255	265	295	265	275
		sample 3	295	300	320	305	285	285	295	295
		Difference (%)	7.95	7.41	5.23	5.23	11.22	**4.68**	6.32	10.13
	5	sample 1	295	305	305	320	265	295	285	295
		sample 2	255	255	285	255	265	295	265	295
		sample 3	300	300	275	315	255	255	255	295
		Difference (%)	7.41	6.32	5.77	**3.05**	14.49	7.95	12.31	3.59
	6	sample 1	305	295	305	335	300	300	300	255
		sample 2	300	255	285	255	300	300	300	295
		sample 3	300	300	275	335	255	255	300	255
		Difference (%)	1.42	7.41	5.77	**0.76**	6.86	6.86	1.96	12.31

NM: Not Measurable

* Difference between the average of predicted fatigue limit of 3 samples and the fatigue limit in SN curve

5-1-2-2 Comparison based on the Loung's method

As mentioned before, the Loung's method involves fitting two regression lines to data points situated distinctly below and above the knee point in each thermal index trend [109]. By determining the intersection of these two lines, the fatigue limit can reliably be estimated.

Because the variation of R_i (the initial slope of the temperature) is not only dependent on the stress level but also the fitting order as well as the time duration used for fitting, the estimated fatigue limits by this index need to be deeply studied as proposed in Figure 71. According to this figure, for all samples, the predicted fatigue limits show almost a plateau when the fitting performed on the time duration of at least 3 seconds, regardless of the type of camera and the fitting order. Although drawing any conclusive finding from sample 1 is quite challenging, thermal acquisition by a cooled camera provides more accurate predictions close to the actual fatigue limit for samples 2 and 3, when employing a linear fitting method (as indicated by the dashed line in Figure 71). From this, for comparing with other thermal indices, it was decided to use the average of predicted fatigue limits obtained from all considered time durations and fitting orders.

In Table 22, fatigue limit predicted using all considered thermal indices are presented. In the last column of the table, the difference between the mean of predicted fatigue limits for each sample and the value obtained from the S-N curve (see Figure 54) is also found.

Based on the first column of Table 22, the predicted values by $T_{2\omega}$ along with a specific calculation of R_i (linear fitting on the data acquired by a cooled camera) demonstrate superior performance and accuracy compared to the others.

Notably, from the differences in the second and third rows of the table, the estimated fatigue limit is very small when the data from a cooled used for measuring R_i. Thus, it can be concluded that using a thermal camera with high sampling rate is preferable for measuring R_i, as mentioned before. Moreover, the same conclusion can be drawn by observing the rankings in Table 22.

Additionally, ΔT, $T_{1\omega}$ and R_c are ranked third to fifth in terms of their predictive accuracy and performance in estimating the fatigue limit.

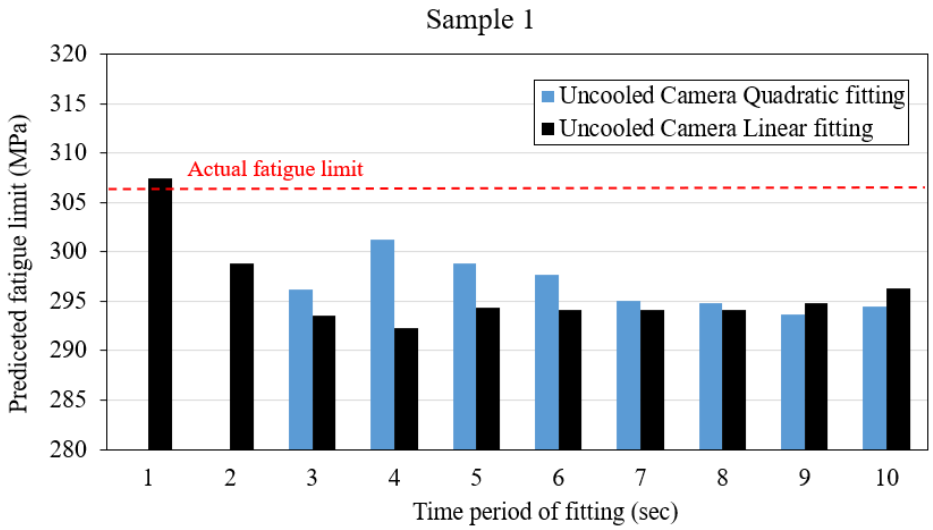

(a)

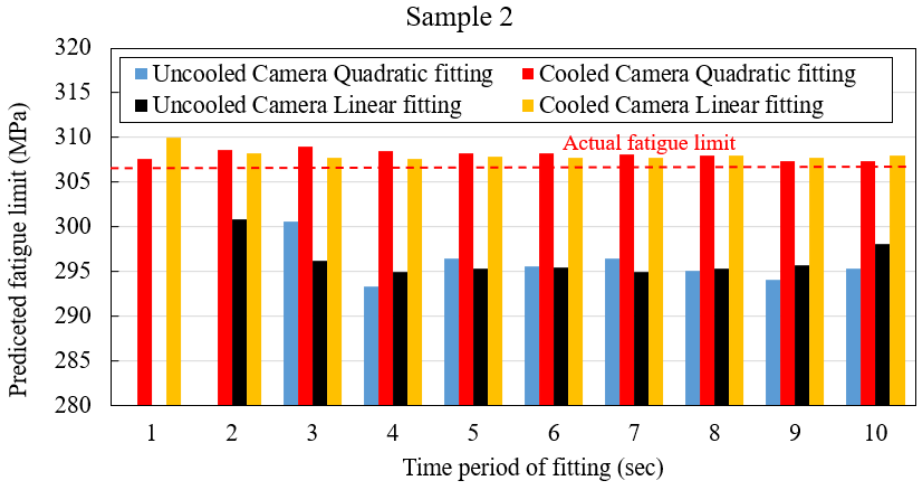

(b)

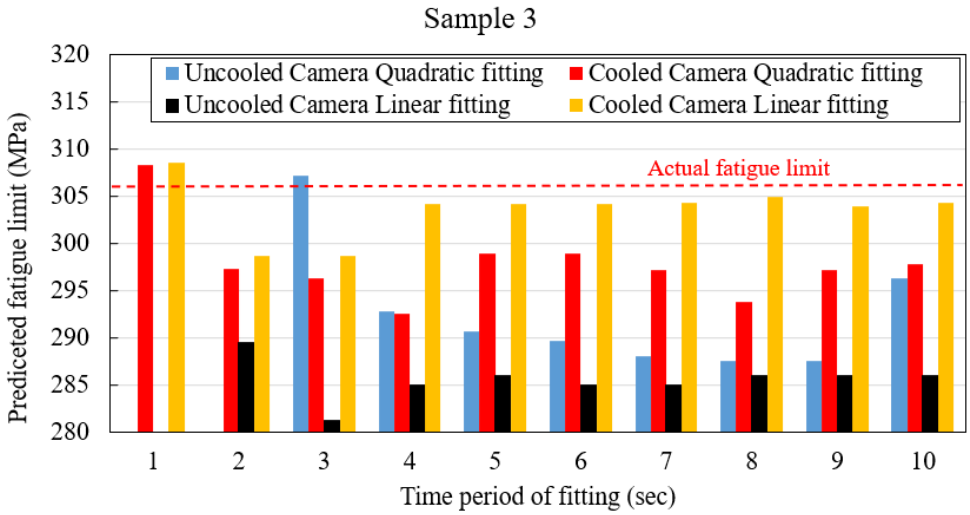

(c)

Figure 71 The fatigue limits predicted based on $\boldsymbol{R_i}$ using Loung's method for (a) sample 1, (b) sample 2 and (c) sample 3

Table 22 Predicted fatigue limit using Loung's method – SS 316

Rank	Method	Predicted fatigue limit (MPa)				Difference* (%)
		Sample 1	Sample 2	Sample 3	Average	
1	$T_{2\omega}$(℃)	305.69	304.33	307.21	305.75	0.1
1	R_i (℃/s), linear fitting - cooled camera	-	308.05	303.53	305.79	0.1
2	R_i (℃/s), quadratic fitting - cooled camera	-	308.09	297.802	302.95	1.0
3	ΔT (℃)	303.35	300.00	300.00	301.12	1.6
4	$T_{1\omega}$(℃)	300.77	297.16	300.62	299.52	2.1
5	R_c (℃/s)	294.24	296.98	299.89	297.04	2.9
6	R_i (℃/s), linear fitting - uncooled camera	296.02	296.34	285.52	292.62	4.4
7	R_i (℃/s), quadratic fitting - uncooled camera	296.48	295.84	259.93	284.08	7.2

*Difference with respect to the fatigue limit from SN curve (306 MPa)

5-2 Numerical results

In this section, the aims are showing how to identify the heat volume producing heat during the fatigue test and studying the effect of loading frequency on SAH of temperature (or generally the heat diffusion effect).

Firstly, the verification of the numerical model is presented. Following this, the impact of the number of points on the surface of the sample used for extracting data and the distribution of unit heat volumes on the numerical output are provided. These factors are crucial for ensuring accuracy in the output.

Next, the focus shifts to presenting the preliminary results from the initial model with randomly distributed heat volumes. Through this comparison, a modified model is developed by adjusting the unit size, showcasing significant improvements in similarity with the experimental data and estimating the heat volume. Before showing of the loading frequency effect on SAH of temperature, numerically, an investigation on the motion-induced noise effect is proposed.

5-2-1 Verification of the numerical model with a single heat source

In this section, the self-heating phenomenon or the temperature increase caused by the heat dissipation due to a cyclic loading is modeled with both constant and cyclic heat sources. As mentioned before, since the load in the fatigue test has a cyclic nature, the correctness of the numerical model should be necessarily examined when it deals with a cyclic heat source. As shown in Figure 39, the accuracy of the numerical model is mainly investigated by comparing it to the analytical solutions of 1D heat equation.

Given the cyclic nature of the load in the fatigue test, adopting a cyclic representation of the heat source

is logical [101]. Once the heat dissipation source is identified or estimated, an approximate temperature distribution can be determined through an analytical procedure involving the solution of the heat equation with certain simplifications. A common approach for this involves expressing the 1st law of thermodynamics for an isotropic and homogeneous material in terms of energy per second for a control volume surrounding the gauge section:

$$\underbrace{\int \left(\rho C \frac{\partial T}{\partial t}\right) dV}_{\text{Internal energy}} = \Big[\underbrace{\int (k\nabla^2 T)\, dV}_{\text{Conduction}} - \underbrace{\int h(T - T_\infty)\, dA}_{\text{Convection}} - \underbrace{\int \epsilon\beta(T^4 - T_\infty^4)\, dA}_{\text{Radiation}}\Big] + \underbrace{\int (\sigma : d\varepsilon) f\, dV}_{\text{Mechanical energy}} \tag{16}$$

Where β, T, A and V are respectively the Stephan-Boltzmann constant, the absolute temperature, the cross-sectional area and volume of the gauge section.

Assuming an arbitrary heat source power $\dot{G}$ within a control volume and a constant cross-section for it, the temperature distribution in one dimensional model can be obtained from the following partial differential equation [162]:

$$\frac{\partial^2 T}{\partial y^2} - \frac{hP}{Ak}(T - T_\infty) - \epsilon\,\beta\,\frac{P}{Ak}(T^4 - T_\infty^4) - \frac{\dot{G}}{k} = \frac{1}{\alpha}\frac{\partial T}{\partial t} \tag{17}$$

Where P is the perimeter of the gauge section. Because difference between T and the ambient temperature ($\theta = T - T_\infty$) is negligible compared to the latter one ($\theta \ll T_\infty$), the third term can be linearized by Taylor expansion around T_∞. Thus, Eq. (17) will be reduced as follows [162]:

$$\begin{cases} \dfrac{\partial^2 \theta}{\partial y^2} - m^2\theta + \dfrac{\dot{G}}{k} = \dfrac{1}{\alpha}\dfrac{\partial \theta}{\partial t} \\ \theta(0,t) = \theta(L,t) = 0 \quad ,\theta(y,0) = 0 \end{cases} \tag{18}$$

Where $m = \sqrt{\frac{(h + 4e\beta T_a^3)P}{Ak}}$ and L represents the effective length of the sample in the "y" direction. Solving the above linear non-homogeneous partial differential equation allows the derivation of the temperature distribution for any heat source (or heat power), $\dot{G}$. Consequently, this framework serves as a valuable theoretical basis for assessing the performance of a numerical model with both constant and cyclic heat sources (by defining $\dot{G}$), through a comparison of the mean temperature and its cyclic behavior obtained from the numerical model with the solution of Eq. (18).

Due to the complexity of Eq. (18), the Maple programming language is used to solve it. The solutions for two type of heat sources are found as follows [190]:

- For a constant heat source of $\dot{G} = g$:

$$\theta(y,t) = \frac{1}{km^2(e^{2mL}-1)}\left\{\left[e^{my} - e^{m(L+y)} - e^{m(2L-y)} + e^{2mL} + e^{m(L-y)} - 1\right] g + \left(\sum_{n=1}^{\infty} \frac{2\sin\left(\frac{n\pi y}{L}\right) e^{-\frac{\alpha t l}{L^2}} gL^2((-1)^n - 1)}{\pi n k l}\right) e^{(2mL-1)} m^2 k\right\} \quad (19)$$

- For a cyclic heat source of $\dot{G} = g(1 + sin(2\pi f t))$ [190]:

$$\theta(y,t) = \sum_{n=1}^{\infty} \frac{1}{kn\pi l(l^2\alpha^2 + \omega^2 L^4)}\left\{2(-1 + (-1)^n)\, gL^2 \sin\left(\frac{n\pi y}{L}\right)\left((l^2\alpha^2 - \omega L^2 l\alpha + \omega^2 L^4)e^{-\frac{\alpha t l}{L^2}} + \omega L^2 l\alpha\cos(\omega t) - l\alpha^2\sin(\omega t) - l^2\alpha^2 + \omega^2 L^4\right)\right\} \quad (20)$$

Where $l = (L^2m^2 + \pi^2 n^2)$, g is the mean value of each heat power and f is the loading frequency (other parameters were defined before).

By assuming $g = 10^7 (\mathrm{W/m^3})$, $f = 11$ Hz, the material characteristics and geometry as in Table 6 and Figure 30, the temperature variation can be found from Eq. (19) and Eq. (20). The numerical temperature was also found by model with the same input variables as in the analytical solution. Figure 40 showed the suggested mesh and boundary conditions for the numerical simulation. The simulations were done on a computer with an Intel Core i7-8700 processor at 3.20GHz, 32.0 GB of RAM and an NVIDIA GeForce GT 1030 graphic card.

The comparison between numerical and analytical results is depicted in Figure 72, examining both the mean temperature and cyclic behavior. The temperature trends from the numerical model align closely with those derived analytically for both constant and cyclic heat sources.

Regarding the stabilized temperature within the last second, the mean temperatures stand at 26.164 ℃ and 26.125 ℃ for the numerical and analytical results, respectively. This yields a negligible error of 0.15%. Furthermore, concerning the temperature amplitude, the numerical simulation and analytical solution exhibit amplitudes of 0.0191℃ and 0.0195℃, respectively, resulting in an error of 2.09%. Thus, with errors at this level, the accuracy of the numerical results is affirmed.

Moreover, an additional verification is also proposed in Appendix C for a constant heat source. Employing both verifications enhances the accuracy of the model verification process.

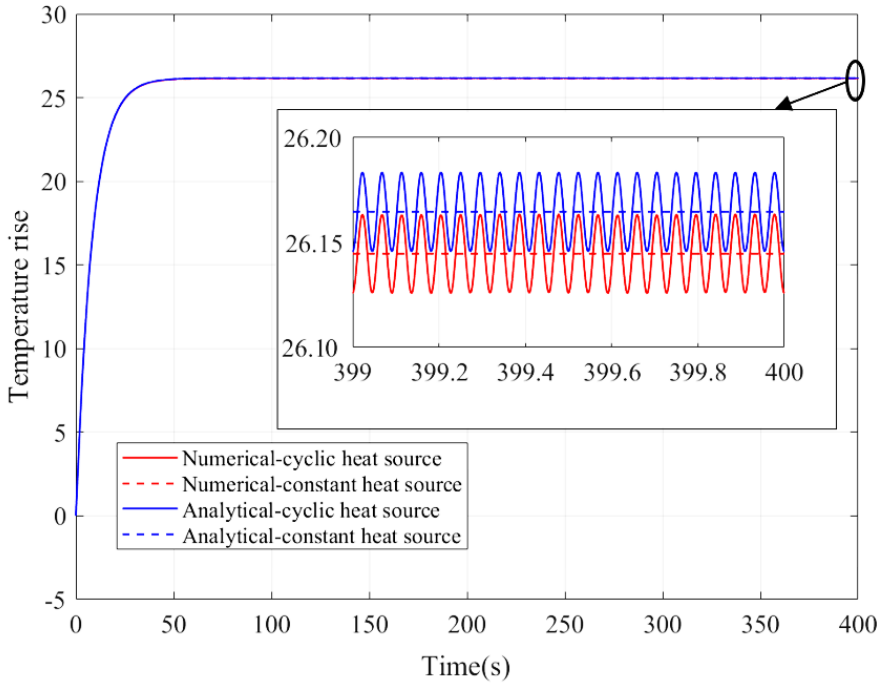

Figure 72 Validation with an analytical solution for the point at y=0: (a) constant heat source and (b) cyclic heat source

5-2-2 Effect of the number of pixels and the distribution of the heat sources

As depicted in Figure 42, before proposing the initial model, some preliminary considerations were planned to study the effect of the number of pixels and the distribution of the heat sources on the numerical output.

For this purpose, a cyclic heat power in the form of $\dot{q}\ (1 + sin(2\pi ft))$ was considered for all randomly distributed unit volumes spreading only in 15% of the gauge volume; where $\dot{q}$ is equal to $\dot{W}_{2\omega}$ for the last loading step in Table 12 ($4.11e7(W/m^3)$) and $f = 11\ Hz$.

The simulations were done on the same computer as before to select an appropriate grid of points between 13*31 and 52*99 for extracting the numerical data and to study the impact of the distribution of the heat units on $T_{2\omega}^{FEM}$.

Table 23 Effect of random distribution and grid of points on mean of $\boldsymbol{T_{2\omega}^{FEM}}$ (unit volume size: $\mathbf{1}\ \boldsymbol{mm^3}$)

		Mean of $T_{2\omega}^{FEM}$ ($T_{2\omega,mean}^{FEM}$)	
Grid of points of surface of gauge volume		13*31	52*99
Random distribution #	1	0.0131	0.0135
	2	0.0124	0.0142
	3	0.0132	0.0137
	4	0.0111	0.0131
	5	0.0122	0.014
	6	0.0131	0.0144
	7	0.0122	0.0138
	8	0.0125	0.0163
	9	0.0137	0.0154
	10	0.0143	0.0155
Mean		0.0128	0.0144
Standard deviation		0.0009	0.001

The results proposed in Table 23 indicate that the number of points in the numerical result can markedly influence the mean of $T_{2\omega}^{FEM}$ ($T_{2\omega,mean}^{FEM}$), thereby suggesting the utilization of the same number of pixels as in the experiment. Conversely, for 10 random distributions, the standard deviation of $T_{2\omega,mean}^{FEM}$ from different distributions are negligible (around 0.001). Hence, it can be inferred that the distribution of unit volumes has no discernible effect on $T_{2\omega,mean}^{FEM}$.

5-2-3 Initial model for heat source quantification

As shown in Figure 42, after collecting the reference data and performing preliminary considerations, the first model for heat source identification is established. For the initial model, a dog bone C45 sample with the cyclic heat defined as $\dot{W}_{2\omega}\ (1 + sin(2\pi\ (2f)\ t))\ (W/m^3)$ for all heat units, each having a size of $1\ mm^3$ were considered; where $f = 11\ Hz$ and $\dot{W}_{2\omega}$ was taken from Table 12. The simulations were conducted on the same computer without any additional computational resources.

Following the steps in Figure 42, firstly, the cyclic heat should be imposed to the entire gauge volume to see if the heat power is enough to satisfy $T_{2\omega}^{FEM} > T_{2\omega}^{exp}$. From Table 24, the numerical output for each loading level satisfies this condition, meaning that the SAH of mechanical energy seemed to be calculated accurately and the whole of the gauge volume cannot dissipate (or be under damage).

Table 24 $T_{2\omega,mean}^{FEM}$ for the heat amplitude of $\dot{W}_{2\omega}$ imposed in the whole of the gauge volume – with noise (unit volume size: $\mathbf{1\ mm^3}$)

$\sigma_a\ (MPa)$	300	310	320	340
$\dot{W}_{2\omega}\ (W/m^3)$	1.70E+07	2.13E+07	2.93E+07	4.11E+07
$T_{2\omega,mean}^{exp}$ (°C)	0.0023	0.0025	0.0054	0.0132
$T_{2\omega,mean}^{FEM}$ (°C) without noise	0.0191	0.0235	0.0352	0.0503
$T_{2\omega,mean}^{FEM}$ (°C) with noise	0.0212	0.0257	0.0374	0.0525

In the next step, the model should be implemented with a total heat volume smaller than the entire gauge volume, essentially utilizing only a fraction of it, since $T_{2\omega}^{FEM} > T_{2\omega}^{exp}$. In this way, the volume fraction that provides $T_{2\omega,mean}^{FEM} \approx T_{2\omega,mean}^{exp}$ can be found for each loading level, the heat volume can be identified.

As shown in Table 25, the volume was identified both with and without considering the previously mentioned noises in the previous section (the movement and thermal acquisition noises).

It can be seen that the total heat volume plays a significant role in the variation of the $T_{2\omega,mean}^{FEM}$. For example, changing the volume fraction from 5% to 10% resulted in an increase of almost 50-100%. For better representation of this variation, the thermal maps and histograms of $T_{2\omega}^{FEM}$ are proposed in Figure 73 and Figure 74 (they are shown only for $\sigma_a = 340\ MPa$ to avoid redundancy).

Table 25 $T_{2\omega,mean}^{FEM}$ in ROI for the heat amplitude of $\dot{W}_{2\omega}$ imposed in a fraction of the gauge volume – without noise (unit volume size: $\mathbf{1\ mm^3}$)

$\sigma_a\ (MPa)$	$\dot{W}_{2\omega}\ (W/m^3)$		Mean of $T_{2\omega}^{FEM}$ without noise							$T_{2\omega}^{exp}$
			Volume fraction (%)							
			5	10	15	20	25	30	60	
300	1.70E+07	Without any noise	**0.0024**	0.0050	0.0056	0.0081	0.0093	0.0104	0.0161	0.0023
		With movement noise	**0.0025**	0.0052	0.0056	0.0082	0.0094	0.0104	0.0162	
		With thermal noise	0.0046	0.0072	0.0078	0.0103	0.0115	0.0126	0.0183	
310	2.12E+07	Without any noise	**0.0029**	0.0062	0.0070	0.0101	0.0115	0.0129	0.0201	0.0025
		With movement noise	**0.0029**	0.0063	0.0071	0.0103	0.0116	0.0131	0.0201	
		With thermal noise	0.0051	0.0084	0.0092	0.0123	0.0137	0.0151	0.0223	
320	2.93E+07	Without any noise	**0.0041**	**0.0086**	0.0096	0.0139	0.0160	0.0179	0.0278	0.0054
		With movement noise	**0.0043**	**0.0086**	0.0098	0.0141	0.0162	0.0181	0.0280	
		With thermal noise	0.0063	0.0108	0.0118	0.0161	0.0182	0.0201	0.0300	
340	4.11E+07	Without any noise	0.0057	0.0113	**0.0135**	0.0195	0.0224	0.0251	0.0389	0.0132
		With movement noise	0.0059	0.0114	**0.0136**	0.0195	0.0224	0.0251	0.0390	
		With thermal noise	0.0079	0.0135	0.0157	0.0217	0.0246	0.0273	0.0411	

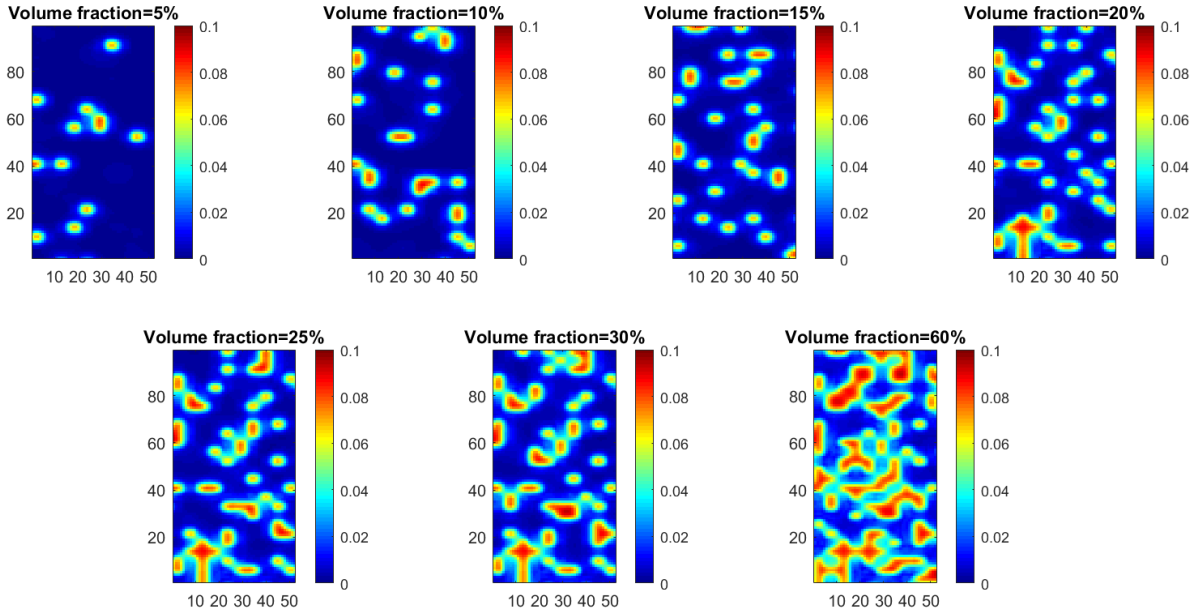

Figure 73 The scaled map of $T_{2\omega}^{FEM}$ in ROI for different volume fraction, $\sigma_a = 340\ MPa$ – with noise (unit volume size: $1\ mm^3$)

From Figure 74, it can be clearly seen that $T_{2\omega}^{FEM}$ tends to spread more between 0 and 0.1 as the volume fraction increases. Specifically, with a volume fraction of 5% of the gauge volume, it concentrates more around 0, while for 60%, it distributes almost uniformly between maximum and minimum values. In other words, increasing the volume fraction leads to a significant rise in the possibility of having more heat sources on the surface of the gauge volume.

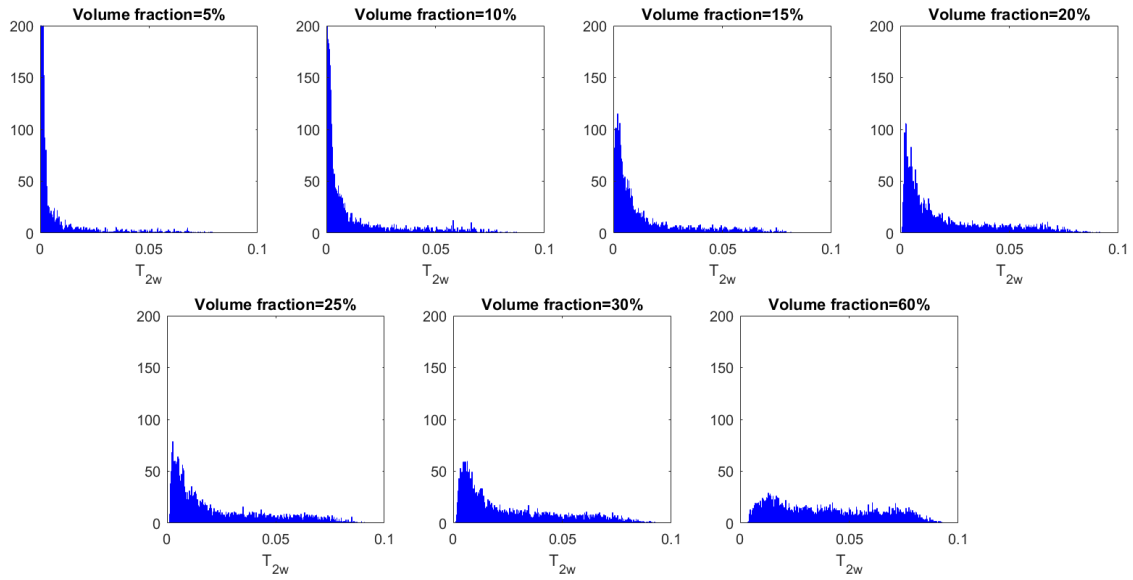

Figure 74 The histograms of $T_{2\omega}^{FEM}$ in ROI for different volume fraction, $\sigma_a = 340\ MPa$ – with noise (unit volume size: $1\ mm^3$)

A better representation for this effect can be seen in Figure 75 where $T_{2\omega,mean}^{FEM}$ rises exponentially by increasing the volume fraction. In addition, for higher heat amplitudes, it is evident that $T_{2\omega,mean}^{FEM}$ is located at a higher level, reflecting the imposition of grater heat power into the material (as a representative of more plastic deformation). Furthermore, the observation suggests that as the magnitude of heat amplitude increases, the rate of increase of $T_{2\omega,mean}^{FEM}$ with the volume fraction also intensifies, indicating a departure from simple linear behavior. It can be expected that, very close to the failure of the material, $T_{2\omega,mean}^{FEM}$ has the maximum possible value. On the contrary, the minimum value belongs to the first loading blocks in the fatigue test.

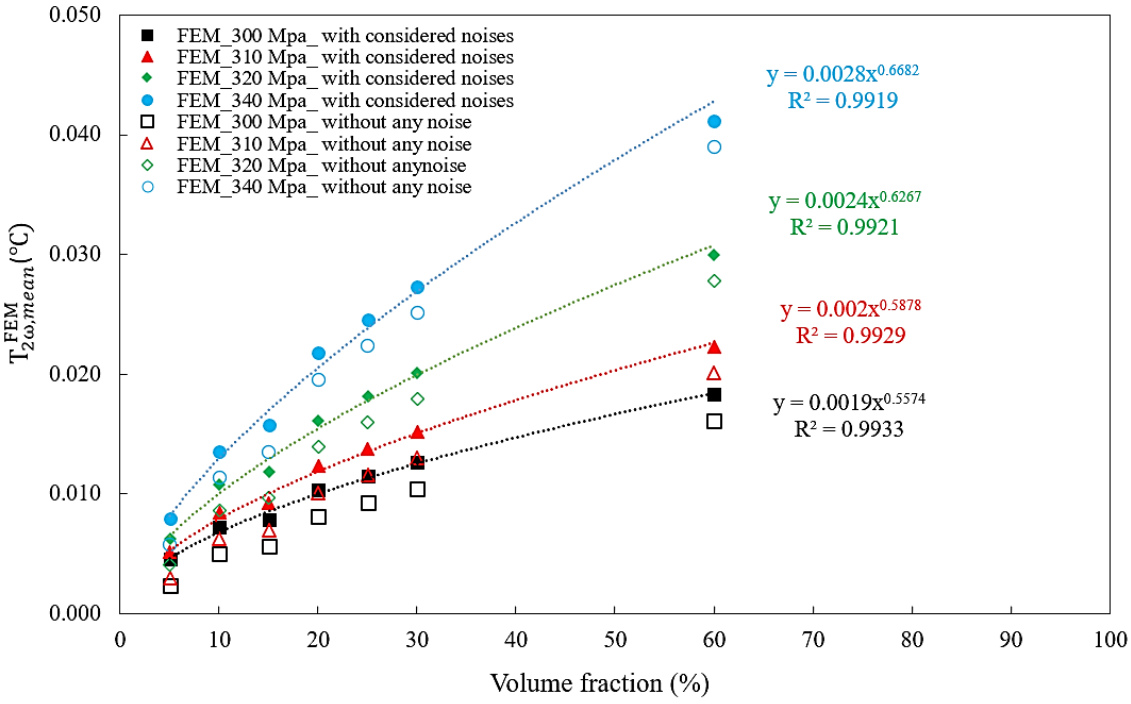

Figure 75 The variation $T_{2\omega,mean}^{FEM}$ in ROI with volume fraction (unit volume size: 1 mm^3)

In Table 25 and Figure 75, the effect of the two types of studied noises, thermal acquisition and sample movement noises, on $T_{2\omega,mean}^{FEM}$ is shown. It is obvious that the noise levels up significantly all $T_{2\omega,mean}^{FEM}$ trends showing the necessity of the noise consideration when working with a validated thermal model. However, as can found from Table 25, this behavior is dominantly due to the thermal acquisition noise effect. Although the movement noise influence is almost negligible, it would not be reasonable to draw any conclusion about the movement noise effect as the accuracy of the elongation measurement is compromised using the extensometer data.

In other words, according to the measurement process of the movement noise in this study, using the extensometer data to obtain the maximum elongation in gauge length and defining a linear

displacement function from one side of the gripper to other side provide only an approximation of the real movement of the points in the material coordinate. However, in order to show undeniable effect of this noise, further investigation is performed based on some hypothetical values for the displacements in ROI in the following section, after proposing the modified numerical model.

Returning to the primary goal of this section, the identified heat volume fractions that satisfy the $T_{2\omega,mean}^{FEM} \approx T_{2\omega,mean}^{exp}$ are found and listed in Table 25. Without considering the noise, the identified volumes producing heat are 5%, 5%, 5-10%, and 15% of the gauge volume for loading amplitudes of 300, 310, 320, and 340 MPa, respectively. However, by considering the noise, the volumes for the first three loading levels are below 5% (1%, 1% and 4%), whereas it is 10% of the gauge volume for the last lading level. Table 26 summarizes the identified volume fractions.

Table 26 Identified volume fractions producing heat for unit volume size of $\mathbf{1}\ \boldsymbol{mm^3}$– with noise

$\sigma_a\ (MPa)$	300	310	320	340
$\dot{W}_{2\omega}\ (W/m^3)$	1.70E+07	2.12E+07	2.93E+07	4.11E+07
Identified volume fractions producing $T_{2\omega,mean}^{FEM} \approx T_{2\omega,mean}^{exp}$ (%)	1	1	4	10

Additionally, the comparison between the numerical and experimental T_{2w} maps and histograms are proposed in Figure 76 and Figure 78. The scaled maps are also provided in Figure 77 for better comparison. From these figures, the resemblance between the numerical and experimental results is quite minimal. Unlike the latter ones, some big clusters are present in the numerical maps (in Figure 76 and Figure 77) which influences the $T_{2\omega}^{FEM}$ distribution, resulting in lower peaks and a more confined spread in the histograms compared to the experimental results (see Figure 78).

Two possible reasons for the presence of such big clusters could be attributed to the size of the unit heat volumes and the way they were distributed. Latter one is out of the control as it should be distributed randomly in the gauge volume of the model (based on the Munier et al. [50]), nevertheless, the model can be modified based on the unit size of the heat volumes, as explored in the next section.

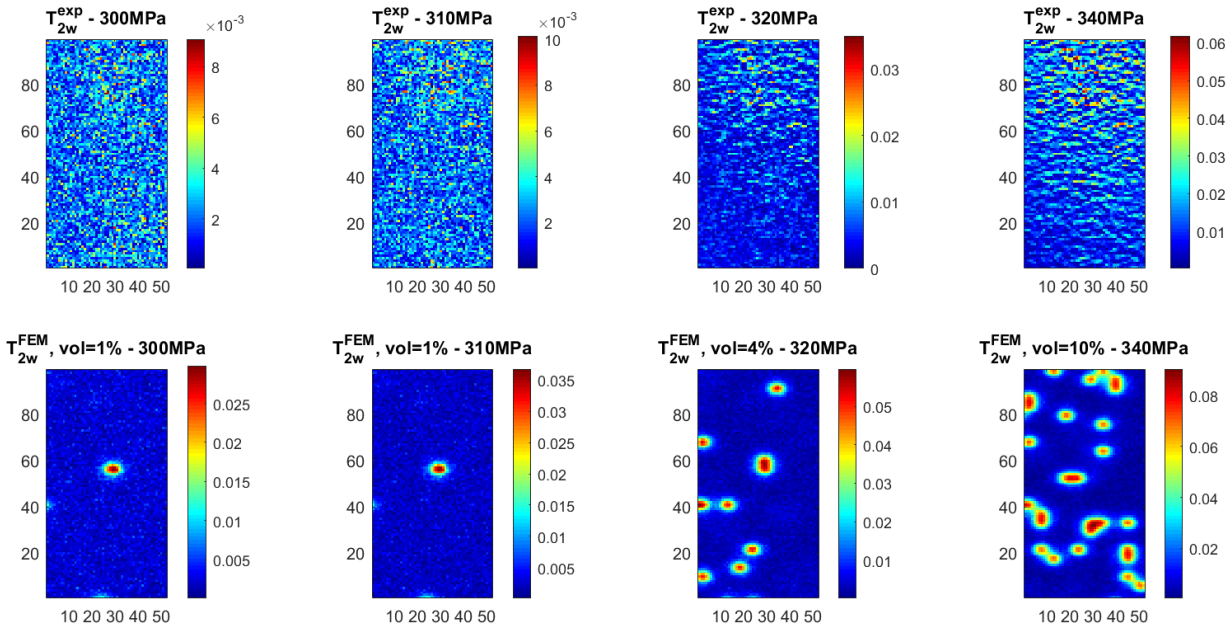

Figure 76 The experimental and numerical maps of $T_{2\omega}^{FEM}$ in ROI– with noise (unit volume size: 1 mm^3)

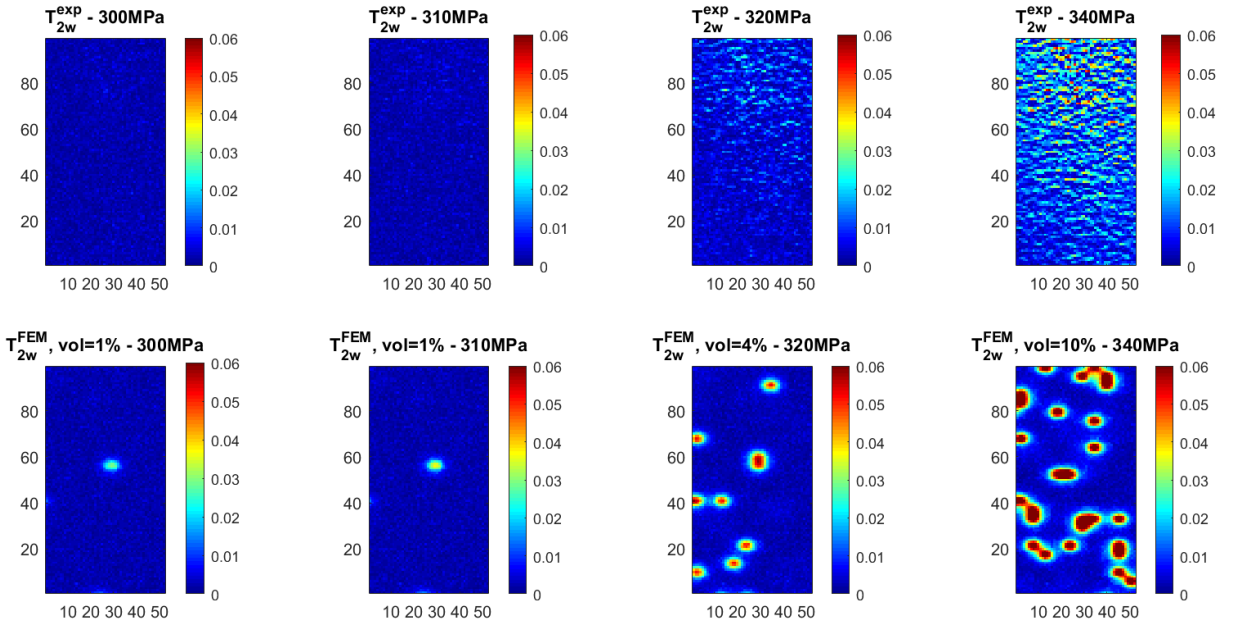

Figure 77 The scaled experimental and numerical maps of $T_{2\omega}^{FEM}$ in ROI– with noise (unit volume size: 1 mm^3)

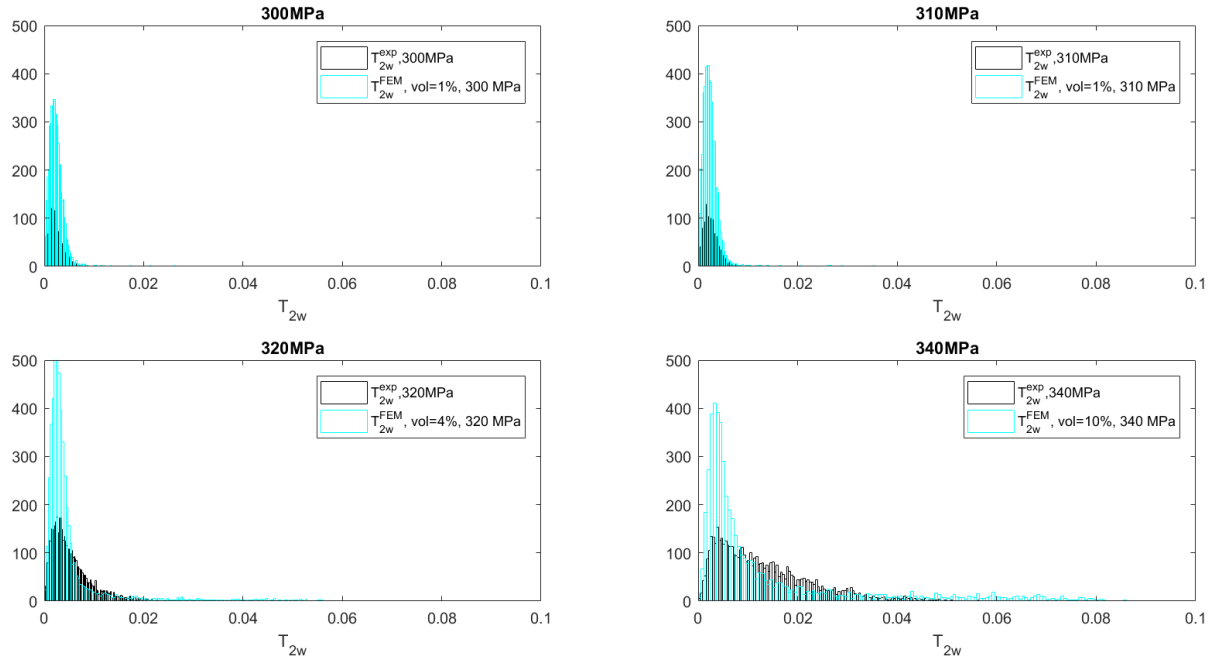

Figure 78 The experimental and numerical histograms of $T_{2\omega}^{FEM}$ in ROI– with noise (unit volume size: 1 mm^3)

5-2-4 Modified model – effect of the unit size of heat volumes

In this section, the size of the unit heat volumes is reduced to smaller values that are computationally manageable. For this aim, three values were considered for the unit volume size, including 0.12500, 0.02700 and 0.015625 mm^3, corresponding to the edge size (see Figure 41) of 0.5, 0.3, and 0.25 mm. It should be noted that 0.25 mm was the minimum value that could be handled with available computational resources, in this study. Unlike for other unit edge sizes that was studied in the same computer as before, a more powerful computer was utilized for 0.25 mm, featuring an Intel processor at 3GHz, 128 cores, 1024 GB of RAM and an NVIDIA Quadro 8000 graphic card.

Initially, it should be investigated whether the heat volumes identified in previous section are influenced by the unit size or not. For this purpose, for a specific loading level of $\sigma_a = 340\ MPa$ and a fixed volume fraction of 10% found in previous section for the unit size of 1 mm^3, $T_{2\omega}^{FEM}$ maps and histograms are compared for all considered unit sizes in Figure 79.

As can be seen, the big clusters related to edge size of 1mm become either smaller for the edge size of 0.5mm or almost disappeared for the edge size of 0.3mm and 0.25mm. Therefore, reducing the unit size helps spreading the heat sources more uniformly throughout the gauge volume, leading to improved qualitative results. Furthermore, as can be seen in Figure 79b, it clearly affects the distribution of $T_{2\omega}^{FEM}$ both in terms of peaks and ranges. Moreover, from Table 27, it is evident that

$T_{2\omega,mean}^{FEM}$ is also affected by the unit size, thereby impacting the identified volume fractions that producing heat.

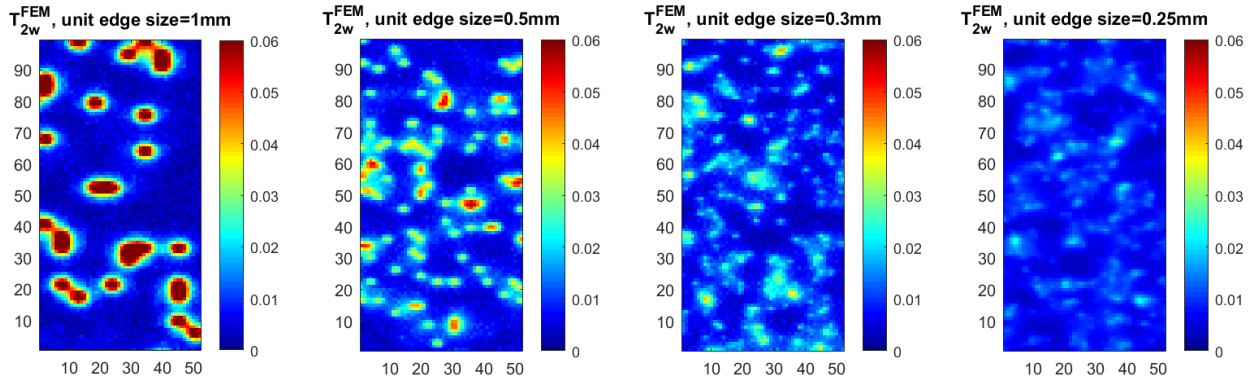

(a)

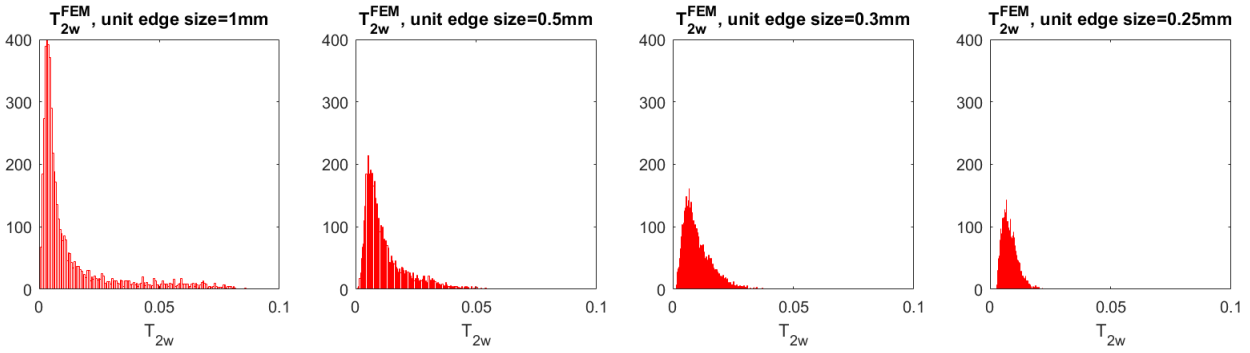

(b)

Figure 79 The scaled numerical maps of $T_{2\omega}^{FEM}$ in ROI for different unit edge size – with noise ($\sigma_a = 340\ MPa$, total heat volume=10% of gauge volume)

Table 27 $\boldsymbol{T_{2\omega,mean}^{FEM}}$ in ROI for different unit edge size – with noise ($\boldsymbol{\sigma_a = 340\ MPa}$, Total heat volume=10% of gauge volume)

Unit volume edge size (mm)	0.1	0.5	0.3	0.25	$\boldsymbol{T_{2\omega,mean}^{exp}}$
$T_{2\omega,mean}^{FEM}$	0.0135	0.0120	0.0102	0.0082	0.0132
Difference with the experimental value (%)	2.27	-9.09	-22.73	-37.88	

The reason for changing $T_{2\omega,mean}^{FEM}$ with the unit size can be attributed to the possibility of positioning of the heat sources on the surface of the gauge (or ROI) volume, where $T_{2\omega}^{FEM}$ is measured. As shown in Table 28, interestingly, when the unit size becomes smaller, the possibility of locating a unit volume on the surface becomes lower. By reducing the number of heat sources on the surface, or in other words, by shifting the unit volumes deeper into the gauge volume (along the thickness), their footprint intensity on the surface of the gauge volume becomes lower. Subsequently, this leads to a reduction in $T_{2\omega,mean}^{FEM}$. Therefore, due to the effect of the unit size on the $T_{2\omega,mean}^{FEM}$, the total heat volume should be

identified again for other loading level, as the difference between $T_{2\omega,mean}^{FEM}$ and $T_{2\omega,mean}^{exp}$ was not negligible for $\sigma_a = 340\ MPa$.

Table 28 The probability of locating an unit heat volume on the surface of the gauge volume with different unit size

The edge size of each heat volume unit (in mm)	1	0.5	0.3	0.25
The size of each heat volume unit (in mm^3)	1	0.125000	0.027000	0.015625
Total possible number of the heat volume units in the gauge volume: N_{GV}	2160	17280	80000	138240
Total number of the heat volume units on surface: N_{unit}	360	1440	4000	5760
Probability that a randomly selected cube is located on the surface (%): $\frac{N_{unit}}{N_{GV}} \times 100$	16.67	8.33	5.00	4.17
Reduction of the probability with respect to the bigger unit size	-	50.1	70.0	74.5

For the unit sizes of 0.3mm and 0.25mm that provide better qualitative thermal maps compared to those for 0.5mm, the heat volumes are found, as shown in Table 29. Similar to the last loading level which exhibits a significant increase in the volume fraction (around 25% increase compared to the volume identified with the unit size of 1mm), the identified volumes for other loading levels are also changed considerably. It should be noted that the percentage values in the 3rd and 4th rows show the difference between $T_{2\omega,mean}^{exp}$ and $T_{2\omega,mean}^{FEM}$, while in the last row, it shows the difference between $T_{2\omega,mean}^{FEM}$ for the unit size of 1mm and two other sizes.

Table 29 Identified heat volumes with the edge size of 0.25 and 3 mm of the heat volume unit – considering the noise

$\sigma_a\ (MPa)$	300	310	320	340
$\dot{W}_{2\omega}\ (W/m^3)$	1.70E+07	2.12E+07	2.93E+07	4.11E+07
$T_{2\omega}^{exp}$	0.0023	0.0025	0.0054	0.0132
$T_{2\omega,mean}^{FEM}$ (Unit size =0.3 mm)	0.0023 (0.0%)	0.0024 (4.0%)	0.0056 (3.7%)	0.0135 (2.3%)
$T_{2\omega,mean}^{FEM}$ (Unit size =0.25 mm)	0.0024 (4.3%)	0.0026 (4.0%)	0.0053 (1.9%)	0.0125 (5.3%)
Volume fraction (%) with the unit size of 0.3 and 0.2mm	0.7(~ 1)	0.8(~ 1)	3.4(~ 4)	12.5
Difference with the volume identified with unit size of 1mm	30%	20%	15%	25%

For each loading level, $T_{2\omega}^{FEM}$ maps and histograms found according to the identified heat volumes are compared with experimental ones in Figure 80 to Figure 87.

In order to analyze effectively the similarity between experimental and numerical histograms (or thermal maps), five distribution functions including Weibull, lognormal, exponential, normal and extreme value were fitted to T_{2w} data. The similarity was checked by ranking the fitted distribution functions based on their log likelihood level. Log likelihood shows how well a function is fitted to the data, a higher value is preferable as it suggests a distribution function that is better suited to the data

[191]. In other words, the log likelihood serves as a tool to compare different distribution functions and determine which one best fits the data. It should be said that the other methods such as Kernel Density Estimation (KDE), Kolmogorov-Smirnov test, Chi-squared test can also be employed for comparing histograms [191]. In addition, besides comparing the numerical and experimental $T_{2w,mean}$, the median and the standard deviation are also compared in these tables. The most appropriate fitting function for each loading level and the unit size are ranked in Table 30 to Table 33.

Although the similarity between experimental and numerical maps shown in Figure 80 to Figure 87, is not clear, analyzing the histograms can be very helpful to draw conclusions.

From Table 30 to Table 33, it is observed that the difference between $T_{2\omega,mean}^{FEM}$ and $T_{2\omega,mean}^{num}$ is minimal, equal or less than 5 % which are negligible. The errors for the median are also relatively acceptable, with the maximum difference being around 15% and 11% for unit sizes of 0.3 and 0.25mm, respectively. Nevertheless, the differences become more pronounced for standard deviation values, with the highest percentages reaching 32% and 65% for the above unit sizes, correspondingly. This indicates that while the central values of the numerical and experimental results closely align, there is a significant disparity in the spread or variability of the values.

In terms of the distribution function adhered to by each dataset, it was found that both numerical and experimental data for 300 MPa and 310 MPa were aligned with either Weibull or lognormal functions. At 320 MPa, it can be observed that the lognormal function is a suitable fit for both numerical and experimental datasets. Although the Weibull function provides the best fit for the experimental data, the log likelihoods of Weibull and lognormal is nearly identical. A similar observation can be made for 340 MPa, where the Weibull is the appropriate function for fitting both types of data. Therefore, some consistency was noted between numerical and experimental results, as both datasets exhibit alignment with either Weibull or lognormal distribution.

One possible reason for the differences in maps and standard deviation could stem from the criterion introduced for heat volume identification. As proposed before in Figure 42, the criterion for heat volume identification was solely defined based on the mean values of T_{2w} ($T_{2\omega,mean}^{exp}$ and $T_{2\omega,mean}^{FEM}$). Thus, it might be beneficial to modify the strategy by incorporating additional statistical measures, such as the standard deviation of T_{2w} within an optimization framework. This refinement could lead to a more comprehensive criterion for predicting the heat volumes and improving the similarity between both data.

Furthermore, several assumptions were made, which are pivotal factors contributing to the observed

differences. These assumptions include: uniformity in size and heat amplitude for all randomly distributed units, a non-interacting regime among heat sources each-others, computational limitations impeding further reduction in the unit size of each heat source and unavailability of accurate displacement for each point on the surface of the sample in ROI used for simulating the motion-induced noise. Of particular significance is the last assumption, which will undergo further examination in the subsequent section to elucidate its impact on $T_{2\omega}^{FEM}$.

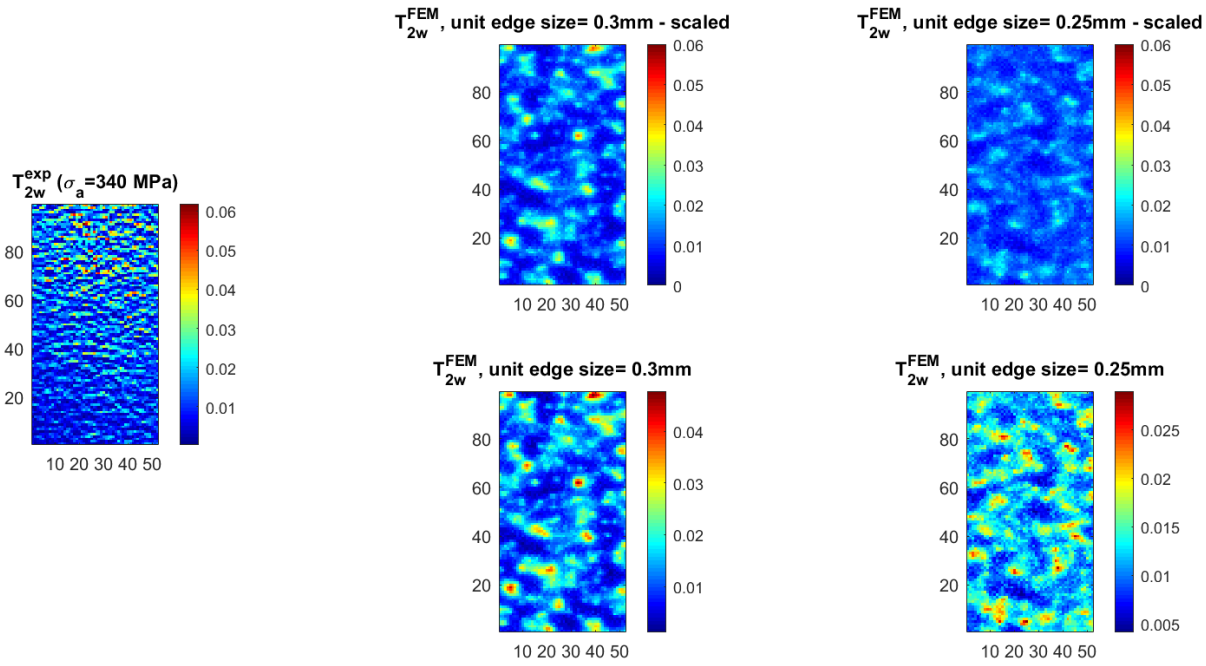

Figure 80 The numerical and experimental maps of T_{2w} in ROI – with noise ($\sigma_a = 340\ MPa$, total heat volume=12.5% of gauge volume)

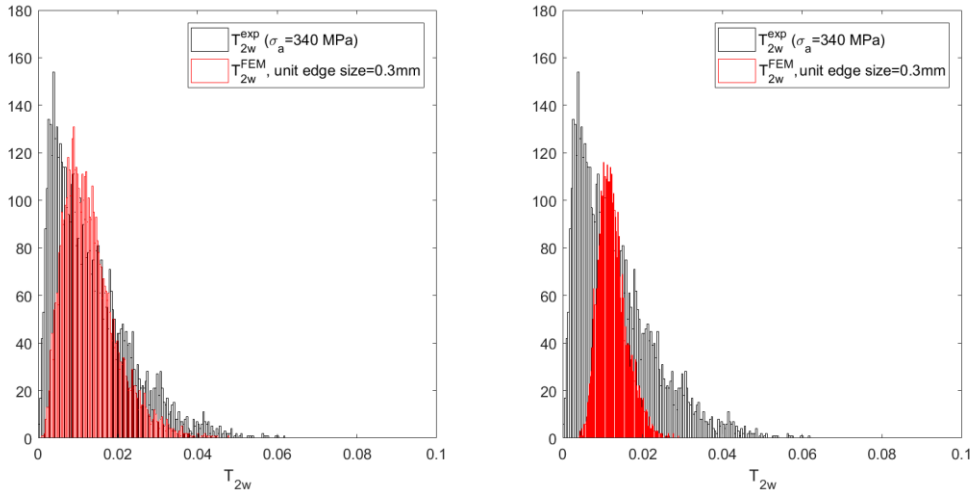

Figure 81 The numerical and experimental histograms of T_{2w} in ROI – with noise ($\sigma_a = 340\ MPa$, total heat volume=12.5% of gauge volume)

Table 30 Statistical comparison between numerical (with noise) and experimental T_{2w} - $\sigma_a = 340\ MPa$

	The edge size (mm)	Difference with respect the experimental value (%)			Log likelihood of the distribution function (■ Rank 1 ■ Rank 2 ■ Rank 3)				
		Mean	Std	Median	Weibull	Lognormal	Exponential	Normal	Extreme Value
$T_{2\omega}^{exp}$	-	-	-	-	17548.9	17434	17117.4	16531.9	15247.4
$T_{2\omega}^{FEM}$	0.3	5.3	32	9.3	18996.3	18518.8	19060.8	18924.7	17267.5
$T_{2\omega}^{FEM}$	0.25	2.3	64	11.1	22020.6	21844.1	22073.7	21746.1	20883.5

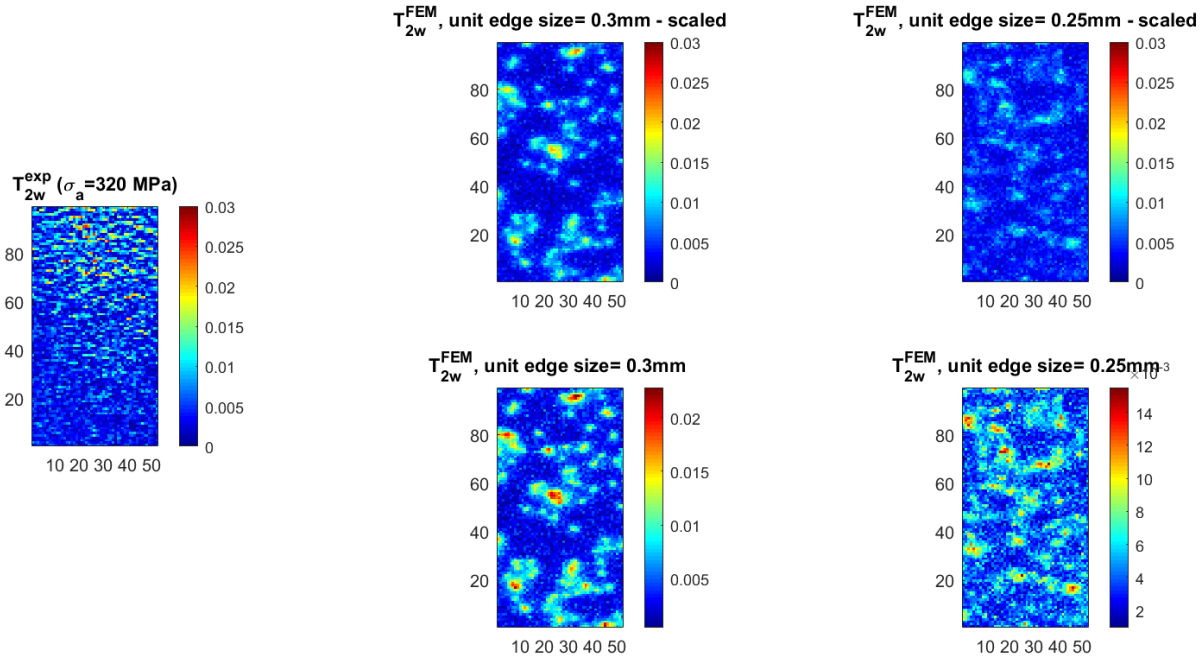

Figure 82 The numerical and experimental maps of T_{2w} in ROI – with noise ($\sigma_a = 320\ MPa$, total heat volume=4% of gauge volume)

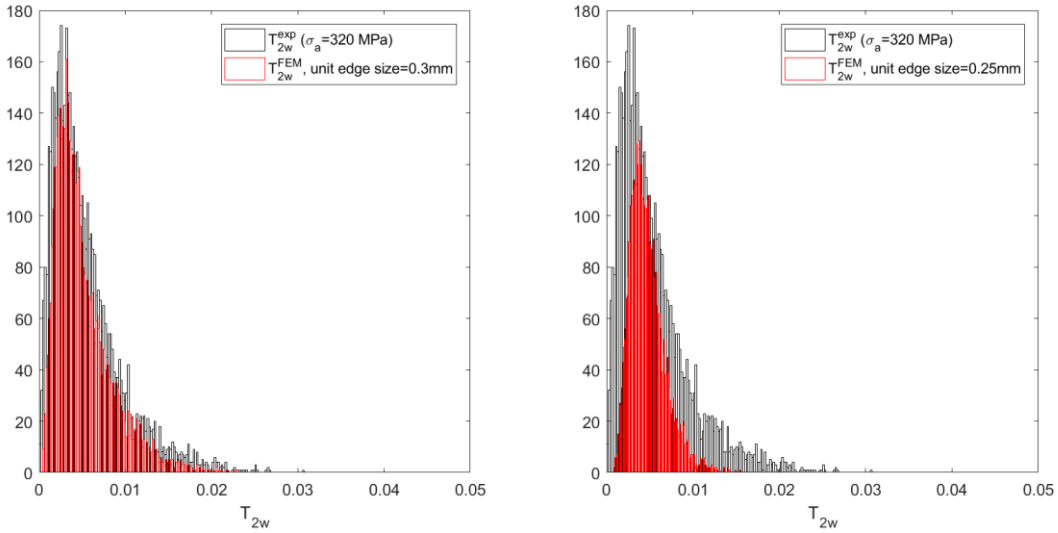

Figure 83 The numerical and experimental histograms of T_{2w} in ROI – with noise ($\sigma_a = 320\ MPa$, total heat volume=4% of gauge volume)

Table 31 Statistical comparison between numerical (with noise) and experimental T_{2w} - $\sigma_a = 320\ MPa$

	The edge size (mm)	Difference with respect the experimental value (%)			Log likelihood of the distribution function (■ Rank 1 ■ Rank 2 ■ Rank 3)				
		Mean	Std	Median	Weibull	Lognormal	Exponential	Normal	Extreme Value
$T_{2\omega}^{exp}$	-	-	-	-	22162.5	22125.1	21730.6	20968.6	19374.5
$T_{2\omega}^{FEM}$	0.3	1.9	20.9	2.7	23028.3	23245.3	23187.6	22174.3	20660.4
$T_{2\omega}^{FEM}$	0.25	3.7	51.7	1.31	24920.2	25164.6	22458.9	24708.8	23448.2

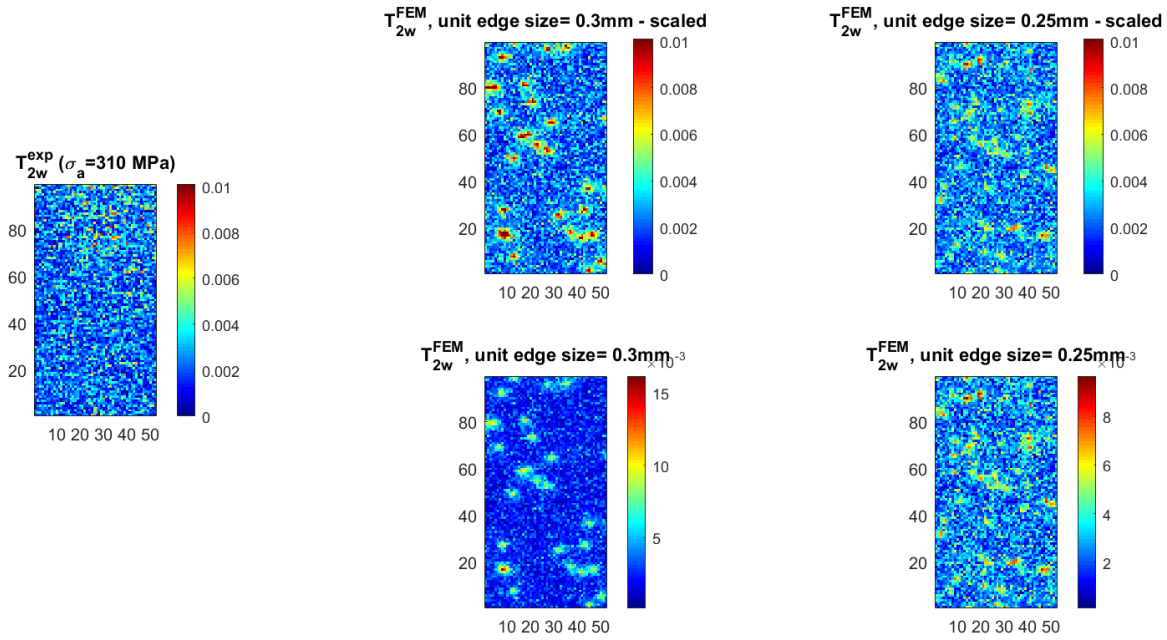

Figure 84 The numerical and experimental maps of T_{2w} in ROI – with noise ($\sigma_a = 310\ MPa$, total heat volume=1% of gauge volume)

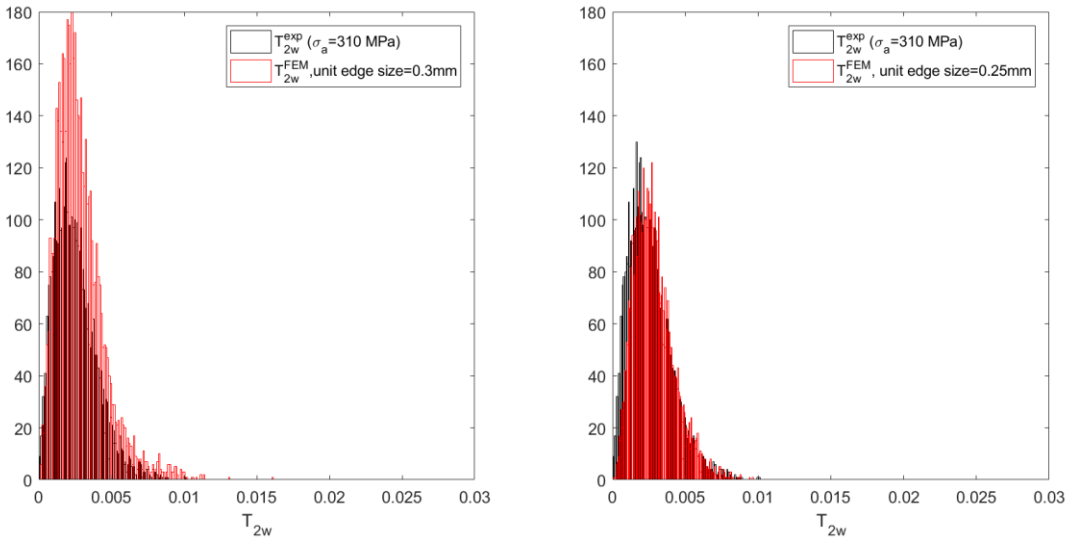

Figure 85 The numerical and experimental histograms of T_{2w} in ROI – with noise ($\sigma_a = 310\ MPa$, total heat volume=1% of gauge volume)

Table 32 Statistical comparison between numerical (with noise) and experimental T_{2w} - $\sigma_a = 310\ MPa$

	The edge size (mm)	Difference with respect the experimental value (%)			Log likelihood of the distribution function (■ Rank 1 ■ Rank 2 ■ Rank 3)				
		Mean	Std	Median	Weibull	Lognormal	Normal	Exponential	Extreme Value
$T_{2\omega}^{exp}$	-	-	-	-	26873.5	26569.2	26402.8	25681.3	25190.5
$T_{2\omega}^{FEM}$	0.3	4	14.5	11.2	26301	26319.6	25707.6	25019.1	23984.4
$T_{2\omega}^{FEM}$	0.25	4	4.4	15.5	26928.9	26832.3	26632	25066	25525.3

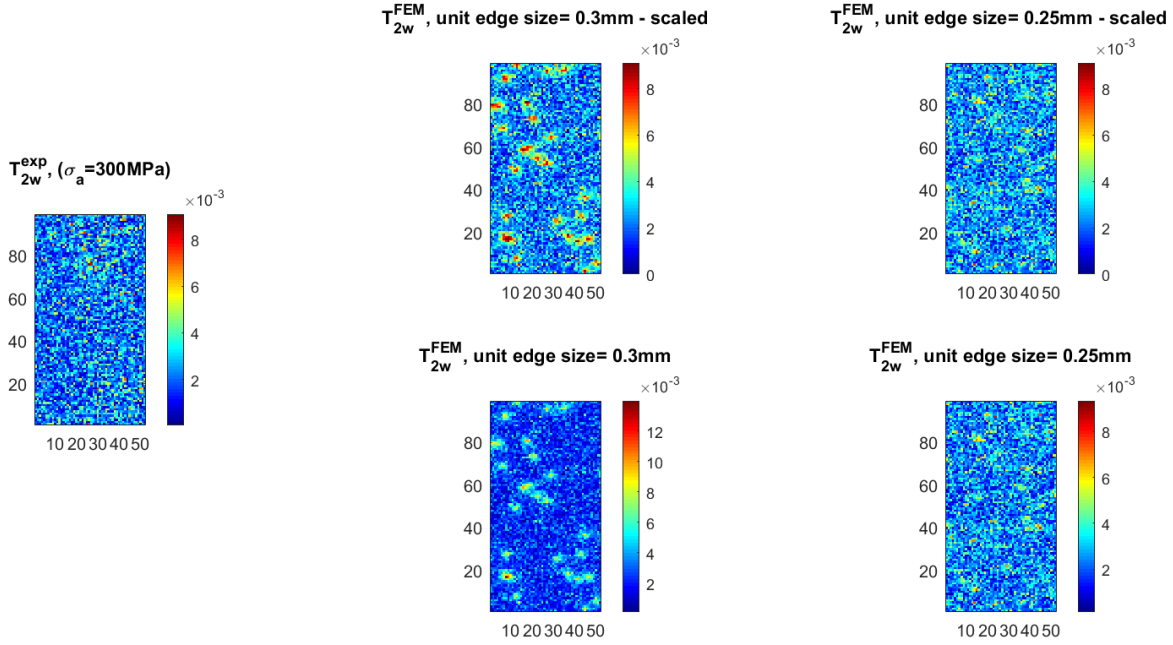

Figure 86 The numerical and experimental maps of T_{2w} in ROI – with noise ($\sigma_a = 300\ MPa$, total heat volume=1% of gauge volume)

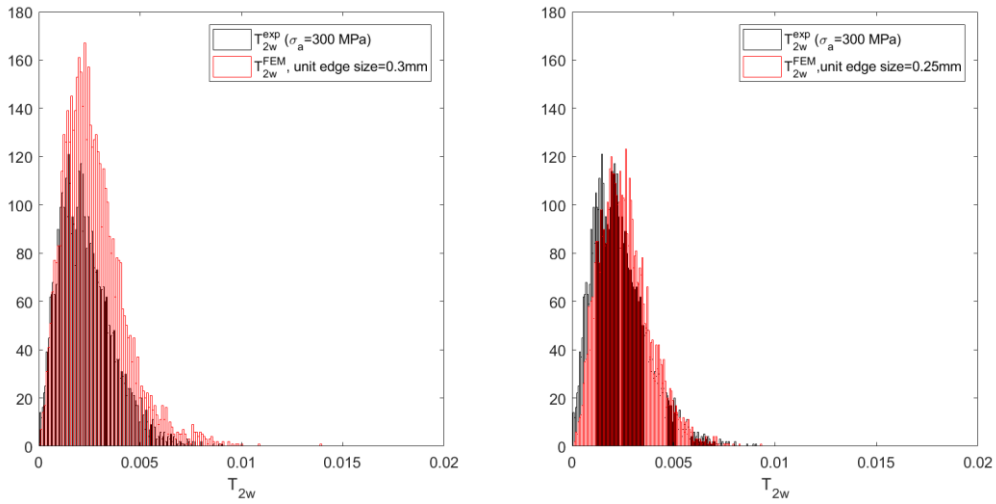

Figure 87 The numerical and experimental histograms of T_{2w} in ROI – with noise ($\sigma_a = 300\ MPa$, total heat volume=1% of gauge volume)

Table 33 Statistical comparison between numerical (with noise) and experimental T_{2w} - $\sigma_a = 300\ MPa$

	The edge size (mm)	Difference with respect the experimental value (%)			Log likelihood of the distribution function (■ Rank 1 ■ Rank 2 ■ Rank 3)				
		Mean	Std	Median	Weibull	Lognormal	Normal	Exponential	Extreme Value
$T_{2\omega}^{exp}$	-	-	-	-	27270.9	26930.4	26841.1	26038.5	25703.8
$T_{2\omega}^{FEM}$	0.3	0	13.0	15.5	26695.3	26569.9	26231	25295.6	24745.9
$T_{2\omega}^{FEM}$	0.25	4.3	7.5	4.9	27480.6	27279.6	27242	26223.4	25521.7

5-3 Further investigation on the motion-induced noise effect

In previous section, the results show that the movement noise effect on thermal data was negligible. In this section the aim is further investigating this effect by considering a hypothetical case.

The motion-induced noise effect might be notable depending on two factors: (i) the maximum elongation which are extracted from the extensometer and imposed on the numerical results, and (ii) the present of high $T_{2\omega}^{FEM}$ values where the displacement is maximum, because they can significantly alter the neighbor values when employing interpolation/extrapolation techniques.

The latter one cannot be investigated as the location of the randomly distributed heat sources cannot be manipulated. Therefore, it is worth considering the effect of the former one with hypothetical and higher maximum elongations than those listed in Table 14.

For the last loading level and randomly distributed unit heat volumes in 12.5% of the gauge volume with unit size of 0.3mm, the movement of the points on the surface of the numerical model is simulated for maximum elongations of 0.1, 0.2 and 0.5 mm. These values are approximately1.7 times, 3.5 times and 8.5 times higher than the measurement from the extensometer (0.0583, the last row in in Table 14).

As shown in Figure 88, by imposing the abovementioned hypothetical elongations on the numerical output, undeniable effect of the displacement (or elongation) can be observed both qualitatively and quantitively.

Qualitatively, the similarity between $T_{2\omega}^{FEM}$ and $T_{2\omega}^{exp}$ maps is improved by increasing the elongation to 0.1 mm. As can be seen, like the experimental map, there is a region on the top of the numerical map where high values of T_{2w} are accumulated. Thus, studying the movement noise deeply and accurately can guide to better explanation of the strange pixels in the experimental map, very close to the moving gripper side (see Figure 53). It can be concluded that the movement of the sample is one potential explanation for presenting them in experimental thermal maps.

It is important to note that opting for an excessively high maximum displacement is not recommended, as it led to a deterioration in the similarity between numerical maps for 0.2 and 0.5 mm of maximum displacement compared to the experimental ones. Such a discrepancy between the extensometer data and these hypothetical values may not be reasonable.

Furthermore, it can also be found in Table 34 that $T_{2\omega,mean}^{FEM}$ deviates more from $T_{2\omega,mean}^{exp}$ by these

elongations; showing the effect of the movement noise on $T_{2\omega,mean}^{FEM}$ and, consequently, emphasizing the necessity of determining the heat volume by considering this type of noise in future works.

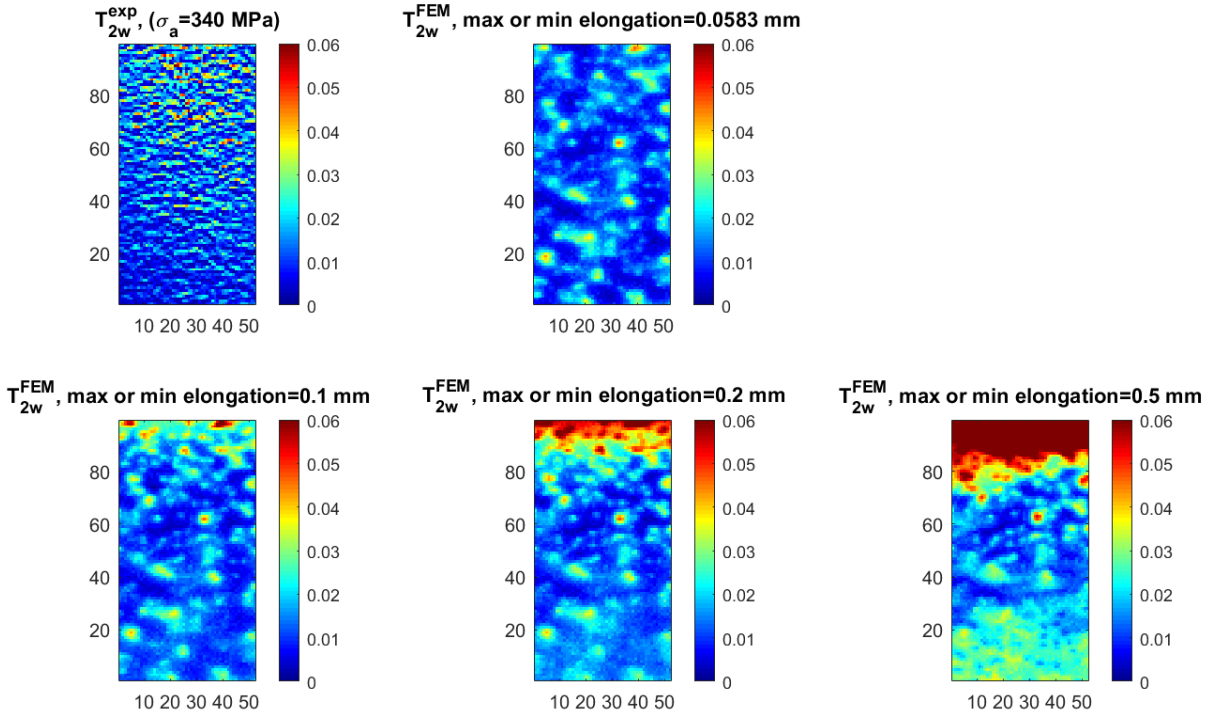

Figure 88 Effect of the maximum elongation on $T_{2\omega}^{FEM}$,
(unit size=0.3 mm, volume fraction=12.5% of the gauge volume, $\sigma_a = 340\ MPa$, with two considered noises)

Table 34 Effect of the maximum elongation on $T_{2\omega,mean}^{FEM}$ (unit size=0.3 mm, volume fraction=12.5% of the gauge volume, $\sigma_a = 340\ MPa$, with two considered noises)

	Maximum elongation of the gauge length imposed in the movement noise (mm)				$T_{2\omega,mean}^{exp}$
	0.0583	0.1	0.2	0.5	
$T_{2\omega,mean}^{FEM}$	0.0135	0.0150	0.0187	0.0318	0.0132

Of course, this investigation relies on assumed values, and any conclusion should be withheld until the accuracy of the measured displacement from the surface of the sample in the fatigue test is ensured. According to this investigation, utilizing more precise strain measurements method, such as the digital image correlation (DIC), can be a useful to delve into the effect of the movement noise.

5-4 Effect of frequency on the SAH of temperature

As previously discussed, high loading frequency may impact thermographic measurements by preventing signal stabilization and inducing sample motion. Therefore, conducting experiments to

analyze the effect of loading frequency on thermal components poses significant challenge. Conversely, a numerical model can serve as a valuable tool for investigating this matter.

In this section, the experimental data from the cyclic loading test at a constant amplitude of 300 MPa under various frequencies is employed to validate numerical results, in terms of $T_{2\omega}$trend with loading frequency.

Verification is conducted within the frequency range of 1.5 to 5 Hz to mitigate the sample movement effect and ensure the attainment of a stabilized temperature. In addition, considering the loading level below the fatigue limit eliminates any considerable damage that could impact on $T_{2\omega}$.

From the experimental data, the SAH of the mechanical energy $\dot{W}_{2\omega}$ was measured and a cyclic heat power as $7.86 \times 10^7\ (1 + sin(2\pi\ (2f)\ t))\ (W/m^3)$ was imposed to each unit heat volume randomly distributed in the gauge volume.

Following the steps in Figure 42, the volume producing heat was found to be around 0.5% of gauge volume. It was estimated with the unit size of 0.3 mm (it was shown to be one of the appropriate sizes for the when comparing with the experimental data, in previous section).

As indicated in Figure 89, both experimental and numerical $T_{2\omega,mean}$ show falling trends with the loading frequency. The error bands positioned both above and below (blue lines in Figure 89) of the experimental curve were calculated from the standard deviation of $T_{2\omega,mean}^{exp}$ obtained from three thermal acquisitions conducted at the stabilized temperature.

Redistributing unit volumes randomly within the same volume fraction of 0.5% or a little smaller can reduce the gap between $T_{2\omega,mean}^{exp}$ and $T_{2\omega,mean}^{FEM}$. As shown in Table 23, the distribution leads to a standard deviation of approximately 0.001, which can be significant for very small values of $T_{2\omega,mean}^{FEM}$.

However, as the focus is only on the trend of $T_{2\omega}$ with the loading frequency, finding the exact volume can be skipped as the same trend can be expected even if the gap is removed.

Returning to the main goal of this section, higher loading frequencies should also be studied to verify this trend, which done numerically in this work. From Figure 90, the same behavior can be seen numerically as loading frequency increases. It can be observed that $T_{2\omega}$ diminishes markedly, leveling off to a plateau, beyond 40 Hz. This phenomenon serves as a constraint for utilizing this thermal index in thermographic methods, posing challenges for its measurement in fatigue characterization, particularly when employing conventional cooled IR-sensors. This discovery highlights another

valuable application of the proposed model: investigating the heat diffusion phenomenon.

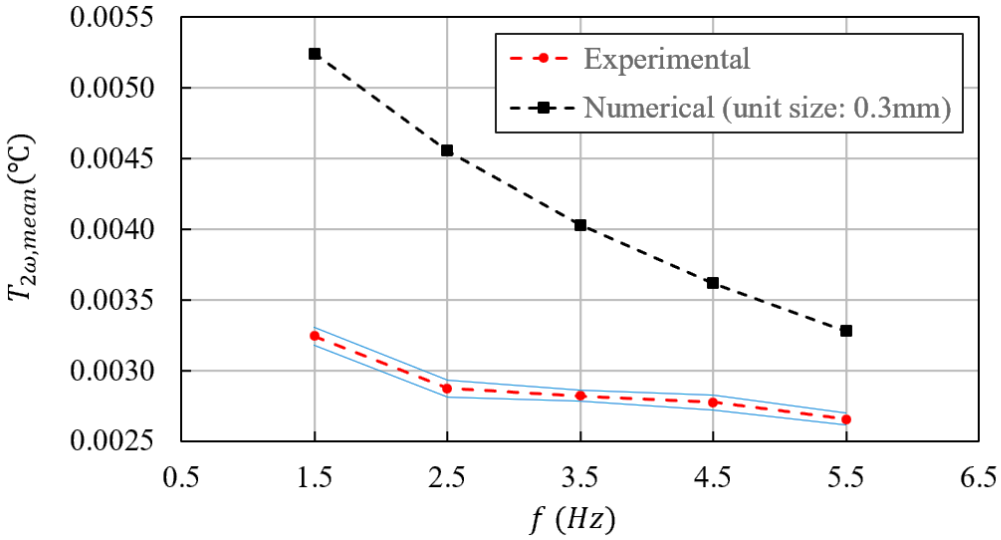

Figure 89 Verification of numerical model on the effect of loading frequency on $T_{2\omega}$ found ($\sigma_a = 300\ MPa$)

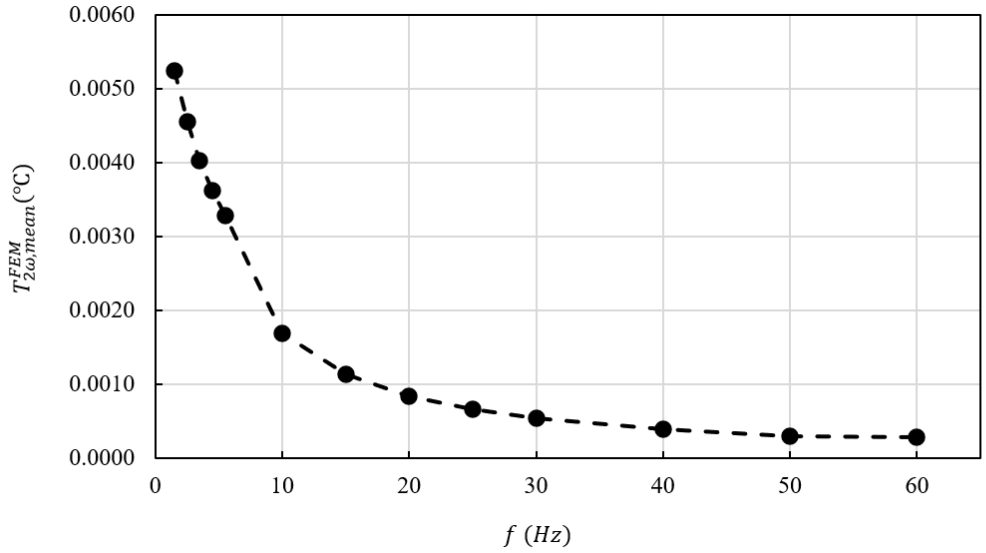

Figure 90 Effect of loading frequency on $T^{FEM}_{2\omega,mean}$ ($\sigma_a = 300\ MPa$)

6 Conclusions

Infrared Thermography has been under review in the last thirty years due to its versatility and potential in the detection of the thermal signature associated with intrinsic energy phenomena due to dissipative processes, specifically those relying on mechanical fatigue.

In this work, firstly, all thermography-based approaches and procedures for rapid estimation of fatigue limit were reviewed to choose an efficient thermal index for studying the heat dissipated during fatigue. For this purpose, all proposed thermal indices were compared together in terms of their capabilities, pros and cons, in fatigue assessment. It was discussed that the harmonic parameters of the temperature signal provide a more robust method for damage assessment than the mean temperature. Thus, the second amplitude harmonic (SAH) of the temperature (T_{2w}) was chosen for the main goal of this study.

This work aims to investigate the heat dissipations during the fatigue test using both experiments and numerical models. Specifically, the intention is to identify the heat-generating volume during fatigue testing using a FEM model, and to study experimentally and numerically how loading frequency affects the fundamental temperature component associated with dissipation. The former assists in assessing the accuracy of assumptions made by prior models, which regard the entire gauge volume as the heat source. On the other hand, the latter explores the impact of the diffusion phenomena, like the effect of the loading frequency in this study, on $T_{2\omega}$, thereby aiding in thermographic measurements. Neither of these inquiries can be exclusively pursued through experimentation alone. Therefore, proposing a hybrid approach that combines a numerical model with experimental data to tackle the aforementioned challenges can be very helpful which is also the primary novelty of this study.

In experimental part of the study, a comprehensive campaign was successfully conducted to acquire the response of SS 316 and C45 samples under both static and cyclic loadings.

The results for SS 316 from stepwise tests were primarily employed for comparing five thermal indices. The strong feature of this comparison is utilizing the same and unique dataset. This comparison involved assessing the difference between the predicted fatigue limit and the value obtained from S-N curve. The comparisons were done based on two methods: the threshold method and the Loung's method. It was demonstrated that the former is highly dependent on its parameters, however, the latter one can be reliably used. From the results, T_{2w} claimed the top rank, underscoring its effectiveness in achieving the main goal of the study. In addition, one of the thermal indices, the slope of the temperature rise at the beginning of the temperature trend, was examined deeply. The analysis carried

out in this study highlights, for the first time, the critical importance of meticulous attention to detail when determining the initial slope of the temperature trend. Consequently, it is recommended to incorporate a greater number of data points and employ a cooled camera for temperature slope measurements. In cases where only an uncooled camera is available, it is advised to perform curve fitting for time durations exceeding 2 seconds, regardless of the fitting order.

On the other hand, the results for C45 were specifically employed for establishing and improving the numerical model, providing reference data (T_{2w}^{exp}) for comparison with numerical results in terms of T_{2w} maps, histograms and the average value of T_{2w} in the ROI, $T_{2w,mean}$.

In the second part of the study, the numerical models are established in COMSOL Multiphysics 5.6 to simulate the temperature distribution on the surface of the specimen.

After selecting the element type and mesh convergency, the verification of the model was mainly done by solving one dimensional heat equation with both constant and cyclic heat sources. It should be emphasized that this solution was obtained for the first time in this work. The mean and the cyclic trend of the temperature from simulation were compared with the analytical solution, showed negligible errors. In addition, another verification was done based on the experimental data and only the mean temperature value. Next, the model was prepared for heat source identification. For this aim, the model modified by introducing randomly distributed heat volumes in the gauge volume of the sample where the dissipation is highly possible to be occurred. Note that this type of heat source was inspired by the work by Munier and his co-workers. It should be noted that the numerical model is created under the assumptions of uniform size and heat amplitude for all randomly distributed unit volumes, a non-interacting behavior between units and a criterion based on the mean value of T_{2w} from the surface of sample.

The numerical results indicated that for higher loading level, the total volume producing heat is increased in size. Moreover, based on the identified total heat volumes, it was found that the dissipation occurs only in a fraction of the gauge volume, not the entire volume. This discovery addresses one of the main controversial issues in fatigue characterization. It challenges the conventional use of hysteresis loops for studying heat dissipation in fatigue because these loops are typically determined from the entire gauge length, while, according to this work, the entire gauge volume does not dissipate.

In addition, the effect of various factors such as the number of points for extracting data in the model, the distribution of heat source, the noise including thermal acquisition noise and the sample movement noise, and the unit size of each heat source was studied on the numerical T_{2w} (T_{2w}^{FEM}). The results are

summarized as follows:

- Unlike the distribution, the number of points for extracting the numerical data influences T_{2w}^{FEM}, it was suggested that they should be at least equal to the number of pixels in the experimental acquisition. It should be noted that the distribution can influence the results if $T_{2w,mean}^{FEM}$ is very small;
- The thermal acquisition noise was shown to elevate $T_{2w,mean}^{FEM}$ level;
- Any conclusion about the undeniable effect of the sample movement noise needs more investigations as more accurate experimental measurements needed;
- The unit size of randomly distributed heat volumes affected T_{2w}^{FEM}, significantly. Albeit with differences, by decreasing the unit size, the similarity between T_{2w}^{FEM} and T_{2w}^{exp}improved, in terms of both thermal maps and histograms.

It is worth noting that for better comparison, the fitted distribution function on numerical and experimental values of T_{2w} was compared together. Quantitively, their differences in mean and median were acceptable, while in standard deviation was not. Actually, the differences in thermal maps and statistical values may be attributed to various reasons:

- First, the criterion employed for identifying heat volumes was primarily relying on mean values, $T_{2w,mean}^{FEM}$ and $T_{2w,mean}^{exp}$. To eliminate the dissimilarity, it is suggested to integrate additional criteria, such as both mean and standard deviation, within an optimization framework.
- The second reason could stem from the assumptions made for creating the numerical model, in terms of the unit size and heat amplitude.
- The third reason is the minimum unit size considered in this work; computational resource limitations hindered further reduction in unit size.
- Additionally, the absence of precise input data for simulating movement noise can be another contributing reason.

Therefore, addressing these issues is crucial for refining the predictive capabilities of the proposed model.

Finally, after verifying the $T_{2w,mean}^{FEM}$ trend with the $T_{2w,mean}^{exp}$ trend for a limited number of loading frequencies, the $T_{2w,mean}^{FEM}$trend was further studied over a wide range of frequencies. It was shown that $T_{2w,mean}^{FEM}$ diminishes notably and reaches a plateau for higher loading frequencies. This phenomenon

acts as a limitation for utilizing T_{2w} in thermographic methods, presenting challenges in its measurement for fatigue characterization, especially when using traditional cooled IR-sensors.

To sum up, this work can be considered as a preliminary study to predict the heat volumes during the fatigue test and determine the differences existed in the assessment of the heat dissipations from the surface measurements and the FEM model. In future endeavors, enhancing the accuracy of data used for movement noise, such as employing Digital Image Correlation (DIC) instead of extensometers, could provide more reliable results. Consideration should also be given to remove simplifications made in the model, reducing the unit size of the heat volume to the order of grain size, enabling a closer correlation between thermal footprint and actual heat sources. Exploring variations in the magnitude and size of heat sources could offer valuable insights. Additionally, investigating other potential noise sources, including the movement of the loading frame and differences in cyclic load forms, can contribute to a more comprehensive understanding. Lastly, the establishment of a thermomechanical model is suggested as it may prove to be more beneficial for fatigue characterization in future research.

Appendix A – Discrete Fourier Transform MATLAB Code [187]

```
function [freq,Am,Ph]=ft_spect(dataIn,dt,varargin)
% --------------------------------INPUT----------------------------------
--
%
% dataIn        The 1D input signal, it can be a row or column vector.
Its
%               value must be a real number.
%
% dt            Time interval or time sampling of the dataIn. It should
be
%               a number with the second unit.
%
% varargin      Combination of OPTIONAL keywords (KeyName) and their
values
%               (value_keyName):
%               e.g. []=ft_spect(dataIn,dt,'keyName#1',value_keyName#1,
...)
%               The first argument is the keyword (it must be a string),
%               and the next argument is its value (could be a string, a
%               number, a vector, or a cell). Each keyword has a default
%               value.
%
% POSSIBLE KEYWORDS ARE:
%
%   'plot'      For defining with spectrum should be display; its value
is
%               a string and it has three options:
%               1) 'a' means only display Amplitude spectrum
%               2) 'p' means only display Phase spectrum
%               3) 'ap' means display both amplitude and phase spectra
%               e.g. [freq,Am,Ph]=ft_spect(dataIn,dt,'plot','ap')
%               Default: 'ap'
%
%   'resolution' For defining frequency resolution (?f). its value must
be
%               a number and its unit is Hz.
%               e.g. [freq,Am,Ph]=ft_spect(dataIn,dt,'resolution',0.001)
%               Default: 0.1 Hz
%
%   'threshold' For defining the threshold value for suppressing floating
%               rounding-off error noise. All amplitudes that their
absolute
%               value are less than this value become zero. Its value
must
%               be a number.
%               e.g. [freq,Am,Ph]=ft_spect(dataIn,dt,'threshold',0.1)
%               Default: 0 (means no thresholding)
%
%   'db'        Display the Amplitude spectrum in decibels. Its value
must
%               be a string and it has two options:
%               1)'y' means convert magnitude to decibels (dB)
```

```
%               2)'n' means don't convert magnitude to decibels
%               e.g. [freq,Am,Ph]=ft_spect(dataIn,dt,'db','y')
%               Default: 'n'
%
%   'deg'       Display the Phase spectrum in degree. Its value must be a
%               string and it has two options:
%               1)'y' means convert radian to degree
%               2)'n' means show phase based on radian
%               e.g. [freq,Am,Ph]=ft_spect(dataIn,dt,'deg','n')
%               Default: 'y'
%
%   'figure'    Display the spectrum in a new window. Its value must be a
%               string and it has two options:
%               1)'y' means create a new window
%               2)'n' means don't create a new window
%               e.g. [freq,Am,Ph]=ft_spect(dataIn,dt,'figure','n')
%               Default: 'y'
%
%   'color'     Definig the line color in amplitude and phase spectra.
Its
%               value must be a string between the following options:
%               'b' for blue; 'r' for red; 'g' for green; 'k' for black
%               'y' for yellow; 'm' for magenta; 'c' for cyan
%               e.g. [freq,Am,Ph]=ft_spect(dataIn,dt,'color','r')
%               Default: 'b'
%
%   'title'     Defining a title for amplitude and phase spectra. Its
value
%               must be a string.
%               e.g. [freq,Am,Ph]=ft_spect(dataIn,dt,'title','this is a
test!')
%               Default: for the amplitude spectrum->'Amplitude spectrum'
%                        for the phase spectrum->'Phase spectrum'
%
%
% -----------------------------OUTPUTS-----------------------------------
--
%
%   freq        Frequency vector
%   Amp         Amplitude vector
%   Ph          Phase vector
%% ---------------------------------DEMO--------------------------------
--
if nargin<1, ft_spect_demo; return; end
%% -------------------------SET DEFAULT VALUES--------------------------
--
varName.plot='ap';
varName.resolution=0.1;
varName.threshold=0;
varName.db='n';
varName.deg='y';
varName.figure='y';
varName.color='b';
varName.title=0;
% ------------------------CHECK OPTIONAL INPUTS-------------------------
--
```

```
for i=1:2:length(varargin)
     if isfield(varName,varargin{i}) %the first argument must be a
keyword
          varName.(varargin{i})=varargin{i+1}; % *
     else
        error([' Non-existent keyword: ' varargin{i} ])
     end
end
% * the second argument is variable value
%% ------------------------------Main Code-------------------------------
--
% Make sure dataIn alwaye be a 1D vector and convert row to column vector
if size(dataIn,1)>=2 && size(dataIn,2)>=2
    error('Input signal should be a 1D signal!')
elseif size(dataIn,1)<2
    dataIn=dataIn';
end
[m,~]=size(dataIn);
Fs =1/dt;                % Sampling frequency
% calculating bin number based on the desire resolution
binNumber=Fs/varName.resolution;
% extending dataIn for reaching to the desired resolution
super_signal=repmat(dataIn,ceil(binNumber/m),1);
%% --------------------------Fourier Transform-------------------------
--
 NFFT=length(super_signal);
 ft =(1/NFFT)*fft(super_signal);
 freq = Fs*(0:(NFFT/2))/NFFT;
 Am=abs(ft);

%% -------------------------Applying threshold-------------------------
--
if varName.threshold==0
    Ph=angle(ft);
else
    ft(Am<varName.threshold)=0;
    Ph=angle(ft);
    Am(Am<varName.threshold)=0;
end
if strcmp(varName.deg,'y')
    Ph=radtodeg(Ph);
end
%% ------------------------------Display---------------------------------
--
% ------------------------Amplitude spectrum-----------------------------
--
if strcmp(varName.plot,'ap') || strcmp(varName.plot, 'a')

    if strcmp(varName.figure,'y'); figure; end
    if strcmp(varName.db,'n')
        plot(freq,2*Am(1:NFFT/2+1),varName.color);
        ylabel('Amplitude')
    else
        plot(freq,mag2db(2*Am(1:NFFT/2+1)),color)
        ylabel('Amplitude (dB)')
    end
```

```
    xlim([-inf max(freq)])
    xlabel('Frequency (Hz)')

    if varName.title~=0
        title(varName.title)
    else
        title('Amplitude spectrum')
    end
end

% -------------------------Phase Spectrum-------------------------------
--
if (strcmp(varName.plot,'ap') || strcmp(varName.plot, 'p'))

    if (strcmp(varName.plot,'ap') || strcmp(varName.figure,'y')); figure;
end
    plot(freq,Ph(1:NFFT/2+1),varName.color)

    if varName.title~=0
        title(varName.title)
    else
        title('Phase spectrum')
    end

    xlabel('Frequency (Hz)')
    if strcmp(varName.deg,'y')
        ylabel('Angle (deg)');ylim([-180 180])
    else
        ylabel('Angle (rad)');ylim([-pi pi])
    end

end
%% ----------------------------DEMO-------------------------------------
--
    function ft_spect_demo

        clear
        clc
        % -------------------------test signal-------------------------
--
        dts=0.032;
        L = 125;
        frequency=[2 4.25 8 12.5 13.25];
        amplitude=[5.6 0.8 0.3 0.75 2.1];
        phase=[-57 30 74 50 -121];

        Fsample = 1/dts;            % Sampling frequency
        t = (0:L-1)*dts;
        s=@(i) amplitude(i)*cos(2*pi*frequency(i)*t+(phase(i)*pi/180));

        signal=0;
        for j=1:length(frequency)
            signal=signal+s(j);
        end

        % ---------------------------Regular FFT----------------------
--
        % NOTICE: Applied as the same as in the "MATLAB 2019b help"
```

```
        f = Fsample*(0:(L/2))/L;
        Y = fft(signal);
        P2 = abs(Y/L);
        P1 = P2(1:floor(L/2)+1);
        P1(2:end-1) = 2*P1(2:end-1);
        % ---------------------Amplitude spectrum-----------------------
--
        subplot(2,1,1)
        plot(frequency,amplitude,'*')
        hold on,plot(f,P1,'g');xlim([-inf max(f)])
        hold
on,ft_spect(signal,dts,'plot','a','resolution',0.001,'figure','n','color'
,'r');
        legend('Real value','Regular FFT','ft spect; resolution=0.001
Hz')

        % ----------------------Phase spectrum--------------------------
--
        subplot(2,1,2)
        plot(frequency,phase,'*')
        hold on; plot(f,radtodeg(angle(Y(1:floor(L/2)+1))),'g'); xlim([-
inf max(f)])
        hold
on,ft_spect(signal,dts,'plot','p','resolution',0.001,'figure','n','color'
,'r','threshold',0.01);
        legend('Real value','Regular FFT','ft spect; threshold
value=0.1')
    end
end
```

Appendix B – Meshing

In this section, two prevalent elements tetrahedral and brick elements were compared for meshing of the model, and then the mesh convergency is provided. For the comparison, 1/8 of a dog bone sample as shown in Figure 38, with the characteristics and geometry in Table A1 and Figure A1(a), were considered. For an arbitrary case, the heat source in the form of Eq. (20) was assumed to be imposed on the 2/3 of the gauge volume with the amplitude of $4.5 \times 10^7 (\mathrm{W/m^3})$ and $f = 11$ Hz; the ambient temperate was $20℃$, as shown in Figure A1. For all investigations, the model was run for 5 seconds and the data related to the red point in Figure A1 was studied.

Table A1 Material parameters for High carbon chromium bearing steel [114]

$\rho\left(\frac{kg}{m^3}\right)$	$C_p\left(\frac{J}{kg\,℃}\right)$	$k\left(\frac{W}{m\,℃}\right)$	$\alpha\left(\frac{1}{℃}\right)$	$h\left(\frac{W}{m^2K}\right)$	ϵ
7850	475	44.5	12.3e-6	5	0.98

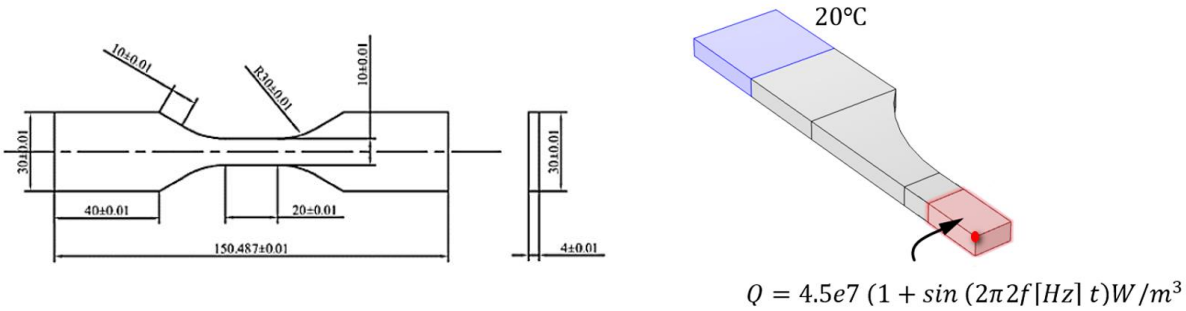

(a) (b)

Figure A1 (a) Geometry of the sample [114] (b) model for meshing

Tetrahedral elements are the default choice in COMSOL for most physics because they work well for all kinds of 3D shapes. These elements seamlessly mesh any 3D volume, irrespective of shape or topology, making them a reliable choice. On the other hand, brick elements offer an intriguing advantage by notably reducing the mesh's element count. The same degrees of freedom for one hexahedron corresponds to six Tetrahedral elements.

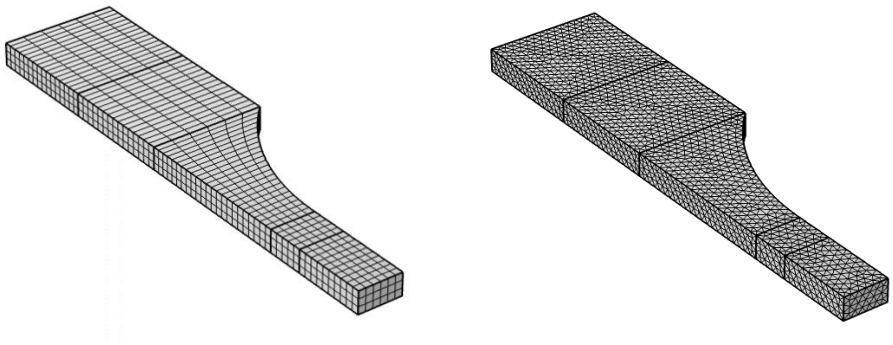

(a) (b)

Figure A1 Meshing with (a) hexahedral and (b) tetrahedral elements (mesh size=1mm)

Using a consistent mesh size of 1 mm resulted in 1242 elements for linear hexahedral elements and 32020 elements for linear tetrahedral elements. Figure A2 demonstrates a full convergence between the temperature trends of both element types. Yet, the computation time differed significantly, with 148 seconds for hexahedral and 405 seconds for tetrahedral elements. Therefore, opting for hexahedral elements is more favorable in terms of computational efficiency.

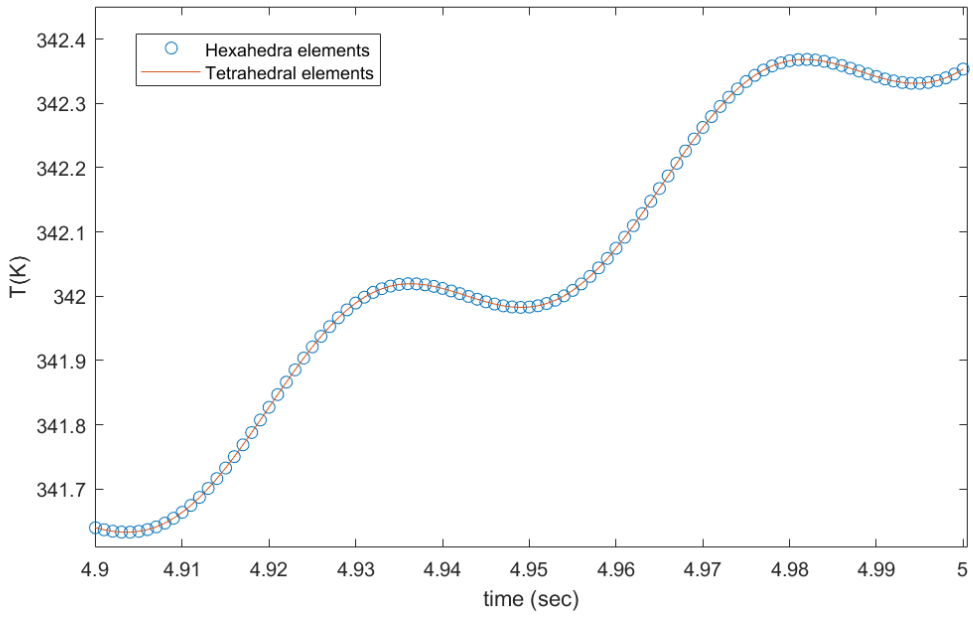

Figure A2 Results with hexahedral and tetrahedral elements

Once the element type is chosen, it is important to evaluate the mesh size. Comparing the temperature at 5 seconds across various mesh sizes using linear hexahedral elements, Table A2 and Figure A3 indicate that the temperature's responsiveness to mesh sizes below approximately 1 mm is minimal. Consequently, this mesh size range is deemed suitable for other simulations in this study. The percentage values in the table shows Difference with respect to the smaller mesh size.

Table A2 Mesh size effect (Linear hexahedral elements)

Mesh size (mm)	0.005	0.004	0.003	0.002	0.001	0.0005	0.00025
T (K)	342.8512 (0.151%)	342.5858 (0.074%)	342.465 (0.038%)	342.4211 (0.025%)	342.3533 (0.006%)	342.3467 (0.004%)	342.3338
Run time (sec)	55 (-98.49%)	58 (-98.41%)	63 (-98.27%)	80 (-97.81%)	148 (-95.94%)	544 (-85.08%)	3647
Number of elements	30	38	50	216	1242	9864	78336

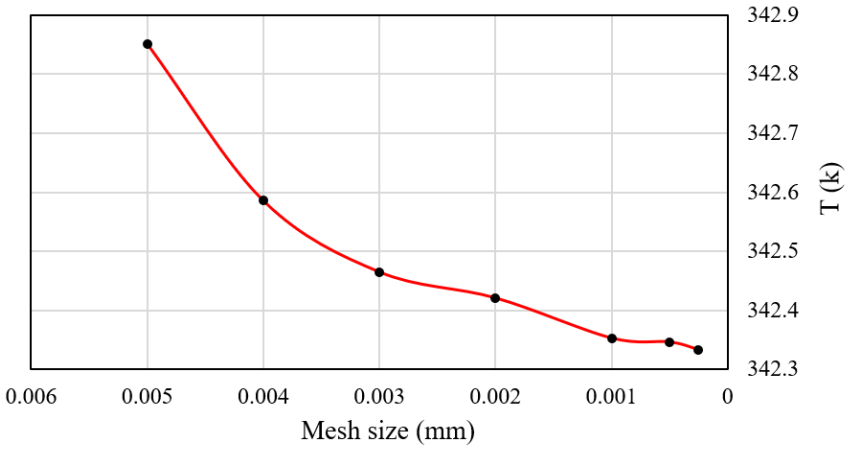

Figure A3 Mesh size effect (Linear hexahedral elements)

In addition, another key factor to be chose for an element is the order of the element. It should be noted that the linearity and higher orders, are tied to how their edges are represented, impacting the volume they cover. Linear elements interpolate edges between two points. Quadratic elements, however, employ quadratic functions for edges, requiring an extra midpoint for the function. Higher-order elements split into "Lagrangian" and "Serendipity" categories. Lagrangian ones feature interior nodes, while Serendipity elements only rely on exterior nodes for their definition. The percentage values in the table shows difference with respect to the Cubic Lagrangian element order. From Table A3, orders bigger than 2 are time consuming without providing better accuracy. Both Quadratic Lagrangian and Quadratic Serendipity elements can be good options, although the second one is more efficient in terms of run time.

Table A3 Element order effect

Element order	Linear	Quadratic Lagrangian	Quadratic Serendipity	Cubic Lagrangian
T (k)	342.3533 (0.005%)	342.3327 (-0.001%)	342.3316 (-0.001%)	342.3355 -
Run time (sec)	148	662	506	3480
	(-0.96%)	(-0.81%)	(-0.85%)	-

Appendix C – Additional verification of the numerical model

In this section, the model is verified further by comparing with the results proposed in the work by Zhao et al. [114], where the constant heat power d_1 in Eq. (3) was found experimentally from the surface temperature.

The numerical simulations were performed for three constant d_1 including 2.13×10^5, 3.95×10^5 and 9.65×10^5 (W/m^3) [114], related to different stress amplitudes and the stress ratio of $R = -1$. For a sample of high carbon chromium bearing steel, the material properties and geometry are shown in Table B1 and Figure B1a, respectively. In Figure B1b, mesh and boundary conditions are proposed. The model is meshed with 750 hexahedral elements (with quadratic Lagrange discretization including 27 nodes for each element) after mesh convergence check (as shown in Figure B1b).

Table B1 Material parameters for High carbon chromium bearing steel [114]

$\rho\left(\frac{kg}{m^3}\right)$	$C_p\left(\frac{J}{kg\,℃}\right)$	$k\left(\frac{W}{m\,℃}\right)$	$\alpha\left(\frac{1}{℃}\right)$	$h\left(\frac{W}{m^2K}\right)$	ϵ
7820	546	38.2	13.3	25	0.98

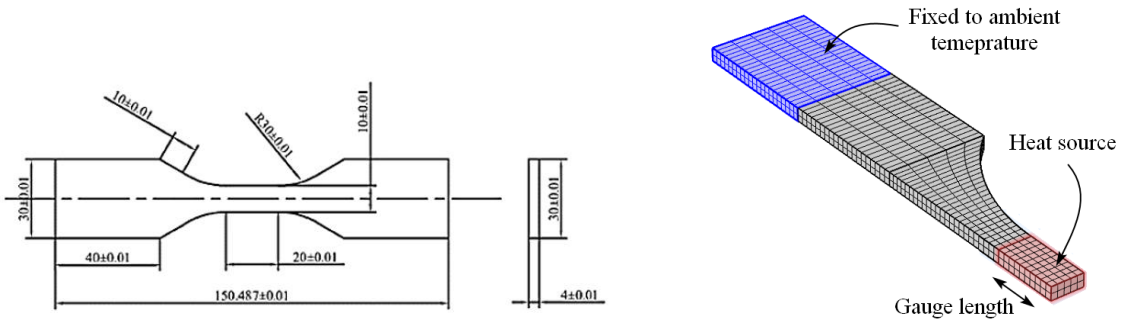

(a) (b)

Figure B1 (a) sample geometry (in mm) [114] and (b) meshing of 1/8 of the model for high carbon chromium steel [114]

As shown in Figure B2, comparisons are performed in terms of the mean temperature of a point located on the top surface of the gauge volume (the red point in Figure B1b) from the beginning to the stabilization phase of the temperature; and in terms of the temperature variation as shown in Figure B3 along the longitudinal direction “y” in Figure 38.

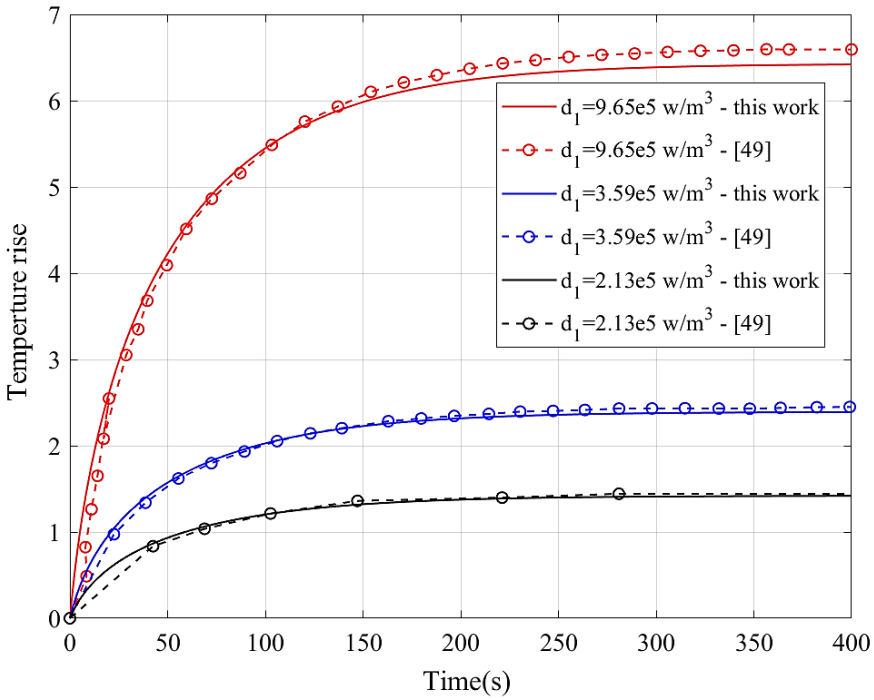

Figure B2 The temperature trend comparison from the beginning to the stabilization phase, for a point located on the top surface of the gauge volume

In Figure B2, for all heat dissipation values of d_1 and after around 300 seconds, the temperature reaches a steady state of heat exchange with the surroundings, as indicated by a plateau in the temperature curve, which is provided by considering radiation and convection in the model. Furthermore, it can be seen from Table B2 that the numerical results are almost overlapped with the experimental ones in terms of stabilized temperature, in which the errors with respect to the experimental value are below 3% for all considered d_1.

Table B2 Comparison of mean temperature for constant and cyclic heat sources

Heat source d_1 (W/m^3)	Mean temperature (℃)		Error with respect to the experimental value (%)
	Experimental [114]	Numerical (present work)	
2.13×10^5	1.441	1.418	1.60
3.59×10^5	2.449	2.393	2.29
9.65×10^5	6.593	6.414	2.71

Moreover, similar to the experimental curve for $d_1 = 9.65 \times 10^5$ (W/m^3), the results demonstrate the highest temperature at the center of the gauge volume (y=0), as shown in Figure B3. Note that the temperature gradient is most noticeable in the gauge length direction, particularly in the middle of the gauge section.

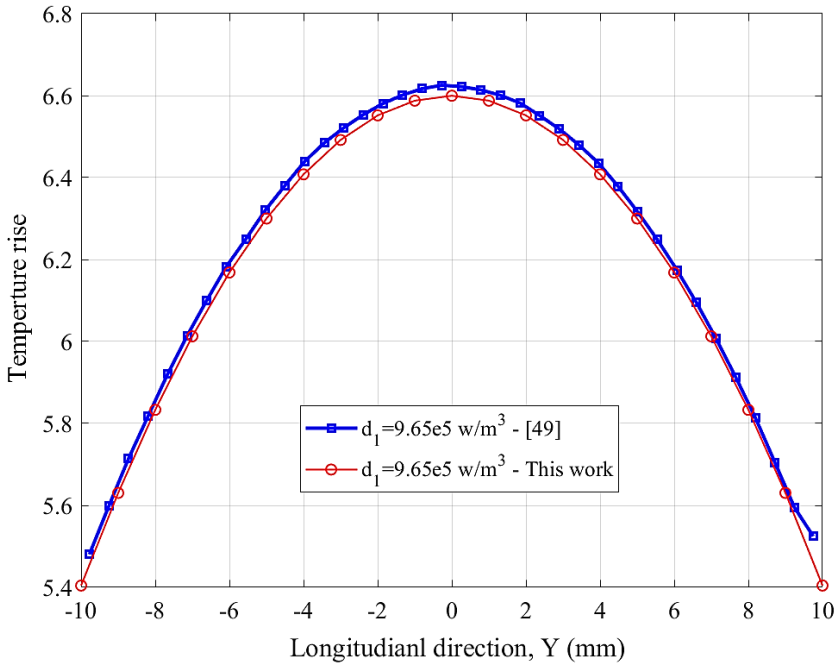

Figure B3 The temperature comparison along the longitudinal direction “y”

From the results, it can be said that the numerical model shows an accurate performance in terms of mean temperature for a constant heat source found experimentally.

Appendix D – Movement noise due to the deformation of the sample

Due to the deformation of the sample during the cyclic load, the points on the material coordinates begins movement, however, they are fixed in the numerical model because the focus was solely on thermal analysis. In this appendix, a method is proposed to include this movement in the numerical output.

A schematic representation is shown in Figure C1. Each pixel of an image acquired from a thermal camera shows the mean temperature of some sub-pixels (the red circle in the figure) surrounded by the pixel. For example, in Figure C1, a single pixel which is shown with a black rectangular, surrounds four sub-pixels. In the numerical simulation, these sub-pixels are defined by points on the surface of the sample, in the same ROI as in experiment.

Like pixels, ROI or the red border in the figure, is fixed in the space both in the experiment and the simulation. In the simulation, ROI includes a grid of points with a fixed distance to each other. While, in the experiment, ROI contains many sub-pixels. Under enough loading level in the experiment, the gauge length which is presented with the black border, undergoes either expansion or contraction, and its size changes frame by frame. Consequently, the distance between sub-pixels changes due to the deformation.

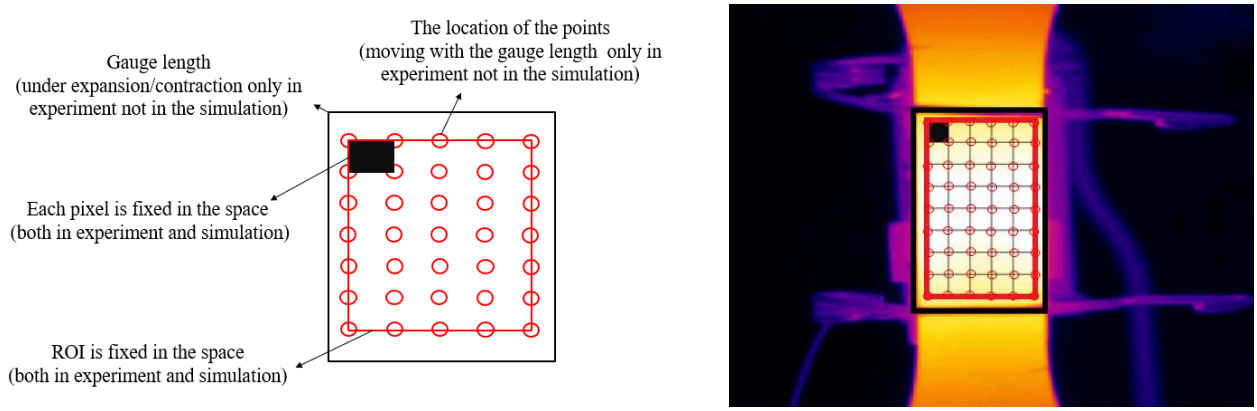

Figure C1 A schematic representation of an image acquired from a thermal camera

During the deformation, the sub-pixels move and locate new positions (yellow circles in the Figure C2). When the displacement of sub-pixels reaches a significant magnitude, they may exit the pixel they previously enclosed, and enter to another one. Sometimes, sub-pixels of a certain pixel might be replaced by new ones from another adjacent pixel. Additionally, it is highly possible that they leave the ROI (in tension when the elongation of the sample is notable) or occupy only a fraction of the ROI (in compression when the sample is contracted). In such a situation, the average temperature of a pixel

can is influenced by these movements. Therefore, the aim is to add the movement to the fixed points in the numerical model.

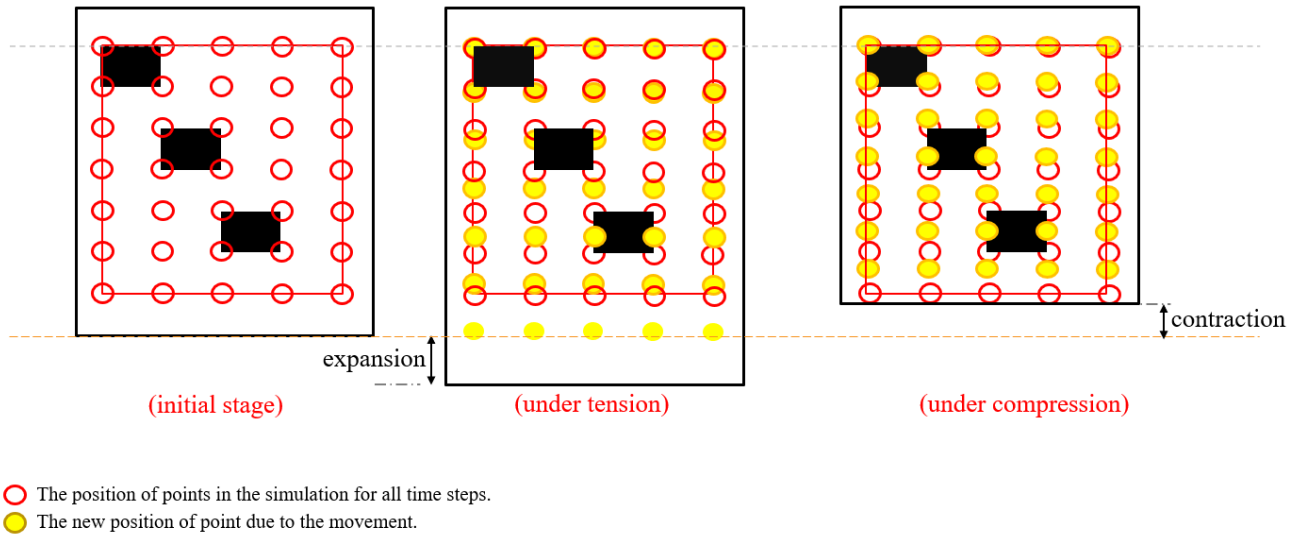

Figure C2 A schematic representation of ROI in tension and compression of the gauge length (in experiment)

Neglecting the deformation in the lateral direction of the gauge length as it is very small, there are two possible methods to quantify the movement of points frame by frame, and impose it on the numerical model:

1- The first one is utilizing thermal images and measuring the expansion and contraction with edge detection function either by IRTA® or MATLAB. In the context of an image, an edge refers to a curve that traces the route of abrupt changes in image intensity, commonly corresponding to object boundaries within a scene. The process of edge detection aims to pinpoint these edges within an image. In order to detect edges of an image, the edge function can be employed. This function seeks locations in the image where intensity undergoes rapid changes, employing one of the following criteria:
   a. points where the magnitude of the first derivative of intensity surpasses a specified threshold,
   b. locations where the second derivative of intensity exhibits a zero crossing [191].
2- The second solution can be reading the strains from the extensometer and finding the contraction or expansion of the gauge length by multiplying the gauge length by the strains.

The big issue with the first one is its dependency on the size of the pixel (pixel ratio = length/number of pixel) in the thermal acquisition. This method does not work if the size of pixel is not small enough, which is the case in this study that led to use the second method. From extensometer, the maximum

and minimum elongations of the gauge length can be found for each cycle when the hysteresis loops are stabilized.

After finding the elongation, it is mandatory to define a relationship between the displacement of points and their distance from the relatively fixed side of the gauge length. From the theory of elasticity [192] and Figure C3, by ignoring the displacement in y direction and the displacement between the fixed gripper and A, the stress filed in the gauge length can be estimated with a two-dimensional plane stress case of a rectangular beam.

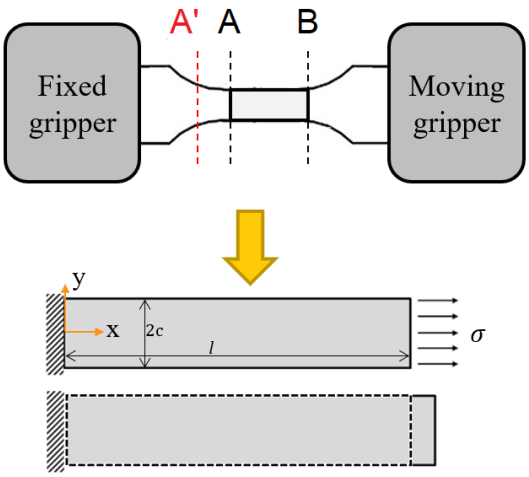

Figure C3 Boundary condition of gauge length

Thus, the boundary condition on this case can be written as follows:

$$\sigma_x(l, y) = T, \sigma_y(x, \pm c) = 0$$

$$\tau_{xy}(x, \pm c) = 0$$

where T is the traction force imposed on the sample through moving gripper at B, σ_x is the stress due to the T, τ_{xy} is the shear stress. From the Hook's law and strain-displacement relations [192]:

$$\frac{\partial u}{\partial x} = \varepsilon_x = \frac{1}{E}(\sigma_x - v\sigma_y) = \frac{T}{E}$$

where e_x is strain, v is possion's ratio and E is the module of elasticity of the material. By integration and neglecting the rigid body terms, the displacement in x direction is as follow:

$$u = \frac{T}{E}x$$

It is obvious that the displacement is a linear function of x between the left and right side of the gauge

length. It should be mention that it is not needed to calculate T and E in this study, instead u can be identified directly from extensometer, frame by frame in each cycle of the load.

To make the displacement behavior of the gauge length more realistic, instead of setting the zero displacement exactly at A (the side of gauge length close to fixed gripper) in Figure C3, it is advisable to position it slightly farther, for example at A' in Figure C3. In this way, the movement of both sides of the gauge length (A and B) is considered, making the assumption of zero displacement more realistic, as A' is closer to the fixed gripper than the A.

After simulating the displacement of the points frame by frame for a load cycle, the new positions of the points in the numerical model are estimated. By utilizing the new positions (corresponding to the yellow circles in Figure C2) as well as the old position (the red circles in Figure C2) and the corresponding temperatures of points in the old position, the temperatures of points in the new positions can be found through the extrapolation and interpolation functions. This can be done in MATLAB, specifically, with “interp2” function. This function benefits from different strategies for interpolating/extrapolating, however, the “spline” was used in this study as it provides both interpolation and extrapolation, simultaneously [191]. About the selected strategy, it needs four points in every dimension. The value at a given query point is determined through cubic interpolation, utilizing the values at adjacent grid points in each dimension. This interpolation relies on a cubic spline with "not-a-knot end conditions". More information and specifics can be found in reference [191].

Appendix E – Thermal maps for SS 316 (sample 2 & 3, stepwise test)

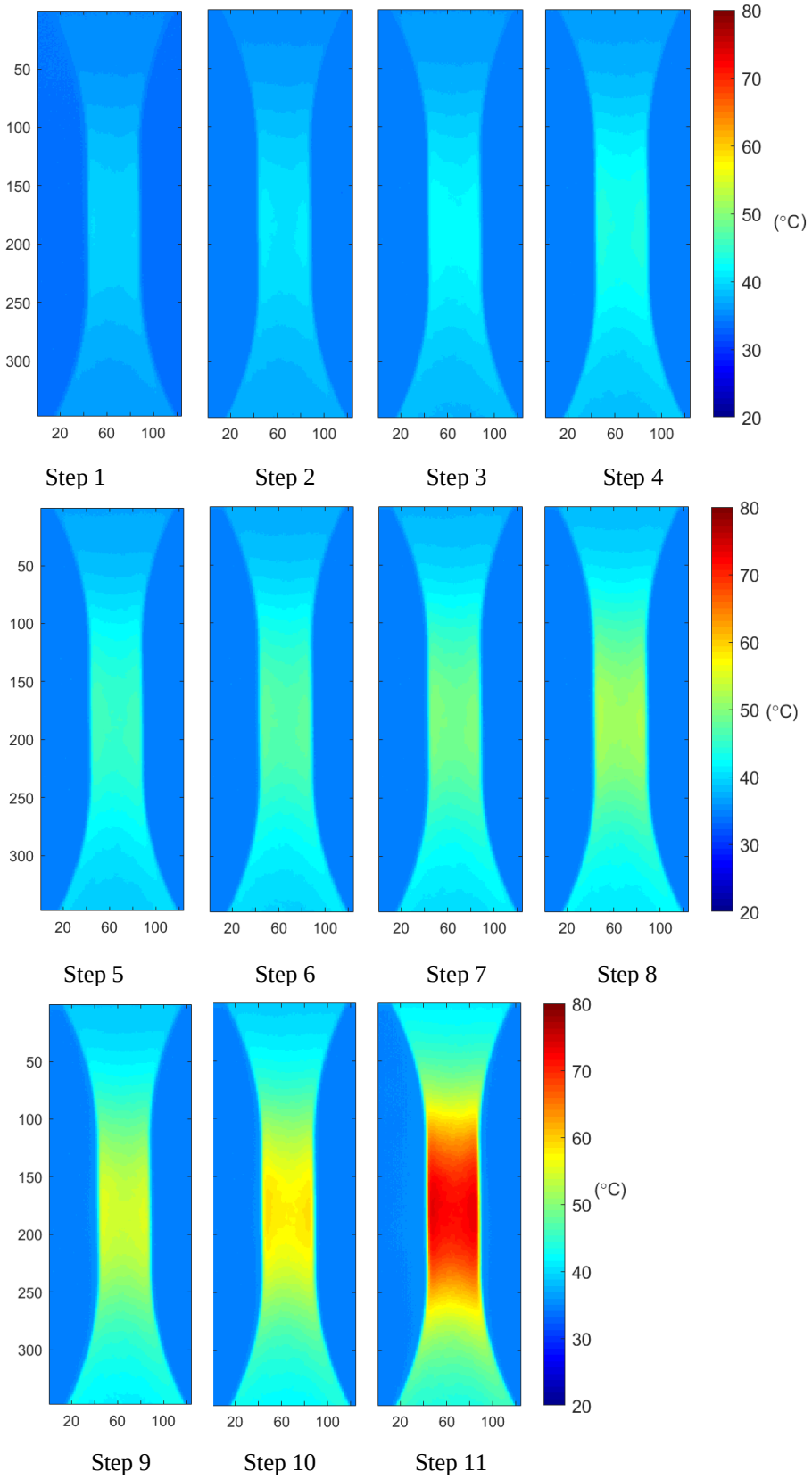

Figure E1 Thermal footprint on the surface of the SS 316 sample for each loading step during stepwise test – sample 1

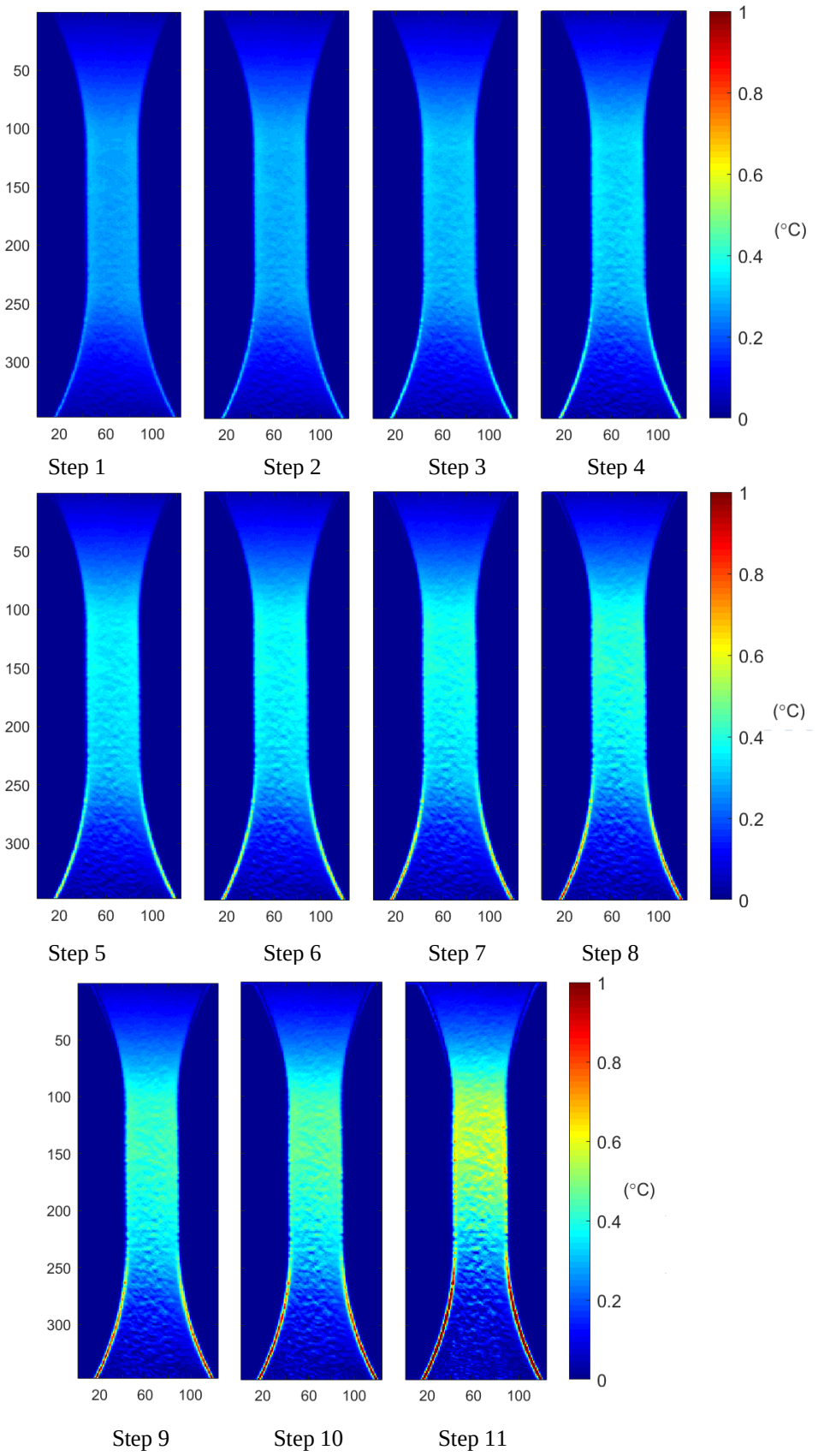

Figure E2 T_{1w} on the surface of the SS 316 sample for each loading step during stepwise test – sample 1

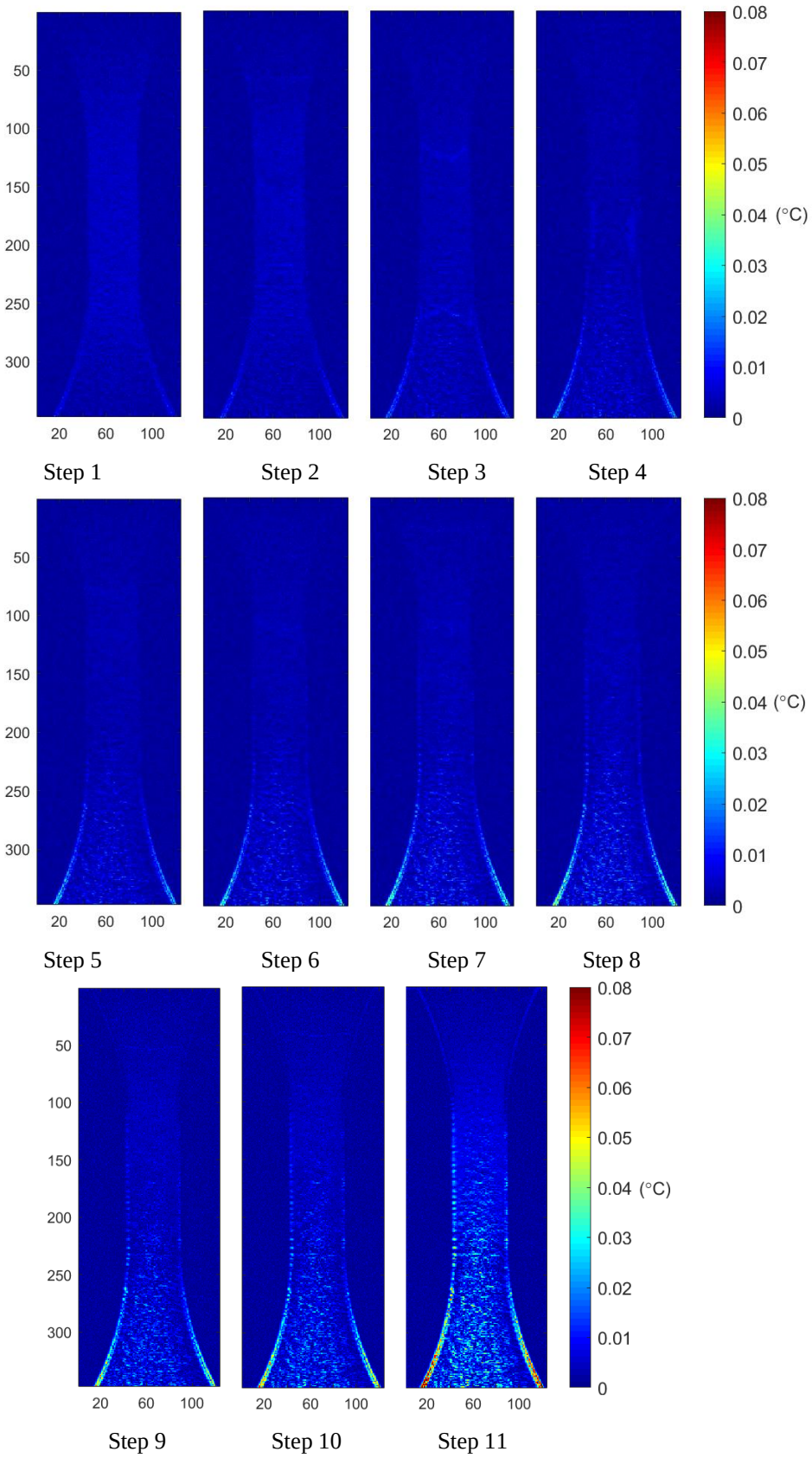

Figure E3 T_{2w} on the surface of the SS 316 sample for each loading step during stepwise test – sample 1

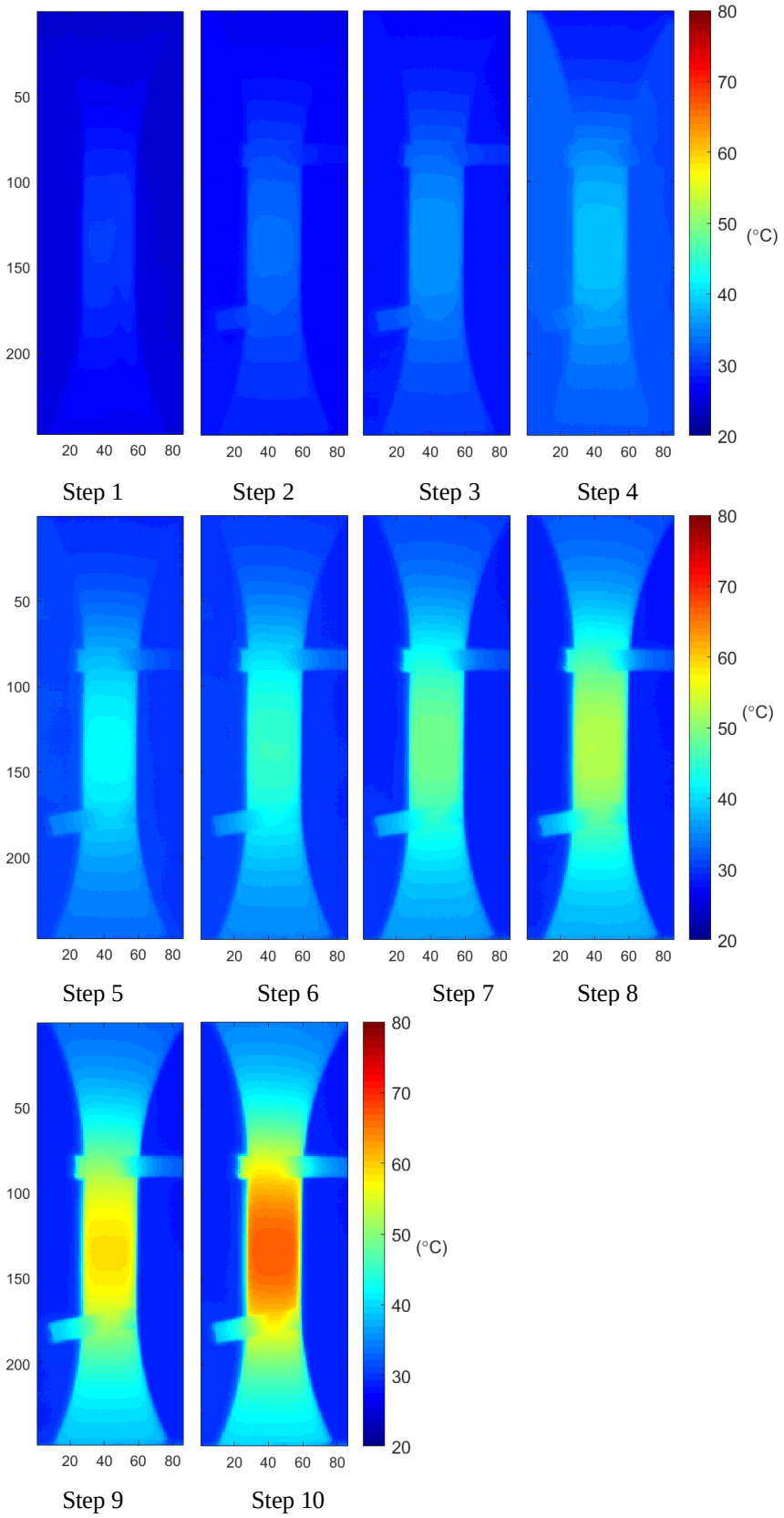

Figure E4 Thermal footprint on the surface of the SS 316 sample for each loading step during stepwise test – sample 2

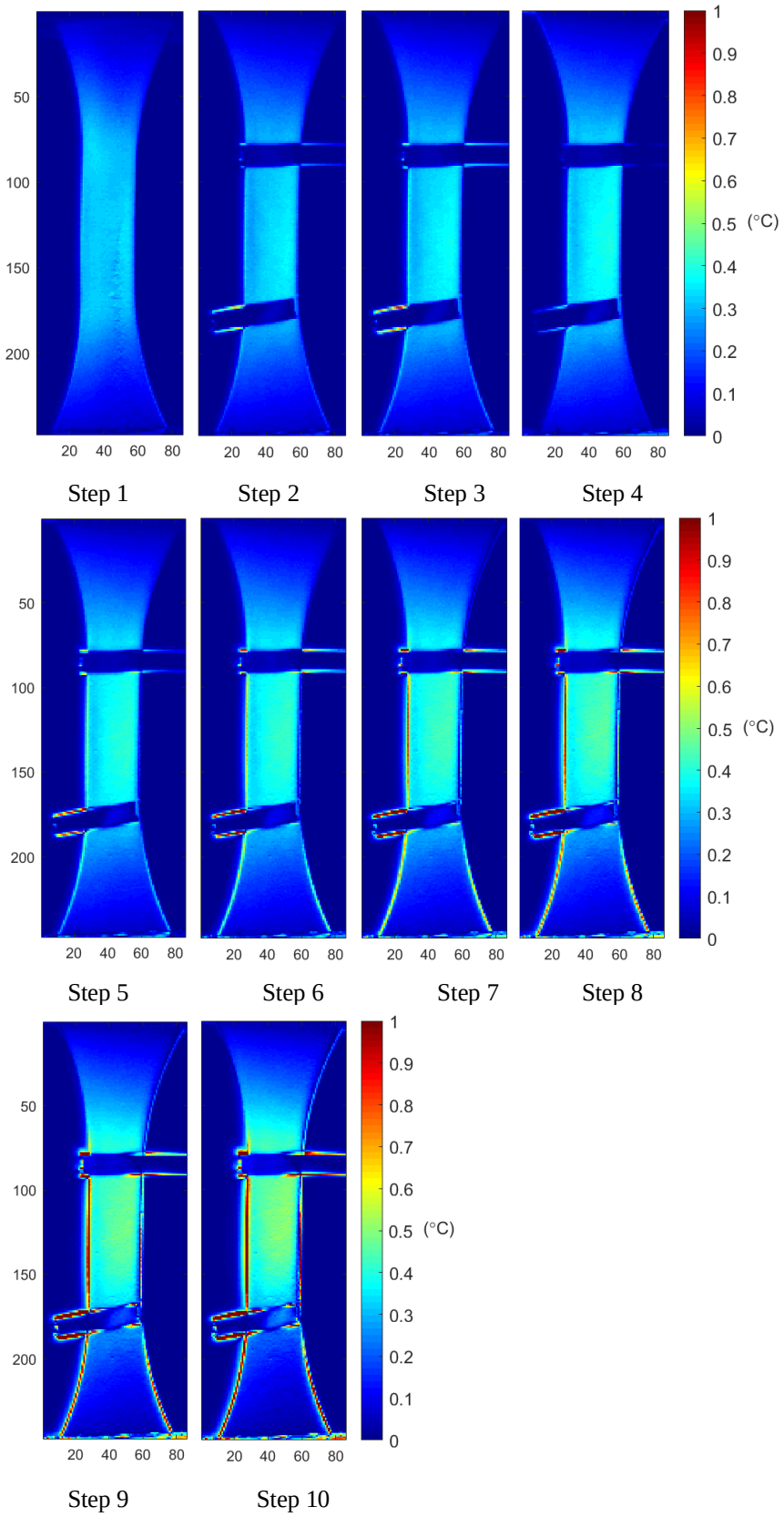

Figure E5 T_{1w} on the surface of the SS 316 sample for each loading step during stepwise test – sample 2

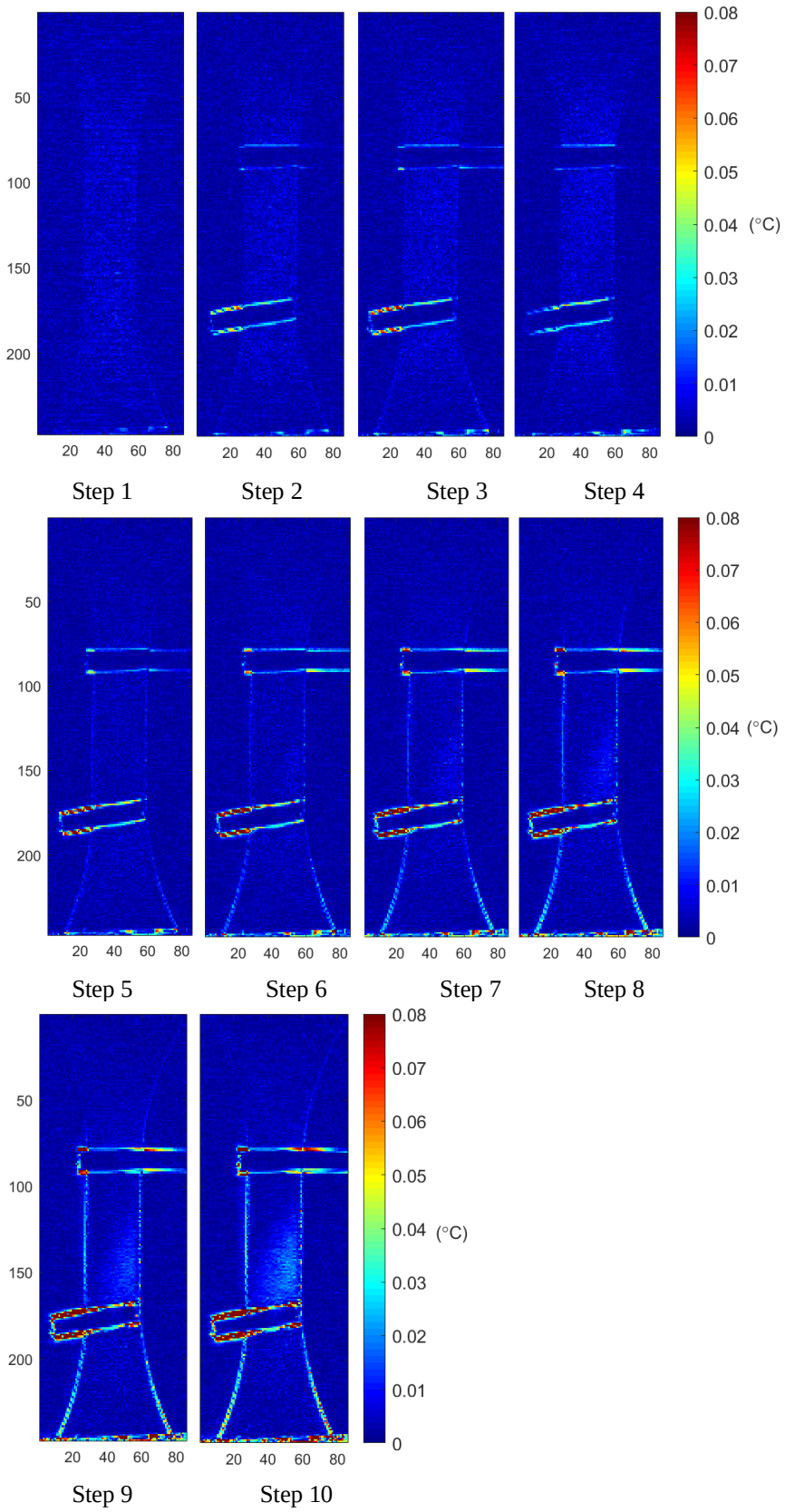

Figure E6 T_{2w} on the surface of the SS 316 sample for each loading step during stepwise test – sample 2

References

[1] S. Suresh, Fatigue of materials, Cambridge solid state science series, 1992.
[2] F. Bjørheim, S.C. Siriwardane, D. Pavlou, A review of fatigue damage detection and measurement techniques, International Journal of Fatigue, 154 (2022) 106556.
[3] R. PIPPAN, C. ZELGER, E. GACH, C. BICHLER, H. WEINHANDL, On the mechanism of fatigue crack propagation in ductile metallic materials, Fatigue & Fracture of Engineering Materials & Structures, 34 (2011) 1-16.
[4] G. Antaki, R. Gilada, Chapter 2 - Design Basis Loads and Qualification, in: G. Antaki, R. Gilada (Eds.) Nuclear Power Plant Safety and Mechanical Integrity, Butterworth-Heinemann, Boston, 2015, pp. 27-102.
[5] J. Schijve, Fatigue of Structures and Materials Springer Dordrecht, 2009.
[6] P.K. Liaw, W.A. Logsdon, J.A. Begley, Fatigue crack growth behavior of pressure vessel steels and submerged arc weldments in a high-temperature pressurized water environment, Metallurgical Transactions A, 20 (1989) 2069-2085.
[7] P.K. Liaw, W.A. Logsdon, The Influence of Load Ratio and Temperature on the Near-Threshold Fatigue Crack Growth Rate Properties of Pressure Vessel Steels, Journal of Engineering Materials and Technology, 107 (1985) 26-33.
[8] A.A. Moss, H.I. Goldberg, Computed tomography, ultrasound, and X-ray : an integrated approach, 1980.
[9] B.C. Larson, W. Yang, G.E. Ice, J.D. Budai, J.Z. Tischler, Three-dimensional X-ray structural microscopy with submicrometre resolution, Nature, 415 (2002) 887-890.
[10] Y.-D. Wang, H. Tian, A.D. Stoica, X.-L. Wang, P.K. Liaw, J.W. Richardson, The development of grain-orientation-dependent residual stressess in a cyclically deformed alloy, Nature Materials, 2 (2003) 101-106.
[11] S. Bagavathiappan, B.B. Lahiri, T. Saravanan, J. Philip, T. Jayakumar, Infrared thermography for condition monitoring – A review, Infrared Physics & Technology, 60 (2013) 35-55.
[12] G. Pitarresi, E.A. Patterson, A review of the general theory of thermoelastic stress analysis, The Journal of Strain Analysis for Engineering Design, 38 (2003) 405-417.
[13] G. Meneghetti, M. Ricotta, Estimating the intrinsic dissipation using the second harmonic of the temperature signal in tension-compression fatigue: Part I. Theory, Fatigue & Fracture of Engineering Materials & Structures, 44 (2021) 2168-2185.
[14] G. Meneghetti, M. Ricotta, Estimating the intrinsic dissipation using the second harmonic of the temperature signal in tension-compression fatigue. Part II: Experiments, Fatigue & Fracture of Engineering Materials & Structures, 44 (2021) 2153-2167.
[15] M. Ricotta, G. Meneghetti, Estimating the intrinsic dissipation using the second-harmonic temperature signal in the tension–tension fatigue, Fatigue & Fracture of Engineering Materials & Structures, 46 (2023) 4218-4238.
[16] S.M. Shepard, Advances in pulsed thermography, in: Advances in Pulsed Thermography. Proc. SPIE - The International Society for Optical Engineering, Thermosense XXVIII, Orlando, Florida, 2001.
[17] N. Rajic, Principal component thermography, Airframes and Engines Division Aeronautical and Maritime Research Laboratory, DSTO-TR-1298, (2002).
[18] C. Ibarra-Castanedo, N.P. Avdelidis, X.P. Maldague, Quantitative pulsed phase thermography applied to steel plates, in: Thermosense XXVII, International Society for Optics and Photonics, 2005.
[19] D.L. Balageas, J.-M. Roche, F.-H. Leroy, W.-M. Liu, A.M. Gorbach, The thermographic signal reconstruction method: A powerful tool for the enhancement of transient thermographic images, Biocybernetics and Biomedical Engineering, 35 (2015) 1-9.
[20] S.L. Angioni, F. Ciampa, F. Pinto, G. Scarselli, D.P. Almond, M. Meo, An analytical model for

defect depth estimation using pulsed thermography, Experimental Mechanics, 56 (2016) 1111-1122.
[21] E. D'Accardi, D. Palumbo, U. Galietti, Experimental procedure to assess depth and size of defects with pulsed thermography, Journal of Nondestructive Evaluation, 41 (2022) 41.
[22] G. Pitarresi, R. Cappello, A. Capraro, V. Pinto, D. Badagliacco, A. Valenza, Frequency modulated thermography-NDT of polymer composites by means of human-controlled heat modulation, in: P. Rizzo, A. Milazzo (Eds.) European Workshop on Structural Health Monitoring, Springer International Publishing, Cham, 2023, pp. 610-618.
[23] E. D'Accardi, R. Krankenhagen, A. Ulbricht, M. Pelkner, R. Pohl, D. Palumbo, U. Galietti, Capability to detect and localize typical defects of laser powder bed fusion (L-PBF) process: an experimental investigation with different non-destructive techniques, Progress in Additive Manufacturing, 7 (2022) 1239-1256.
[24] G. Dell'Avvocato, D. Gohlke, D. Palumbo, R. Krankenhagen, U. Galietti, Quantitative evaluation of the welded area in resistance projection welded (RPW) thin joints by pulsed laser thermography, SPIE, 2022.
[25] N. Montinaro, D. Cerniglia, G. Pitarresi, Evaluation of vertical fatigue cracks by means of flying laser thermography, Journal of Nondestructive Evaluation, 38 (2019) 48.
[26] I. Jiménez-Fortunato, D.J. Bull, O.T. Thomsen, J.M. Dulieu-Barton, Quantitative microbolometer-based thermoelastic stress analysis, Optics and Lasers in Engineering, 160 (2023) 107276.
[27] J. Dulieu-Barton, Thermoelastic stress analysis, Optical Methods For Solid Mechanics, John Wiley & Sons, (2012) 345-366.
[28] N. Harwood, W.M. Cummings, Thermoelastic stress analysis, Adam Hilger, Bristol, UK, 1991.
[29] D. Palumbo, R. De Finis, U. Galietti, Thermoelastic stress analysis as a method for the quantitative non-destructive evaluation of bonded CFRP T-joints, NDT & E International, 124 (2021) 102526.
[30] W.J. Wang, J.M. Dulieu-Barton, Q. Li, Assessment of non-adiabatic behaviour in thermoelastic stress analysis of small scale components, Experimental Mechanics, 50 (2010) 449-461.
[31] P. Stanley, Beginnings and early development of thermoelastic stress analysis, Strain, 44 (2008) 285-297.
[32] C.E. Feltner, J.D. Morrow, Microplastic strain hysteresis energy as a criterion for fatigue fracture, Journal of Basic Engineering, 83 (1961) 15-22.
[33] A. Chrysochoos, H. Louche, An infrared image processing to analyse the calorific effects accompanying strain localisation, International Journal of Engineering Science, 38 (2000) 1759-1788.
[34] P. Foti, D. Santonocito, P. Ferro, G. Risitano, F. Berto, Determination of fatigue limit by static thermographic method and classic thermographic method on notched specimens, Procedia Structural Integrity, 26 (2020) 166-174.
[35] M. Amiri, M.M. Khonsari, Nondestructive estimation of remaining fatigue life: thermography technique, Journal of Failure Analysis and Prevention, 12 (2012) 683-688.
[36] M.P. Luong, Infrared thermographic scanning of fatigue in metals, Nuclear Engineering and Design, 158 (1995) 363-376.
[37] G. La Rosa, A. Risitano, Thermographic methodology for rapid determination of the fatigue limit of materials and mechanical components, International Journal of Fatigue, 22 (2000) 65-73.
[38] A. Geraci, G.L. Rosa, A. Risitano, L'infrarosso termico nelle applicazioni meccaniche. CRES Symp, in: CRES Symposium, ATA Ingegneria Automotoristica Catania, Italy, 1983.
[39] T. Catalbiano, A. Geraci, M. Orlando, Analisi tramite infrarosso termico di provini sollecitati a fatica, Il progettista industriale, (1984).
[40] R. De Finis, D. Palumbo, F. Ancona, U. Galietti, Fatigue limit evaluation of various martensitic stainless steels with new robust thermographic data analysis, International Journal of Fatigue, 74 (2015) 88-96.
[41] R. De Finis, D. Palumbo, U. Galietti, A multianalysis thermography-based approach for fatigue and damage investigations of ASTM A182 F6NM steel at two stress ratios, Fatigue & Fracture of

Engineering Materials & Structures, 42 (2019) 267-283.
[42] G.L. Rosa, A. Risitano, Application of a new methodology to determine the fatigue limit using thermal infrared techniques, in: 17th Symposium on Experimental Mechanics, Warsaw, Poland, 1996, pp. 498–503.
[43] M.P. Luong, Infrared thermography of fatigue in metals, SPIE, 1992.
[44] A. Geraci, G.L. Rosa, A. Risitano, Influence of frequency and cumulative damage on the determination of fatigue limit of materials using the thermal infrared methodology, in: 15th Symposium on Experimental Mechanics of Solids, Warsaw, Poland, 1992, pp. 63–65a.
[45] J.C. Krapez, D. Pacou, G. Gardette, Lock-in thermography and fatigue limit of metals, in: 2000 Quantitative InfraRed Thermography, 2000.
[46] P. Bremont, P.D. Potet, Démodulation synchrone des images thermiques. Application à l'analyse expérimentale des structures, Journée de la Société Française des Thermiciens, Thermographie Quantitative, (1994).
[47] D. Shiozawa, T. Inagawa, T. Washio, T. Sakagami, Fatigue limit estimation of stainless steels with new dissipated energy data analysis, Procedia Structural Integrity, 2 (2016) 2091-2096.
[48] T. Boulanger, A. Chrysochoos, C. Mabru, A. Galtier, Calorimetric analysis of dissipative and thermoelastic effects associated with the fatigue behavior of steels, International Journal of Fatigue, 26 (2004) 221-229.
[49] D. Rigon, F. Berto, G. Meneghetti, Estimating the multiaxial fatigue behaviour of C45 steel specimens by using the energy dissipation, International Journal of Fatigue, 151 (2021) 106381.
[50] R. Munier, C. Doudard, S. Calloch, B. Weber, Determination of high cycle fatigue properties of a wide range of steel sheet grades from self-heating measurements, International Journal of Fatigue, 63 (2014) 46-61.
[51] J. Gough, A description of a property of Caoutchouc, or India rubber; with some reflections on the cause of the elasticity of this substance, Memoirs of the Literary and Philosophical Society of Manchester, 1 (1805) 288–295.
[52] N. Ranc, D. Wagner, P.C. Paris, Study of thermal effects associated with crack propagation during very high cycle fatigue tests, Acta Materialia, 56 (2008) 4012-4021.
[53] O.A. Plekhov, O.B. Naimark, Theoretical and experimental study of energy dissipation in the course of strain localization in iron, Journal of Applied Mechanics and Technical Physics, 50 (2009) 127-136.
[54] F. Curà, G. Curti, R. Sesana, A new iteration method for the thermographic determination of fatigue limit in steels, International Journal of Fatigue, 27 (2005) 453-459.
[55] C. Colombo, L. Vergani, Thermographic applications for the rapid estimation of fatigue limit, Procedia Structural Integrity, 24 (2019) 658-666.
[56] M. Amiri, M.M. Khonsari, Life prediction of metals undergoing fatigue load based on temperature evolution, Materials Science and Engineering: A, 527 (2010) 1555-1559.
[57] M. Amiri, M.M. Khonsari, Rapid determination of fatigue failure based on temperature evolution: Fully reversed bending load, International Journal of Fatigue, 32 (2010) 382-389.
[58] G. Meneghetti, Analysis of the fatigue strength of a stainless steel based on the energy dissipation, International Journal of Fatigue, 29 (2007) 81-94.
[59] N.F. Enke, B.I. Sandor, Cyclic plasticity analysis by differential infrared thermography, in: In Proceedings of the VII International Congress on Experimental Mechanics, Cincinnati, OH, USA, 1988, pp. 830–835.
[60] J.-C. Krapez, D. Pacou, C. Bertin, Application of lock-in thermography to rapid evaluation of fatigue limit in metals, Workshop on Advanced Infrared Technology and Applications, (1999).
[61] G. Pitarresi, R. Cappello, Evaluation of crack-closure by second harmonic thermoelastic stress analysis, International Journal of Fatigue, 164 (2022) 107116.
[62] D. Palumbo, U. Galietti, Thermoelastic Phase Analysis (TPA): a new method for fatigue behaviour analysis of steels, Fatigue & Fracture of Engineering Materials & Structures, 40 (2017) 523-

534.
[63] R. De Finis, Application of thermal methods based on infrared thermography for the mechanical characterisation of materials, in: Polytechnic University of Bari, Bari, Italy, 2017.
[64] M. Mehdizadeh, M.M. Khonsari, On the application of fracture fatigue entropy to variable frequency and loading amplitude, Theoretical and Applied Fracture Mechanics, 98 (2018) 30-37.
[65] G. Gaussorgues, Infra-red Thermography, Springer, 1994.
[66] C. Meola, G.M. Carlomagno, A. Squillace, G. Giorleo, The use of infrared thermography for nondestructive evaluation of joints, Infrared Physics & Technology, 46 (2004) 93-99.
[67] X.P.V. Maldaque, Infrared Methodology and Technology, Nondestructive Testing Monographs and Tracts, Gordon and Breach Science Publishers, 1994.
[68] P. Stanley, W.K. Chan, Quantitative stress analysis by means of the thermoelastic effect, The Journal of Strain Analysis for Engineering Design, 20 (1985) 129-137.
[69] S. Offermann, J.L. Beaudoin, C. Bissieux, H. Frick, Thermoelastic stress analysis under nonadiabatic conditions, Experimental Mechanics, 37 (1997) 409-413.
[70] R.A. Tomlinson, A.D. Nurse, E.A. Patterson, ON DETERMINING STRESS INTENSITY FACTORS FOR MIXED MODE CRACKS FROM THERMOELASTIC DATA, Fatigue & Fracture of Engineering Materials & Structures, 20 (1997) 217-226.
[71] P.R. Guduru, A.T. Zehnder, A.J. Rosakis, G. Ravichandran, Dynamic full field measurements of crack tip temperatures, Engineering Fracture Mechanics, 68 (2001) 1535-1556.
[72] J.A. Charles, F.J. Appl, J.E. Francis, Using the scanning infrared camera in experimental fatigue studies, Experimental Mechanics, 15 (1975) 133-138.
[73] M. Naderi, M. Amiri, M.M. Khonsari, On the thermodynamic entropy of fatigue fracture, Proceedings of the Royal Society A: Mathematical, Physical and Engineering Sciences, 466 (2010) 423-438.
[74] J.M. Dulieu-Barton, P. Stanley, Applications of thermoelastic stress analysis to composite materials, Strain, 35 (1999) 41-48.
[75] F.A. Díaz, E.A. Patterson, J.R. Yates, Application of thermoelastic stress analysis for the experimental evaluation of the effective stress intensity factor, Frattura ed Integrità Strutturale, 7 (2013) Pages 109-116.
[76] O. Breitenstein, C. Schmidt, F. Altmann, D. Karg, Thermal Failure Analysis by IR Lock-in Thermography, in: 6th (Ed.) Microelectronics Failure Analysis Desk Reference, ASM International, 2011.
[77] B.B. Lahiri, S. Bagavathiappan, T. Jayakumar, J. Philip, Medical applications of infrared thermography: A review, Infrared Physics & Technology, 55 (2012) 221-235.
[78] W. Thomson, On the Dynamical Theory of Heat, with numerical results deduced from Mr Joule's Equivalent of a Thermal Unit, and M. Regnault's Observations on Steam, Earth and Environmental Science Transactions of The Royal Society of Edinburgh, 20 (2013) 261-288.
[79] W. Thomson, On the thermoelastic, thermomagnetic, and pyroelectric properties of matter, Philosophical Magazine Series 1, 5 4-27.
[80] B.M. A., Thermoelasticity and Irreversible Thermodynamics, Journal of Applied Physics, (1956).
[81] J.D. Marrow, Cyclic plastic strain energy and fatigue of metals, STM STP 378, (1995) 45-84.
[82] R.V. M., n analysis of low cycle fatigue based on hysteresis energy, Fatigue & Fracture of Engineering Materials & Structures, 3 (1980) 75-84.
[83] V. Kliman, M. Bílý, Hysteresis energy of cyclic loading, Materials Science and Engineering, 68 (1984) 11-18.
[84] H. Rosner, S. Sathish, N. Meyendorf, Thermographic characterisation of fatigue, in: D. Thompson, D. Chimenti (Eds.) Review of progress in QNDE, New York, 2001.
[85] M.M. Pedersen, Introduction to metal fatigue, in, Aarhus University, 2018.
[86] R.I. Stephens, A. Fatemi, R.R. Stephens, H.O. Fuchs, Metal fatigue in engineering, 2nd ed., Wiley, 2000.

[87] E.H. Jordan, Notch-root plastic response by temperature measurement, Experimental Mechanics, 25 (1985) 24-31.
[88] A. Nourian-Avval, M.M. Khonsari, Rapid prediction of fatigue life based on thermodynamic entropy generation, International Journal of Fatigue, 145 (2021) 106105.
[89] J.A. Ewing, W. Rosenhain, Experiments in micro-metallurgy:- effects of strain. Preliminary notice, Proceedings of the Royal Society of London, 65 (1900) 85-90.
[90] J. Bauschinger, Ueber die veranderungen der elastizitatsgrenze und der festigkeit des eisens und stahls durch strecken, quetschen, erwarmen abkiihlen und durch oftmals wiederholte belastung, Mitt: Mech-Tech Lab., XIII Miinchen, (1986).
[91] A.L. Audenino, E.M. Zanetti, P.M. Calderale, Assessment of internal damping in uniaxially stressed metals: exponential and autoregressive methods, Journal of Dynamic Systems, Measurement, and Control, 120 (1998) 177-184.
[92] Y. Murakami, Metal fatigue: effects of small defects and nonmetallic inclusions, 2nd ed., Academic Press, 2019.
[93] J.A. Ewing, J.C.W. Humfrey, VI. The fracture of metals under repeated alternations of stress, Philosophical Transactions of the Royal Society of London. Series A, Containing Papers of a Mathematical or Physical Character, 200 (1903) 241-250.
[94] T. Sakai, A. Nakagawa, N. Oguma, Y. Nakamura, A. Ueno, S. Kikuchi, A. Sakaida, A review on fatigue fracture modes of structural metallic materials in very high cycle regime, International Journal of Fatigue, 93 (2016) 339-351.
[95] S. Srivatsan, T.S. Sudarshan, Mechanisms of fatigue crack initiation in metals: role of aqueous environments, Journal of Materials Science, 23 (1988) 1521-1533.
[96] A. Chrysochoos, V. Huon, F. Jourdan, J.-M. Muracciole, R. Peyroux, B. Wattrisse, Use of full-field digital image correlation and infrared thermography measurements for the thermomechanical analysis of material behaviour, Strain, 46 (2010) 117-130.
[97] H. Mughrabi, Dislocations in Fatigue, in: Dislocations and properties of real materials, Institute of Metals, London, 1985.
[98] O. Scott-Emuakpor, T. George, C. Cross, M.-H.H. Shen, Hysteresis-loop representation for strain energy calculation and fatigue assessment, The Journal of Strain Analysis for Engineering Design, 45 (2010) 275-282.
[99] D.R. Fancher, Stress-strain hysteresis loops and rheological epicycles, in, The University of Arizona, 1943.
[100] B.J. Lazan, Effect of damping constants and stress distribution on the resonance response of members, Journal of Applied Mechanics, 20 (1953) 201-209.
[101] R. De Finis, D. Palumbo, U. Galietti, On the relationship between mechanical energy rate and heat dissipated rate during fatigue for a C45 steel depending on stress ratio, Fatigue & Fracture of Engineering Materials & Structures, 44 (2021) 2781-2799.
[102] C. Colombo, M. Sansone, L. Patriarca, L. Vergani, Rapid estimation of fatigue limit for C45 steel by thermography and digital image correlation, The Journal of Strain Analysis for Engineering Design, 56 (2021) 478-491.
[103] J.L. Chaboche, D. Nouailhas, D. Pacou, P. Paulmier, Modeling of the cylic response and ratchetting effects on inconel-718 alloy, European Journal of Mechanics A-solids, 10 (1991) 101-121.
[104] C.T. Lachowicz, Calculation of the elastic–plastic strain energy density under cyclic and random loading, International Journal of Fatigue, 23 (2001) 643-652.
[105] C. Colombo, G. Fumagalli, F. Bolzoni, G. Gobbi, L. Vergani, Fatigue behavior of hydrogen pre-charged low alloy Cr–Mo steel, International Journal of Fatigue, 83 (2016) 2-9.
[106] V. Crupi, An unifying approach to assess the structural strength, International Journal of Fatigue, 30 (2008) 1150-1159.
[107] N. Connesson, F. Maquin, F. Pierron, Experimental energy balance during the first cycles of cyclically loaded specimens under the conventional yield stress, Experimental Mechanics, 51 (2011)

23-44.
[108] F. Maquin, F. Pierron, Heat dissipation measurements in low stress cyclic loading of metallic materials: From internal friction to micro-plasticity, Mechanics of Materials, 41 (2009) 928-942.
[109] M.P. Luong, Fatigue limit evaluation of metals using an infrared thermographic technique, Mechanics of Materials, 28 (1998) 155-163.
[110] M. Naderi, M.M. Khonsari, An experimental approach to low-cycle fatigue damage based on thermodynamic entropy, International Journal of Solids and Structures, 47 (2010) 875-880.
[111] C. Mareau, Micromechanical modeling of self-heating and microplasticity in steels under cyclic loading, in, Arts et Métiers ParisTech, 2007.
[112] C. Doudard, S. Calloch, P. Cugy, A. Galtier, F. Hild, A probabilistic two-scale model for high-cycle fatigue life predictions, Fatigue & Fracture of Engineering Materials & Structures, 28 (2005) 279-288.
[113] A.E. Morabito, A. Chrysochoos, V. Dattoma, U. Galietti, Analysis of heat sources accompanying the fatigue of 2024 T3 aluminium alloys, International Journal of Fatigue, 29 (2007) 977-984.
[114] A. Zhao, J. Xie, Y. Zhao, C. Liu, J. Zhu, G. Qian, S. Wang, Y. Hong, Fatigue limit evaluation via infrared thermography for a high strength steel with two strength levels, Engineering Fracture Mechanics, 268 (2022) 108460.
[115] A. Chrysochoos, B. Wattrisse, J.-M. Muracciole, Y.E. Kaïm, Fields of stored energy associated with localized necking of steel, Journal of Mechanics of Materials and Structures, 4 (2009).
[116] H. Louche, A. Chrysochoos, An infrared image processing to analyse the calorific effects accompanying strain localisation, International Journal of Engineering Science, 38 (2000) 1759-1788.
[117] R.D. Finis, D. Palumbo, A. Pirinu, A. Saponaro, F.W. Panella, R. Nobile, U. Galietti, Fatigue behaviour assessment of C45 steel by means of energy-based methods, in: IOP Conference Series: Materials Science and Engineering, 2021.
[118] C.E. Stromeyer, W.E. Dalby, The determination of fatigue limits under alternating stress conditions, Proceedings of the Royal Society of London. Series A, Containing Papers of a Mathematical and Physical Character, 90 (1914) 411-425.
[119] G. Curti, G.L. Rosa, M. Orlando, A. Risitano, Analisi tramite infrarosso termico della temperatura limite in prove di fatica, XIV Convegno Nazionale AIAS, (1986).
[120] M. Zaeimi, R. De Finis, D. Palumbo, U. Galietti, Fatigue limit estimation of metals based on the thermographic methods: A comprehensive review, Fatigue & Fracture of Engineering Materials & Structures, 47 (2024) 611-646.
[121] V. Crupi, E. Guglielmino, M. Maestro, A. Marinò, Fatigue analysis of butt welded AH36 steel joints: thermographic method and design S–N curve, Marine Structures, 22 (2009) 373-386.
[122] X.G. Wang, V. Crupi, X.L. Guo, Y.G. Zhao, Quantitative Thermographic Methodology for fatigue assessment and stress measurement, International Journal of Fatigue, 32 (2010) 1970-1976.
[123] G. Fargione, A. Geraci, G. La Rosa, A. Risitano, Rapid determination of the fatigue curve by the thermographic method, International Journal of Fatigue, 24 (2002) 11-19.
[124] X.G. Wang, V. Crupi, X.L. Guo, E. Guglielmino, A thermography-based approach for structural analysis and fatigue evaluation, Proceedings of the Institution of Mechanical Engineers, Part C: Journal of Mechanical Engineering Science, 226 (2011) 1173-1185.
[125] X.G. Wang, V. Crupi, C. Jiang, E. Guglielmino, Quantitative Thermographic Methodology for fatigue life assessment in a multiscale energy dissipation framework, International Journal of Fatigue, 81 (2015) 249-256.
[126] E. Feng, X. Wang, C. Jiang, V. Crupi, Quantitative thermographic method for fatigue life prediction under variable amplitude loading, Fatigue & Fracture of Engineering Materials & Structures, 45 (2022) 1199-1212.
[127] A. Aeran, S. Vantadori, A. Carpinteri, S.C. Siriwardane, D. Scorza, Novel non-linear relationship to evaluate the critical plane orientation, International Journal of Fatigue, 124 (2019) 537-543.

[128] Y. Huang, S.X. Li, S.E. Lin, C.N. Shih, Using the method of infrared sensing for monitoring fatigue process of metals, Materials Evaluation, 42 (1984) 1020-1024.
[129] R. Botny, J. Kaleta, A method for determining the heat energy of the fatigue process in metals under uniaxial stress: Part 1. Determination of the amount of heat liberated from a fatigue-tested specimen, International Journal of Fatigue, 8 (1986) 29-33.
[130] N.G. Meyendorf, H. Rösner, V. Kramb, S. Sathish, Thermo-acoustic fatigue characterization, Ultrasonics, 40 (2002) 427-434.
[131] M. Liakat, M.M. Khonsari, An experimental approach to estimate damage and remaining life of metals under uniaxial fatigue loading, Materials & Design, 57 (2014) 289-297.
[132] M. Liakat, M.M. Khonsari, Rapid estimation of fatigue entropy and toughness in metals, Materials & Design (1980-2015), 62 (2014) 149-157.
[133] W. Weber, Ueber die specifische wärme fester körper, insbesondere der metalle, Annalen der Physik, 96 (1830) 177-213.
[134] W. Thomson, II. On the dynamical theory of heat, with numerical results deduced from Mr. Joule's equivalent of a thermal unit, and M. Regnault's observations on steam, The London, Edinburgh, and Dublin Philosophical Magazine and Journal of Science, 4 (1852) 8-21.
[135] H. N., C. W.M., Thermoelastic stress analysis, New York: National Engineering Laboratory, Adam Hilger, 1991.
[136] A.K. Wong, J.G. Sparrow, S.A. Dunn, On the revised theory of the thermoelastic effect, Journal of Physics and Chemistry of Solids, 49 (1988) 395-400.
[137] G. Pitarresi, E.A. Patterson, A review of the general theory of thermoelastic stress analysis, The Journal of Strain Analysis for Engineering Design, 38 (2003).
[138] A.K. Wong, R. Jones, J.G. Sparrow, Thermoelastic constant or thermoelastic parameter?, Journal of Physics and Chemistry of Solids, 48 (1987) 749-753.
[139] A.K. Wong, S.A. Dunn, J.G. Sparrow, Residual stress measurement by means of the thermoelastic effect, Nature, 332 (1988) 613-615.
[140] T. Sakagami, S. Kubo, E. Tamura, T. Nishimura, Identification of plastic-zone based on double frequency lock-in thermographic temperature measurement, in, 2013.
[141] U. Galietti, D. Palumbo, R.D. Finis, F. Ancona, Fatigue damage evaluation with new thermal methods, in: 3rd International Workshop on Advanced Infrared Technology and Applications, Tourin, Italy, 2013.
[142] U. Galietti, D. Palumbo, R.D. Finis, F. Ancona, Fatigue limit evaluation of martensitic steels with thermal methods, in: Conference QIRT 2014, Bordeaux, France, 2014.
[143] J.M. Dulieu-Barton, Introduction to thermoelastic stress analysis, Strain, 35 (1999) 35-39.
[144] R. Cappello, G. Meneghetti, M. Ricotta, G. Pitarresi, On the correlation of temperature harmonic content with energy dissipation in C45 steel samples under fatigue loading, Mechanics of Materials, 168 (2022) 104271.
[145] R. De Finis, D. Palumbo, U. Galietti, Mechanical behaviour of stainless steels under dynamic loading: an investigation with thermal methods, Journal of Imaging, 2 (2016).
[146] T.M. Jasper, LXVII. The value of the energy relation in the testing of ferrous metals at varying ranges of stress and at intermediate and high temperatures, The London, Edinburgh, and Dublin Philosophical Magazine and Journal of Science, 46 (1923) 609-627.
[147] R.F. Hanstock, Damping capacity, strain hardening and fatigue, Proceedings of the Physical Society, 59 (1947) 275.
[148] D. Liao, S.-P. Zhu, J.-W. Gao, J. Correia, R. Calçada, G. Lesiuk, Generalized strain energy density-based fatigue indicator parameter, International Journal of Mechanical Sciences, 254 (2023) 108427.
[149] S.-P. Zhu, Y. Liu, Q. Liu, Z.-Y. Yu, Strain energy gradient-based LCF life prediction of turbine discs using critical distance concept, International Journal of Fatigue, 113 (2018) 33-42.
[150] D. Liao, S.-P. Zhu, Energy field intensity approach for notch fatigue analysis, International

Journal of Fatigue, 127 (2019) 190-202.
[151] S.-P. Zhu, Z.-Y. Yu, Q. Liu, A. Ince, Strain energy-based multiaxial fatigue life prediction under normal/shear stress interaction, International Journal of Damage Mechanics, 28 (2019) 708-739.
[152] D. Shiozawa, T. Inagawa, T. Washio, T. Sakagami, Accuracy improvement in dissipated energy measurement by using phase information, Measurement Science and Technology, 28 (2017) 044004.
[153] R. Cappello, S. Cutugno, G. Pitarresi, Detection of crack-closure during fatigue loading by means of Second Harmonic Thermoelastic Stress Analysis, Procedia Structural Integrity, 39 (2022) 179-193.
[154] M. Ricotta, M. Veronese, G. Meneghetti, Estimating the Specific Heat Loss from Temperature Measurements in Tension-Tension Fatigue: Theory and Experiments, in: P. Rizzo, A. Milazzo (Eds.) European Workshop on Structural Health Monitoring, Springer International Publishing, Cham, 2023, pp. 600-609.
[155] G. Meneghetti, M. Ricotta, Evaluating the heat energy dissipated in a small volume surrounding the tip of a fatigue crack, International Journal of Fatigue, 92 (2016) 605-615.
[156] G. Meneghetti, M. Ricotta, The heat energy dissipated in the material structural volume to correlate the fatigue crack growth rate in stainless steel specimens, International Journal of Fatigue, 115 (2018) 107-119.
[157] G. Meneghetti, M. Ricotta, The use of the specific heat loss to analyse the low- and high-cycle fatigue behaviour of plain and notched specimens made of a stainless steel, Engineering Fracture Mechanics, 81 (2012) 2-16.
[158] M. Ricotta, G. Meneghetti, B. Atzori, G. Risitano, A. Risitano, Comparison of experimental thermal methods for the fatigue limit evaluation of a stainless steel, Metals, 9 (2019) 677.
[159] D. Rigon, M. Ricotta, G. Meneghetti, An analysis of the specific heat loss at the tip of severely notched stainless steel specimens to correlate the fatigue strength, Theoretical and Applied Fracture Mechanics, 92 (2017) 240-251.
[160] D. Skibicki, A. Lipski, Ł. Pejkowski, Evaluation of plastic strain work and multiaxial fatigue life in CuZn37 alloy by means of thermography method and energy-based approaches of Ellyin and Garud, Fatigue & Fracture of Engineering Materials & Structures, 41 (2018) 2541-2556.
[161] M. Naderi, M. Khonsari, Real-time fatigue life monitoring based on thermodynamic entropy, Structural Health Monitoring, 10 (2011) 189-197.
[162] J.Y. Jang, M.M. Khonsari, On the evaluation of fracture fatigue entropy, Theoretical and Applied Fracture Mechanics, 96 (2018) 351-361.
[163] M. Liakat, M.M. Khonsari, On the anelasticity and fatigue fracture entropy in high-cycle metal fatigue, Materials & Design, 82 (2015) 18-27.
[164] A. Haghshenas, J.Y. Jang, M.M. Khonsari, On the intrinsic dissipation and fracture fatigue entropy of metals, Mechanics of Materials, 155 (2021) 103734.
[165] Q. Guo, X. Guo, J. Fan, R. Syed, C. Wu, An energy method for rapid evaluation of high-cycle fatigue parameters based on intrinsic dissipation, International Journal of Fatigue, 80 (2015) 136-144.
[166] M. Mehdizadeh, M.M. Khonsari, On the role of internal friction in low-and high-cycle fatigue, International Journal of Fatigue, 114 (2018) 159-166.
[167] A. Risitano, G. Risitano, Determining fatigue limits with thermal analysis of static traction tests, Fatigue & Fracture of Engineering Materials & Structures, 36 (2013) 631-639.
[168] C.E. Bottani, G. Caglioti, Thermoelastic instabilities in metals, Physica Scripta, T1 (1982) 65-70.
[169] A. Risitano, D. Corallo, G. Risitano, A. Sirugo, Determinazione del limite di fatica mediante prove quasistatiche, in: Proceedings XXXIX AIAS National Conference, 2010.
[170] G. Risitano, E. Guglielmino, D. Santonocito, Rapid energetic approaches for the fatigue limit assessment in a medium carbon steel, Procedia Structural Integrity, 33 (2021) 748-756.
[171] P. Foti, G. Risitano, F. Berto, D. Santonocito, Evaluation of the energetic release during tensile tests in notched specimens by means of experimental and numerical techniques, IOP Conference

Series: Materials Science and Engineering, 1038 (2021) 012038.
[172] G. Risitano, D. Santonocito, Experimental and numerical assessment of the end of the thermoelastic effect during static traction test, Procedia Structural Integrity, 28 (2020) 1449-1457.
[173] P. Corigliano, F. Cucinotta, E. Guglielmino, G. Risitano, D. Santonocito, Fatigue assessment of a marine structural steel and comparison with thermographic method and static thermographic method, Fatigue & Fracture of Engineering Materials & Structures, 43 (2020) 734-743.
[174] A. International, ASTM E 466, Standard practice for conducting force controlled constant amplitude axial fatigue tests of metallic materials, in, 1996.
[175] R. De Finis, D. Palumbo, L.M. Serio, L.A.C. De Filippis, U. Galietti, Correlation between thermal behaviour of AA5754-H111 during fatigue loading and fatigue strength at fixed number of cycles, Materials, 11 (2018) 719.
[176] S. Deane, N.P. Avdelidis, C. Ibarra-Castanedo, H. Zhang, H. Yazdani Nezhad, A.A. Williamson, T. Mackley, X. Maldague, A. Tsourdos, P. Nooralishahi, Comparison of Cooled and Uncooled IR Sensors by Means of Signal-to-Noise Ratio for NDT Diagnostics of Aerospace Grade Composites, Sensors (Basel), 20 (2020).
[177] A. Chrysochoos, B. Berthel, F. Latourte, S. Pagano, B. Wattrisse, B. Weber, Local energy approach to steel fatigue, Strain, 44 (2008) 327-334.
[178] R. De Finis, D. Palumbo, M.M. da Silva, U. Galietti, Is the temperature plateau of a self-heating test a robust parameter to investigate the fatigue limit of steels with thermography?, Fatigue & Fracture of Engineering Materials & Structures, 41 (2018) 917-934.
[179] R.D. Finis, D. Palumbo, A. Pirinu, A. Saponaro, F.W. Panella, R. Nobile, U. Galietti, Fatigue behaviour assessment of C45 steel by means of energy-based methods, IOP Conference Series: Materials Science and Engineering, 1038 (2021) 012015.
[180] A. Risitano, G. Fargione, E. Guglielmino, Definition of the linearity loss of the surface temperature in static tensile tests, Frattura ed Integrità Strutturale, 8 (2014) pages 201-210.
[181] R. Kawai, T. Yoshikawa, Y. Kurokawa, Y. Irie, H. Inoue, Rapid evaluation of fatigue limit using infrared thermography: comparison between two methods for quantifying temperature evolution, Mechanical Engineering Journal, 4 (2017) 17-00009-00017-00009.
[182] R. De Finis, D. Palumbo, F. Ancona, U. Galietti, Fatigue behaviour of stainless steels: a multi-parametric approach, in: S. Quinn, X. Balandraud (Eds.) Residual Stress, Thermomechanics & Infrared Imaging, Hybrid Techniques and Inverse Problems, Volume 9, Springer International Publishing, Cham, 2017, pp. 1-8.
[183] P. Lepitre, S. Calloch, M. Dhondt, M. Surand, C. Doudard, Identification of the damage scenarios under cyclic loading of a coated 300M steel by infrared thermography measurements, Physical Sciences Forum, 4 (2022) 30.
[184] A. Fernández-Canteli, E. Castillo, A. Argüelles, P. Fernández, M. Canales, Checking the fatigue limit from thermographic techniques by means of a probabilistic model of the epsilon–N field, International Journal of Fatigue, 39 (2012) 109-115.
[185] J.J.R. Faria, L.G.A. Fonseca, A.R. de Faria, A. Cantisano, T.N. Cunha, H. Jahed, J. Montesano, Determination of the fatigue behavior of mechanical components through infrared thermography, Engineering Failure Analysis, 134 (2022) 106018.
[186] A. Mahmoudi, M.M. Khonsari, A Thermodynamic Framework for Rapid Prediction of S-N Curves Using Temperature Rise at Steady-State, Experimental Mechanics, (2023).
[187] A. Aghayan, P. Jaiswal, H.R. Siahkoohi, Seismic denoising using the redundant lifting scheme, GEOPHYSICS, 81 (2016) V249-V260.
[188] Q. Guo, F. Zaïri, W. Yang, Evaluation of intrinsic dissipation based on self-heating effect in high-cycle metal fatigue, International Journal of Fatigue, 139 (2020) 105653.
[189] D. Palumbo, R. De Finis, F. Ancona, U. Galietti, Damage monitoring in fracture mechanics by evaluation of the heat dissipated in the cyclic plastic zone ahead of the crack tip with thermal measurements, Engineering Fracture Mechanics, 181 (2017) 65-76.

[190] M. Zaeimi, R. De Finis, D. Palumbo, U. Galietti, Numerical Simulation of the Heat Dissipation During the Fatigue Test, in: C. Franck, K. Kasza, J. Estrada, R. De Finis, G. Ólafsson, S. Gururaja, J. Furmanski, A. Forster, P. Kolluru, M. Prime, T. Berfield, C. Aydiner (Eds.) Challenges in Mechanics of Biological Systems and Materials, Thermomechanics and Infrared Imaging, Time Dependent Materials and Residual Stress, Volume 2, Springer Nature Switzerland, Cham, 2024, pp. 83-90.
[191] The MathWorks, Inc. (2023). MATLAB version: R2023b. Accessed: January 14, 2024. Available: https://it.mathworks.com/help/images/edge-detection.html.
[192] M.H. Sadd, Elasticity: Theory, Applications, and Numerics, 3rd ed., Elsevier, 2014.